

Observations in the plasma sheet during substorm activity

Thesis submitted for the degree of
Doctor of Philosophy at the
University of Leicester

By

Jonathan Storey

Radio and Space Plasma Physics Group
Department of Physics and Astronomy
University of Leicester

February 2000

UMI Number: U121392

All rights reserved

INFORMATION TO ALL USERS

The quality of this reproduction is dependent upon the quality of the copy submitted.

In the unlikely event that the author did not send a complete manuscript and there are missing pages, these will be noted. Also, if material had to be removed, a note will indicate the deletion.



UMI U121392

Published by ProQuest LLC 2013. Copyright in the Dissertation held by the Author.
Microform Edition © ProQuest LLC.

All rights reserved. This work is protected against
unauthorized copying under Title 17, United States Code.



ProQuest LLC
789 East Eisenhower Parkway
P.O. Box 1346
Ann Arbor, MI 48106-1346

Observations in the plasma sheet during substorm activity

Jonathan Storey

This thesis presents a statistical study of the plasma sheet location and thickness of the plasma sheet boundary layer, including the effect of magnetic and solar wind conditions. Next are presented two case studies of in-situ particle data from the Polar spacecraft as it entered and passed through the near-Earth plasma sheet during substorm activity. These data sets are compared with in-situ magnetic field measurements, from the Magnetic Fields Experiment (MFE), and remote observations of the aurora from the Ultra-Violet Imager (UVI). The latter, in conjunction with ground magnetograms, allow us to place the in-situ plasma flows in the overall context of the substorm phases. In the first case study the spacecraft entered the plasma sheet boundary layer (PSBL) and observed field-aligned ion beams, which were connected with field-aligned current signatures in MFE. When Polar entered the PSBL its footprint mapped to the poleward edge of an auroral double oval. Then, a decrease in the number and energy of the ions occurred, which coincided with the spacecraft footprint entering the central low-luminosity region of the UV double oval. After the spacecraft entered the CPS an expansion phase onset occurred, and Polar observed large ion count rate increases and dipolarisation of the magnetic field. When Polar entered the PSBL in the second case study, which again coincided with entry into the auroral oval, there was evidence of pseudobreakups. Then the PSBL retreated over the spacecraft, which was mirrored in the ionosphere by equatorward motion of the auroral oval. Polar returned to the PSBL and rapidly entered the CPS when a substorm expansion phase onset occurred. Due to the large amount of substorm activity during these case studies, emphasis is placed on the use of both remote observations of the aurora and ground-based data to place the in-situ measurements in context.

Acknowledgements

I would like to thank Dr. Mark Lester (supervisor) for his assistance and blatant overuse of his red pen throughout my postgraduate studies. I would also like to thank Mr. Derek Fry for getting me interested in Physics in the first place.

Thanks also to everyone in the Radio and Space Plasma Physics Group for constructive comments, help and coding assistance, as well as dragging me off for coffee when the need arose.

I would also like to thank the Polar Operations Group at R.A.L. for providing some of the coding and lots of the data used in this study. Also, thanks to Reiner Friedel at LANL and Jeremy Faden at Iowa for writing the PaPCo package and making much of the data available.

Many thanks to all of the Polar instrument teams, without whom this work could not have been performed, specifically the CAMMICE, CEPPAD, Hydra, MFE and UVI teams. I would also like to thank the IMAGE, Greenland and SAMNET magnetometer institutions for providing the ground magnetic data used in this thesis. Also thanks to PPARC for funding my studies.

I would also like to thank my friends up in Leeds, especially Mark and Stu, for forcing me to go out to the pub even though I really wanted to keep working.

Finally I would like to thank my Mum and Dad, my Grandparents and Dinah for love and support throughout the last 25 years. Thank you.

For Gramps, Grandad and Dinah

Contents

Chapter 1	The Solar-Terrestrial Environment and the Plasma Sheet	1
1.1	Introduction	1
1.2	The Sun and the Solar Wind	1
1.3	The Magnetosphere	3
1.4	Magnetospheric Structure	4
1.4.1	The Tail Lobes	4
1.4.2	The Plasma Sheet	5
1.4.3	The Radiation Belts	5
1.4.4	The Plasmasphere	5
1.5	The Ionosphere	6
1.6	The Aims of the study	7
Chapter 2	Review of Substorms and Associated Signatures	8
2.1	Introduction	8
2.2	Substorm Phases	8
2.2.1	The Growth Phase	8
2.2.2	The Expansion Phase	9
2.2.3	The Recovery Phase	10
2.3	Auroral Observations	10
2.4	Ground Magnetic Variations	12
2.5	Magnetospheric Magnetic Variations	14
2.6	Plasma Sheet Variations	15
2.7	Substorm Phenomenological Models	17
2.7.1	Near-Earth Neutral Line Model	18
2.7.2	Flow-Braking Model	19
2.7.3	Current Disruption Model	20
2.7.4	Boundary-Layer-Dynamics Model	21
2.7.5	Magnetosphere-Ionosphere Coupling Model	22
2.7.6	Ballooning Instability Model	22
2.7.7	Other Models	23
2.7.8	Summary: The Kiruna Conjecture	23
Chapter 3	Instrumentation	26
3.1	Introduction	26
3.2	The Polar Spacecraft	26
3.2.1	Charge And Mass Magnetospheric Ion Composition Experiment	27

3.2.2	Hot Plasma Analyser (Hydra)	29
3.2.3	Comprehensive Energetic Particle and Pitch Angle Distribution Experiment	30
3.2.4	Magnetic Fields Experiment	31
3.2.5	Ultra-Violet Imager	32
3.3	Ground Magnetometers	33
3.4	The Wind Spacecraft	34
3.4.1	The Magnetic Field Investigation	35
3.4.2	The Solar Wind Experiment	35
3.5	The Los Alamos Geostationary Satellite Fleet	36
3.6	Concluding Remarks	37
Chapter 4	Statistical Study of the Plasma Sheet	38
4.1	Introduction	38
4.2	Determination of Location of Plasma Regimes	38
4.3	PSBL Location	40
4.4	CPS Location	43
4.5	Cause of Seasonal Variation	44
4.6	PSBL Thickness	46
4.7	Effect of Magnetic Activity	48
4.8	Effect of IMF B_z	49
4.9	Effect of Solar Wind Dynamic Pressure	53
4.10	Other Parameters	53
4.11	Summary	54
Chapter 5	Investigation of substorm-associated features in the plasma sheet observed by the Polar satellite: 9 th April 1996 case study	56
5.1	Introduction	56
5.2	The Interval – 9 th April 1996	56
5.3	Observations	56
5.3.1	Ground Magnetometer Networks	56
5.3.2	LANL Geosynchronous Spacecraft	61
5.3.3	Polar Ultra-Violet Imager	61
5.3.4	Polar CAMMICE	63
5.3.5	Other Particle Instruments: CEPPAD and Hydra	64
5.3.6	Polar Magnetic Fields Experiment	67
5.4	Discussion	68
5.5	Summary	74

Chapter 6	Pseudobreakup and Substorm effects on the high latitude plasma sheet: 17th May 1996 case study	77
6.1	Introduction	77
6.2	The Interval – 17 th May 1996	77
6.3	Observations	77
6.3.1	Solar Wind Conditions	77
6.3.2	Ground Magnetometer Networks	78
6.3.3	Polar Ultra-Violet Imager	81
6.3.4	Polar CAMMICE	83
6.3.5	Other Particle Instruments: CEPPAD and Hydra	85
6.3.6	Polar Magnetic Field Experiment	86
6.4	Discussion	88
6.5	Summary	93
Chapter 7	Summary and Conclusions	95
7.1	Introduction	95
7.2	Summary of Results	95
7.3	Further Work	100
Appendix 1	Co-ordinate Systems	102
Appendix 2	Polar UVI images from 9th April 1996	103
Appendix 3	Polar UVI Images from 17th May 1996	104
References		105

CHAPTER 1

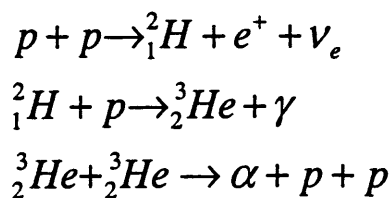
The Solar-Terrestrial Environment

1.1. Introduction

Magnetospheric substorms have been one of the most stimulating research topics in solar terrestrial physics for many years, although much work still needs to be done. One of the main problems with studying substorms in the magnetosphere is the lack of continuous measurements over a large volume of the magnetosphere. As satellites are the only method of directly measuring the plasma properties the only data available are point measurements made by spacecraft. Although the number of available spacecraft is increasing there are many regions only lightly sampled. One such area, the high-latitude plasma sheet, is investigated in this thesis. The aim of this chapter is to introduce the necessary background material that is needed to place the thesis material in the general context of the field of Solar-Terrestrial Physics. A more detailed review of substorms and the plasma sheet can be found in Chapter 2.

1.2. The Sun and the Solar Wind

In astronomical terms, the Sun is an average middle-aged star of spectral type G2V and magnitude 4.8. At the core of the Sun nuclear fusion occurs continuously and the temperatures are believed to exceed 15 million K. The fusion generates $\sim 4 \times 10^{26}$ W inside the Sun, which must be radiated away to maintain equilibrium. The energy is produced by fusion where the dominant process is the proton-proton chain.



where 'p' is a proton, ' γ ' represents the production of a gamma ray, ' α ' is a He^{2+} particle and ' ν_e ' is a neutrino. This energy produced by this process is moved from the core primarily by radiation, but convection takes over in the outer part of the Sun. The plasma is ionised and in motion, hence we have currents that lead us to a magnetic field with a continually changing structure due to the activity in the convection layer. Figure 1.1 shows the standard model of the Sun, with variation of temperature, density and nuclear reaction rate. The convective motion from below that brings the energy from the interior disturbs the visible solar surface, producing granules. This visible surface is known as the photosphere. The other obvious

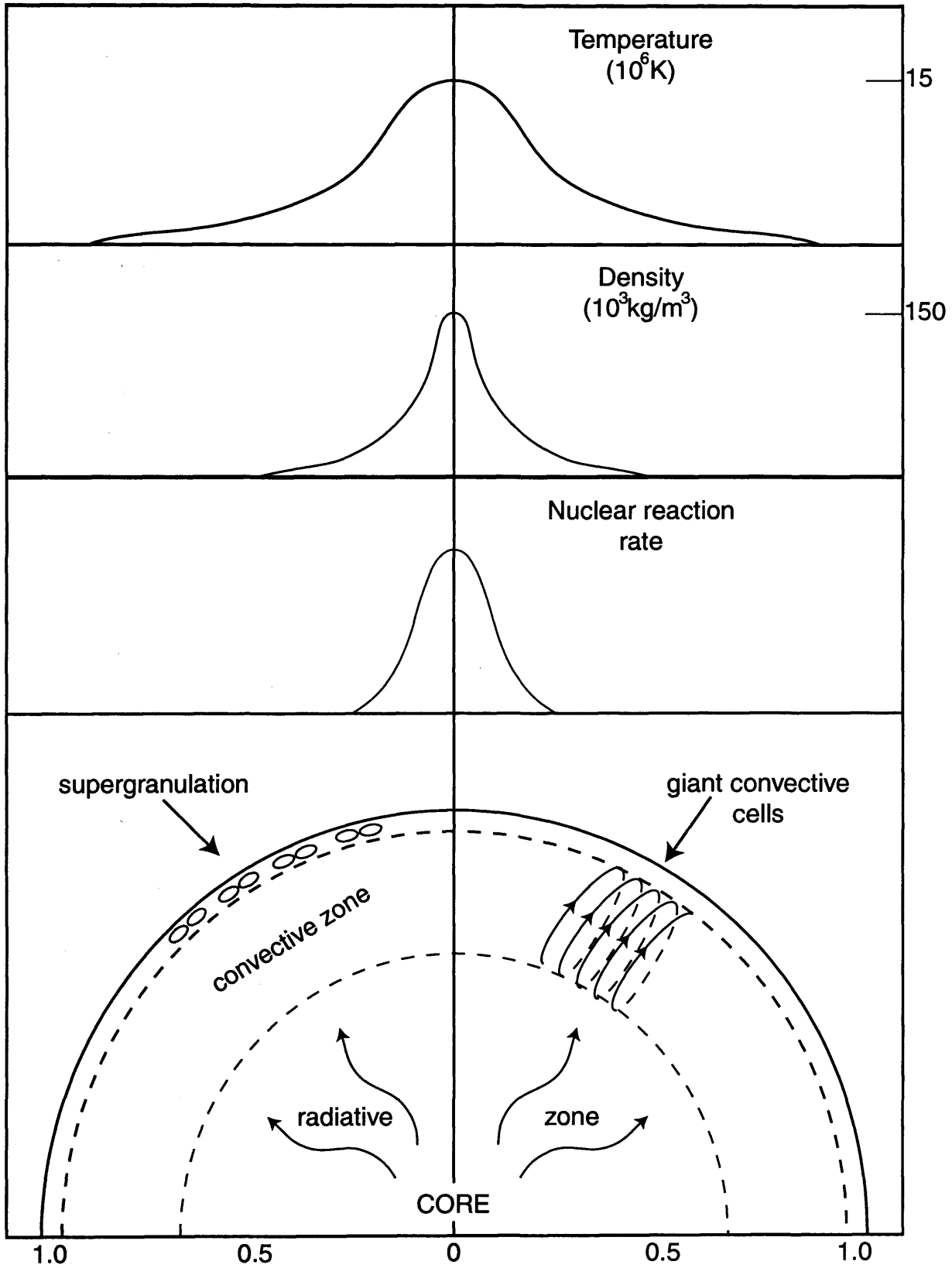


Figure 1.1: The standard solar model with the variation of temperature, density and nuclear reaction rate with radial distance [based on standard solar model of *Bahcall and Haxton, 1989*]

features on the surface are sunspots, which are magnetically disturbed regions that are cooler than the surroundings. Sunspots are too small to see with the naked eye, but with the invention of the telescope, observations were made of this phenomenon. Galileo Galilei was one of the first to study them, but very few sunspots were observed. It has since been shown that this was due to the Maunder minimum, when very few sunspots were measured from about 1645 – 1700. It was not until 1851 when it was discovered that sunspots occurred in an 11 year cycle, as shown in Figure 1.2. As this solar cycle progresses, latitudinal differential rotation of the sun causes the magnetic field to deform, strengthening near the equator and causing sunspots at higher latitudes and in larger numbers. Every 11 years the field polarity reverses, giving a total solar cycle of 22 years.

Outside the photosphere are the chromosphere and the corona. Inside the chromosphere complex structures can evolve, all of which are due to the way plasma interacts with the magnetic field. Prominences are large clouds of cool gas (larger than Earth) which lie high in the atmosphere. They can remain in place for months and, although the exact cause is unknown, one theory states they are caused by radiative instability. Bright regions are also seen, which are called active regions. The stronger active regions tend to lie above sunspots. This part of the atmosphere has temperature of $\sim 10\,000$ K compared with a temperature of ~ 2 million K in the corona. The corona is the outermost part of the solar atmosphere, in which the most spectacular solar displays are observed, such as solar flares and coronal mass ejections (CMEs). Solar flares are spectacular ‘explosions’ of magnetic energy from the corona, releasing huge quantities of energy in a very short timescale. CME’s are huge clouds of coronal plasma that are ejected from the sun at high speeds (up to 2000 km s^{-1}). The CME plasma drags the magnetic field with it and if it strikes the Earth’s magnetosphere may cause a geomagnetic storm [e.g. *Taylor et al.*, 1994].

To a solar-terrestrial physicist the Sun is much more than a massive ball of ionised gas, mainly hydrogen (90 %) and helium (10 %) [*Kivelson & Russell*, 1995]. Solar-terrestrial physicists are generally more concerned with the solar wind. This is formed by the solar corona expanding (due to the gas pressure at the base of the solar corona being sufficiently high that the plasma cannot be contained by the Sun’s gravity) and merging with the interplanetary plasma and dust to become the solar wind. Therefore the solar wind is a hot plasma that streams out of the sun at a velocity typically of hundreds of kilometres per second and fills the surrounding space, which is known as the heliosphere. The plasma leaving the solar corona moves out more or less radially and the magnetic field is dragged with it. As the sun continues to rotate, the interplanetary magnetic field (IMF) is dragged into an

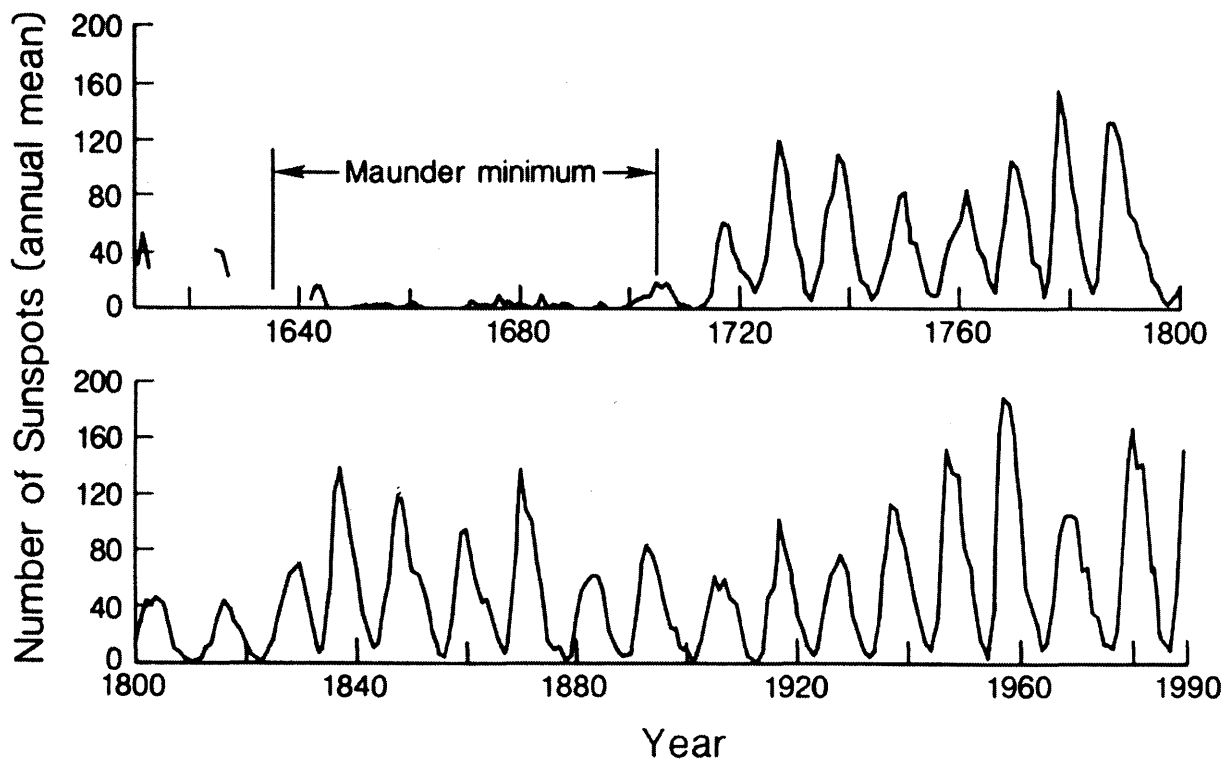


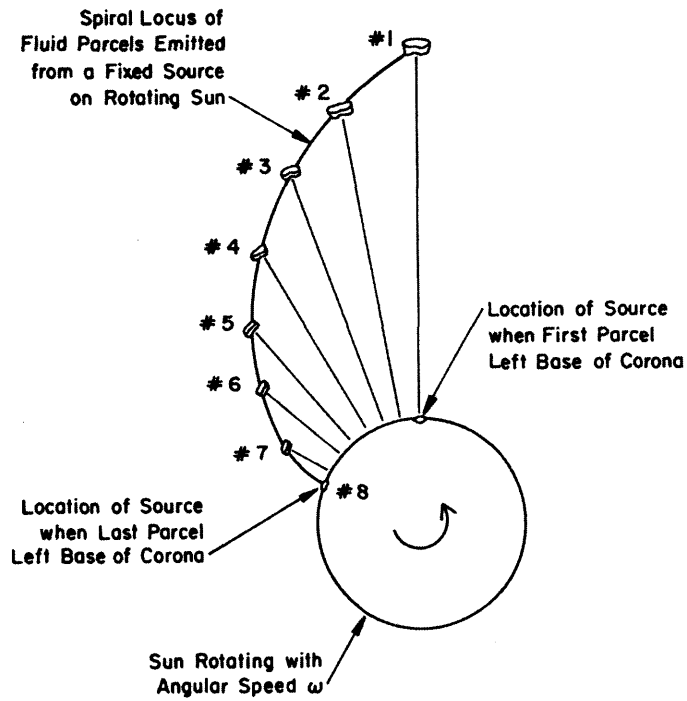
Figure 1.2: The sunspot cycle since 1610 AD including the 'Maunder Minimum'.

Archimedean spiral (Figure 1.3a), which overall is known as the Parker spiral (Figure 1.3b). The solar wind is not isotropic, but has three components with different sources. Much of the solar wind comes from coronal holes that produce high-speed streams ($>600 \text{ km s}^{-1}$ at 1 AU). Slower wind comes from open field lines (often) above active regions ($<400 \text{ km s}^{-1}$). Finally, there are very high-speed transient flows possibly associated with CMEs. The solar wind is significantly influenced by solar activity and transmits that to Earth, which is immersed within it. This is the basis of Solar-Terrestrial Relations.

1.3. The Magnetosphere

Gauss and Weber founded a chain of magnetic observatories around the world and discovered that the surface field of the Earth was almost entirely internal and principally dipolar. This dipole field is tilted at $\sim 11^\circ$ to the rotation axis with a present day moment of about $8 \times 10^{15} \text{ T m}^3$. *Chapman and Ferraro* [1930] correctly predicted that this dipole magnetic field provides an effective obstacle to the solar wind plasma. Therefore the Earth's magnetic field is 'swept' back by the solar wind, which is a supersonic ($200 - 1000 \text{ km s}^{-1}$), fully ionised plasma flowing from the Sun, as mentioned above. The 'frozen-in' field line approximation implies that the IMF cannot merge or diffuse into the Earth's field, suggesting that the solar wind cannot penetrate the Earth's field and vice-versa, and hence the Earth's field is confined to a cavity known as the magnetosphere. The magnetic pressure balance between the ram pressure of the solar wind and the Earth's magnetic field pressure determines that the boundary between the two forms at $\sim 10 R_E$, but varies with the level of magnetic activity. This boundary is known as the magnetopause. The dipole field and magnetosphere are greatly stretched tailward by the solar wind, leading to the picture shown in Figure 1.4. The 'frozen-in' approximation forbids any interchange of particles or energy between the solar wind and the magnetosphere, but there are satellite observations that contradict this and have discovered solar wind ions in the magnetosphere [e.g. *Grande et al.*, 1996]. There are other problems with this configuration, connected to the fact that the solar wind is supersonic. This is faster than a pressure wave can travel upstream towards the Sun to deflect the solar wind. Therefore a shock wave forms like that in front of a jet aircraft, which is known as the bow shock. Behind the bow shock the solar wind is slowed to subsonic speeds, allowing the shocked plasma to flow around the magnetosphere. This region is known as the magnetosheath, where the plasma has been slowed, compressed and heated, and is extremely turbulent. When the magnetosheath field differs greatly in direction from the field of the magnetosphere (such as when the IMF is aligned southward), the 'frozen-in' approximation breaks down at the magnetopause. Magnetic flux tubes from different regions now find themselves on a single flux tube. Field lines diffuse into the magnetopause current sheet from

(a)



(b)

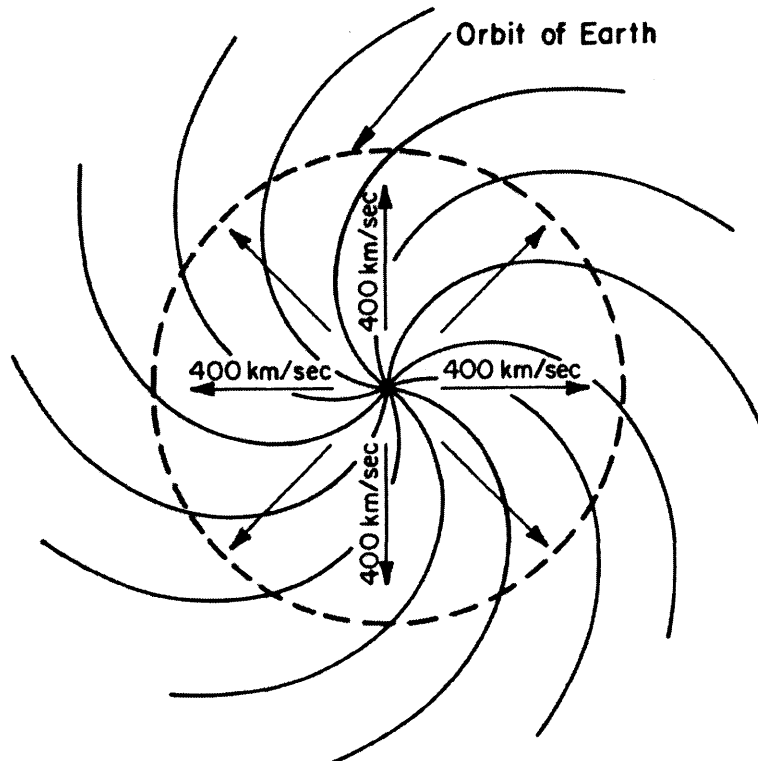


Figure 1.3: The Parker spiral. (a) schematic showing how the solar magnetic field develops into an Archimedean spiral due to rotation. (b) the overall configuration of the solar magnetic field in the ecliptic plane [adapted from *Parker, 1963*].

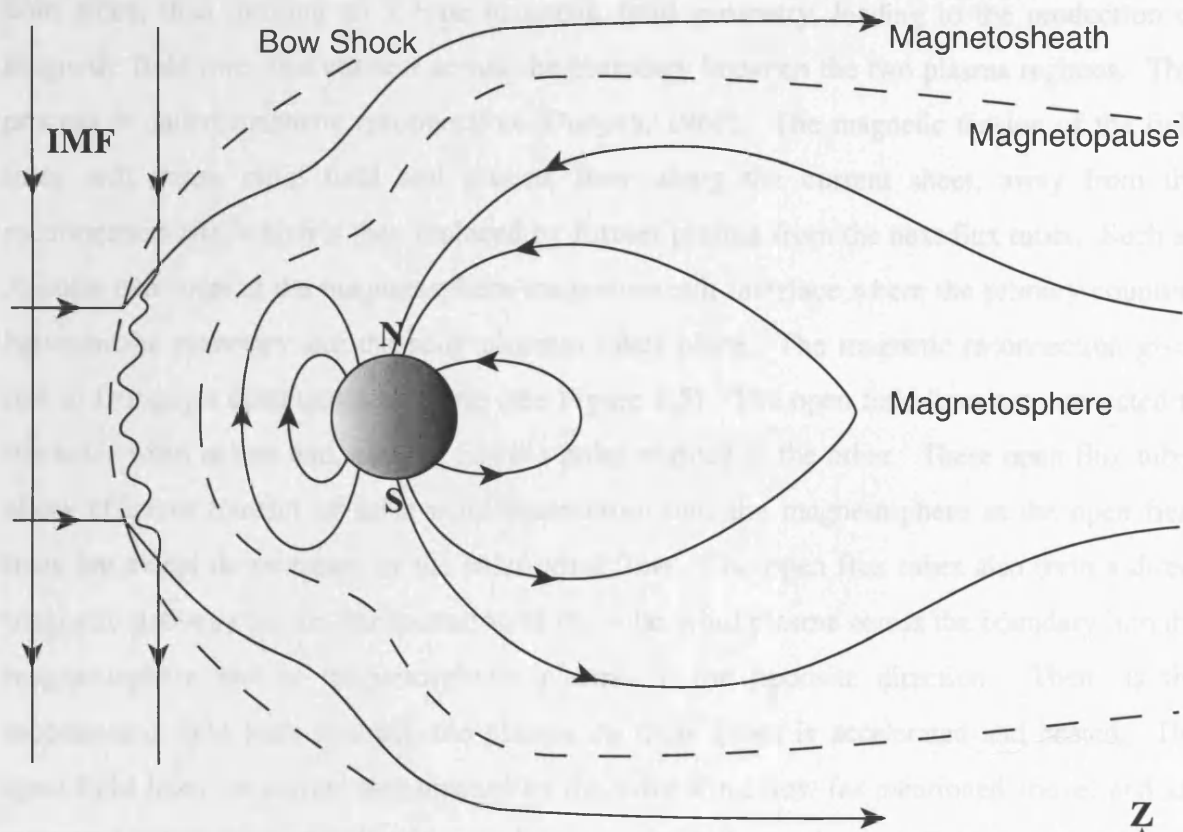


Figure 1.4: The closed magnetosphere.

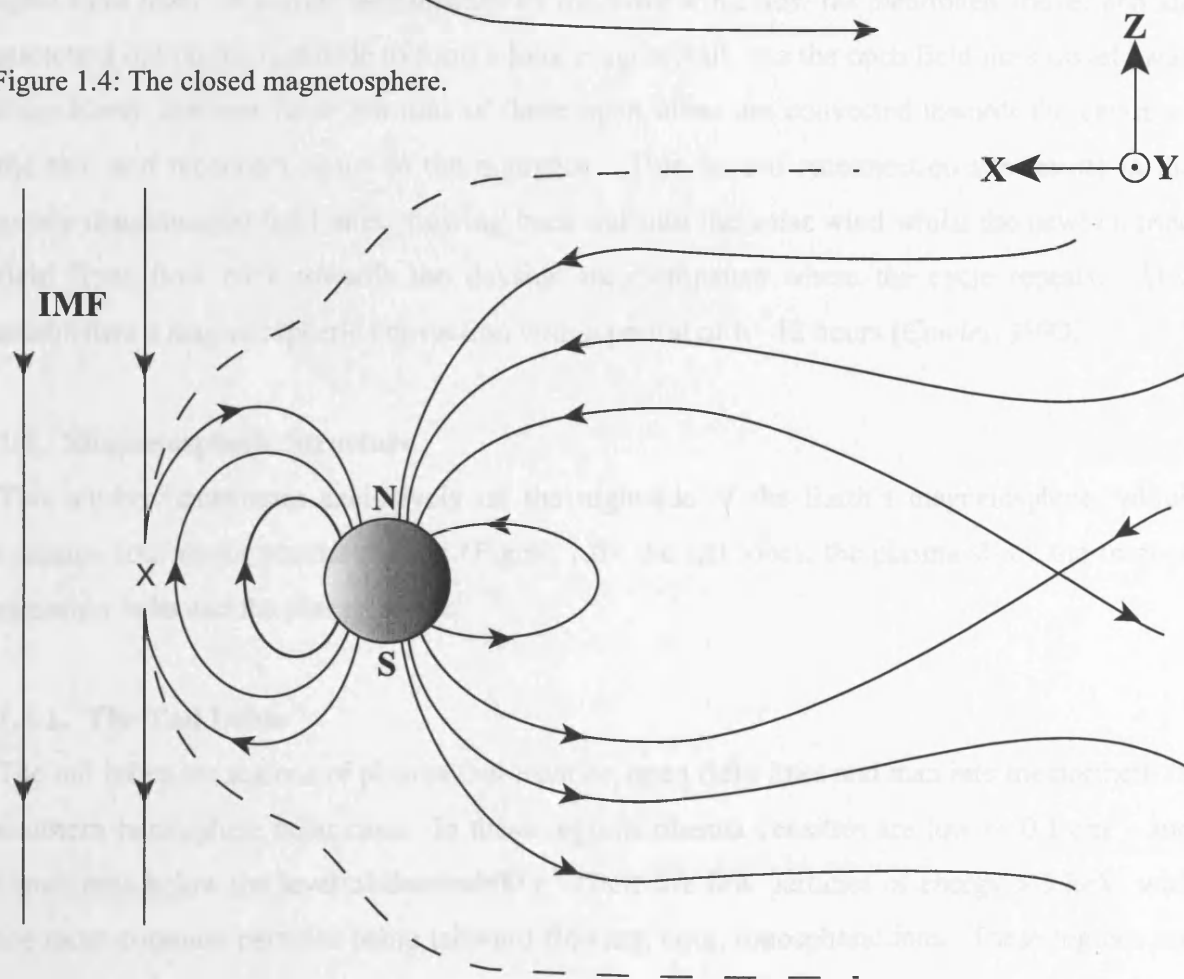


Figure 1.5: Dungey's Open magnetosphere.

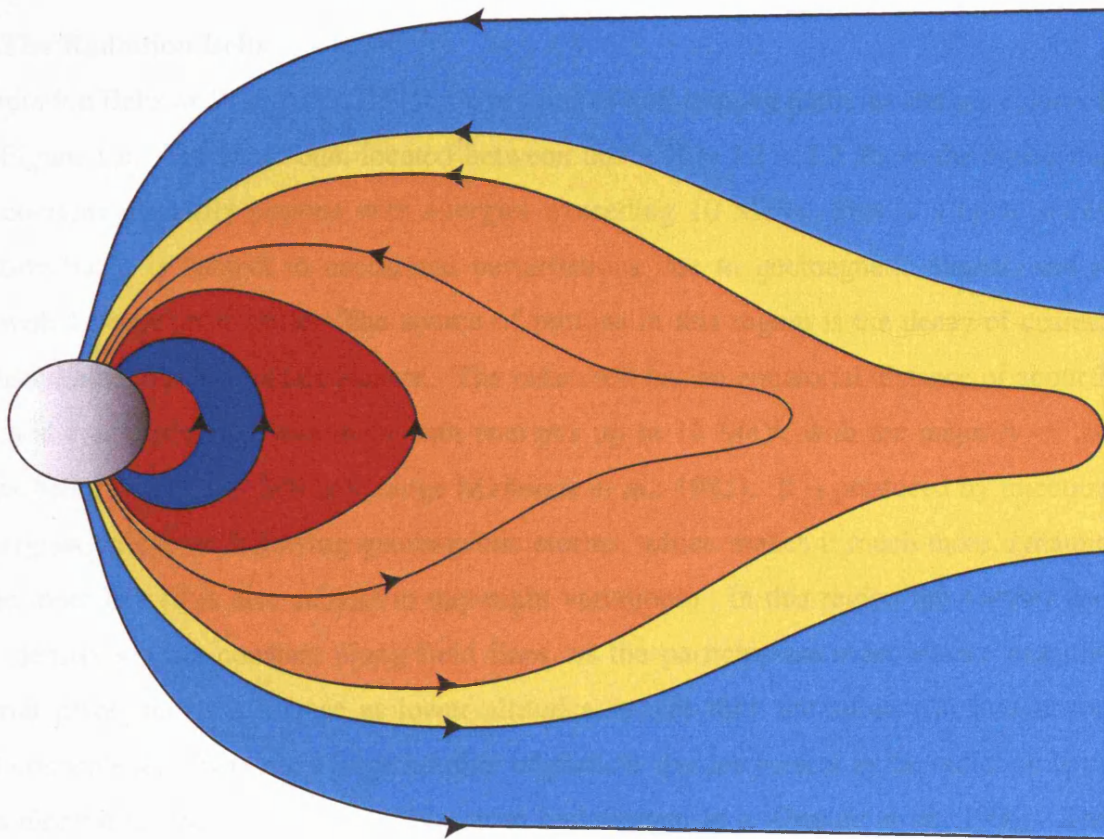
both sides, thus forming an X-type magnetic field geometry, leading to the production of magnetic field lines that connect across the boundary between the two plasma regimes. This process is called magnetic reconnection [Dungey, 1961]. The magnetic tension of the field lines will cause rapid field and plasma flow along the current sheet, away from the reconnection site, which is then replaced by further plasma from the next flux tubes. Such an X-point can form at the magnetosphere-magnetosheath interface where the primary coupling between the planetary and the solar plasmas takes place. The magnetic reconnection gives rise to Dungey's open magnetosphere (see Figure 1.5). The open field lines are connected to the solar wind at one end, and the Earth's polar regions at the other. These open flux tubes allow efficient transfer of solar wind momentum into the magnetosphere as the open field lines are swept downstream by the solar wind flow. The open flux tubes also form a direct magnetic pathway for the transportation of the solar wind plasma across the boundary into the magnetosphere and of magnetospheric plasma in the opposite direction. Then, as the reconnected field lines contract, the plasma on these tubes is accelerated and heated. The open field lines are carried antisunward by the solar wind flow (as mentioned above) and are stretched out on the nightside to form a long magnetotail. As the open field lines travel away from Earth, the near-Earth portions of these open tubes are convected towards the centre of the tail, and reconnect again on the nightside. This far-tail reconnection site results in the newly disconnected field lines flowing back out into the solar wind whilst the newly closed field lines flow back towards the dayside magnetopause where the cycle repeats. This establishes a magnetospheric convection with a period of 6–12 hours [Cowley, 1993].

1.4. Magnetospheric Structure

This study concentrates exclusively on the nightside of the Earth's magnetosphere, which contains four major plasma regions (Figure 1.6), the tail lobes, the plasma sheet, the trapped radiation belts and the plasmasphere.

1.4.1. The Tail Lobes

The tail lobes are regions of plasma that exist on open field lines and map into the northern or southern hemisphere polar caps. In these regions plasma densities are low ($< 0.1 \text{ cm}^{-3}$) and sometimes below the level of detectability. There are few particles of energy $> 5 \text{ keV}$, with the most common particles being tailward flowing, cool, ionospheric ions. These regions are coloured light blue in Figure 1.6.



- Plasmasphere
- Radiation Belts
- Central Plasma Sheet
- Plasma Sheet Boundary Layer
- Tail Lobe

Figure 1.6: Schematic showing structure of the nightside magnetosphere (not to scale).

1.4.2. The Plasma Sheet

The plasma sheet is comprised of two regions, the plasma sheet boundary layer and the central plasma sheet. The plasma sheet boundary layer is coloured yellow in Figure 1.6, whilst the central plasma sheet is coloured orange. This thesis is mainly concerned with the entry of the Polar spacecraft into the plasma sheet boundary layer (PSBL) and subsequently into the central plasma sheet (CPS), with particular reference to substorm phase. As this is one of the main features of this study, the plasma sheet is discussed in detail in Chapter 2.

1.4.3. The Radiation Belts

The Radiation Belts or 'Van Allen Belts' are regions of hot, trapped particles and are coloured red in Figure 1.6. The inner one, located between about $X = 1.1 - 3.3 R_E$ in the equatorial plane, contains primarily protons with energies exceeding 10 MeV. This is a fairly stable population but it is subject to occasional perturbations due to geomagnetic storms, and it varies with 11-year solar cycle. The source of protons in this region is the decay of cosmic ray induced albedo from the atmosphere. The outer belt has an equatorial distance of about 3 - 9 R_E and contains mainly electrons with energies up to 10 MeV, with the majority of the particles being in the 20 - 200 keV range [Krimigis *et al.*, 1985]. It is produced by injection and energisation events following geomagnetic storms, which makes it much more dynamic than the inner belt (it is also subject to day-night variations). In this region the number and energy density are not constant along field lines, as the particles are most intense near the equatorial plane and less intense at lower altitudes, where they are subject to loss in the neutral atmosphere. There are a large number of particle species present in the radiation belts such as electrons, protons, helium, carbon, iron and oxygen [e.g. Grande *et al.*, 1996]. The particle motion in this region is given by the charge polarity, with ions moving west and electrons drifting east [e.g. Roederer, 1970; Reeves *et al.*, 1991]. Most of the ring current is carried by these trapped particles, and all of the trapped particles contribute to the ring current.

1.4.4. The Plasmasphere

The plasmasphere is a torus-shaped, dense region of cold plasma that that approximately co-rotates with the Earth. Therefore, the ionospheric plasma at mid-latitudes can expand upward along the magnetic field lines and fill them until the plasma gas pressure is equalised along the entire field line, although gravity and centrifugal action must also be considered, creating the plasmasphere. Therefore, the plasmasphere is basically an upward extension from the ionosphere and is coloured dark blue in Figure 1.6. Analysis of 'whistler' waves at the

Earth's surface have shown that this region has a moderately high density ($>100 \text{ cm}^{-3}$) of cold ($\sim 1 \text{ eV}$) plasma.

1.5. The Ionosphere

As radiation from the sun passes through the atmosphere it is absorbed. This causes heating of the gases, dissociation of the molecules and free electrons are released (ionisation). The rate at which the electrons are produced is proportional to the density of the gas and also the intensity of the ionising radiation. The gas concentration decreases with increasing height and so at high altitudes the rate of production is small. As the radiation passes into the more dense atmosphere the rate increases. As more radiation is absorbed in this more dense region, the intensity begins to fall. It follows that the rate of production must also begin to decrease. Therefore, there is a point where the intensity of the radiation falls more quickly than the density of the gas increases, forming a peak in the rate of production. In 1931 Chapman derived this point for a single gas with an absorption coefficient that remains constant over all wavelengths. The resulting profile is called the 'Chapman Layer'. Of course the real ionosphere is more complicated than a single layer. The primary reason being that there are several gases of different masses present, whose concentrations vary differently with height. Ionisation rates will also vary for different species. Ionisation is also produced by high energy particles emitted from the Sun and present in the cosmic background. The amount of ionisation produced in this way is generally much less than that produced by electromagnetic radiation, but becomes very important at night when there is little or no solar illumination. It is also important at times of high magnetic activity and at the lowest altitudes where the electromagnetic radiation cannot reach.

The overall ionospheric plasma density is a balance between the rate at which the electrons are produced and the rate at which they are lost, mainly by recombination and diffusion. Once again, these rates vary with altitude. These varying rates of production and loss result in a complex profile of electron concentration, producing several distinct layers (Figure 1.7). The D-region extends from about 50 to 90 km, but is only present during daytime. The E-region covers the 90 – 160 km range, with peak density occurring at 110 km. At this altitude the electrons are decoupled from the ions and neutrals, and drift with $\mathbf{E} \times \mathbf{B}$ velocity, thereby generating a current. The F-region extends from 160 km upwards, with no significant currents in evidence.

Perhaps the most important ionospheric effect (in the context of this study) is the production of auroral displays due to the precipitation of energetic particles from the plasma sheet.

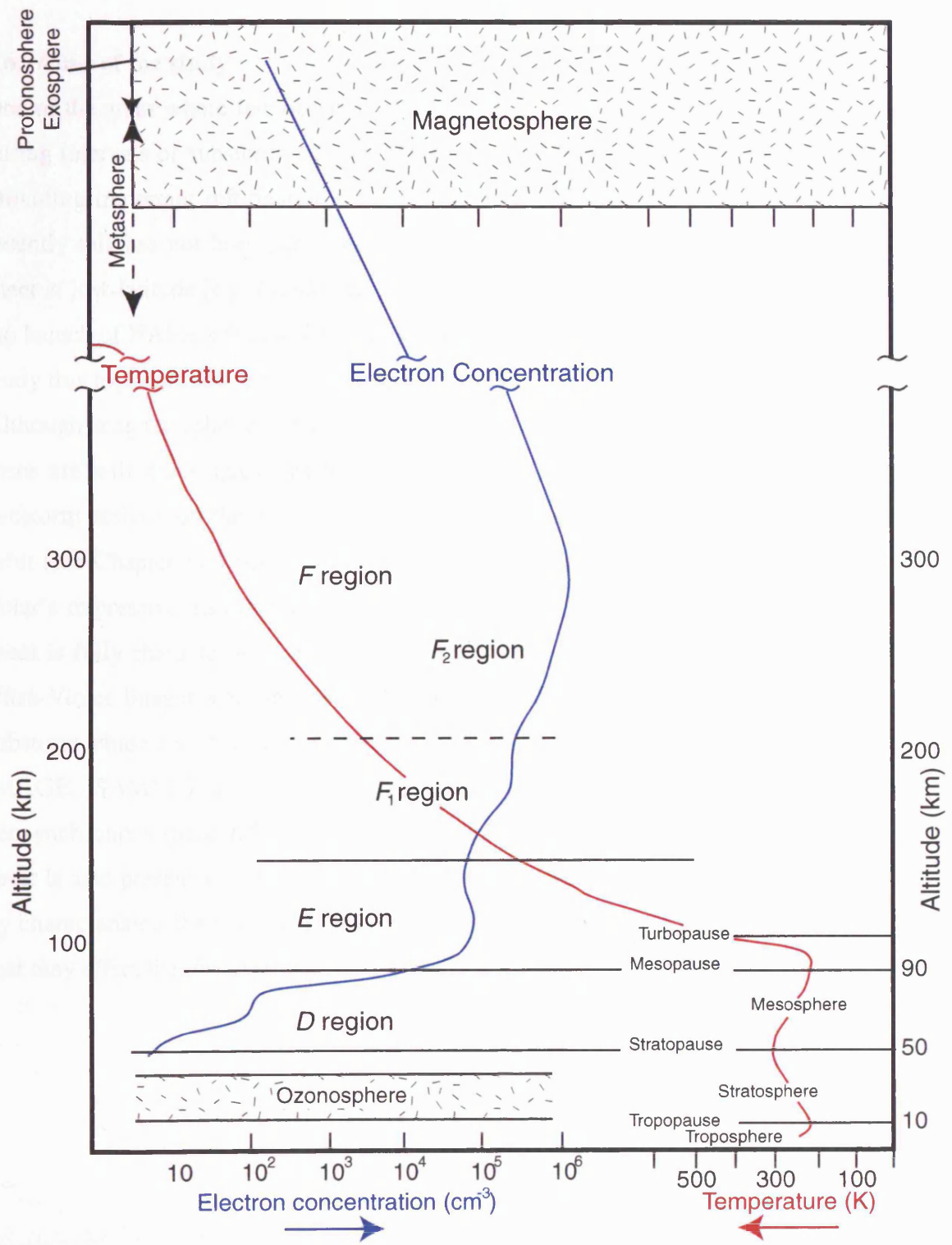


Figure 1.7: Electron concentration and temperature profiles of the Earth's ionosphere.

Precipitating electrons also enhance the E-region currents, known as the auroral electrojet. During magnetospheric substorms these effects are greatly increased, but this is explained in greater detail in Chapter 2.

1.6. Aims of the study

One of the areas where few observations have been made is the plasma sheet at high-latitude during intervals of substorm activity. This region can be mapped back into the magnetotail, providing important information on the location of the substorm acceleration region. Until recently this has not been possible, and so many studies have been made inside the plasma sheet at low-latitude [e.g. *Dandouras et al.*, 1986a; *Baumjohann et al.*, 1990]. However, with the launch of NASA's Global Geospace Science (GGS) Polar spacecraft, it is now possible to study this high-latitude region as the spacecraft is in a high inclination, eccentric, polar orbit. Although magnetospheric substorms have been studied in great detail throughout the years there are still many questions left unanswered. Through the use of Polar the effects of substorm activity on the magnetotail will be investigated. As Polar is in a high inclination orbit (see Chapter 3) it passes through the plasma sheet at relatively high-latitude. By using Polar's impressive instrument payload of particle and field detectors the high-latitude plasma sheet is fully characterised. These observations are compared with auroral images from the Ultra-Violet Imager also on Polar. The Polar measurements are also placed in context of substorm phase by utilising background data sets such as ground magnetometers from the IMAGE, SAMNET and Greenland magnetometer networks, the Los Alamos fleet of geosynchronous spacecraft, and finally the Wind spacecraft. A statistical study of the plasma sheet is also presented, which allows the subsequent case studies to be understood more fully by characterising the plasma sheet under average conditions and exploring any other factors that may affect the observations.

CHAPTER 2

Review of Substorms and Associated Signatures

2.1. Introduction

As is well known, the Earth's magnetic field undergoes variations that are caused by sources external to the Earth. Many different variations have been observed, one of which is known as a substorm and is studied in this thesis. The Dungey cycle, described in Chapter 1 is not a steady cycle, with the amount of magnetic flux being transported into the nightside being larger than the amount transferred back to the dayside. This results in a build up of flux in the nightside that leads to the triggering of a mechanism, the auroral signatures of which were termed 'auroral substorms' by *Akasofu* [1964], and the magnetic signatures themselves became known as 'polar magnetic substorms'. All of these are now known to be manifestations of a specific magnetospheric disturbance, which is termed as a 'magnetospheric substorm'. Since *Akasofu* characterised the auroral substorm there have been many investigations of this phenomenon, leading to the substorm being characterised as a sequence of events divided into three distinct phases: growth, expansion and recovery. Different auroral and magnetospheric features are associated with each of these phases and these are reviewed in this chapter. The various models used to describe substorms are also reviewed in this chapter.

2.2. Substorm Phases

In the original definition of an auroral substorm, only two phases were described: expansion and recovery. The idea of the growth phase was introduced by *McPherron* [1970], although this remained controversial for some time. It is now, however, generally accepted that the substorm comprises of three phases, the growth, expansion and recovery phases. These three phases have been studied in great detail both individually and as a whole, and are described in the next sections.

2.2.1. The Growth Phase

As mentioned above, *McPherron* first introduced the concept of the substorm growth phase. The growth phase is essentially a period lasting between 30 and 120 minutes [*Lester et al.*, 1993], when energy supplied by the solar wind is stored in the magnetotail as enhanced magnetic energy. Following a southward turning of the IMF, the dayside magnetopause reconnection site moves earthward, as the ionospheric currents cannot develop rapidly enough to transport magnetic flux from the nightside back to the dayside. Therefore, there is erosion

of the dayside magnetosphere and an increase in the magnetic flux in the magnetotail lobes, which causes the magnetotail to flare. This flaring may allow the solar wind to exert more pressure, which is balanced by increased magnetic pressure within the tail lobes, which in turn causes the plasma sheet to thin. As the growth phase continues the near-Earth current sheet becomes thinner and more intense, the field becomes very weak and tail-like in the equatorial plane causing the magnetotail to be stretched. The increased lobe pressure and thinned current sheet results in the plasma sheet being thinned [e.g. *Hones et al.*, 1984]. Another consequence of the reconfiguration of the magnetotail is a dropout of geosynchronous particle fluxes, which is described in detail in section 2.6. The thinning and dropout begin just before the end of the growth phase and the onset of the expansion phase. In the high-latitude ionosphere, the auroral oval moves equatorwards and so there is an increase in the polar cap area – see section 2.3 for details of auroral variations. A brightening of the aurora, usually in the pre-midnight sector follows this and it is at this point that the expansion phase onset is said to begin. There is another important feature that occurs during the growth phase that is known as ‘pseudobreakup’. *McPherron* [1991] noted that pseudobreakups are similar to substorm expansion phase onsets, typically comprising of auroral brightening, Pi2 pulsations and a weak enhancement of the westward electrojet. Therefore it is difficult to determine the difference between a pseudobreakup and a small substorm. The distinguishing features are that pseudobreakups have a short lifetime (< 1 hour), extreme localisation, weak magnetic perturbations on the ground, and lack of development into a full expansion phase onset. For more information on pseudobreakup and the substorm growth phase see *Koskinen et al.* [1993].

2.2.2. The Expansion Phase

The cause of the expansion phase onset is the main problem involving substorms, with many different models having been proposed. These models are discussed in section 2.6, and only a general phenomenological description of the expansion phase is given here.

When the expansion phase onset occurs, the equatorward-most auroral arc intensifies, usually in the pre-midnight sector. This enhanced arc then undergoes both poleward and westward expansion, eventually covering a large portion of the nightside oval (see section 2.3). These auroral intensifications coincide with Pi2 pulsations and magnetic bays being observed on the ground (see section 2.5). At this time the inner and middle magnetosphere rapidly reconfigure from a stressed, tail-like geometry, to a more dipolar state in the central plasma sheet. This process is known as dipolarisation of the plasma sheet [e.g. *Kokubun and McPherron*, 1981]. Substantial particle acceleration and energisation, along with an injection

of hot (up to MeV) plasma into the region of geostationary orbit on the nightside also accompanies the expansion phase onset [*Deforest and McIlwain, 1971*]. Also, the magnetic energy content of the magnetotail lobes, which increases in the growth phase, is seen to decrease during the substorm expansion phase in many cases [*McPherron et al., 1993*]. This energy is released by an instability in the cross tail current that leads to 20 – 30 % [*Sauvaud, 1992*] of the cross tail current being redirected down a field-aligned current (FAC) through the ionosphere, and back into the magnetotail via a second FAC. This redirection of the cross-tail current leads to the formation of the Substorm Current Wedge (SCW) (see section 2.5). The ionospheric portions of these current systems flow in enhanced-conductivity channels at high-latitude, and are called the auroral electrojets. Although the electrojets exist before expansion phase onset, they are greatly enhanced by the addition of these expansion phase currents. Further downtail a closed magnetic loop structure, or ‘plasmoid’, may be observed. Therefore, the expansion phase can be considered as the primary energy release phase, with the breakup of an auroral arc and subsequent formation of other auroral features, an intensification of the westward electrojet, a Pi2 pulsation and the possible ejection of a plasmoid.

2.2.3. The Recovery Phase

The recovery phase is the final phase of the substorm process, and is normally believed to represent the end of the energy input from the solar wind to the magnetosphere. Ultimately, this is true but there are still features that appear to be part of the energy release during the recovery phase, specifically in the midtail region [e.g. *Sauvaud et al., 1984; Hones, 1992*]. There are also certain auroral features only associated with the recovery phase, such as the auroral double oval (see section 2.3). In the near-Earth tail, the recovery phase appears as a decay of the SCW and subsequent slow return to quiet time configurations of the magnetic field and so corresponds to a return to the ‘ground state’ of the system. For more information on the signatures of the recovery phase see *Baker et al. [1994]*.

2.3. Auroral Observations

Perhaps the most impressive of the substorm phenomena is the auroral enhancement. The auroral oval becomes extremely dynamic during periods of magnetic activity. Auroral observations have been recorded since ancient times, but it was not until the 1960’s that the most significant advances were made. *Feldstein [1960; 1963]* realised that the aurora resembled an oval shape on a global scale, which lies at higher magnetic latitudes on the dayside portion of the ionosphere than on the nightside. Shortly afterwards, *Akasofu [1964]*

introduced the concept of an auroral substorm through an extensive analysis of simultaneous all-sky camera photographs taken from a number of observatories. This showed that

“Auroras all along the auroral oval (not the auroral zone) can be of quiet form for a certain period. But, such a quiet condition is often intermittently disrupted, particularly during geomagnetic storms. The breakdown of the quiet condition is often abrupt, and occurs first near the equatorward edge of the oval in the midnight sector. Soon the active features spread in all directions, poleward, westward and eastward along the oval, and equatorward. After this explosive spread, auroral activity gradually subsides all along the auroral oval. This auroral activity over the entire polar region is described in terms of the auroral substorm.”

- From Akasofu [1968].

Akasofu produced Figure 2.1, which represents this description schematically. In this representation the quiet aurora is altered as a result of a single auroral breakup. The point where the activation is initially observed is termed the onset location, which is placed close to magnetic midnight and at the equatorward edge of the auroral oval (Figures 2.1b & c). Therefore, the activity appears to occur in two separate stages: expansion phase (5 to 30 minutes; Figures 2.1b – d) and recovery phase (30 minutes to 3 hours; Figures 2.1e & f). Expansion covers the time of the motion in all directions after breakup, while recovery is the relaxation back to the quiet-time distribution. Given that Akasofu had only a series of ground based auroral observations this representation is very good. However, substorm activity is too complex for such a schematic to represent all possible variations, and as satellites became available and with them, global auroral imaging, more comprehensive descriptions were produced. Figure 2.2 shows such a schematic, based upon Viking UV images of the aurora [Cogger & Elphinstone, 1992]. The first picture (Figure 2.2a) in the schematic shows the auroral oval at the end of the growth phase and beginning of the expansion phase. The next picture (Figure 2.2b) shows the expansion phase progressing, followed by the start of the recovery phase (Figure 2.2c) with Figures 2.2d, e and f showing three possible variations during the recovery phase. The key differences between the Viking auroral substorm and the Akasofu representation are the recognition of the growth phase auroral activity and the potential for the variety of this auroral activity.

With such a schematic a standard auroral substorm can be described. Throughout the growth phase the quiet-time oval moves equatorwards, until it reaches the position shown in Figure 2.2a. At expansion phase onset an intensification occurs close to magnetic midnight, forming the auroral bulge. This auroral bulge is filled with intense auroral emission, with a Westward

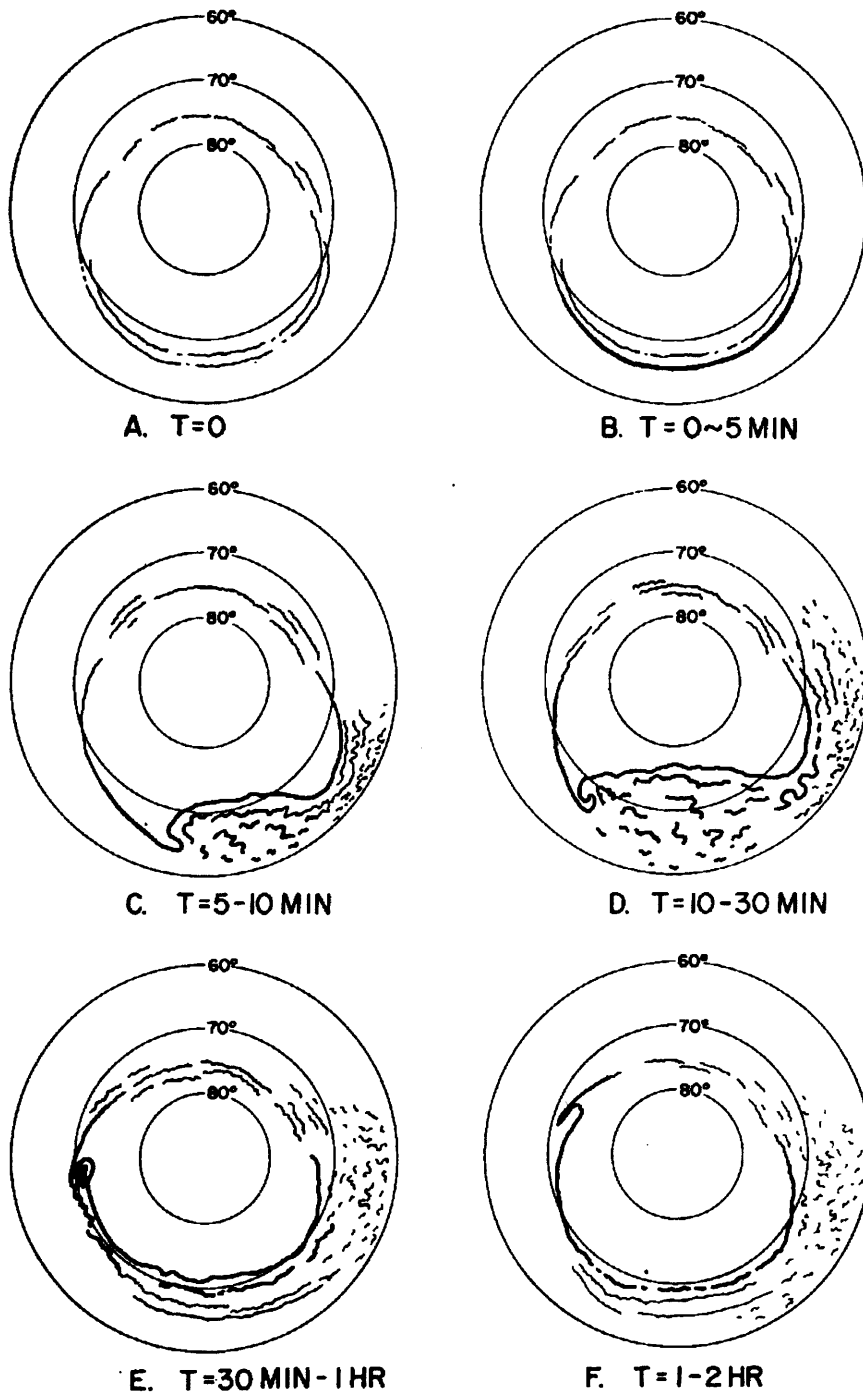
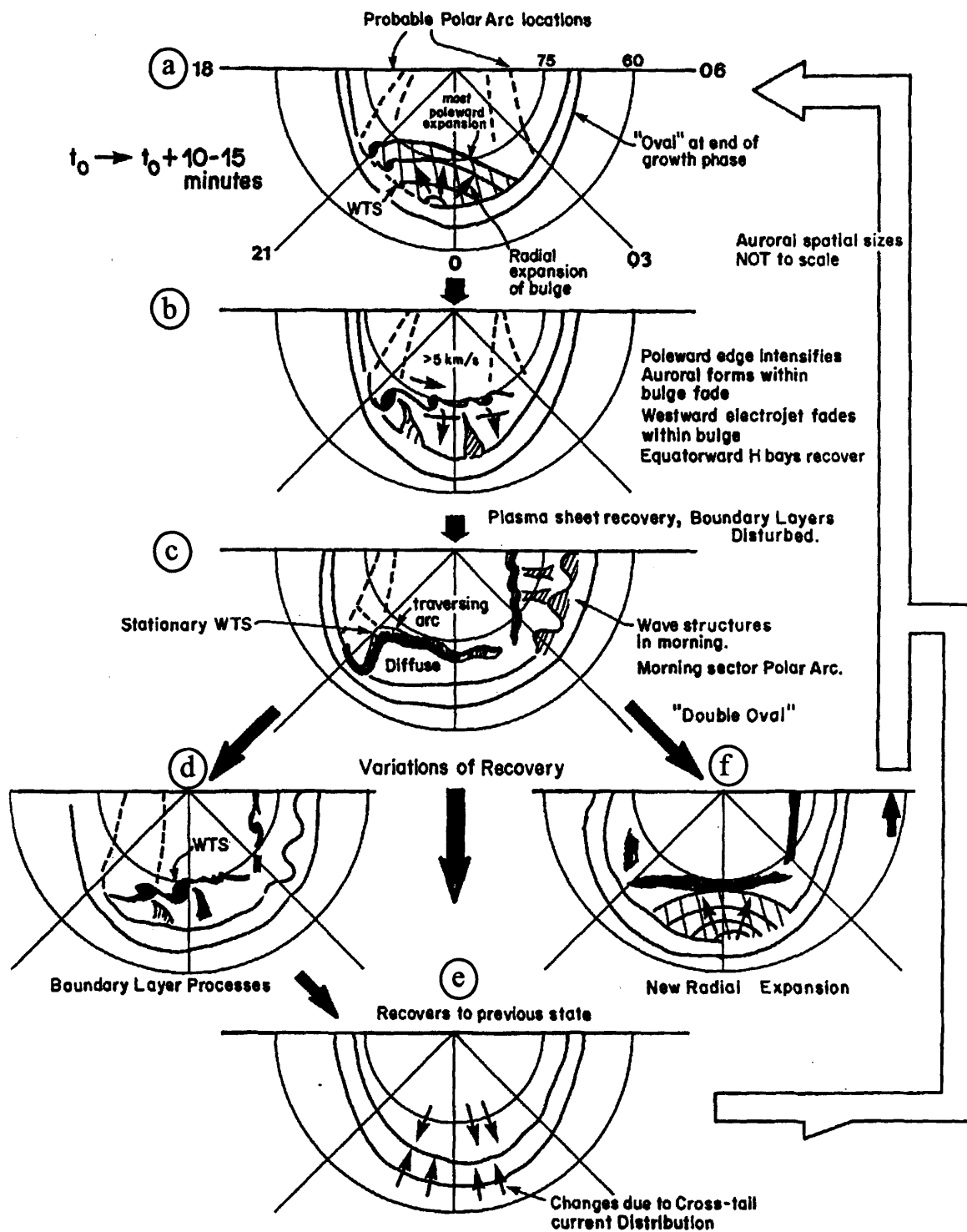


Figure 2.1: Schematic to show development of auroral substorm, generalised from multiple observations [from *Akasofu*, 1968].



VIKING AURORAL SUBSTORM

Figure 2.2: Auroral substorm development from expansion phase onset through recovery phase as viewed by the UV imager on the Viking Satellite [from Cogger and Elphinstone, 1992].

Travelling Surge (WTS) at its westward extremity (Figure 2.2a). The poleward expansion may not be continuous, but may instead consist of a series of arcs forming in stepwise fashion on the poleward edge of the bulge, although satellite data leave this ambiguous. Towards the end of the expansion phase the high-latitude intensifications begin to move eastward, forming a series of spiral forms (Figure 2.2b). At this time the auroral forms within the bulge and the WTS begin to fade, leading to the start of the recovery phase. Optical omega (Ω) bands are then seen in the poleward portion of the most equatorward oval in the morning sector and the beginning of a 'double oval' structure [Elphinstone & Hearn, 1992] is seen (Figure 2.2c). After this fading there are three possible methods of recovery. The first involves an activation of boundary layer processes in which surges are formed on the poleward arc system (Figure 2.2d). The second involves the poleward motion of the equatorward oval and subsequent fading or equatorward motion of the aforementioned oval (Figure 2.2e). The final route is the 'double oval', where there is a main equatorward oval and a second parallel auroral band 5 - 10 ° poleward (Figure 2.2f). This is usually due to a second substorm activation whilst the initial substorm is still in the recovery phase. The initially intensified arc has drifted polewards as in panel e, but the second intensification occurs on the equatorward arc as in panel a, thus forming a double oval. This particular method of recovery is perhaps the most interesting as it involves a decrease in the intensity of the central region of the aurora, but often with a brightening of the poleward band. However, this is still a somewhat simplified description of the auroral substorm and the reader is directed to *Elphinstone et al.* [1996] for a more detailed review of this subject.

2.4. Ground Magnetic Variations

The ground magnetic variations observed during substorms are measured by the various ground magnetometer networks. These networks use a variety of co-ordinate systems (see Appendix 1) and so the description below uses the XYZ ground co-ordinate system. At substorm expansion onset a substantial portion of the cross-tail current is redirected along a magnetic field line into the ionosphere, through the auroral electrojet, and back to the equatorial magnetosphere via another field-aligned current (FAC). This current system is termed the Substorm Current Wedge (SCW) as mentioned earlier and is shown in Figure 2.3. The SCW occurs when "*the cross-tail current is disrupted and 'short-circuited' in the ionosphere*" [McPherron *et al.*, 1973]. This current system gives rise to magnetic signatures that are observed by ground magnetometers (Figure 2.4). Magnetic bays in the high-latitude X- (north-south) and Z-(vertical) components result from the auroral or substorm electrojet and so give latitudinal information on its location, whilst bays in the mid-latitude magnetograms can be used to find the longitude position of the substorm current wedge

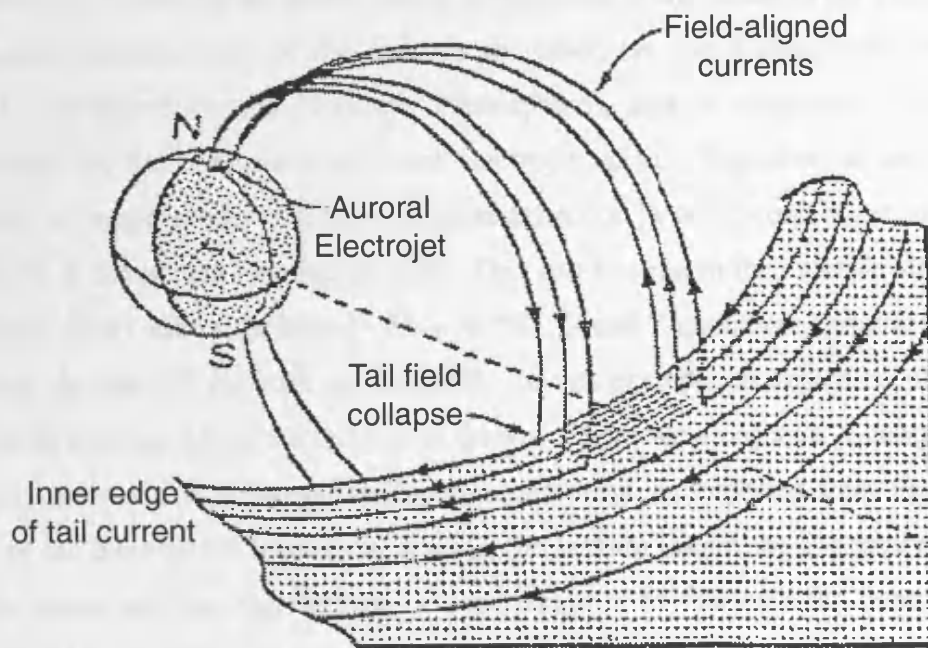


Figure 2.3: Schematic of the Substorm Current Wedge [from McPherron *et al.*, 1973].

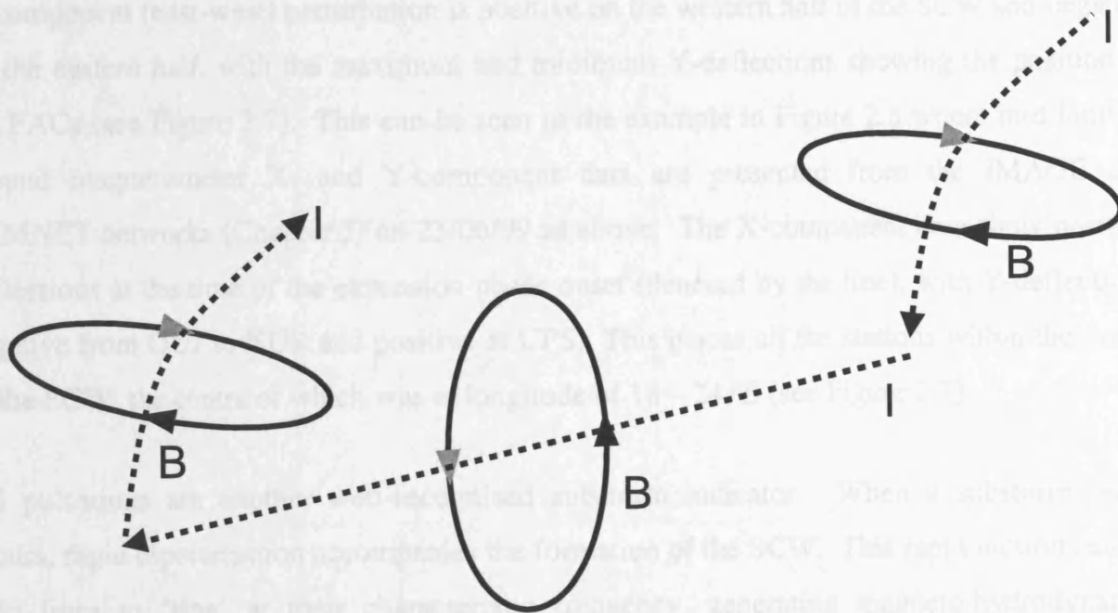


Figure 2.4: The magnetic field produced by the substorm current system in the ionosphere.

[Clauer & McPherron, 1974; Lester *et al.*, 1983]. The high-latitude X-component undergoes a negative deflection (termed magnetic bays), with the largest bay occurring at the centre of the electrojet. If the magnetometer station is poleward of the centre of the electrojet then the high-latitude Z-component of the field is increased (as the Z-component of the field is positive downwards in the Northern Hemisphere), and is decreased if the station is equatorward of the electrojet (westward electrojet only). Therefore, at the centre of the electrojet we would expect to see a maximum deflection in the X-component, and a change in sign of the Z-component (see Figure 2.5). This can be seen in the example shown in Figure 2.6, which shows auroral-latitude ($\sim 65 - 70^\circ\text{N}$) X- and Z-component ground magnetic field data from the IMAGE network on 23/06/99. In this example an expansion phase onset has occurred at the time where the red line is drawn. There were negative X-component bays at this time and positive and negative Z-component bays, as expected from Figure 2.5. The centre of the electrojet is located by finding the latitude where the Z-component deflection changes sense and the X-deflection is a maximum. In this case the centre was located between MAS and ABK, at a latitude of $\sim 69^\circ\text{N}$.

Mid-latitude stations conversely are generally affected mainly by the FAC parts of the SCW. The X-component perturbation of the mid-latitude is positive inside this structure, whereas the Y-component (east-west) perturbation is positive on the western half of the SCW and negative on the eastern half, with the maximum and minimum Y-deflections showing the position of the FACs (see Figure 2.7). This can be seen in the example in Figure 2.8 where mid-latitude ground magnetometer X- and Y-component data are presented from the IMAGE and SAMNET networks (Chapter 3) on 23/06/99 as above. The X-component data show positive deflections at the time of the expansion phase onset (denoted by the line), with Y-deflections negative from OIJ to NUR and positive at UPS. This places all the stations within the limits of the SCW, the centre of which was at longitude of $18 - 24^\circ\text{E}$ (see Figure 2.7).

Pi2 pulsations are another well-recognised substorm indicator. When a substorm onset occurs, rapid dipolarisation accompanies the formation of the SCW. This rapid motion causes field lines to 'ring' at their characteristic frequency, generating magneto-hydrodynamic waves. Wave packets of period 20 – 200 seconds can be seen by ground magnetometers on the Earth. Filtering the mid-latitude magnetometer data can identify these wave packets, termed Pi2 pulsations. Figure 2.9 shows the mid-latitude X-component data from Figure 2.8 filtered between 20 – 200s to show these Pi2 pulsations. The start of the Pi2 pulsation determines the timing of either an expansion phase onset (as in this example) or subsequent

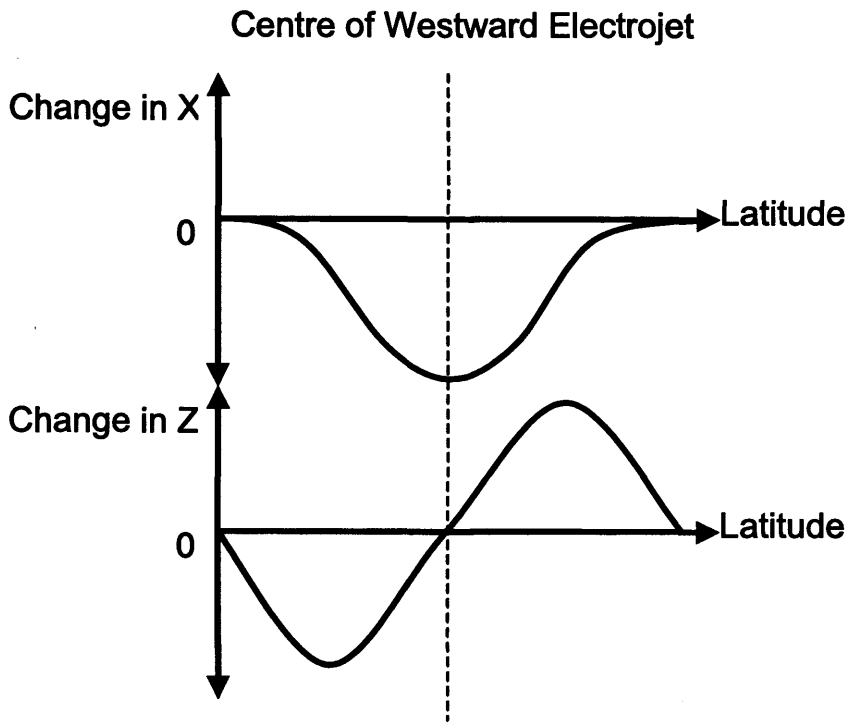


Figure 2.5: The variation of the X- and Z-components of the magnetic field as the electrojet system passes.

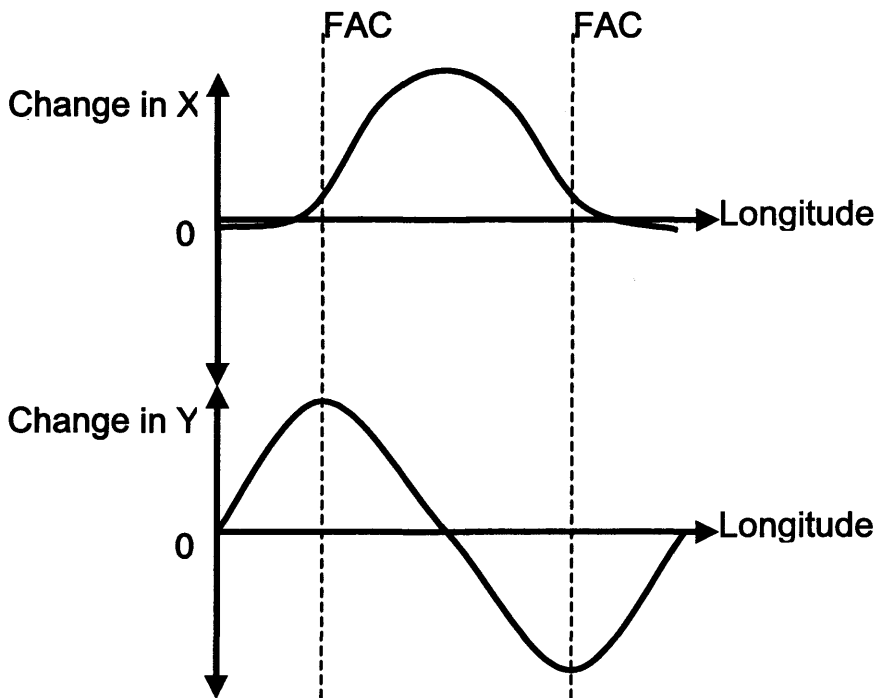


Figure 2.7: The longitudinal position of the SCW as determined by mid-latitude magnetograms.

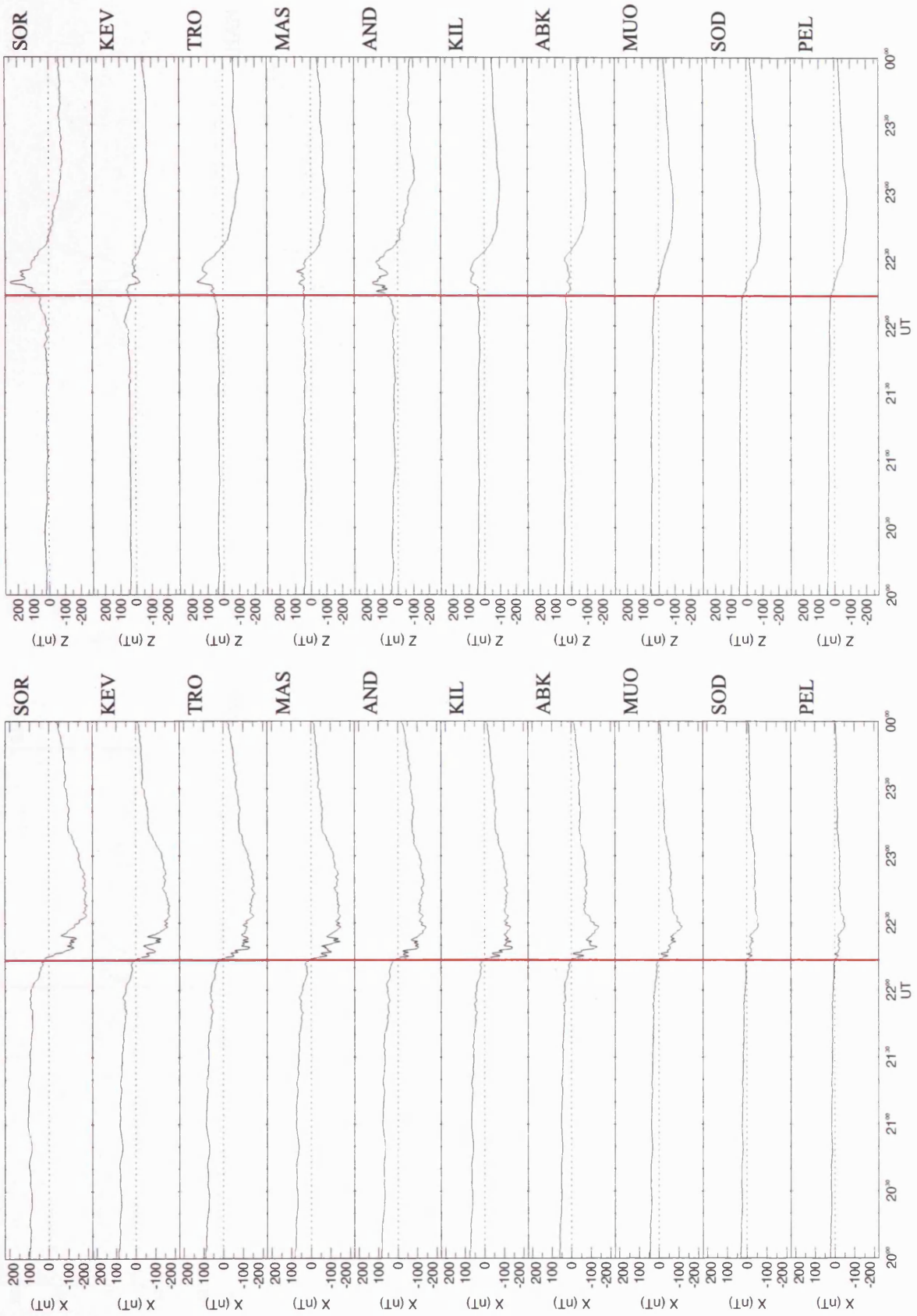


Figure 2.6: Ground magnetometer X- and Z-component data from auroral latitudes on 23/06/99 to show location of the enhanced westward electrojet at substorm expansion phase onset.

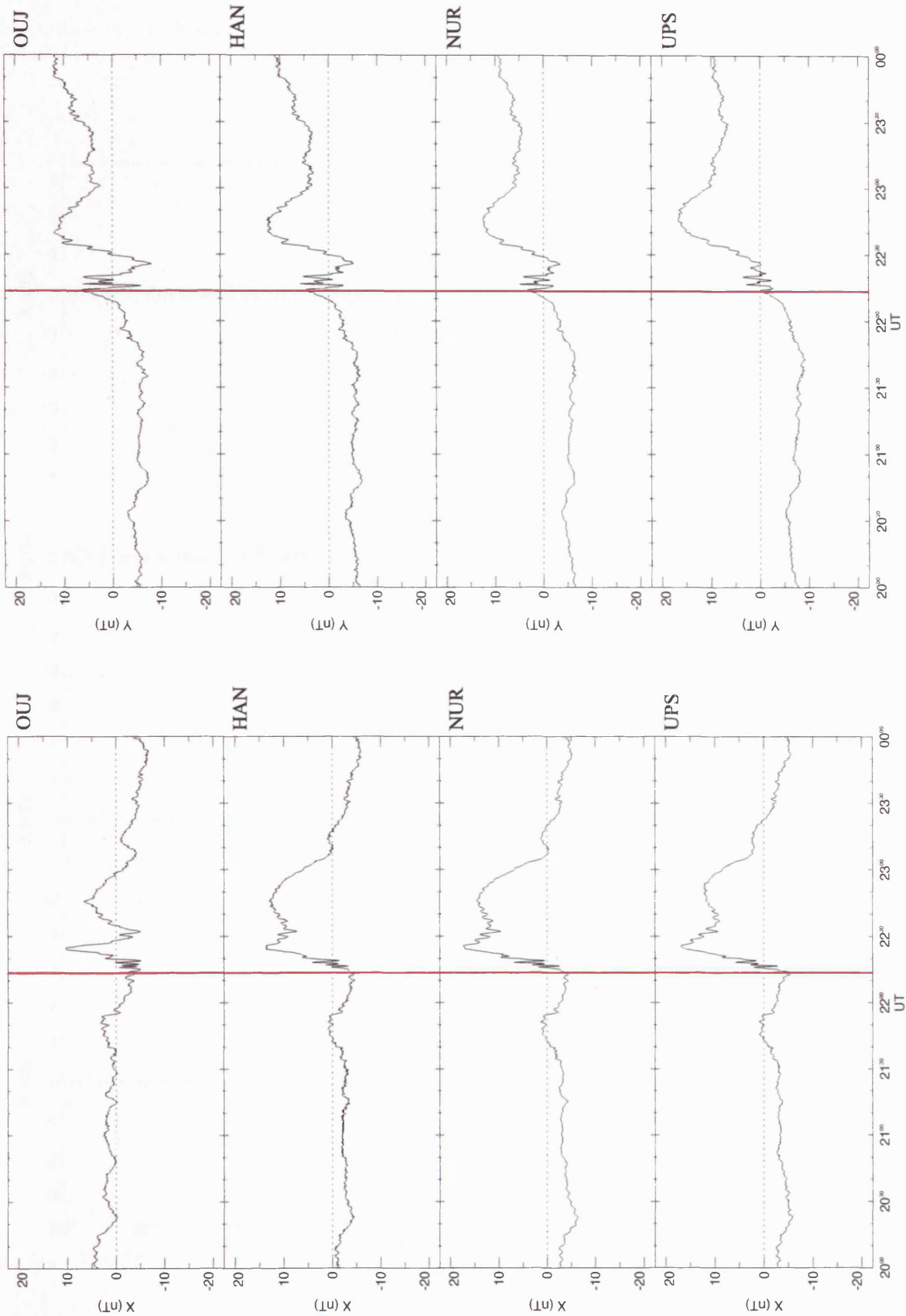


Figure 2.8: Ground magnetometer X- and Y-component data from mid-latitude on 23/06/99 to show location of the SCW and FACs at substorm expansion phase onset.

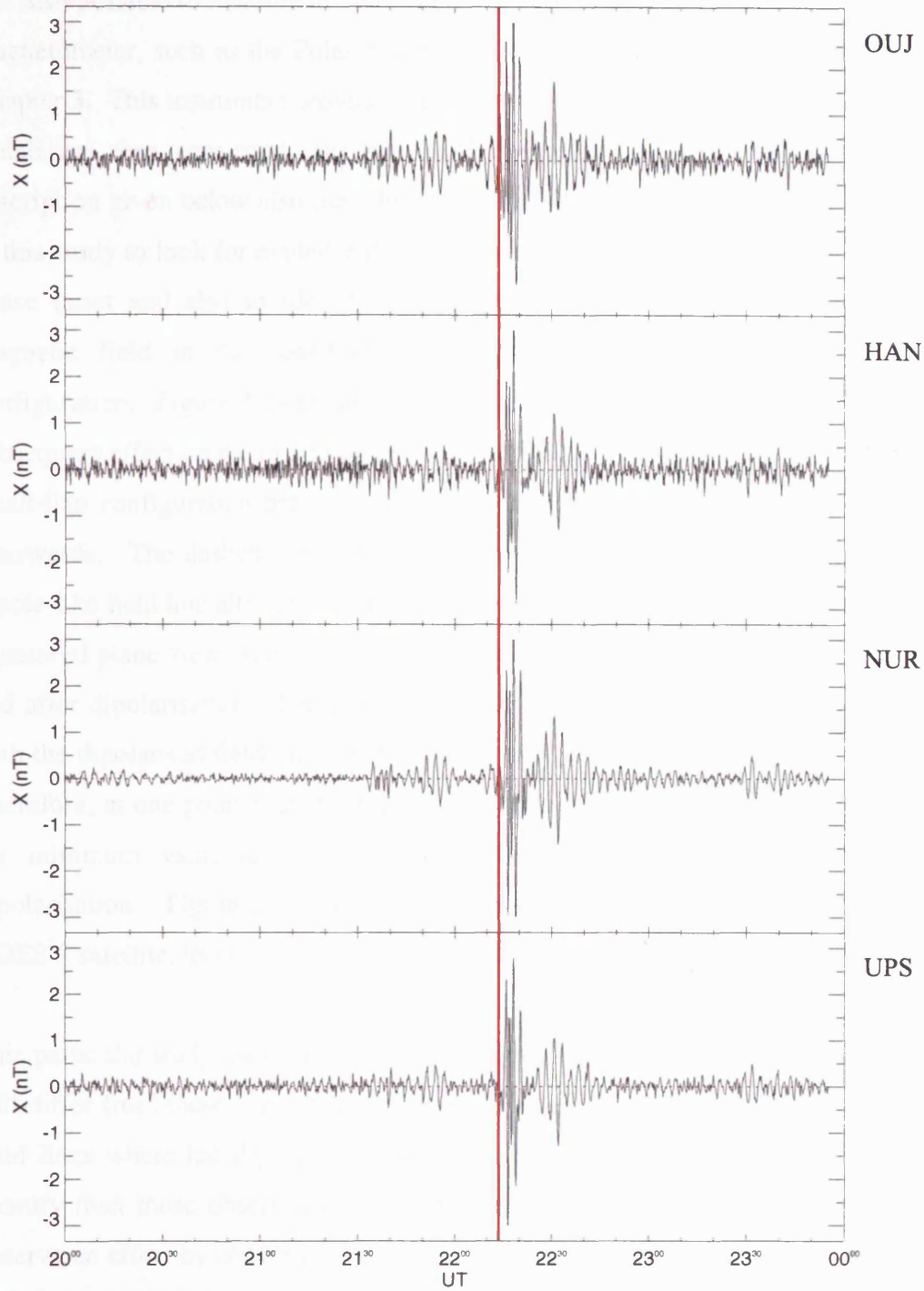


Figure 2.9: Ground magnetometer X-component data from mid-latitude on 23/06/99 filtered between 20 -0200 s to show Pi2 pulsations and hence the timing of substorm expansion phase onset.

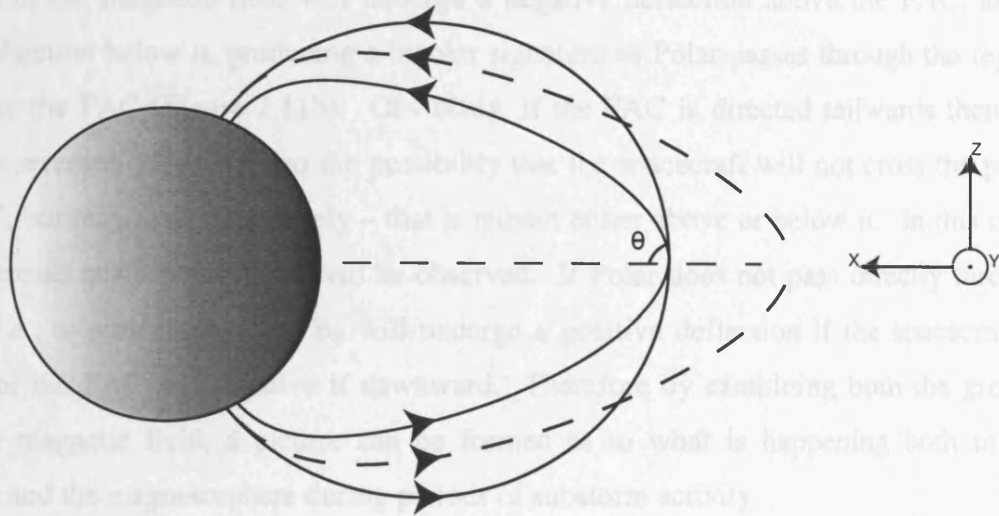
intensification. Pseudobreakups often have similar features to those described above, but generally of less magnitude.

2.5. Magnetospheric Magnetic Variations

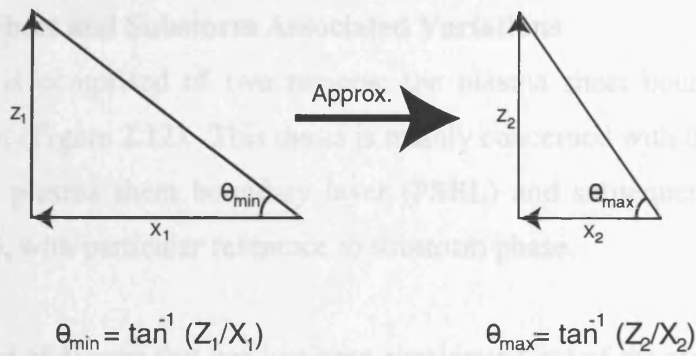
It is also possible to measure in-situ magnetospheric magnetic variations by using a spacecraft magnetometer, such as the Polar Magnetic Fields Experiment (MFE), which is described in Chapter 3. This instrument provides values of the in-situ magnetic field in three components, which are then converted into the GSM co-ordinate system (Appendix 1), and so the description given below also uses this co-ordinate system. This particular instrument is used in this study to look for evidence of dipolarisation of the Earth's magnetic field at expansion phase onset and also to identify field-aligned currents. As a dipolarisation occurs, the magnetic field in the near-Earth geomagnetic tail will take on a more dipole-like configuration. Figure 2.10 presents an exaggerated schematic of a dipolarised field and the subsequent effect on the in-situ magnetic field measurements. Figure 2.10a shows the field in a tail-like configuration before expansion phase onset, and in the dipole-like configuration afterwards. The dashed field line is an approximation of the field line that becomes the dipole-like field line after dipolarisation. If a spacecraft located in geostationary orbit near the equatorial plane views such a dipolarisation, then different field lines will be observed before and after dipolarisation. These different field lines are represented by the solid field lines, with the dipolarised field line mapping polewards of the tail-like field line in the ionosphere. Therefore, at one point near the equator the angle of the field would be seen to change from the minimum value to the maximum value (Figure 2.10b) as a result of the field dipolarisation. Figure 2.10c shows an example of such a dipolarisation observed by the GOES 7 satellite, located near the equatorial plane, on 23/01/89 [Milan, 1994].

This particular study uses a spacecraft in a high inclination orbit, Polar, and so the signatures will differ from those presented in Figure 2.10c. Polar is typically at high-latitude when on field lines where the dipolarisation occurs. Therefore, the variations are more difficult to identify than those observed closer to the equatorial plane. Even so, it is still possible to observe an effect by converting the magnetic field into a field angle in the $X_{\text{GSM}} - Z_{\text{GSM}}$ plane and determining if this angle has changed from a tail-like to a dipole-like configuration. Care needs to be taken, however, as dipolarisation can only be identified with any certainty from measurements taken on closed field lines, as field lines in the lobes are connected to the IMF and so will not undergo such an obvious change.

(a)



(b)



(c)

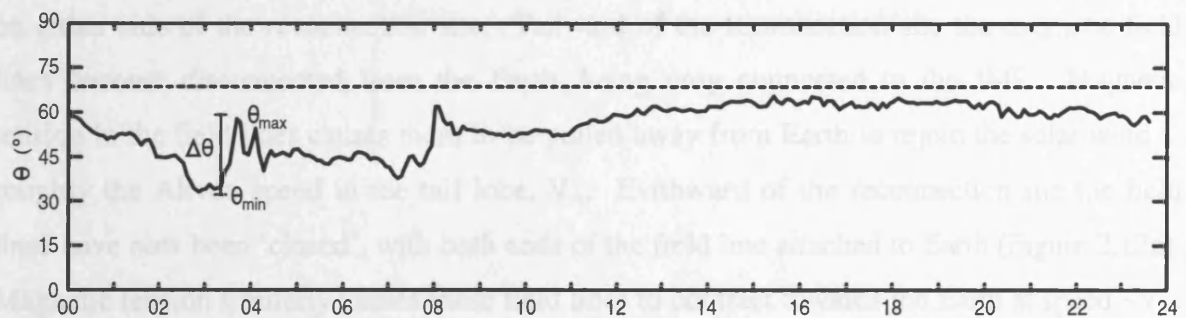


Figure 2.10: An exaggerated schematic of a dipolarised field and the subsequent effect on the in-situ magnetic field measurements. (a) field in a tail-like configuration before expansion phase onset and dipole-like afterwards. (b) geostationary spacecraft would observe angle of the field changing from the minimum to the maximum value. (c) an example of such a dipolarisation observed by the GOES 7 satellite on 23/01/89 [from Milan, 1994].

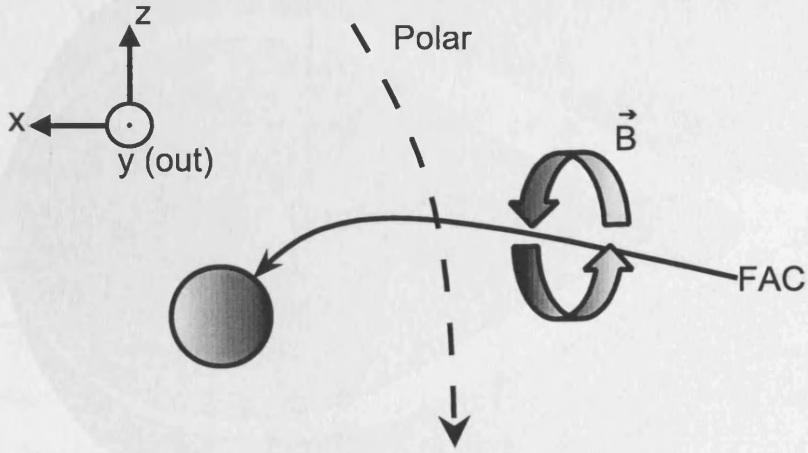
MFE can also be used to identify the presence of field-aligned currents. The magnetic field undergoes a bipolar variation in B_Y due to the passage of the magnetic field due to the current (Figure 2.11a). As the spacecraft begins to experience the effects of the FAC, the y-component of the magnetic field will undergo a negative deflection above the FAC, and a positive deflection below it, producing a bipolar signature as Polar passes through the region occupied by the FAC (Figure 2.11b). Obviously, if the FAC is directed tailwards then the variation is reversed. There is also the possibility that the spacecraft will not cross the plane of the FAC, but may sense it remotely – that is remain either above or below it. In this case, only an increase or decrease in B_Y will be observed. If Polar does not pass directly through the FAC (i.e., to either side) then B_Z will undergo a positive deflection if the spacecraft is duskward of the FAC and negative if dawnward. Therefore by examining both the ground and in-situ magnetic field, a picture can be formed as to what is happening both in the ionosphere and the magnetosphere during periods of substorm activity.

2.6. The Plasma Sheet and Substorm Associated Variations

The plasma sheet is comprised of two regions; the plasma sheet boundary layer and the central plasma sheet (Figure 2.12). This thesis is mainly concerned with the entry of the Polar spacecraft into the plasma sheet boundary layer (PSBL) and subsequently into the central plasma sheet (CPS), with particular reference to substorm phase.

The PSBL is formed of plasma that has just been accelerated out of the nightside reconnection region in the magnetotail. Reconnection in this region begins with inflow of plasma from the tail lobes, but, as reconnection occurs, there is a difference between the two outflow regions on either side of the reconnection site. Tailward of the reconnection site the magnetic field lines become disconnected from the Earth, being only connected to the IMF. Magnetic tension in the field lines causes them to be pulled away from Earth to rejoin the solar wind at roughly the Alfvén speed in the tail lobe, V_A . Earthward of the reconnection site the field lines have now been ‘closed’, with both ends of the field line attached to Earth (Figure 2.12a). Magnetic tension similarly causes these field lines to contract towards the Earth at speed $\sim V_A$. Tail lobe plasma moving into the current sheet is consequently accelerated and flows out in jets directed along the field lines on either side of the current sheet. A typical particle’s motion just earthward of the reconnection site is presented in Figure 2.12b. This shows the particle approaching the current sheet and then oscillating around the field reversal boundary, and accelerating along it due to the electric field, E_Y , in the direction of the current. A Lorentz force due to B_Z acts on the particle in the X-direction, turning it away from the reconnection site. The particle is then no longer trapped by magnetic forces within the current

(a)



(b)

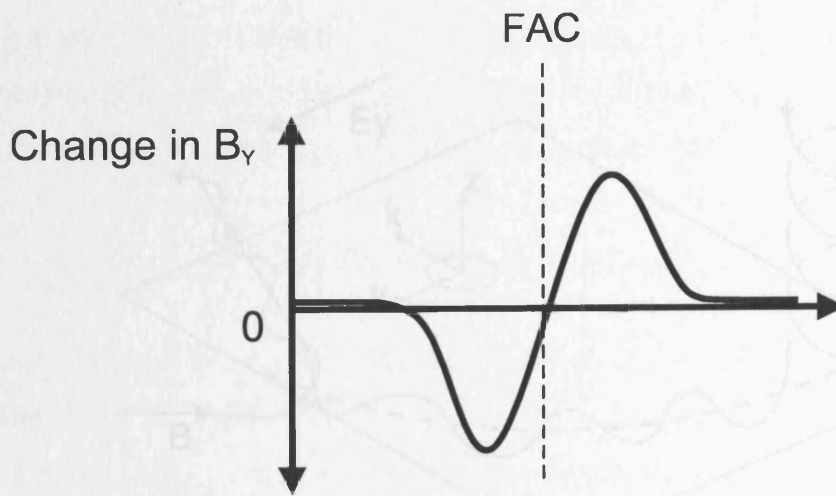


Figure 2.11: The effect of a FAC on the magnetic field as the spacecraft passes through the region. (a) Schematic of Polar passing through FAC; (b) effect of FAC on the in situ magnetic field.

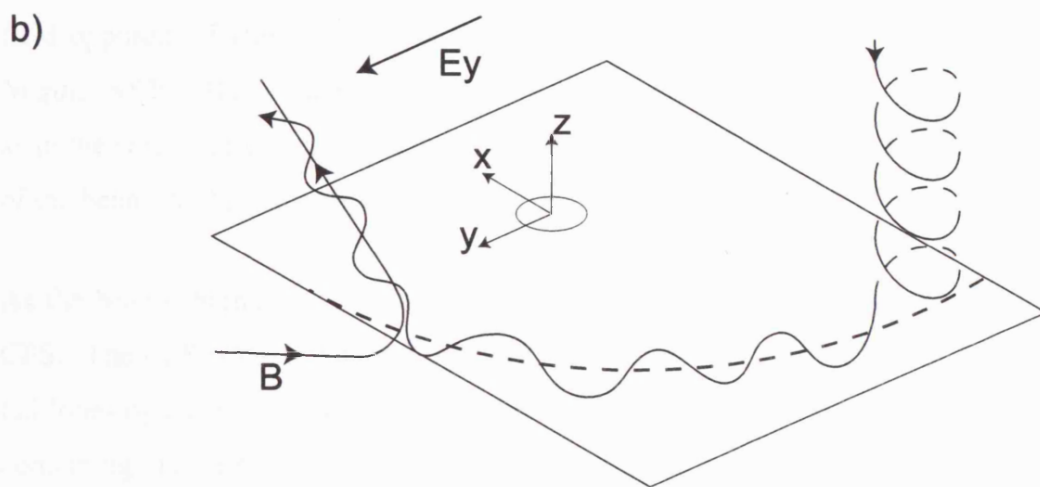
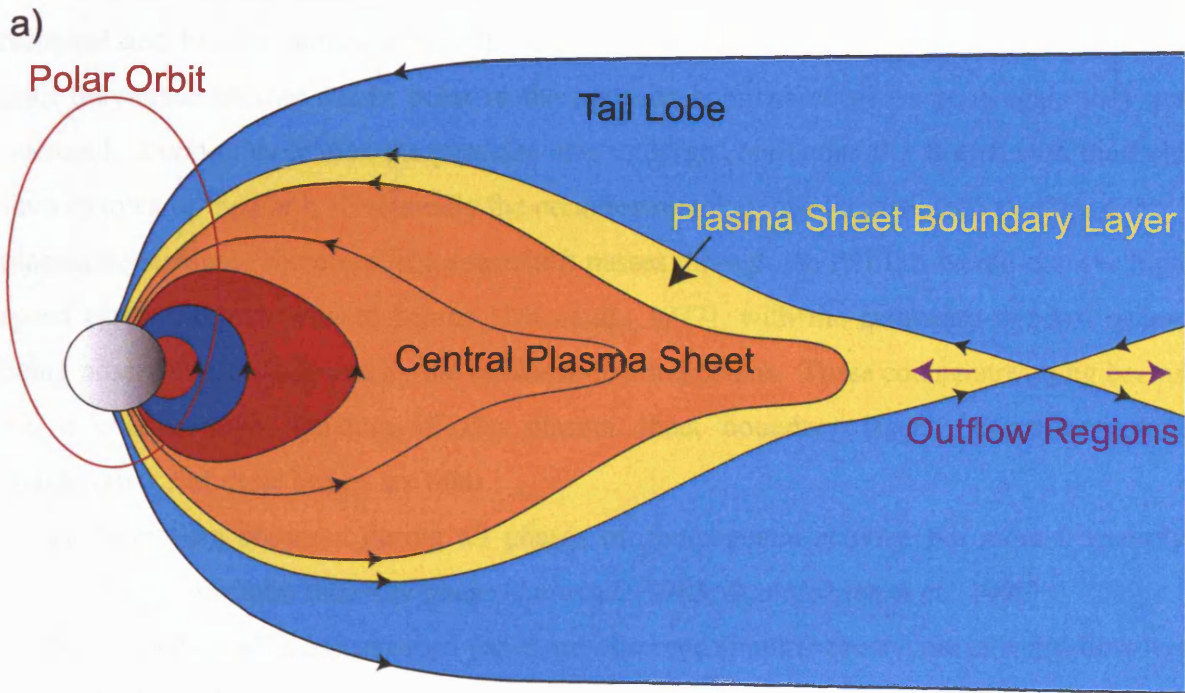


Figure 2.12: (a) Schematic showing the two outflow regions and the two distinct regions of the plasma sheet; the Plasma Sheet Boundary Layer (PSBL) and the Central Plasma Sheet (CPS). (b) Schematic of non-adiabatic ion motion in a current sheet in the neutral line rest frame [from Cowley, 1986].

sheet and exits as an almost field-aligned beam [Cowley, 1985]. These field-aligned beams travel along almost the field lines until they reach a point where they undergo magnetic mirroring (due to the increasing magnetic field strength closer to Earth) where they are reflected and become almost field-opposed. They continue along the field line once more until they reach another mirror point in the opposite hemisphere where once again they are mirrored. During this motion the particles also undergo continuous $\mathbf{E} \times \mathbf{B}$ drift with the field lines in towards the Earth. Eventually the counterstreaming ions thermalize to produce a 'hot' plasma population. Therefore, if a spacecraft passes through the PSBL it would observe high speed earthward and tailward beams [Lui *et al.*, 1977], with the earthward-directed beams being observed first, followed by the tailward-directed beams. These counterstreaming beams are a characteristic signature of the plasma sheet boundary layer. Some important characteristics of these beams are that:

- a) beams are observed during all phases of geomagnetic activity, but more frequently during substorm recovery phase [Lui *et al.*, 1983; Baumjohann *et al.*, 1990];
- b) when earthward and tailward flows are observed simultaneously, the tailward flow has higher velocity than earthward one [Forbes *et al.*, 1981];
- c) anisotropic ion distributions in the PSBL develop into an isotropic distribution in the CPS [Williams, 1981].

The ions in these beams exhibit flow speeds of hundreds of km s^{-1} principally field-aligned or field-opposed. There have been many studies of these flows [e.g. Cattell & Mozer, 1984; Nagai, 1982;1991], but there are very few that have observed the flows at such high-latitude as in the studies discussed in Chapters 5 and 6. Furthermore, these studies allow the mapping of the beams to the coincident auroral activity.

As the beams thermalize, the flux tube, now containing more isotropic plasma, becomes the CPS. The CPS is the region surrounding the neutral sheet current and is separated from the tail lobes by the PSBL. During solar minimum it is comprised of particles with mixed origin containing ions of mostly solar wind origin during geomagnetically quiet intervals and ions of mainly ionospheric origin during active intervals [e.g. Hones *et al.*, 1972; Daglis *et al.*, 1991]. During solar maximum there will be an increased population of solar wind ions, especially during active periods. These particles exist as hot (keV) particles that have nearly symmetric velocity distributions, with a number density of $0.2 - 1 \text{ cm}^{-3}$ [e.g. Nakamura *et al.*, 1992].

The most common plasma feature observed during substorm periods is the plasma sheet compression and stretching, and subsequent injection and energisation of plasma. During the substorm growth phase (section 2.2.1) the plasma sheet is thinned beyond $\sim -15 R_E$, as shown

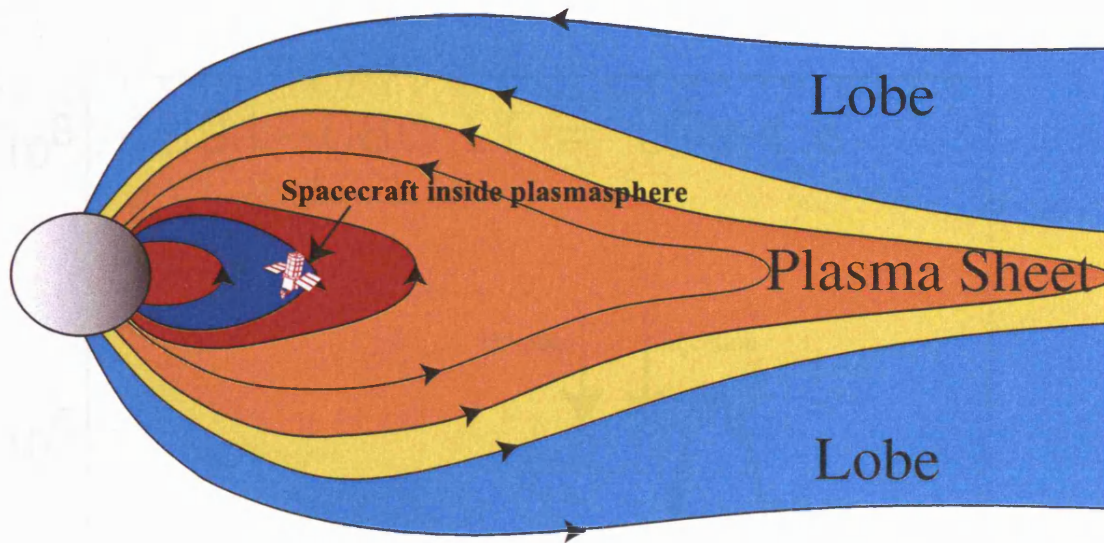
in Figure 2.13, which shows a schematic of the magnetotail configuration (a) before and (b) after dipolarisation. This schematic also presents possible plasma sheet stretching/compression and dipolarisation effects at geosynchronous orbit. Figure 2.14 presents example geosynchronous particle data during an interval of substorm activity. These data are electron flux from the LANL geosynchronous spacecraft 1991 – 080 on 17/11/96. At 19:05 UT the spacecraft began to measure a particle dropout and experienced an injection at 19:14 UT. The more energetic electrons were observed before the less energetic, showing that the injection did not occur at the spacecraft but was relatively close as velocity dispersion is small, but evident. Energetic particle dropouts are common features of the growth phase, but the cause of these has been ascribed to differing mechanisms. One possible mechanism is shown in Figure 2.13a, where an eastward induction electric field is generated in the midnight region due to earthward motion of the current sheet. This ‘stretches’ the dipole field into a more tail-like configuration [e.g. *McPherron*, 1970]. This ‘stretching’ causes the plasmasphere to move over the geosynchronous region. As the plasmasphere is a dense region of cold plasma there is a dropout in the energetic particles observed by a geosynchronous spacecraft [*Moldwin et al.*, 1996]. At expansion phase onset the spacecraft will observe an injection of plasma that also causes the plasma sheet to thicken once more. Combined with dipolarisation, this also causes the plasmasphere to retreat back over the geosynchronous region (Figure 2.13b).

A spacecraft in a high inclination orbit, such as Polar, will also observe changes in the plasma population during substorm intervals. Figure 2.15 presents another dipolarisation schematic, this time showing the effect on Polar. If the spacecraft is in a region of open field lines before the dipolarisation (Figure 2.15a) then it is possible that the magnetic reconfiguration will cause the open/closed field line boundary to move over the spacecraft (Figure 2.15b). The plasma signature of this will involve the spacecraft observing small numbers of low-energy lobe particles before the entry and large numbers of higher-energy plasma sheet particles afterwards. It is important not to confuse this with the spacecraft’s usual entry into the plasma sheet. Therefore background data sets need to be used to determine if a particular entry into the PSBL is due to dipolarisation (and hence is a temporal variation) or simply the spacecraft motion in its orbit (spatial variation). Chapter 6 deals with such an interval.

2.7. Substorm Phenomenological Models

Whilst substorms have been studied for many years they remain one of the most contentious aspects of solar-terrestrial physics. Many different phenomenological models have been suggested for substorms and so a brief overview of the main ones will be presented here.

(a)



(b)

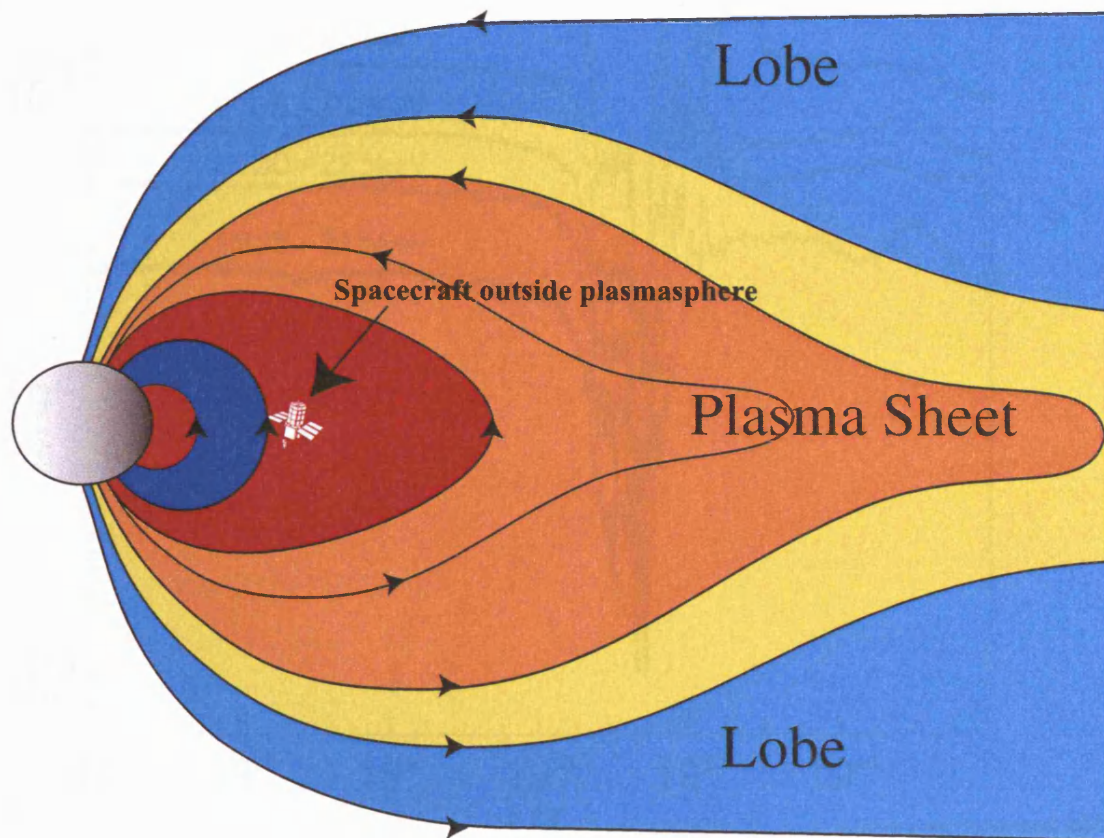


Figure 2.13: Schematic to show effects of dipolarisation on the magnetotail. (a) During growth phase tail is compressed and stretched such that near-Earth field becomes more tail-like and so plasmasphere moves over geosynchronous region. (b) After dipolarisation at expansion phase onset the near-Earth field lines return to a dipole configuration and so the plasmasphere retreats back over the geosynchronous region.

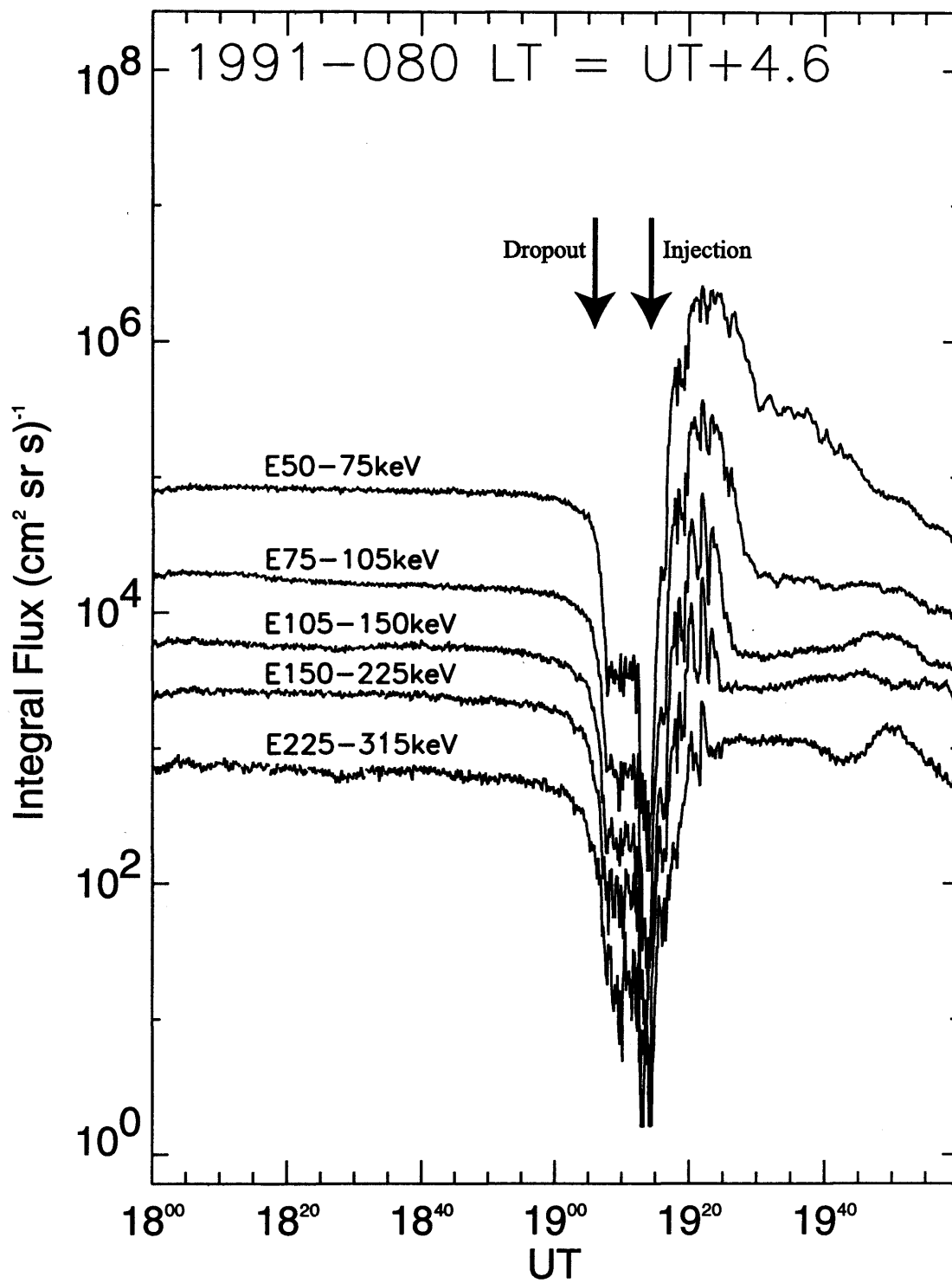


Figure 2.14: Example of plasma dropout during the growth phase, followed by an injection at expansion phase onset.

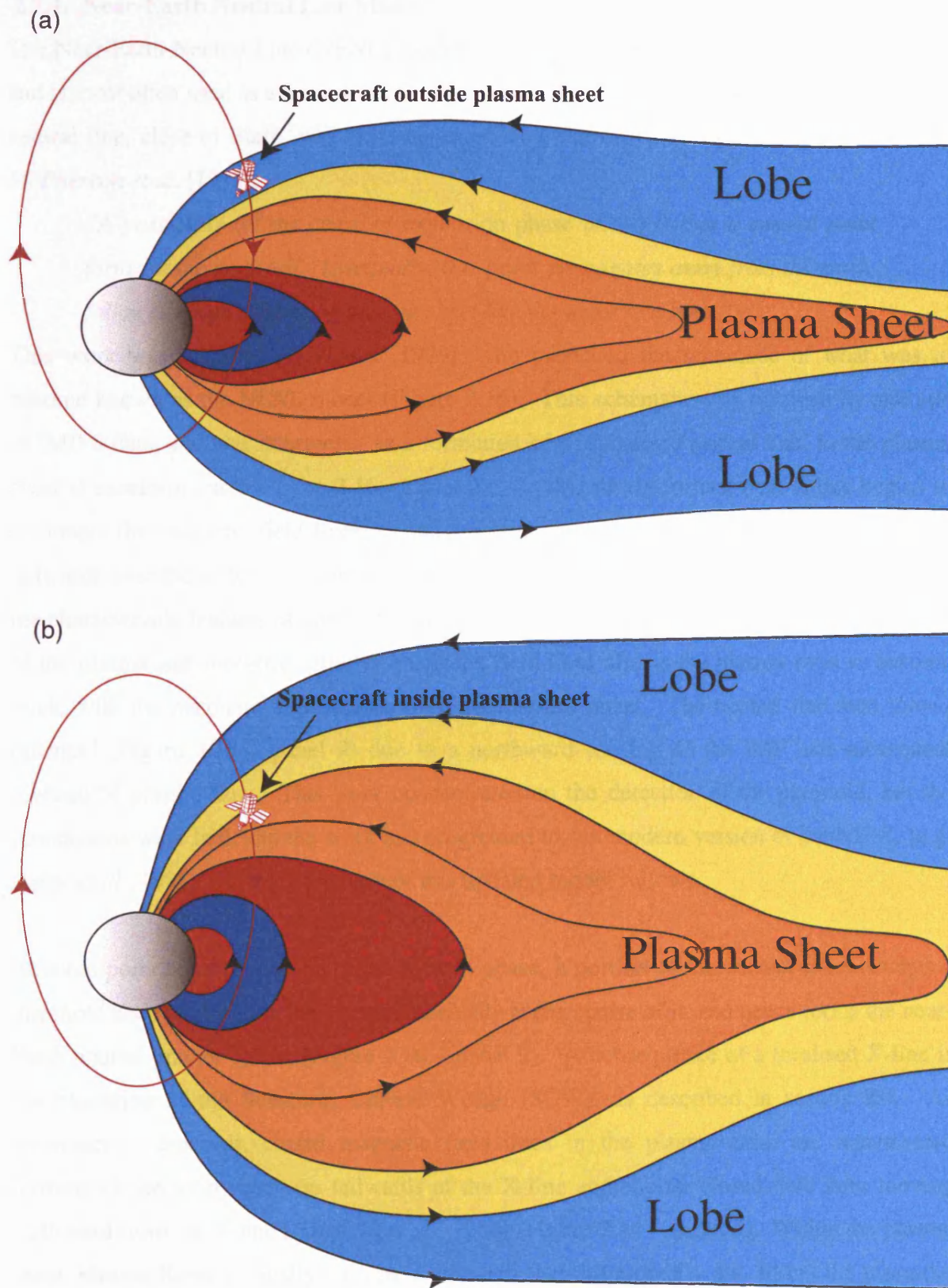


Figure 2.15: Schematic to show effects of dipolarisation on the magnetotail as in Figure 2.13, but with Polar's orbit shown. (a) Before dipolarisation Polar is outside the plasma sheet. (b) After dipolarisation Polar is inside the plasma sheet.

2.7.1. Near-Earth Neutral Line Model

The Near-Earth Neutral Line (NENL) model is perhaps the most established substorm model and is most often used as a framework for discussion of substorm studies. The formation of a neutral line, close to Earth, was first suggested as a cause of the expansion phase onset by *McPherron et al.* [1973]:

“A possibility (of the cause of expansion phase onset) is that a neutral point forms in the near tail. Eventually, this point propagates away from the earth, followed by an expanding plasma sheet like the wake of a boat.”

This work was followed by *Hones* [1979], who produced the schematic of what was to become known as the NENL model (Figure 2.16). This schematic was obtained by analysis of IMP-8 data, and was interpreted as a formation of a ‘substorm neutral line’ in the plasma sheet at substorm onset (Figure 2.16 – panel 2). As this newly formed neutral line begins to reconnect the magnetic field lines, closed magnetic loop structures are formed and ejected tailwards over the next four minutes (Figure 2.16 – panels 3 to 8). This ‘plasmoid’ is one of the characteristic features of the NENL model. Earthward of the neutral line the confinement of the plasma and energetic particles on closed field lines allows the plasma sheet to become thick, with the magnetic field less tail-like than before onset. The neutral line then moves downtail (Figure 2.16 – panel 9) due to a northward turning of the IMF and subsequent reversal of plasma flow. This work concentrated on the detection of the plasmoid, but the foundations were laid, and the work has progressed to the modern version of the NENL [e.g. *Baker et al.*, 1996]. A brief summary of this updated model follows.

At some point towards the end of the growth phase, a portion of the current sheet reaches a threshold and reconnection begins spontaneously at the centre of it, and hence forms the near-Earth neutral line, or X-line (Figure 2.16 – panel 2). A consequence of a localised X-line is the formation of the Substorm Current Wedge (SCW), as described in section 2.4. As reconnection proceeds, closed magnetic field lines in the plasma sheet are reconnected forming closed loop structures tailwards of the X-line and shorter closed field lines moving earthward from the X-line [*Fairfield et al.*, 1984] (Figure 2.16 – panel 3). Within the plasma sheet, plasma flows vertically into the X-line and then horizontally out, filling the plasmoid tailward of the X-line and accelerating plasma earthwards. Once the open field lines of the tail lobes reconnect, they wrap around the plasmoid formed earlier and begin to ‘drag’ it downtail as there is no force holding it in place (Figure 2.16 – panels 4-8). As the plasmoid moves downtail the plasma sheet tailward of the near-Earth X-line collapses to a thin sheet (Figure 2.16 – panel 8). Subsequently, open flux of the tail lobe reconnects at the X-line to form closed field lines earthward and open IMF lines tailward of the X-line. This continues

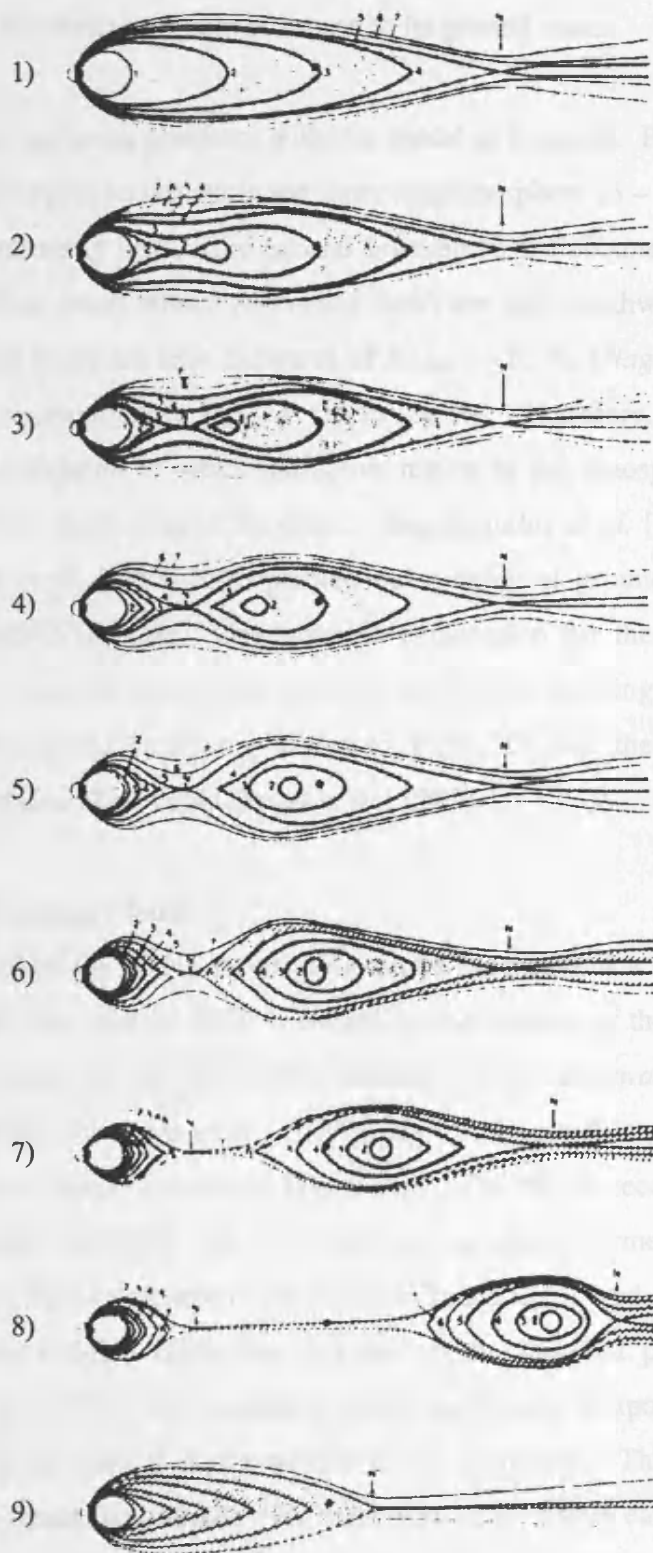


Figure 2.16: Schematic of the NENL model in which a reconnection site close to Earth is responsible for expansion phase onset [from Hones, 1979].

for a few minutes, until the X-line is forced tailwards by the increasing magnetic pressure in the plasma sheet. As the X-line retreats downtail, the substorm current systems and auroral activity decrease. This is the start of the recovery phase with all disturbances eventually dying out and the magnetosphere returning to its ground state.

However, there are some problems with this model as it stands. Perhaps the most important is that substorms appear to initiate in the inner magnetosphere ($6 - 10 R_E$) from the mapping of the auroral luminosity just before auroral breakup [e.g. *Pulkkinen et al.*, 1991; *Baker et al.*, 1996]. However, onset-related earthward flows are seen earthwards of $X_{GSM} = -30 R_E$, and mostly tailward flows are seen tailwards of $X_{GSM} = -20 R_E$ [*Nagai et al.*, 1997]. This places the NENL at approximately $X_{GSM} = -20$ to $-30 R_E$. Therefore, the NENL appears to form tailward of the location to which the active region in the ionosphere maps. Another major problem involves the timing of the onset. *Angelopoulos et al.* [1994], *Sergeev et al.* [1995] and *Shiokawa et al.* [1998] have pointed out a delay of ground-based substorm signatures from a tailward flow onset. One possible explanation for these problems is described in section 2.7.2. Another possibility involves the NENL forming as a precursor to a current disruption that occurs somewhat closer to Earth, or that the current disruption triggers reconnection after a short delay [*Baker et al.*, 1996].

2.7.2. Flow-Braking Model

Although based on the NENL model, this can be examined as a model in its own right. This model uses the idea that the SCW is caused by the braking of the earthward high-speed flow that has been accelerated by the NENL reconnection [*Hasegawa*, 1979; *Hesse & Birn*, 1991; *Haerendel*, 1992; *Shiokawa et al.*, 1997]. The model itself is proposed by *Shiokawa et al.* [1998] and a schematic is shown in Figure 2.17. The NENL reconnection (1) produces high-speed, earthward travelling ions earthward of the newly formed near-Earth X-point. The high-speed ion flow in the neutral sheet (2) is suddenly braked at the boundary between the dipole-like and tail-like field lines (3) due to the tailward pressure force suggested by *Shiokawa et al.* [1997]. The transition from a tail-like to a dipole-like field configuration is the result of a dawnward inertia current at the boundary. The braking of fast earthward directed flow forms this current. As these fast flows travel earthward the motion must be braked somewhere near to the pressure maximum (inside $\sim 10 R_E$). The corresponding inertial force is directed earthward, and it drives an electric current which points eastward – the dawnward inertia current [*Haerendel*, 1992]. The dawnward inertia current can be the cause of the cross-tail current disruption (3) as suggested and checked by *Haerendel* [1992]. At the flow-braking point, FACs can be generated by shear of the flow velocity at both the dawn and

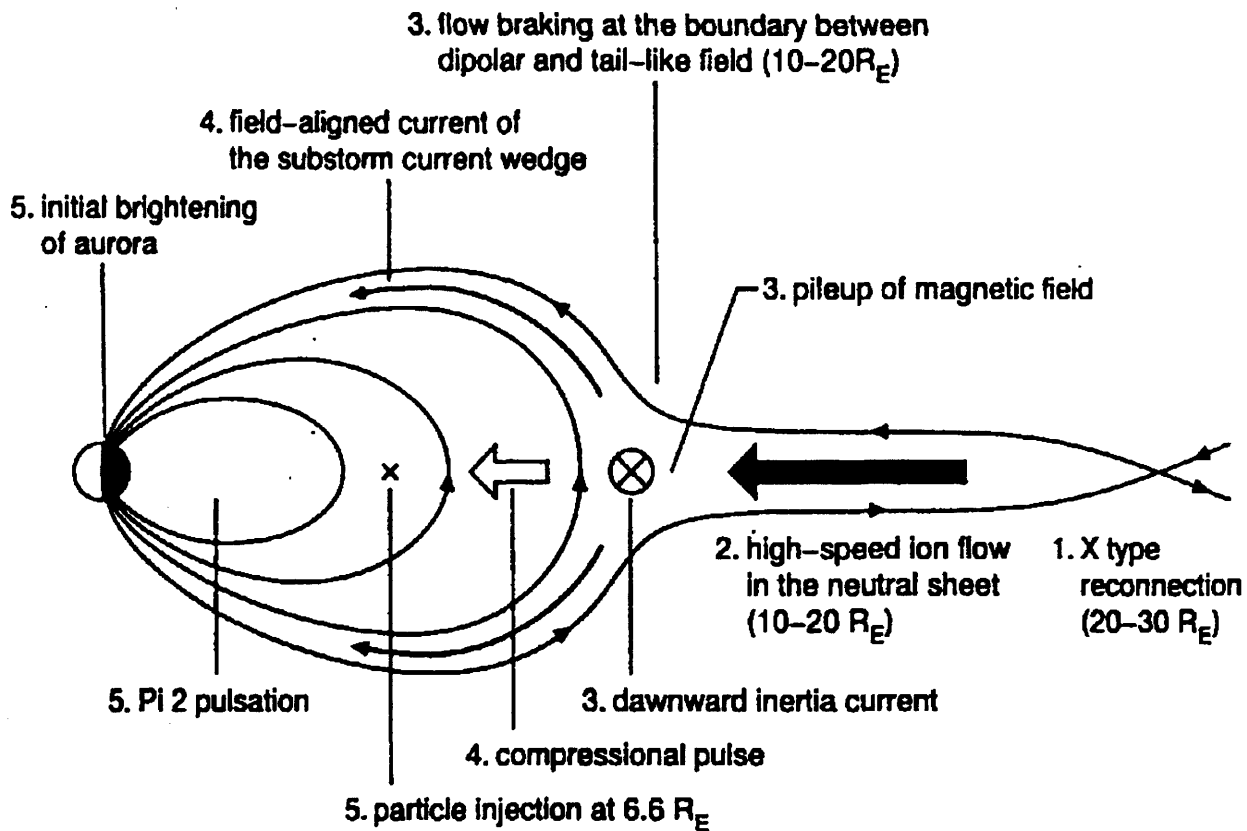


Figure 2.17: The proposed flow-breaking model of the current wedge formation during the initial stage of the substorm expansion phase [from *Shiokawa et al.*, 1998].

dusk edges of the flow region [Hasegawa, 1979]. The FACs that are generated are downward in the dawn sector, and upward in the dusk sector – the SCW (4) and hence auroral intensification occurs (5). It should also be noted that the enhancement of earthward kinetic pressure due to the flow burst compresses the inner magnetosphere at the flow-braking point. Therefore, these flow bursts can cause compressional pulses (4) and hence Pi2 pulsations (5). Finally, at the braking point of the flow, which is the boundary between dipole-like and tail-like field regions, particles start drift motions in the dipole-like field. Therefore, the flow-braking point should correspond with the injection boundary. However, the injection boundary is well inside $10 R_E$, whilst the flow-braking point is likely to be tailwards of this region. An important point is that the high-speed flows are only observed for the first few minutes of the expansion phase onset. Therefore this model can only be responsible for the initial stage of the substorm expansion phase onset, with some additional process needed during the following stage of the expansion phase.

2.7.3. Current Disruption Model

Chao *et al.* [1977] realised that one of the most important effects of a substorm was the thinning of the plasma sheet, and so they developed a 1D model for this feature, which has become known as the Current Disruption (CD) model. The basis of this model involves launching a fast mode MHD rarefaction wave in the tailward direction along the plasma sheet.

A non-planar fast MHD rarefaction wave is assumed to be launched in the near-Earth plasma sheet and is propagating in a model field of the plasma sheet [Kan, 1973] as shown in Figure 2.18. The wave fronts are constructed using Huygen's principle and it is seen that they become increasingly planar and more perpendicular to the magnetic field as the wave propagates tailward. Behind the rarefaction wave, the pressure along the X-direction will be reduced more than in the perpendicular direction. Therefore, as the pressure behind the rarefaction wave becomes lower than across the plasma sheet boundary, the boundary is forced to move toward the neutral sheet. Thus, the plasma sheet behind the wave is thinned by perpendicular compression. One problem with this model is that the predicted amount of thinning is less than that observed. The discrepancy is attributed to the assumption in the model in which the magnetic flux is conserved during thinning. This should lead to a large increase in the magnetic field intensity, which has not been observed. Thus, a significant amount of magnetic flux must have been removed from the plasma sheet during thinning. Therefore, the amount of thinning predicted by the model is underestimated.

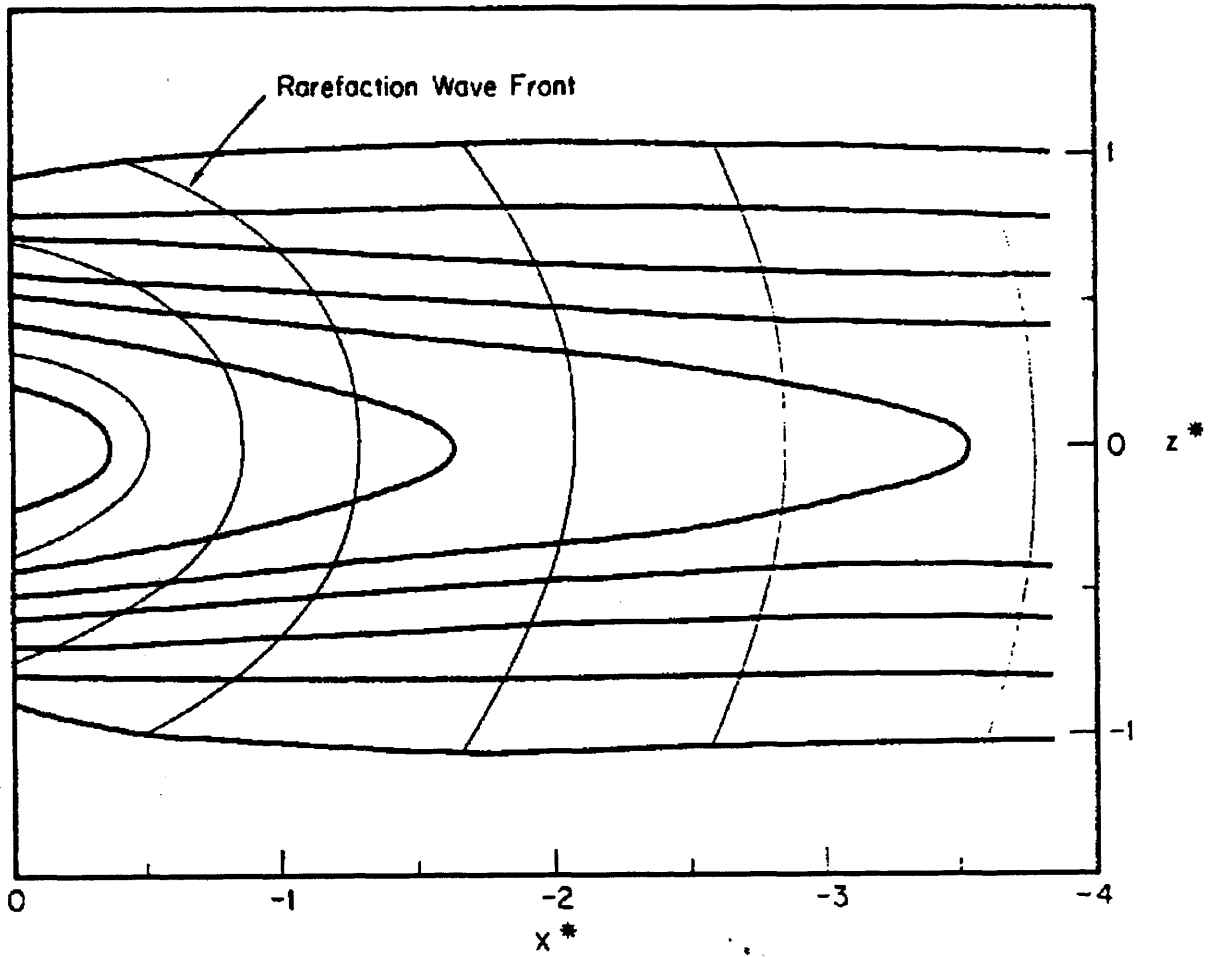


Figure 2.18: The CD Model. The fronts of the fast MHD rarefaction wave (thin curves) propagating in a model tail field (heavy curve) [from *Chao et al.*, 1977].

The original study by *Chao et al.* [1977] only briefly mentioned a possible mechanism of generating the rarefaction wave. It was considered as a consequence of a reduction in the cross-tail current. This reduction will induce a large voltage which can, in turn, cause a high-speed ($\mathbf{E} \times \mathbf{B}$) drift motion of plasma, which means that the magnetic energy in the inductive circuit is converted into the kinetic energy of the plasma. No detailed discussion of this generation mechanism is given in the original work, but several have been suggested since. One such example is presented in *Lui et al.* [1991] where a thin current sheet develops in the inner magnetosphere during the substorm growth phase for the same reason as in the NENL model. As the current sheet thins, the ions become non-adiabatic and begin to stream across the current sheet where they interact with adiabatic electrons drifting in the opposite direction (the kinetic cross-field-streaming instability), producing lower hybrid waves [*Lui et al.*, 1990]. At the same time, the lower-hybrid-drift instability is driven by the density gradient on the boundary of the plasma sheet. These two instabilities combine to produce anomalous resistance in the plasma sheet that disrupts the cross-tail current. This current must continue to flow due to the high inductance of the tail circuit, so it is diverted along the field lines into a SCW configuration. This is known as the Cross-field Current Instability model (CCI). There is still the matter of explaining plasmoid formation, so it is proposed that at some point downtail, late in the expansion phase, these effects initiate reconnection and the subsequent generation of a plasmoid.

2.7.4. Boundary-Layer-Dynamics Model

In this model, developed by *Rostoker & Eastman* [1987], the substorm expansion phase reflects the development of a Kelvin-Helmholtz Instability (KHI) at the interface separating the central plasma sheet (CPS) and the plasma sheet boundary layer/low-latitude boundary layer (PSBL/LLBL). Once again the substorm begins with the IMF turning southwards and thus increasing the energy input from the solar wind. This leads to an increase in the circulation in the CPS and LLBL cells, which, in turn, leads to an increased momentum shear at the CPS/LLBL boundary. Normally, this momentum shear is insufficient to produce any instability, but it is proposed that the expansion phase be triggered by a burst of reconnection at the far tail X-point. This enhanced momentum density is sufficient to produce wave activity, via the KHI, over an azimuthally limited area of the dusk sector CPS/LLBL interface (Figure 2.19). As shown by *Thompson* [1983], this leads to the development of parallel electric fields (and hence particle precipitation) on field lines crossing the boundary. Therefore, growth of the KHI generates a current wedge, corresponding to the westward travelling surge in the ionosphere. The FACs associated with this wedge, which thread the

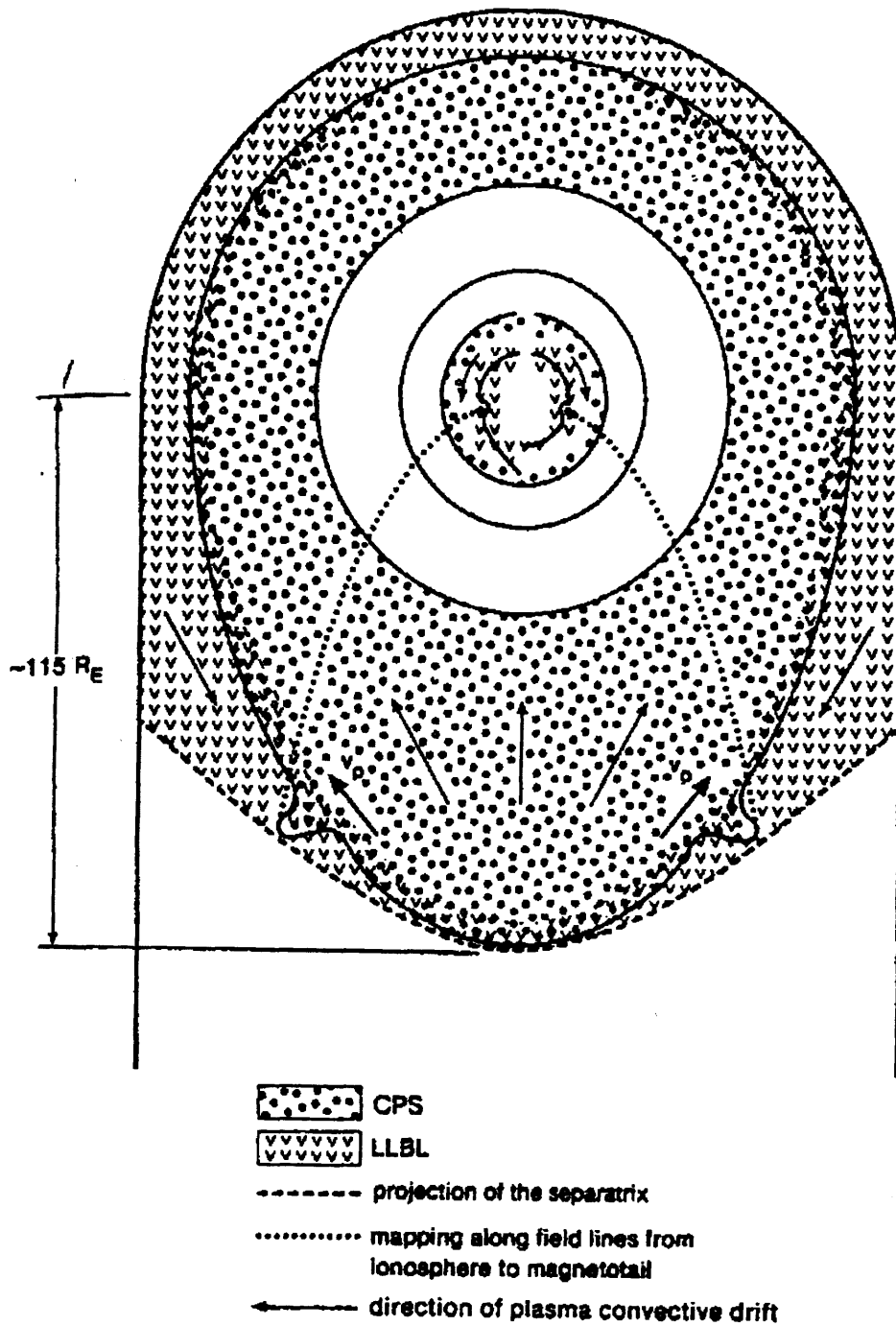


Figure 2.19: The BLD Model. Waves are formed due to the Kelvin-Helmholtz Instability at the outer edge of the CPS [from *Rostoker and Eastman, 1987*].

PSBL on their way to the CPS/LLBL interface, provide the B_Y and B_Z magnetic disturbances observed at expansion phase onset.

2.7.5. Magnetosphere – Ionosphere Coupling Model

Kan & Sun [1985] developed a model to explain the WTS and Pi2 pulsations as a consequence of an enhancement in magnetospheric convection. This model has recently been incorporated into a globally integrated substorm model [*Kan*, 1998]. The growth phase of the substorm begins when the IMF turns southward. At this time the polar cap potential increases, sunward convection enhances and the near-Earth cross-tail current intensifies. Next, dipolarisation in the near-Earth plasma sheet occurs at expansion phase onset. This can be triggered by flow braking (section 2.7.2) or by the northward turning of the IMF, blocking sunward convection. The intense dipolarisation electric field launches a pair of oppositely propagating Alfvén waves toward the conjugate ionosphere. These Alfvén waves carry with them FACs and can lead to the formation of the SCW. Expansion phase onset begins in the ionosphere shortly afterwards when the Alfvén wave is reflected at the ionosphere and, over repeated bounces between conjugate ionospheres, brightens the onset arc and intensifies the SCW and the auroral electrojet. Dipolarisation is also accompanied by thinning of the plasma sheet, which leads to nightside reconnection in the $\sim 20 - 30 R_E$ region that sustains the ongoing expansion phase. The expansion phase ends as the dipolarising region expands downtail where the tail current is less intense.

2.7.6. Ballooning Instability Model

This model was derived by *Roux et al.*[1985] from GEOS 2 field and particle data in conjunction with ground-based instrumentation close to the spacecraft's footprint. The model is interpreted as the formation of a spatial boundary between a region of dipole-like and tail-like field lines, analogous to a heavy fluid resting on a light fluid. The pressure gradients of the energetic ions and the magnetic field both point earthward in the dipole-like region and tailward in the tail-like region. Ballooning modes are driven by the interaction of the ion pressure gradient with a local region of suitable magnetic curvature. Eventually, the transition region from dipole-like to tail-like field lines becomes unstable and a surface wave develops and propagates westward as a result of the westward travelling ions. As a consequence of the instability, polarisation electric fields develop due to the accumulation of energetic ions and electrons at both the western and eastern edges of the wave. Excess energetic ions must be neutralised by electrons from the ionosphere; hence there is an earthward-directed current at the western edge. Extracting ions from the ionosphere is too slow, and so the excess electrons are removed by creating a tailward-directed current at the eastern edge. Thus, FACs

successively flow earthward and tailward (Figure 2.20) along magnetic field lines in order to maintain charge neutrality. This bimodal current system leads to a disruption in the cross-tail current [Roux *et al.*, 1991]. Pi2 pulsations can be described in terms of transient magnetic signatures in the auroral region, caused by the unsteady nature of this current system. Observations have been made by all-sky camera images and GEOS 2 showing the WTS is observed in the ionosphere at the same time as the instability forms. Hence it seems that the WTS could be the image of the instability, formed in the upper atmosphere by the precipitating electrons. These results suggest that the general expansion of auroral arcs to the north, and their azimuthal expansion, are the consequences of a ballooning instability that starts developing in the inner plasma sheet and later expands until it covers most, if not all, of the plasma sheet.

2.7.7. Other Models

Several other models have been devised that attempt to explain substorms. These include the Thermal Catastrophe model [Smith *et al.*, 1986], which involves energy entering the magnetotail by Alfvén waves generated at the dayside magnetopause. The subsequent absorption of these waves increases the temperature in the PSBL to a value much larger than the equilibrium temperature. The heating rate then increases dramatically causing a runaway temperature rise – thermal catastrophe.

Another model is the Tearing Mode Instability [Schindler, 1974] in which the instability can dissipate energy, stored in the current systems and magnetic field of the Earth's magnetotail. One suggested cause of such an instability is a shear in the tail magnetic field [Büchner *et al.*, 1991]. These models, whilst possible, have not been significantly developed and so have gained little support over the more popular models.

2.7.8. Summary: The Kiruna Conjecture

At the first International Conference on Substorms (ICS-1) the Kiruna Conjecture was proposed by Kennel [1992]. This attempts to summarise the main models and place the substorm signatures in temporal order. An approximate, but not strict, temporal sequence is reproduced below [from Kennel, 1992].

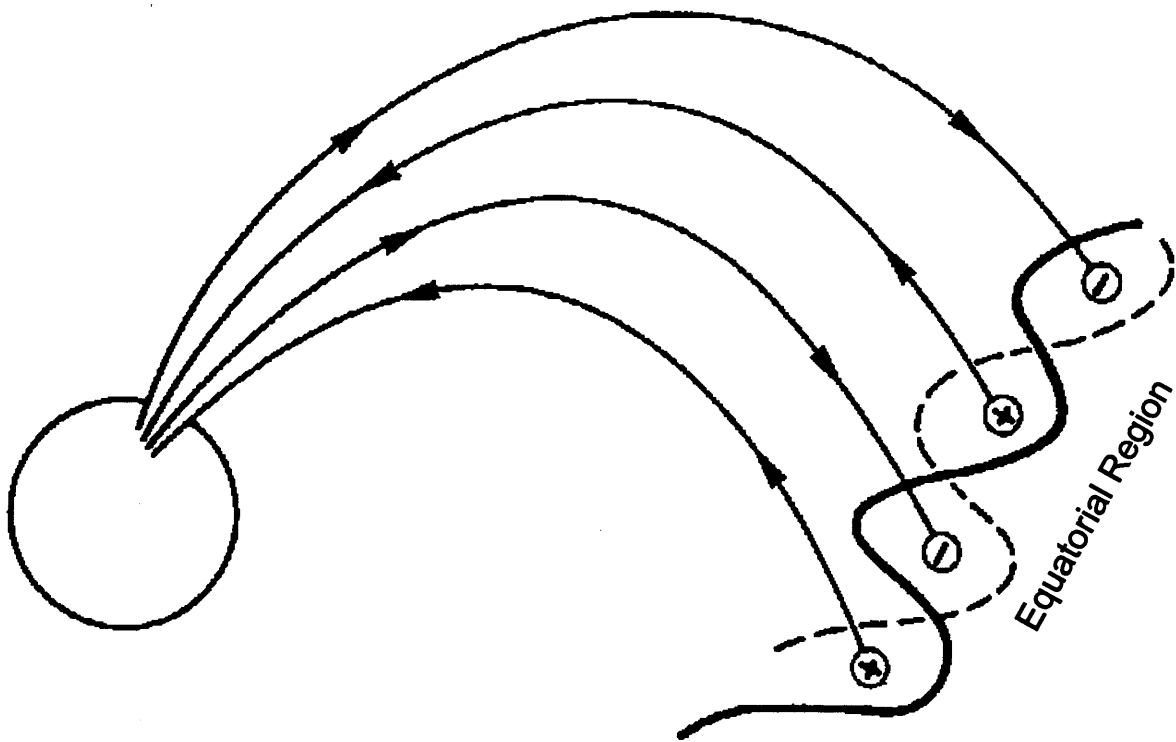


Figure 2.20: Sketch showing the field-aligned current structures associated with the development of the Ballooning Instability [from Roux *et al.*, 1991].

Auroral Ionosphere	Geosynchronous	Magnetosphere
Activation of dayside arcs, transient high-speed flows		Dayside reconnection
E-field increases	E-field increases	Tail-lobe fluxes increase
Equatorward arc motion	Current sheet approaches Earth	Magnetopause moves inward, increased tail flaring
Fadings/pseudo onset	Pseudo-dipolarisations, injections	
Brightening of onset arc		
Formation of WTS	Dipolarisation/Injection, Pi2	
Expansion of auroral bulge	Expansion of current wedge	Plasma sheet reconnection at NENL
Brightening of poleward traversing arc		Plasmoid formation
Contraction of auroral bulge	Weakening of current wedge	Plasmoid retreat, Travelling Compression Regions Neutral line retreat

The main aim of the Kiruna Conjecture is to demonstrate the different ideas of the main models and point out possible difficulties. A summary of the main models is reproduced in Figure 2.21. In this figure the three main models are shown with their main features in temporal order. It should be noted that, whilst still of some use, the Kiruna Conjecture was devised in 1992 and so does not include the more recent developments such as flow braking in the NENL (section 2.7.2) that answer some of the difficulties outlined by Kennel. One interesting suggestion is that onset and dipolarisation may not be directly related to plasma sheet reconnection (and subsequent production of plasmoid). This would suggest that the *“onset, WTS and attendant changes in the near-Earth magnetotail are governed by relatively local processes that are tightly coupled to the ionosphere, whereas plasma sheet reconnection and plasmoid formation are relatively independent and larger-scale responses to an increased throughput of magnetic flux in the global convection pattern.”* [from Kennel, 1992]. If this is the case, then plasma sheet reconnection could appear at a time that is not associated with substorm signatures. This is an interesting idea, but one that is yet to be observed by any instrumentation, but demonstrates how much work still needs to be done before the phenomena of the magnetospheric substorm is completely understood.

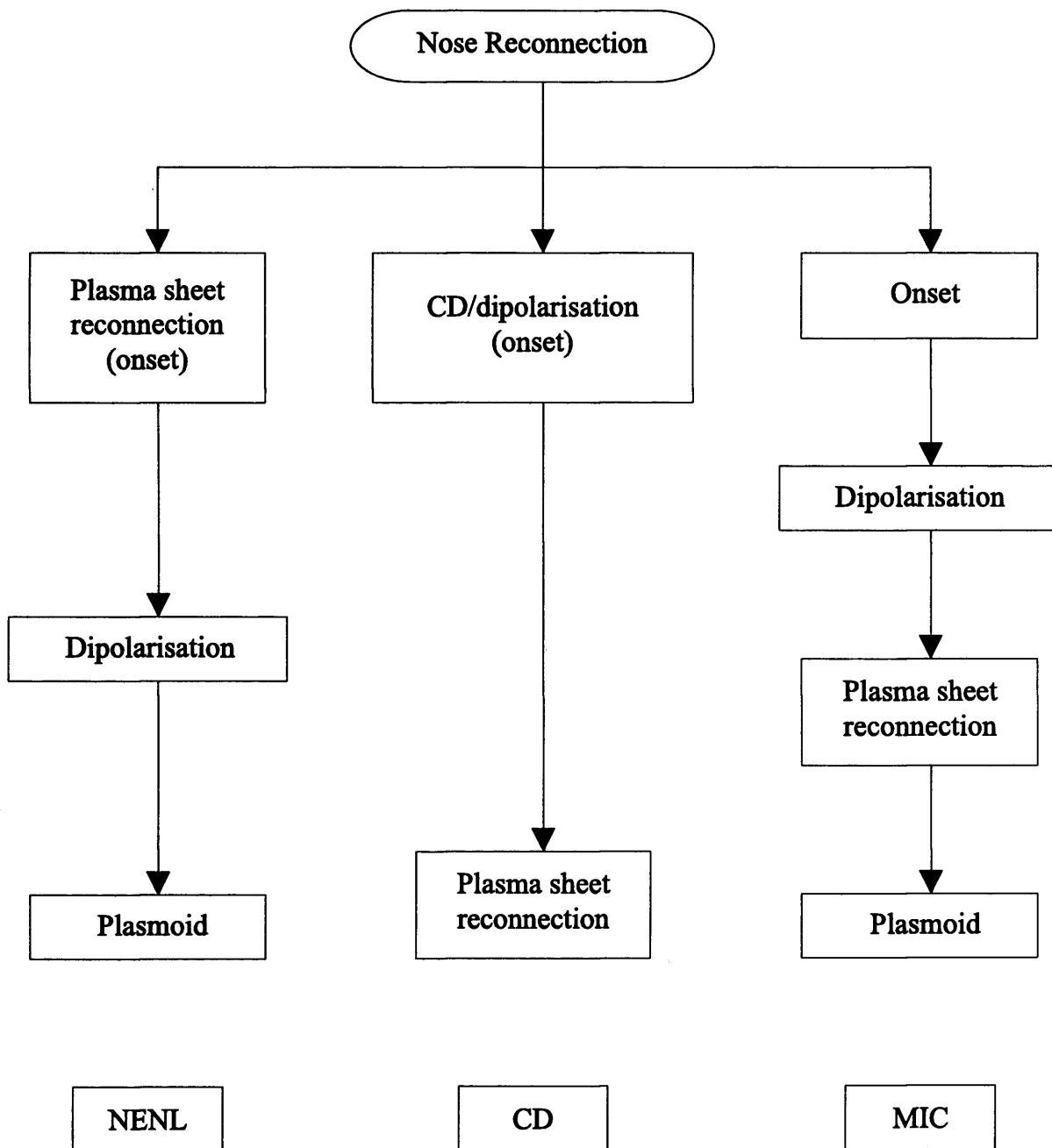


Figure 2.21: The Kiruna Conjecture, from *Kennel* [1992]. Summary of the three main substorm models, the Near-Earth Neutral Line (NENL), the Current Disruption (CD) and the Magnetosphere - Ionosphere Coupling (MIC) models [from *Hall*, 1997].

The study detailed in this thesis involves spacecraft observations in a location not used before for substorm studies. The spacecraft in question carries an ideal set of in-situ instrumentation, and also carries three auroral imagers. The location of the spacecraft is such that it traverses a region that maps into the magnetotail, including the substorm onset location, but is also close to Earth and so the spacecraft position can be mapped into the ionosphere to a fair degree of accuracy. This mapping allows the direct comparison of auroral and ground magnetic features with in-situ particle and magnetic field observations, giving a unique combination for substorm studies.

CHAPTER 3

Instrumentation

3.1. Introduction

When performing any kind of study of a magnetospheric topic there will always be one major problem, the spatial/temporal ambiguity. That is, if a spacecraft enters a region of high energy plasma it is impossible to know for sure if the high energy plasma is a spatial feature, and so existed in that region before the spacecraft appeared, or if the plasma is a temporal feature, and so has just entered the locale of the spacecraft from elsewhere. In the context of a substorm study other background data sets can be used to determine if there is any substorm activity and provide accurate timing information, thereby helping to resolve the spatial/temporal problem. The primary instruments are on-board the Polar spacecraft, with background data sets from Wind, the Los Alamos National Laboratory fleet of spacecraft and the ground-based IMAGE, SAMNET and Greenland magnetometer chains. These background data sets provide information on particle dropouts and injections, Pi2 pulsations and magnetic bays in ground magnetometers. Other instruments allow the interval to be placed into context by examining the IMF orientation and observing any auroral displays. Therefore, this thesis study makes use of several different instruments, located both on spacecraft and on the ground.

3.2. The Polar Spacecraft

Polar is the second of NASA's Global Geospace Science (GGS) spacecraft that also form part of the International Solar Terrestrial Physics Program (ISTP). The launch of Polar occurred at 06:24 EST on February 24th, 1996 from Space Launch Complex 2 at VAFB. Figure 3.1 shows a schematic of the spacecraft with the locations of the various instruments included. The spacecraft is in a highly elliptical orbit, with parameters given in Table 3.1.

Initially apogee was over the northern polar region, but has been moving towards the equator at $\sim 15^\circ$ per year. The nominal mission duration was two years, but a three year extended mission has been approved. Figure 3.2 presents a schematic of the Polar orbit, illustrating how the orbit varies as the mission progresses (Figure 3.2a) and how the orbit varies with respect to the Sun (Figure 3.2b). The orbit is fixed in the Earth's frame of reference, but varies in the Sun's frame due to the Earth's orbit around the Sun. Thus the spacecraft is inbound on the nightside during spring (passes from north polar cap into the plasma sheet) and is outbound during autumn (passes from the plasma sheet into the north polar cap).

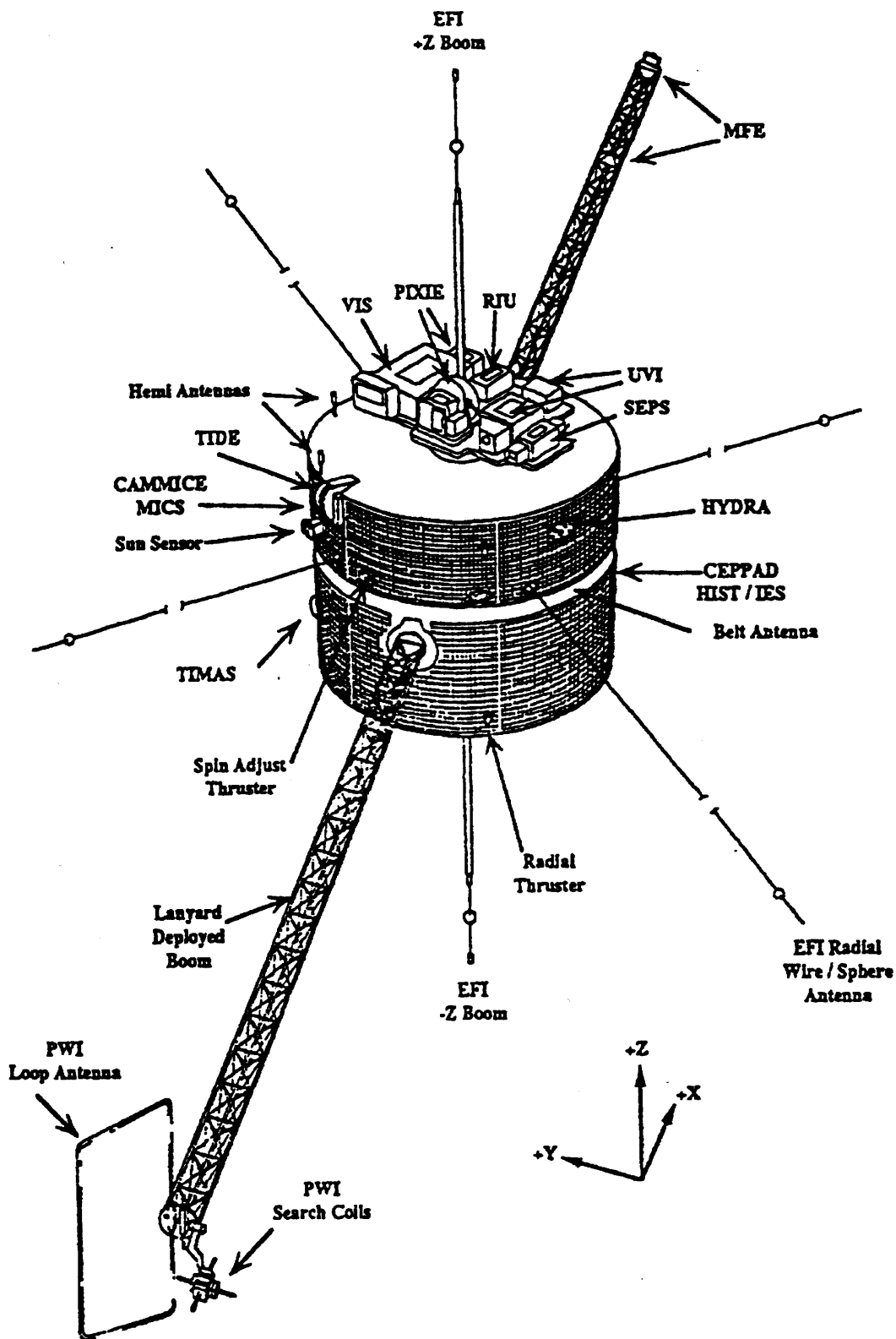


Figure 3.1: Schematic of the Polar spacecraft showing the impressive array of instruments.

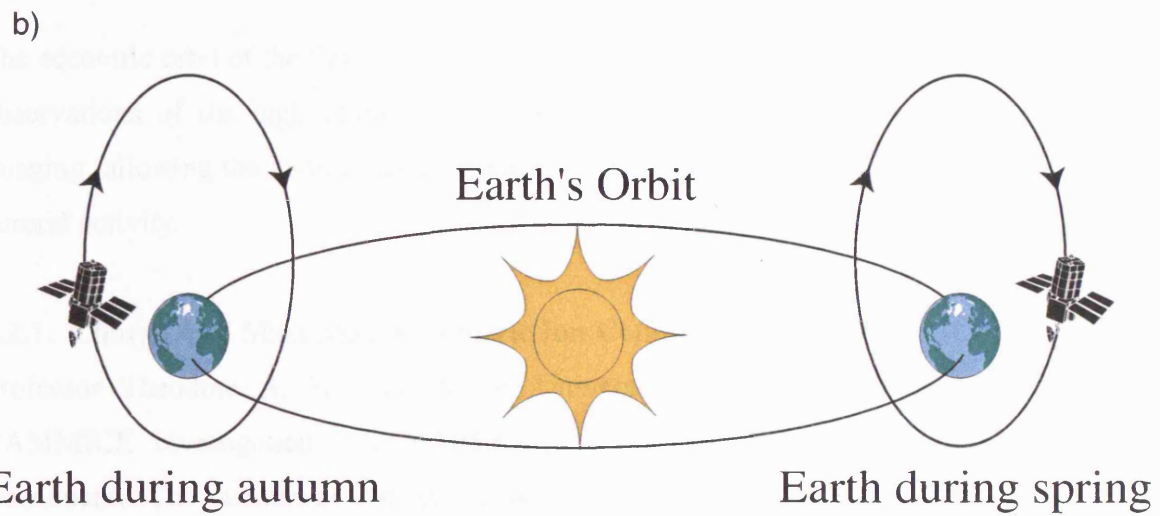
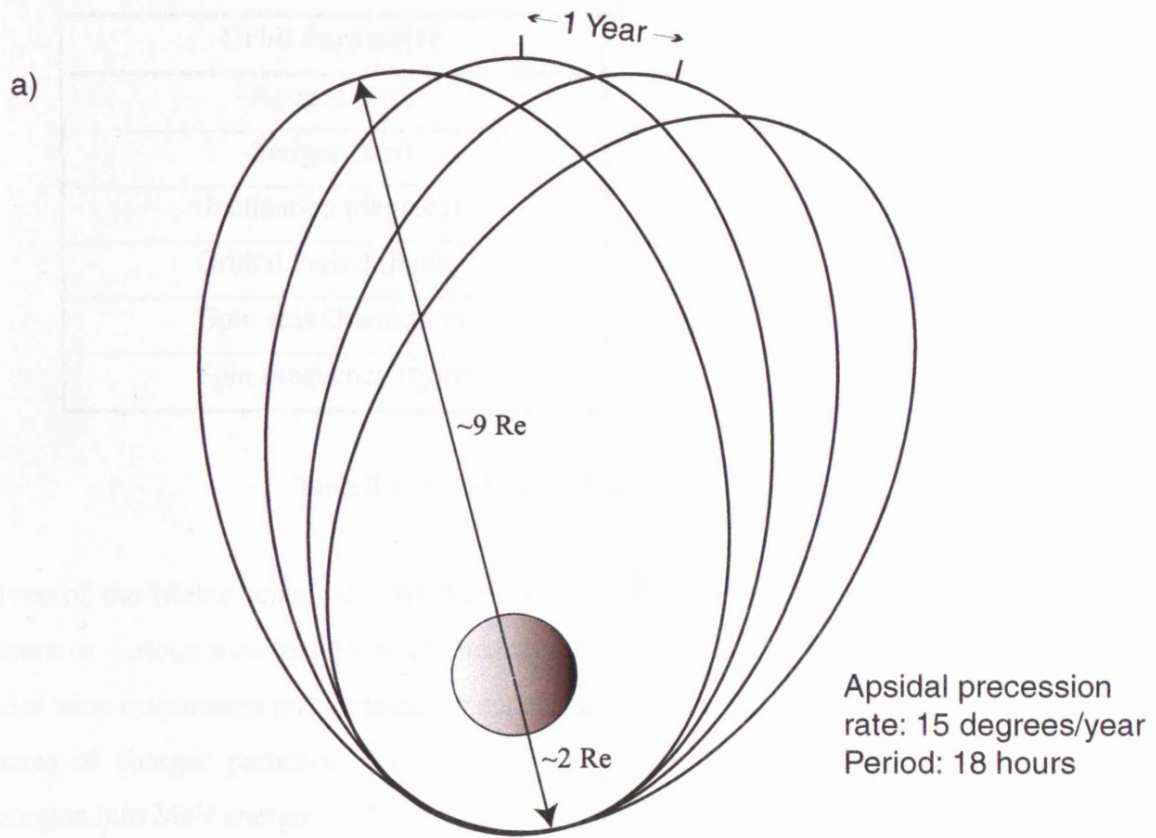


Figure 3.2: Schematic representation of the Polar orbit. (a) showing the precession and period (b) showing the seasonal variation with respect to the Sun.

Orbit Parameter	Value
Apogee (km)	11 500 (~1.8 R _E)
Perigee (km)	57 000 (~9 R _E)
Inclination (degrees)	85.90
Orbital Period (hours)	~18
Spin axis Orientation	Normal to orbital plane
Spin Frequency (rpm)	10

Table 3.1: Summary of Polar orbital parameters

Three of the twelve scientific instruments on-board the Polar satellite are used to image the aurora in various wavelengths when the satellite is high over the northern polar region. The other nine instruments make measurements in-situ around the entire orbit. They measure the fluxes of charged particles, electrons and protons, as well as heavier ions, from thermal energies into MeV energies. They measure magnetic and electric fields, plus electromagnetic waves. Figure 3.1 also shows the location of many of the instruments on-board the spacecraft. The work presented in this thesis study makes use of several of Polar's instruments that will be described in the following subsections.

The eccentric orbit of the Polar spacecraft, and its extensive instrument payload, allow unique observations of the high-latitude magnetosphere to be made in conjunction with auroral imaging, allowing the in-situ magnetospheric observations to be placed in context relative to auroral activity.

3.2.1. Charge And Mass Magnetospheric Ion Composition Experiment (CAMMICE)

Professor Theodore A. Fritz of Boston University is the Principal Investigator of the CAMMICE investigation. CAMMICE is, as its name suggests, an ion composition instrument. The instrument consists of two sensor systems designed to measure the charge and mass composition within the Earth's magnetosphere over the energy range of ~1 keV/Q to 60 MeV/Q. These two sensor systems are the Heavy Ion Telescope (HIT) and the Magnetospheric Ion Composition Sensor (MICS). This study makes use of only the MICS data, and so details of the HIT will not be presented here. A photograph of MICS on Polar is shown in Figure 3.3, and is essentially the same instrument as the MICS that was used on VIKING and CRRES [Wilken *et al.*, 1992].

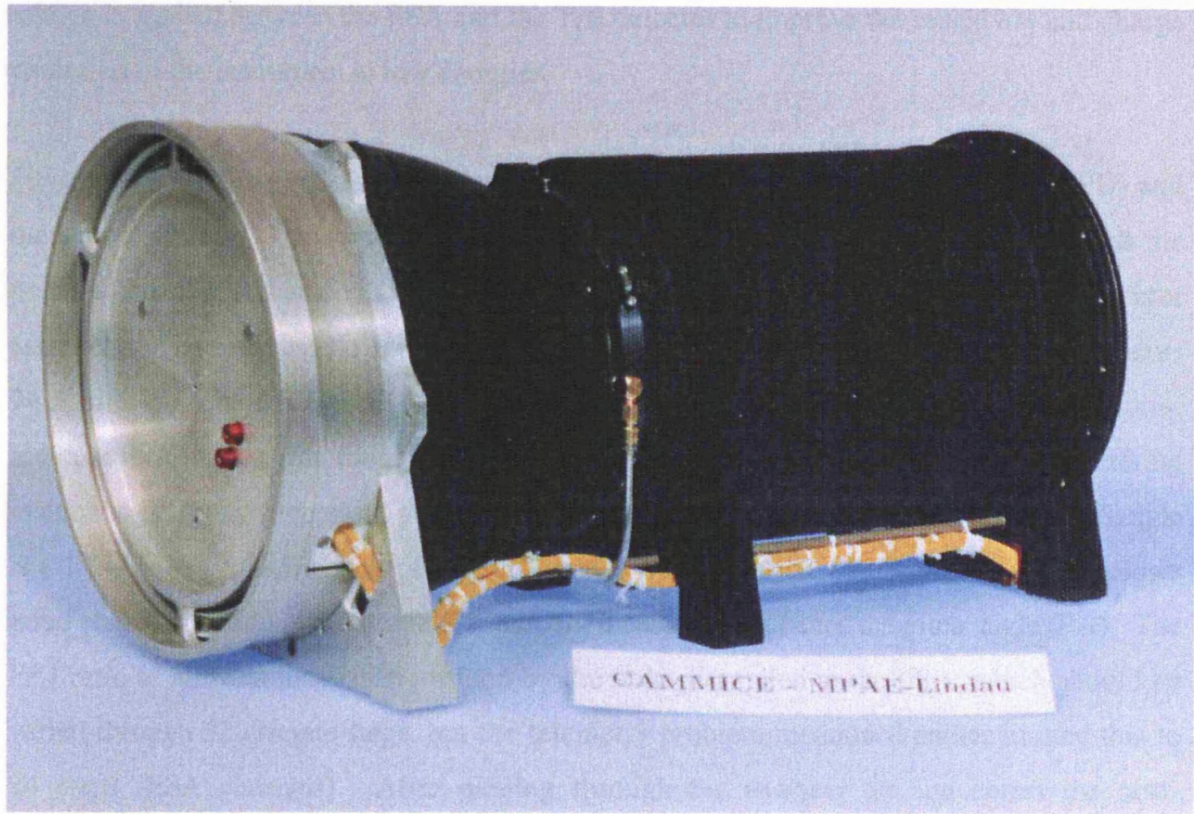


Figure 3.3: Photograph of the MICS detector assembly before launch.

The MICS instrument provides a full characterisation of incident ions by not only measuring dynamic quantities (vector velocity and energy) but also characterises the particle's nature (ionic charge Q and nuclear mass A). The accepted energy range was initially $\sim 1 - 430$ keV/ Q , but due to a telemetry problem, this was reduced to $\sim 1 - 200$ keV/ Q after launch. The detection technique is based on a combined time-of-flight, T , and energy, E , measurement. By adding an electrostatic filter (ESA) that accepts only particles with a defined energy per charge (E/Q) ratio allows the determination of the ionic charge, Q . A post-accelerating voltage is applied between the ESA and the T/E detector to improve the sensitivity and charge resolution of the instrument at low energies.

Physically, MICS comprises of two separate systems, the digital processing unit (DPU) and the sensor system. The sensor system is the 'front end' of the instrument and contains the particle detectors and analogue electronics. Figure 3.4 is a schematic of the analyser/detector assembly. The electrostatic analyser (ESA) has an annular opening aperture of inner radius 74.5 mm and outer radius 77.5 mm. Before entering the gap between deflecting plates, incident ions must pass through a collimating entry element (COLL.) that reduces scattering inside the ESA and suppresses particles with oblique trajectories. The collimation half-angle is 1.1° and the geometric factor of the collimator is $0.07 \text{ cm}^2 \text{ sr}$. This narrow aperture allows good characterisation of the particle's incident direction, and hence the pitch angle (PA). The E/Q ratio of allowed ions is determined by the voltage applied to the ESA, which should be varied through 32 discrete steps, but the telemetry problem mentioned earlier limited this to 24 steps (ESA channels). After passing through the analyser the ion enters the post-acceleration stage that increases its energy for increased sensitivity. The ion now enters the time-of-flight (TOF) unit. The entry element of this unit is a thin carbon foil (FOIL) typically of density $5 \mu\text{g}/\text{cm}^2$. Ions with sufficient energy produce secondary electrons as they pass through the foil. These electrons are accelerated to 1 keV and are collected on a microchannel plate (MCP). The MCP output signal serves as the START signal for the TOF measurement. The ion now must traverse the flight path, S , before delivering its residual energy into the solid state detector (SSD). Once again secondary electrons are produced and transferred to a second MCP that gives the STOP signal for the TOF measurement. Therefore a TOF and an energy have been measured. The electronic signals generated in the sensor system are transferred to the DPU for evaluation and pre-processing, before being sent to the telemetry system.

With a time-of-flight, T , and an energy, E , the ion mass, A , can be determined as

$$A \propto E \cdot T^2$$

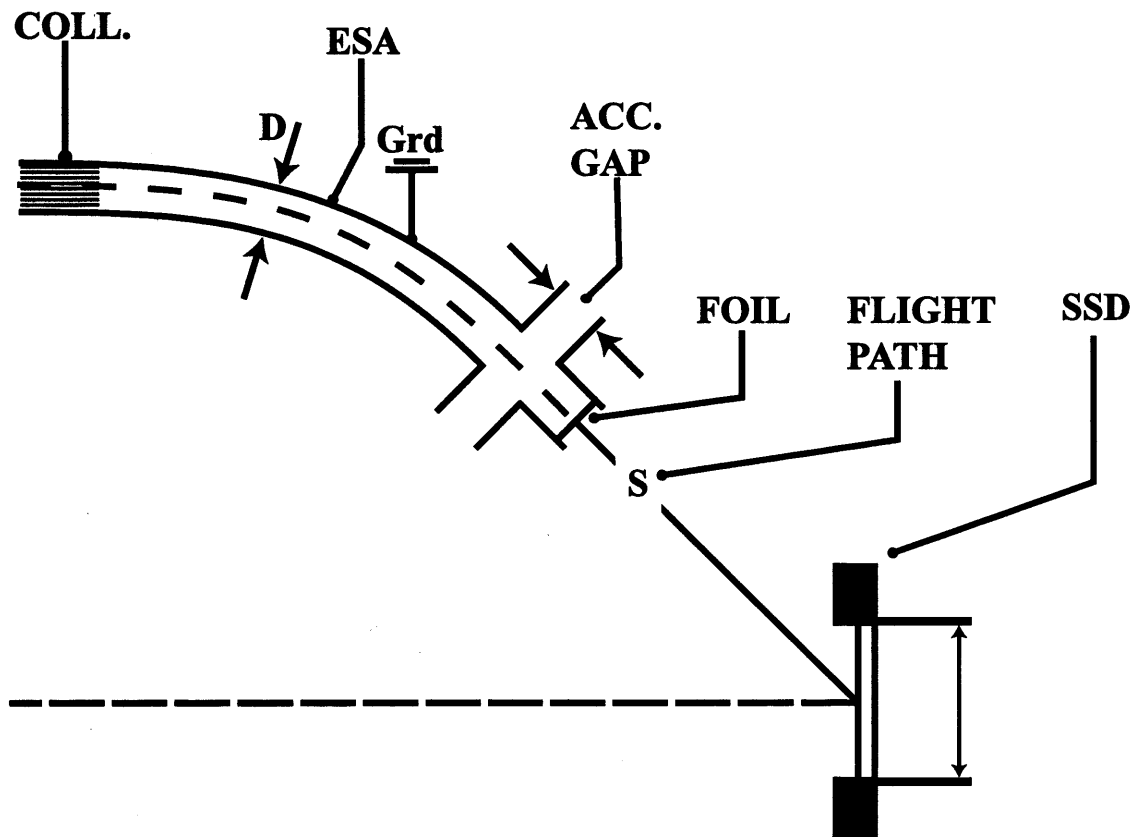


Figure 3.4: Schematic of the MICS analyser/detector assembly [from *Wilken et al.*, 1992].

and as the ESA steps give the E/Q ratio, the ionic charge, Q, can be found. Hence the ion is completely characterised with a mass, A, energy, E, ionic charge, Q, and pitch angle (PA) with a time resolution of 197.5 s and a pitch angle resolution of $\sim 11^\circ$. CAMMICE is the primary instrument of this study and, in conjunction with Hydra and CEPPAD, provides information on the magnetospheric ion population to determine the region the spacecraft is currently passing through. Also, the pitch angle information allows any field-aligned/opposed ion beams to be identified and studied, which is especially important in the plasma sheet boundary layer.

3.2.2. Hot Plasma Analyser (Hydra)

Professor J. D. Scudder is the Principal Investigator of the Hydra instrument. Full details of this instrument can be found in *Scudder et al.* [1995]. Hydra is a hot plasma analyser on-board the Polar spacecraft and consists of a suite of particle analysers that sample the velocity space of electrons and ions up to 35 keV/q in three dimensions, with a routine time resolution of 0.5 s. The Hydra instrument is deployed in five separate packages mounted at various points on Polar as illustrated in Figure 3.5. These are two parallel plate imaging analysers (PPA's), two sets of 127° electrostatic analysers (ESA's) and the data processing unit (DPU). There are two pairs of diagonally opposed electro-optical sensor units. The first is the DuoDeca Electron Ion Spectrometer (DDEIS), which contains 12 narrow (10° FW) fields of views (defined by 127° cylindrical ESA's) to sample electrons and ions (photographed in Figure 3.6). The second pair comprises the PPA's, each with a conical (30° FW) field of view. The energy selection of the PPA is performed by a parallel plate ESA that samples electrons with a much higher angular resolution than those in the DDEIS. The individual ESA's in the DDEIS unit 1 and the centre line of the PPA unit 1 point in the $-Z_{SC}$ direction (labelled 'down' in Figure 3.5), whilst the individual ESA's in the DDEIS unit 2 and the centre line of the PPA unit 2 point in the $+Z_{SC}$ direction (labelled 'up' in Figure 3.5). Deployed in this arrangement the instrument can cover 4π strd at each energy level. As the spacecraft rotates a full survey is acquired in 0.5 s of the three dimensional energy-angle distribution.

The DDEIS is comprised of six pairs of unencumbered anti-collinear fields of view, each of the two boxes of the DDEIS having six ESA's, and so the DDEIS measures electron and ion spectra in broad angular bins at twelve look directions in 1.15 s energy sweeps from 12 eV to 18 keV. Alternate sweeps simultaneously measure all twelve directions for electrons and then ions, yielding a time resolution for either species of 2.3 s. As the spacecraft rotates, complete coverage of all pitch angles is obtained. The PPA measures electrons only and provides fine

HYDRA EXPERIMENT - POLAR SPACECRAFT

Relative angular location of the boxes mounted on the experiment shelves

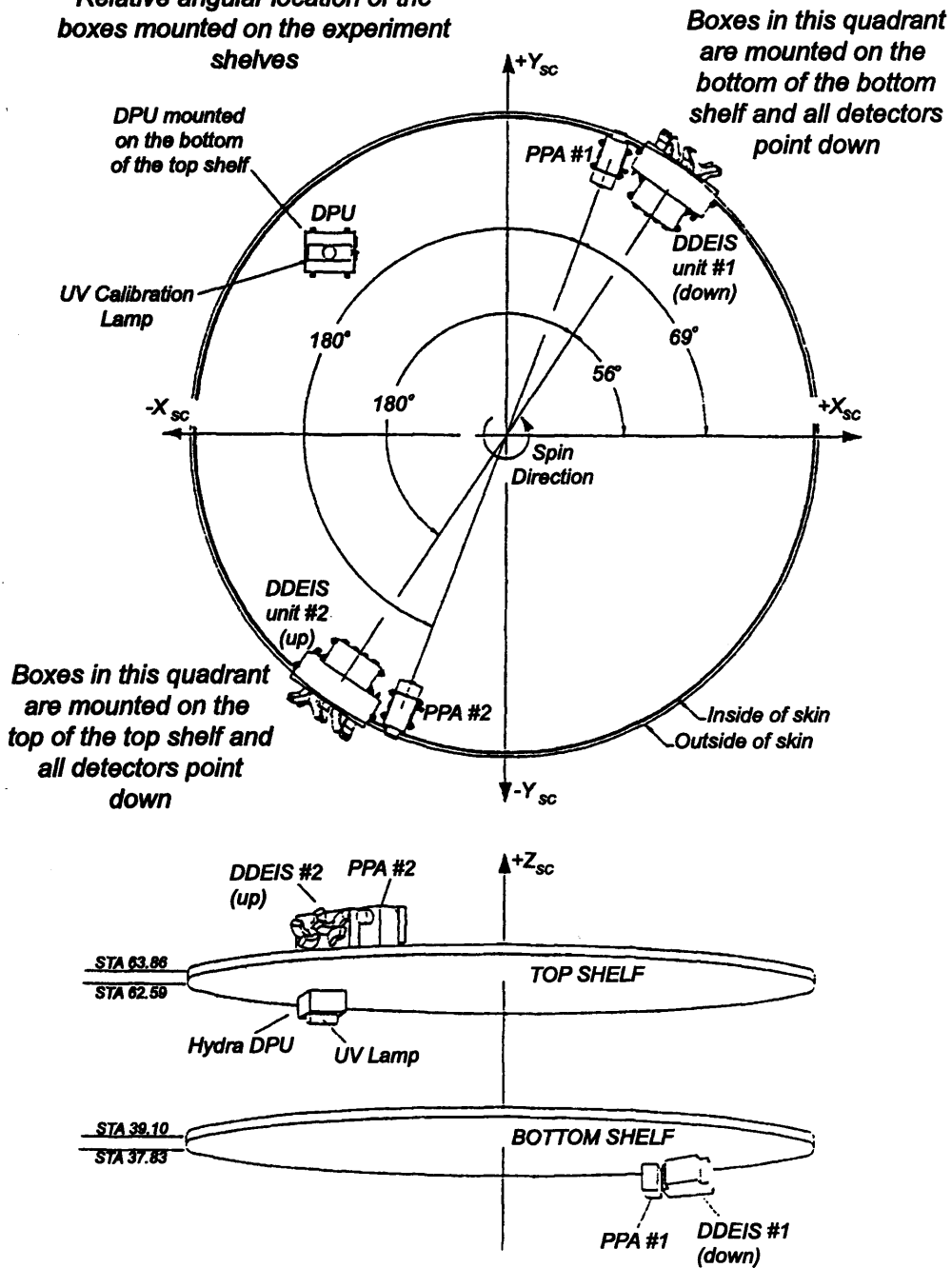


Figure 3.5: Shelf isometric of spacecraft equipment decks locating Hydra boxes [from Scudder et al., 1995].

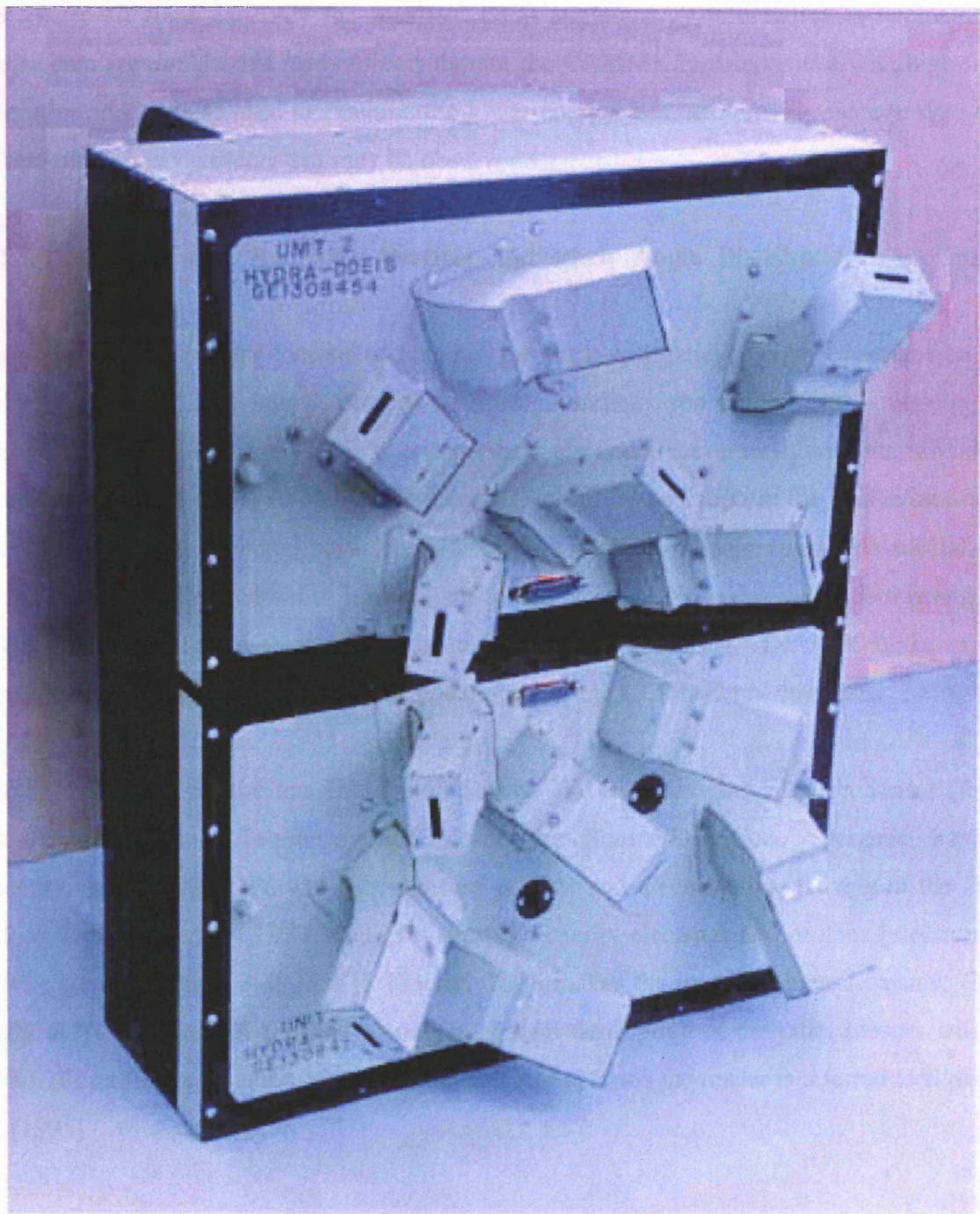


Figure 3.6: Photograph of the two DDEIS detector assemblies before launch.

angular resolution. A half spin is required for complete pitch angle coverage, yielding a time resolution of 25 s for an eight-point energy sweep. PPA pitch angles are sorted 'on-the-fly' as the spacecraft spins and only the resultant pitch angle-energy information is telemetered. Hydra data are used in this study to corroborate the CAMMICE observations with high-time resolution, but are also used to examine the lower-energy data, and provide electron data and information on any currents that may be observed.

3.2.3. Comprehensive Energetic Particle and Pitch Angle Distribution Experiment (CEPPAD)

The CEPPAD experiment consists of four sensors for investigating energetic particles on the Polar spacecraft. These sensors provide 3-D proton and electron angular distributions in the energy range of ~20 keV to ~1 MeV, energetic proton and electron measurements extending to energies greater than ~10 MeV, high angular and time resolution in the source/loss-cone and data on energetic neutral particles. All sensors operate in conjunction with special on-board data processing units that control sensor data acquisition modes while performing in-flight data processing, data compression, and telemetry formatting. Dr. J. B. Blake of the Aerospace Corporation is the Principal Investigator of the CEPPAD investigation.

The four detectors are the Imaging Proton Sensor (IPS), the Imaging Electron Sensor (IES), the High Sensitivity Telescope (HIST) and the Source/Loss-Cone Energetic Particle Spectrometer (SEPS). IPS and IES measure protons and electrons respectively in the 20 – 500 keV energy range. HIST measures the high-energy electrons and protons (electrons \geq 350 keV and protons \geq 3.25 MeV). Finally, SEPS makes the loss cone measurements. This study only makes use of IPS and so only a general description of the other sensors will be given. For a full explanation of each of the detector systems the reader is referred to *Blake et al.* [1995].

IES uses ion-implanted silicon solid state strip detectors to sense energetic electrons. Simultaneous flux measurements as a function of pitch-angle and energy are achieved by the novel geometry of the IES sensor, which has a 180 x 35 ° field of view. The IES is sensitive to energetic electrons ranging from 30 keV to 500 keV. An aluminium mylar foil placed in front of each strip detector eliminates protons of energies below 350 keV as well as a light response. HIST (located under the IES) uses three detector elements to measure electrons from 350 keV to 10 MeV and protons from 2.15 to 80 MeV. Detector A is a 300 mm thick, 300 mm² surface-barrier. Detector B is a 2000 μ m thick, 200 mm² ORTEC surface-barrier. Detector C is a Bicron plastic scintillator with a Hamamatsu R3668 photomultiplier tube. The

HIST attempts to provide a "clean" measurement of very energetic electrons. The SEPS instrument is located on the Polar despun platform along with the auroral imagers, and is independent of the other CEPPAD sensors. SEPS measures both the energetic electron and ion fluxes in the magnetic field-aligned loss and source cone regions with high sensitivity and fine angular and temporal resolution.

Figure 3.7 presents a photograph of the IPS assembly before launch. IPS is similar in form and function to the IES. The IPS uses a monolithic ion-implanted solid-state detector that is discretely segmented into multiple pixels. The detector sits behind a collimation stack at the "focal plane" of a "pin-hole camera", thereby imaging a slice of phase space. Three identical heads, each with three non-overlapping look directions ($20^\circ \times 12^\circ$) provide collectively an instantaneous snapshot of a $180^\circ \times 12^\circ$ wedge of phase space. Figure 3.8 presents a schematic of one of the detector heads and the detector board assembly. The large pixels marked 0, 2 and 4 in Figure 3.8b are sized to yield equal geometric factors for particles incident through the collimator assembly. Pixel 1 monitors penetrating radiation and pixel 3 can be used under conditions of high counting rate. As a consequence of spacecraft rotation, the IPS maps out a full 4π sr image within a single 6 s spin period. Flux measurements are obtained as a function of pitch-angle and energy each 1/32nd of a spin. A low energy threshold of ~ 12 keV is the result of an extremely thin detector "window" and low-noise support electronics, with sixteen energy bins spanning the low energy threshold to a maximum of ~ 1.5 MeV. Energy spectral resolution is programmable where both the low and high thresholds may be selected in-flight and where energy bins may be either linear or semi-logarithmic across that range. In-flight auto-calibration is achieved through an internal pulse generator consisting of both a discrete but calibrated dual-source and a semi-continuous uncalibrated source. CEPPAD IPS data are used in this study as corroborating evidence of the region and features observed by CAMMICE, with an improved temporal resolution for more exact timing.

3.2.4. Magnetic Fields Experiment (MFE)

The Principal Investigator of the Magnetic Field Experiment (MFE) on the Polar spacecraft is Prof. C. T. Russell of UCLA. MFE is designed to measure the vector magnetic field at the spacecraft location in three ranges: plus to minus 700 nT, 5700 nT, and 47000 nT. MFE consists of two triaxial fluxgate magnetometer sensors mounted on a 6 m boom with associated electronics inside the spacecraft. The location of these magnetometers can be seen in Figure 3.1 and a photograph of one of the sensors can be found in Figure 3.9. The use of two separate sensors provides redundancy, and their different locations along the boom, one

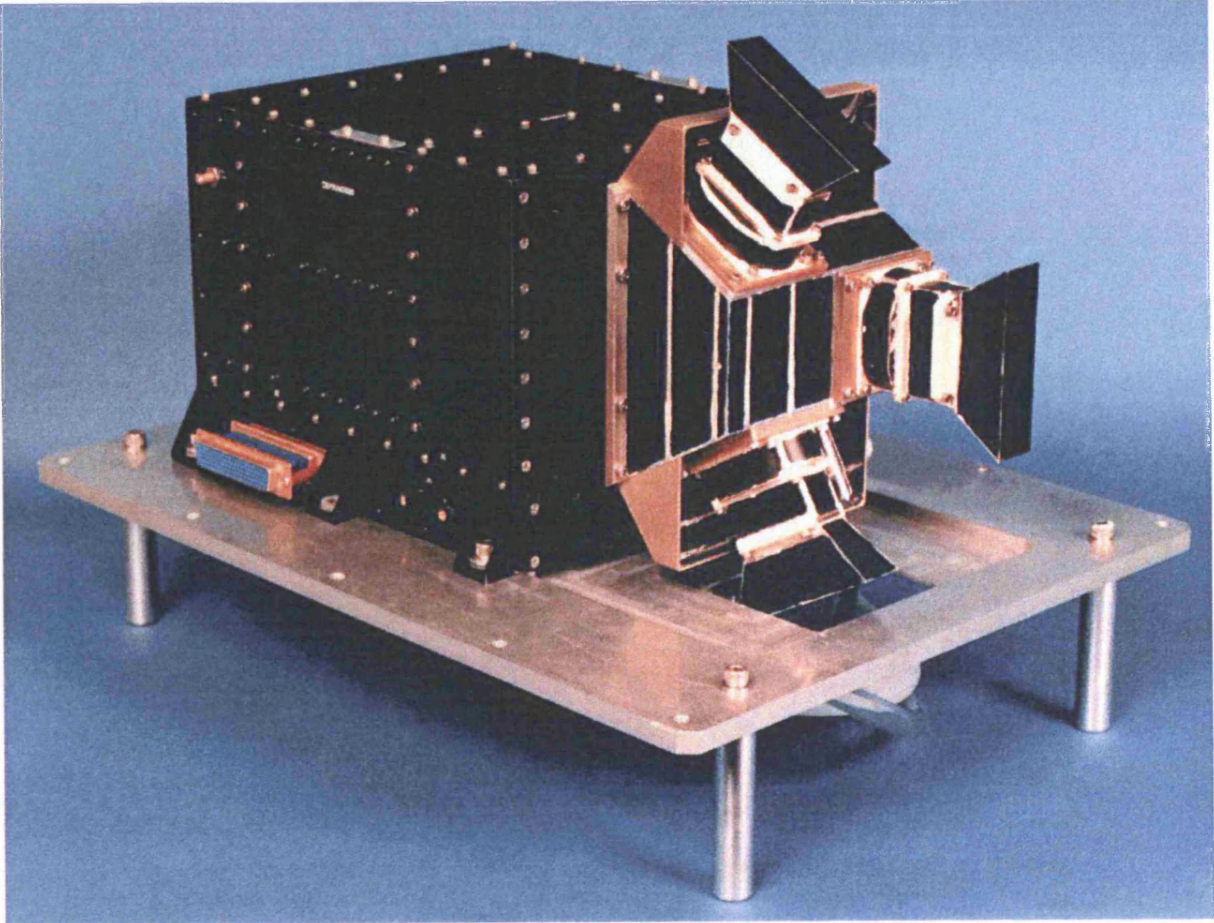
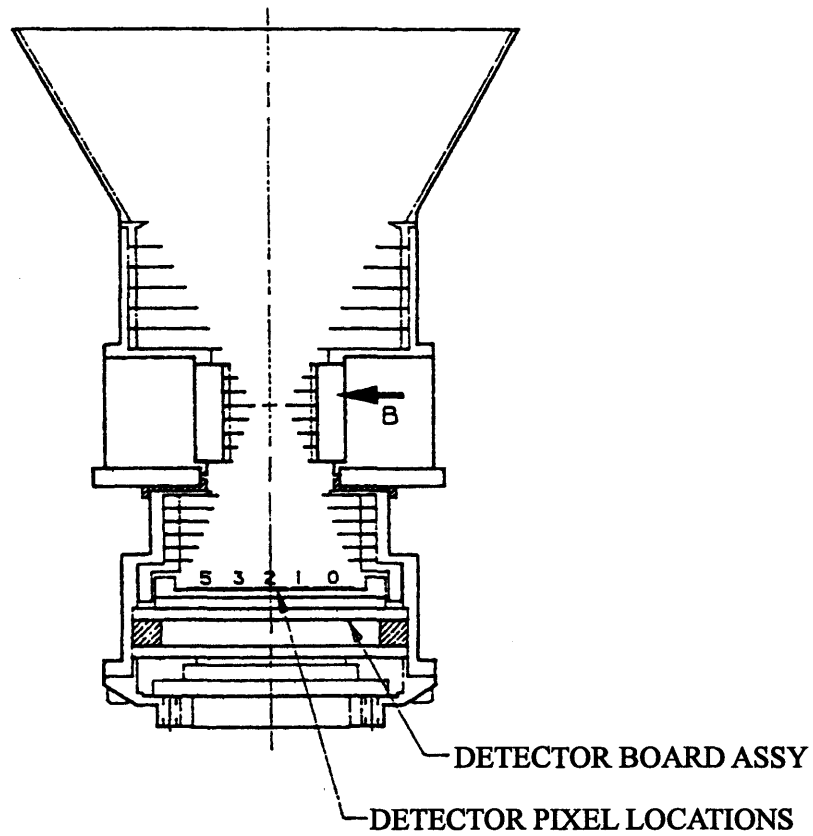


Figure 3.7: Photograph of the IPS detector assembly before launch. Note the three sensor heads.



MICRON DETECTOR SCHEMATIC LAYOUT

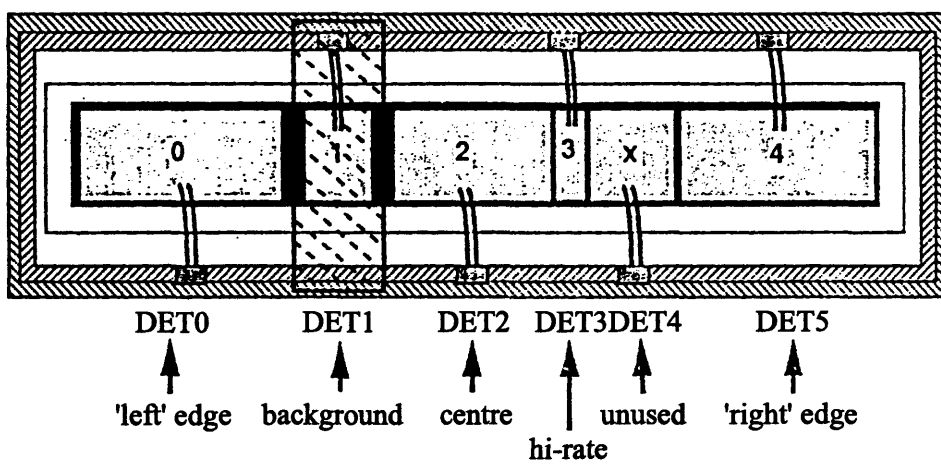


Figure 3.8: The IPS detector. (a) Assembly drawing showing one of the IPS heads. (b) Schematic of a single IPS detector showing the six panels surrounded by the guard ring [from *Blake et al.*, 1995].

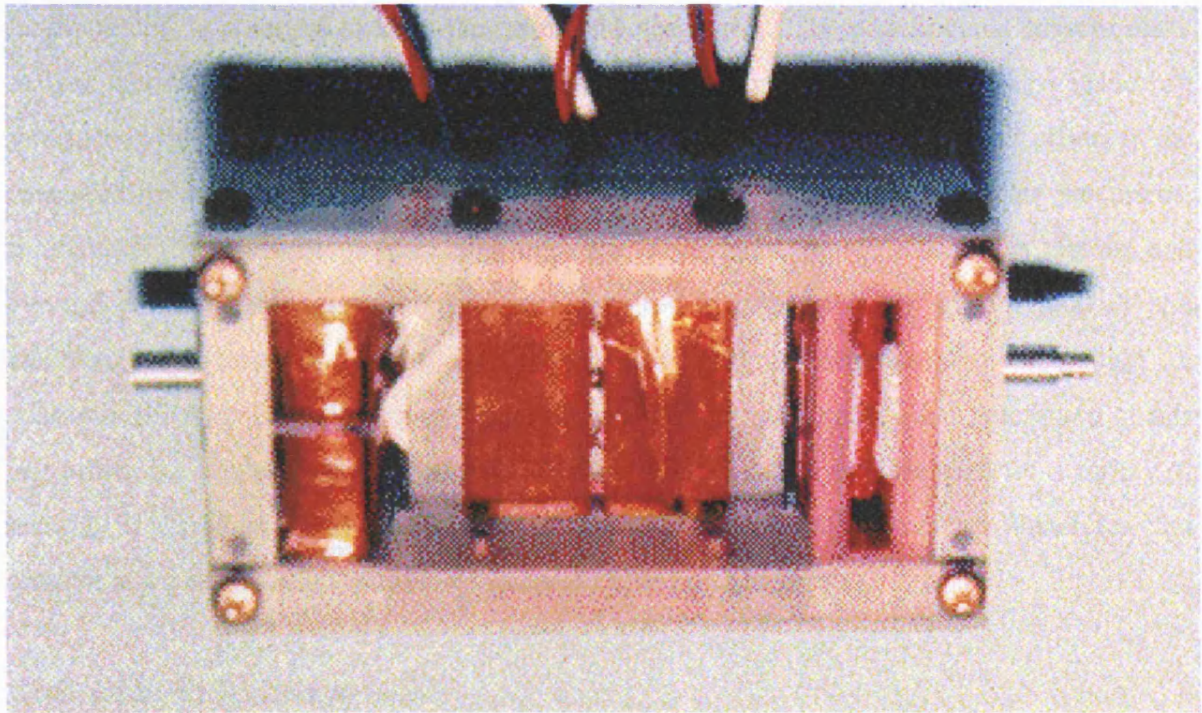


Figure 3.9: Photograph of the MFE detector assembly before launch.

~7.2 m from the spacecraft axis (at the boom end), and the other at ~5.2 m, provides a measure of the spacecraft contribution to the measured fields.

The fluxgate sensors are ring core-types, each containing a 'driver' coil and a 'sense/feedback' coil surrounding a ring-shaped magnetically permeable core. The drive coil is used to force the core into saturation twice during each drive cycle, while the feedback coil zeros out any DC field in the core. When the presence of external DC fields in the core are sensed by the appearance of second harmonics of the drive frequency, the current in the feedback coil is changed to keep the core field near zero. Three orthogonal sensors make each of the two fluxgate units. 'Flippers' can mechanically change a sensor in the spacecraft spin plane with the one along the spin axis in order to determine any zero-level offsets in the measured fields. The magnetometer is a fully redundant system with duplicate processors, analogue-digital converters, spacecraft interface electronics, power conversion circuits and two independent basic magnetometers, one designed to measure fields up to 47,000 nT and one designed to measure fields up to 5500 nT. Each magnetometer has two outputs that are continuously available, a low range and a high range. For a more detailed description of this instrument the reader is directed to *Russell et al.* [1995]. MFE data are used for a variety of reasons in this study, but primarily to examine any field-aligned current signatures and observe any dipolarisation effects at substorm expansion phase onset.

3.2.5. Ultra-Violet Imager (UVI)

The Principal Investigator of the Ultra-Violet Imager (UVI) is Prof. George Parks from the University of Washington. The instrument is located on the despun platform on the Polar spacecraft. A photograph of UVI already covered by its thermal blanket can be found in Figure 3.10. The instrument operates in the far ultraviolet (FUV) and is capable of imaging the auroral oval in sunlight and in darkness. The instrument has an 8° circular field of view and is located on the despun platform, which permits simultaneous imaging of the entire oval at apogee for moderately disturbed times. The three-mirror, unobscured-aperture optical system provides excellent imaging over this full field of view, with an angular resolution of 0.6 milliradians/pixel. There are four FUV filters that have been designed to allow accurate spectral separation of the features of interest. These are given in Table 3.2. For the purpose of this thesis work the Lyman-Birge-Hopfield long band (LBHI) was selected, as this filter shows all UV auroral emission. This filter is chosen to peak at ~ 1700 Å as O₂ absorption is very weak. For a full explanation of the filters and instrument as a whole see *Torr et al.* [1995].

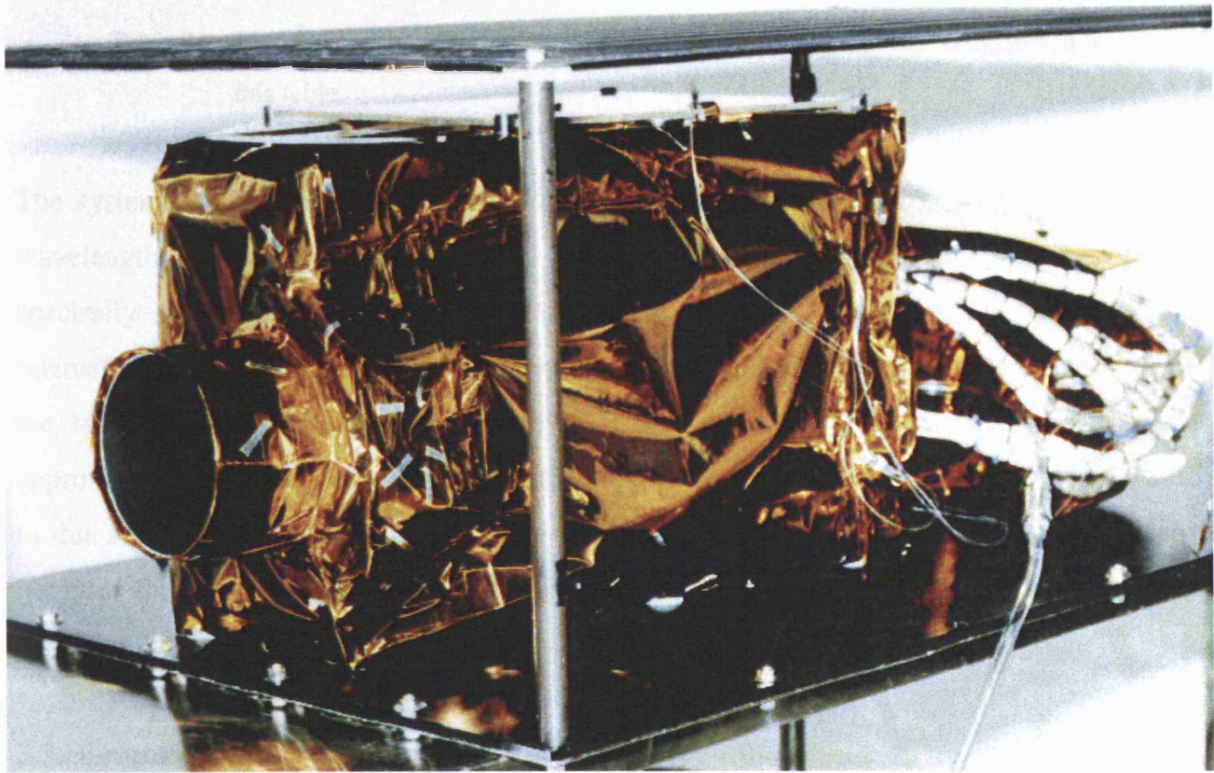


Figure 3.10: Photograph of the UVI camera in its thermal blanket assemblies before launch.

λ (Å)	Feature	Purpose	$\Delta \lambda$ (Å)
1304	O _I	Atomic oxygen	30
1356	O _I	Characteristic energy, O ₂	50
~1500	N ₂ LBH/N _I	Characteristic energy, O ₂	80
~1700	N ₂ LBH/N _I	Total energy	90
~1900	Scattered sunlight	Contaminant	100

Table 3.2: Features are separated by special interference filters that are summarised in this table.

The system has been designed to provide ten orders of magnitude blocking against longer wavelength (primarily visible) scattered sunlight, thus allowing the first imaging of key, spectrally resolved, FUV diagnostic features in the fully sunlit midday aurora. The intensified-CCD detector has a nominal frame rate of one frame every 37 seconds. However, the instrument cycles through the different filters such that a LBHI image is available approximately every six minutes, but occasionally more frequently. The UVI images are used in this study to ascertain the auroral activity relative to the spacecraft footprint, and thereby compare the in-situ magnetospheric observations with those observed in the ionosphere and on the ground.

3.3. Ground Magnetometers

Throughout this study data from many different ground magnetometer stations are used from three magnetometer networks. The networks used are the International Monitor for Auroral Geomagnetic Effects (IMAGE), the UK Sub-Auroral Magnetometer Network (SAMNET) and the Greenland magnetometer network. Each station consists of a magnetometer, the most usual kind being a triaxial fluxgate magnetometer, having replaced analogue magnetometers such as the La Cour. Figure 3.11 is a map showing the location of the three networks and the constituent stations.

The IMAGE magnetometer array has been through a number of guises, including the 'EISCAT Magnetometer Cross' from 1982 – 91 with a sampling interval of 20 s and a resolution of 1 nT. Since 1991 the network has been known as IMAGE [Viljanen *et al.*, 1997]. The IMAGE network spans Scandinavia and the Svalbard archipelago (Figure 3.11 - diamonds), from 60 – 80 °N. The IMAGE array uses the XYZ co-ordinate system (see Appendix 1) with a sampling rate of 10 s and a minimum resolution of 1 nT (0.1 nT at

permanent observatories). In this study IMAGE is mainly used to latitudinally identify the location of the auroral electrojet as described in Chapter 2. The IMAGE magnetometer data are collected as a Finnish - German - Norwegian - Polish - Russian - Swedish project, with the Finnish Meteorological Institute being the PI institute.

SAMNET began taking data on the 1st of October, 1987 at its stations in the UK, the Faroe Islands, Sweden, Norway, Finland, Iceland and Russia (Figure 3.11 – asterix). The SAMNET network records the magnetic field in the HDZ co-ordinate system (see Appendix 1) with a 1 s sampling interval. Data from the IMAGE stations at Nurmijärvi, Kilpisjärvi and Hankasalmi are also incorporated into the SAMNET array. In this study SAMNET data are primarily used to determine the longitudinal location of the substorm current wedge (and associated field-aligned currents) as described in Chapter 2. SAMNET is a PPARC National Facility deployed and operated by the University of York. The reader is directed to *Yeoman et al.* [1990] for more information.

The Greenland magnetometer stations used in this study are all located on both the east and west coasts of Greenland (Figure 3.11 – squares). There is another magnetometer chain on Greenland called MAGIC that is located inland, but is not used here. Data is recorded in the HDZ co-ordinate system as with SAMNET, but with only 20 s (used in this study) or 1 minute sampling intervals. These data are used in this thesis work to examine western features and latitudinally locate any auroral electrojet systems close to Greenland (see Chapter 2). The Danish Meteorological Institute operates the Greenland coastal magnetometer network. The reader is directed to *Friis-Christensen et al.* [1988] for more information.

3.4. The Wind Spacecraft

The Wind spacecraft is Polar's sister spacecraft in the GGS program. Wind was launched on November 1, 1994 and so was the first of the two NASA spacecraft in the Global Geospace Science and, like Polar, has an impressive array of instruments (Figure 3.12). Wind was initially positioned in a sunward, multiple double-lunar swingby orbit with a maximum apogee of $250 R_E$. This was followed by a halo orbit at the Earth-Sun L1 point until November 1998 when Wind began a six-month series of "petal" orbits that take it out of the ecliptic plane, bringing it as close as $10 R_E$ and as far as $80 R_E$ from Earth at an angle of up to 60° from the ecliptic plane. These orbits allow the spacecraft's instrument suite to sample solar wind conditions sunward of the Earth for much of the time. In this study data are used from two of the Wind instruments - the magnetic field investigation and the solar wind experiment.

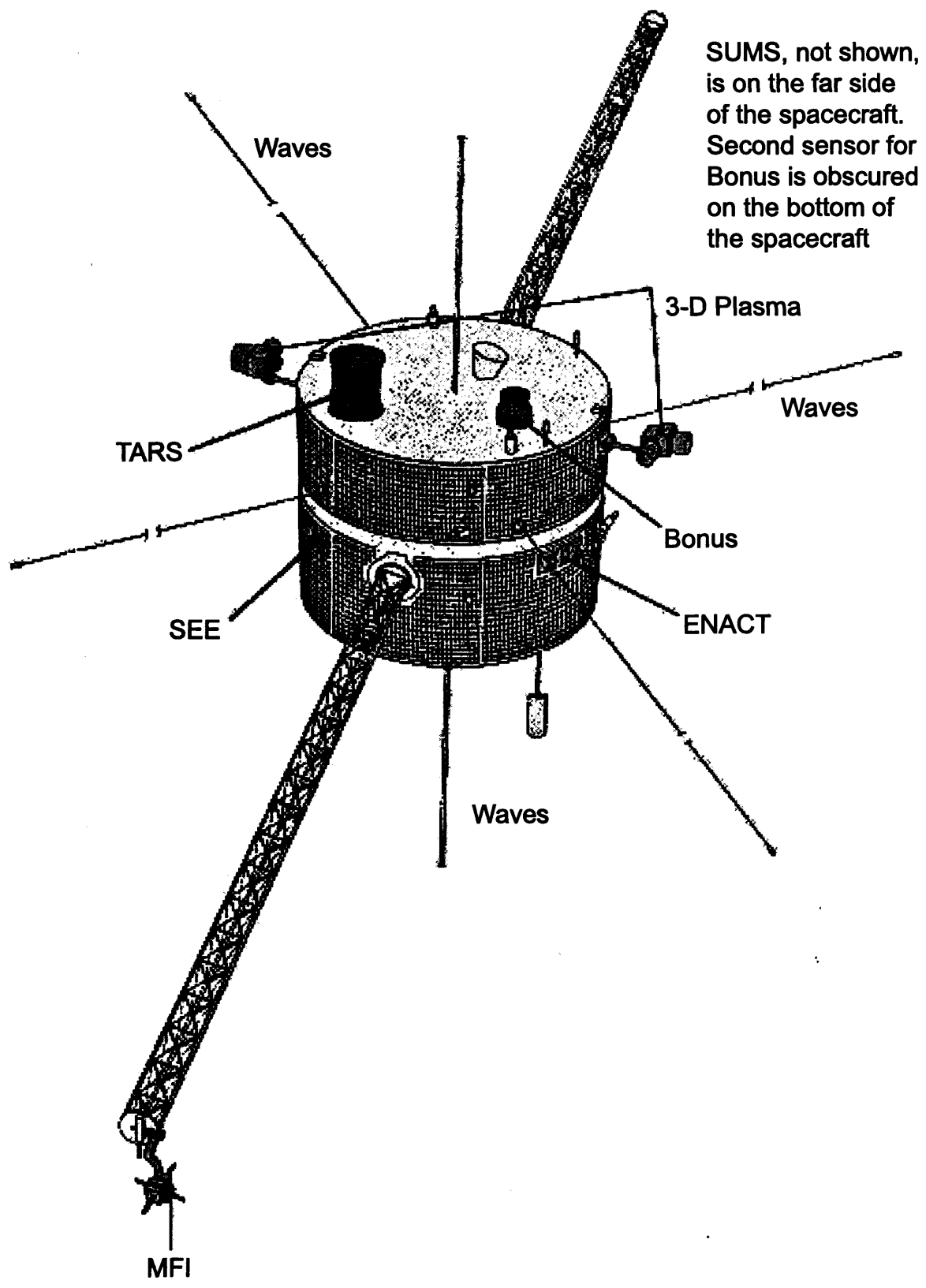


Figure 3.12: Schematic of the Wind spacecraft showing the location of the instruments.

3.4.1. The Magnetic Field Investigation (MFI)

The basic instrumentation selected for the Wind Magnetic Field Investigation (MFI) is based on the magnetometers previously developed for the Voyager, ISPM, GIOTTO, and Mars Observer missions. The basic configuration consists of dual, wide range (± 0.001 to ± 65536 nT) triaxial fluxgate magnetometers mounted remote from the spacecraft body on a deployable boom, a 12-bit resolution A/D converter system and a microprocessor controlled data processing and control unit (DPU). The configuration and operation of MFI is much the same as the Polar MFE instrument and the reader is directed both to section 3.2.4 and to *Lepping et al.* [1995] for more information. MFI is used in this study to determine the orientation of the interplanetary magnetic field.

3.4.2. The Solar Wind Experiment (SWE)

SWE is a comprehensive integrated collection of sensors that allow the instrument to determine several parameters for the solar wind, such as velocity, density and temperature, as well as determining the ion (protons and alphas) and electron distributions. The instrument consists of five sensors mounted in separate boxes, with an instrument layout very similar to that of Hydra on-board Polar (Figure 3.5) but with two Faraday Cups in place of the PPA units and two VEIS units in place of the Hydra DDEIS units. The VEIS is similar in design to the Hydra DDEIS in that it consists of two sets of electrostatic analysers, although only six are used in total compared with twelve in the DDEIS. The data from VEIS is not used in this study and so the reader is directed to *Ogilvie et al.* [1995] for further details of both the VEIS and Faraday Cup subsystems.

The Faraday Cup subsystem is used to determine distribution functions and basic flow parameters of the ion component of the solar wind. Figure 3.13 presents a schematic cross section of a typical Faraday Cup sensor. It contains a series of wire-mesh, planar grids knitted from tungsten wire and two semi-circular collector plates. The velocity distribution function of ions is measured by applying a sequence of voltages to the "modulator" grid. With voltage V applied to the grid, only particles having energy/charge, E/Q , greater than V will be able to pass through the grid and continue on to strike the collector plate where they produce a measurable current. As normally operated, the grid voltage is varied between two voltages V_1 and V_2 at a frequency of a 200 Hz. Thus particles normally incident on the grid and having E/Q between V_1 and V_2 , produce a current on the collector plates that is synchronously detected and integrated on a capacitor for a fixed time interval. The resulting voltage is then converted to a digital signal using an ADC. As the difference between V_1 and V_2 is variable, the E/Q bandwidth is variable, unlike an ESA. The flow direction can be

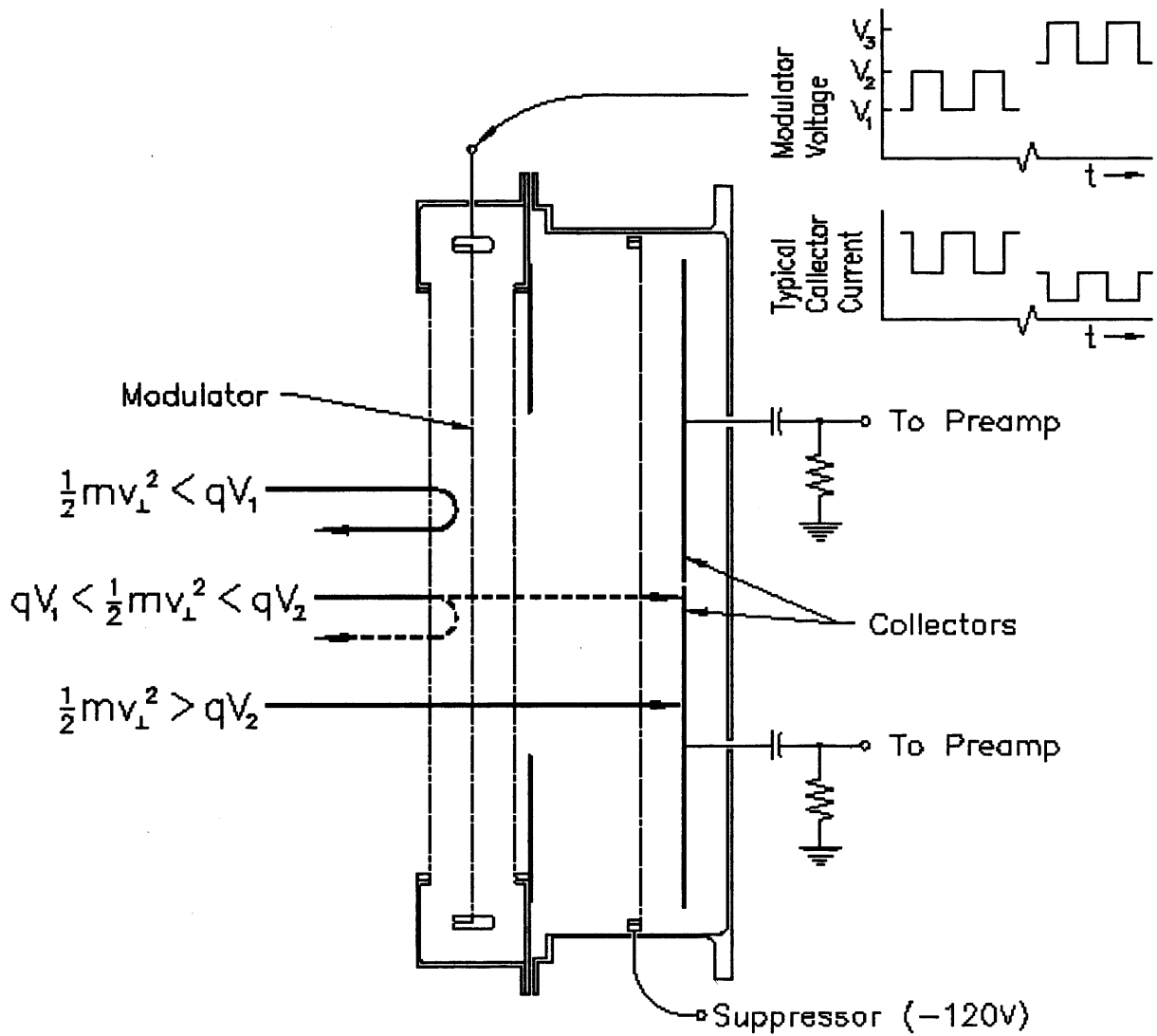


Figure 3.13: The Wind SWE Faraday Cup response to positive ions [from *Ogilvie et al.*, 1995].

determined to better than one degree with this instrument. Finally, this instrument provides measurements of the velocity distribution function and absolute density determinations in the supersonic solar wind as it encompasses the whole distribution and has no energy-dependent efficiency corrections unlike more complicated instruments. The data from SWE are used in Chapter 4 to examine the effects of the solar wind dynamic pressure on the location of the plasma sheet boundary layer.

3.5. The Los Alamos Geostationary Satellite Fleet

The Los Alamos National Laboratory (LANL) is responsible for a fleet of geostationary spacecraft from which energetic particle data has been received for 20 years. Since 1989 these data have been collected by the Synchronous Orbit Plasma Analyser, SOPA, instrument [Belian *et al.*, 1992], which replaced the earlier Charged Particle Analyser (CPA). The SOPA detector measures electrons from 50 keV to approximately 26 MeV, ions from 50 keV up, and heavier ions in various channels with energies in the MeV range. The nominal energy levels for electrons, protons, and heavy ions are the same for all satellites carrying the SOPA detectors. The SOPA instrument is designed to provide high spatial, high-resolution energetic particle measurements at geosynchronous orbit on spinning satellites. As such it monitors electrons, protons, helium, carbon, nitrogen, and oxygen ions individually. The instrument consists of three solid state detector telescopes that accept particles from three different directions relative to the spacecraft spin axis. Each telescope consists of a thin, 4 μm , 10 mm^2 front detector followed by a thick, 3000 μm , 25 mm^2 back detector. A collimator, with 11° (full width) field of view fronts the detector stack. Shielding completely surrounds the active solid state detectors providing protection from side penetrating particles, particularly MeV electrons and protons.

The spacecraft are all in geostationary orbit ($\sim 6.6 R_E$), nominally at 0° latitude and fixed geographic longitudes. The satellites used in this study are 1990-095, 1991-080 and 1994-094. The satellite locations are presented in terms of spacecraft local time (LT), such that 1990-095 LT = UT - 2.5, 1991-080 LT = UT + 4.6 and 1994-084 LT = UT + 6.8. Therefore, at 0 UT the three spacecraft would be located at 21:30, 04:36 and 06:48 MLT respectively (Figure 3.14). The data from these spacecraft are limited to 50 – 315 keV electrons and 50 – 400 keV protons as the higher energy channels suffer from strong electronic noise. Theoretically, data coverage is 24 hours per day, but data gaps exist, mostly due to the switching of ground receivers between satellites. The LANL fleet is ideally positioned to study the effect of magnetic activity on the plasma sheet, primarily the particle dropouts and injections expected during substorms.

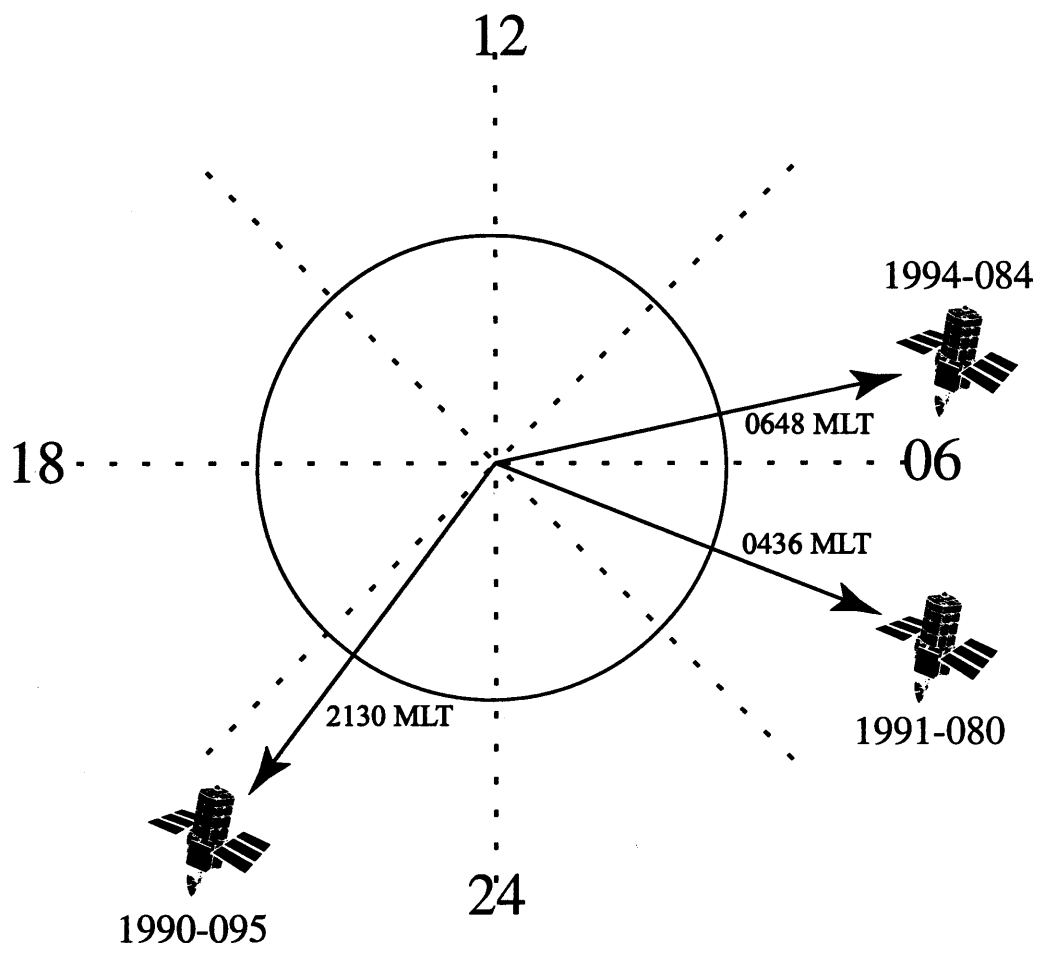


Figure 3.14: The MLT positions of the three LANL spacecraft at 0 UT.

3.6. Concluding Remarks

Information has been given on the various instruments used throughout this thesis. The main instruments are located on the Polar spacecraft, with perhaps the most important being CAMMICE, Hydra and UVI. CAMMICE and Hydra provide in-situ ion and electron data in the high-latitude magnetosphere and UVI allows these data to be placed in context of the auroral activity by mapping the spacecraft footprint into the ionosphere. The other data sets provide further information on such factors as ground magnetic activity and solar wind conditions. It is extremely difficult to perform studies such as those described in Chapters 5 & 6 by only looking at in-situ particle data, and so the background data sets are also used to help resolve any spatial/temporal ambiguities. Even so, there are still problems that cannot be solved with one spacecraft in a fixed orbit and it is not until missions such as Cluster are available that these problems may be resolved.

CHAPTER 4

Statistical study of the plasma sheet

4.1. Introduction

This chapter details a statistical study of the position of the plasma sheet boundary layer (PSBL) and the central plasma sheet (CPS) as measured by the Polar spacecraft at high-latitude in the Northern Hemisphere, including a study of the thickness of the PSBL. When the PSBL and CPS are studied from high latitude there are both advantages and disadvantages. The Polar spacecraft passes through the plasma sheet over a range of L-shells (in this case L between 9 & 6) at an altitude of about 5 – 7 R_E . This region of the plasma sheet maps into the magnetotail and will effectively cover a large portion of the plasma sheet in the tail in a short period of time. The problem lies in the shortness of this time. Unfortunately, as the spacecraft cuts through the PSBL there is a limited amount of data – usually no more than one hour. However, in most cases there is sufficient data to allow a meaningful study.

The study interval was limited to the months of April, May, October and November in 1996, 1997 and 1998, as Polar is within ~1 hour MLT of local midnight on the Earth's nightside in these months. The selection of orbits close to local midnight is based on the need to characterise the PSBL and CPS location for later case studies that concentrate on this local time sector. The two separate intervals are referred to as 'summer' (April and May) and 'winter' (October and November) in this chapter, although they do not coincide exactly with summer and winter solstices. This work is intended to characterise the location of the plasma sheet under certain magnetic and solar wind conditions. A superposed epoch analysis of the PSBL and CPS location as a function of IMF and solar wind pressure is also provided.

4.2. Determination of location of plasma regions

In order to identify the position when Polar entered the PSBL and CPS, a set of conditions were defined, which were based on previous observations. Data from the CAMMICE and Hydra particle instruments on board Polar (see Chapter 3) were compared with these previous observations and the location derived. These instruments produce energy, number density and pitch angle data of the particle population. *Eastman et al.* [1984] defined various regions of the magnetotail in terms of particle properties by examining ISEE 1 and 2 data. As these spacecraft were initially in 29° inclination orbits with apogee at 22.6 R_E they were sampling a much lower-latitude region of the plasma sheet. Later in the mission the orbit was altered

such that higher-latitudes were sampled including the tail lobes. As the earlier work was performed in a different region to that discussed in this chapter, it is possible that there will be differences between the characteristics listed in Table 4.1 and the Polar observations. This early work provides an initial method of identifying the regions, but will not be taken as the absolute values.

	Tail Lobe	PSBL	CPS
Average energy (keV)	0.01 – 0.1	0.5 – 5.0	2.0 – 5.0
Plasma density (cm ⁻³)	0.01 – 0.1	0.1 – 0.3	0.2 – 1.0
Field-aligned Beams	No	Mostly	Occasionally

Table 4.1: Plasma characteristics for some of the nightside plasma regions.

The characteristics presented in Table 4.1 were used with the particle data as a first approximation to determine the time when Polar entered the PSBL and the CPS. The average energy information cannot be determined exactly from the plots used, but the electron number density can. The field-aligned beams can be seen in the CAMMICE pitch angle data as enhancements at 0°, 180 ° and 360 °. Unfortunately these characteristics can be unreliable as, under certain conditions, the number density may not reach 0.1 cm⁻³ in the PSBL and field-aligned ion beams may not be detected. At these times other factors are examined. The tail lobes are a region of low density, low energy particles, whilst the PSBL is a region of higher density, higher energy particles. Therefore, the PSBL can often be identified from the energy-time spectrograms as a sudden increase in count rates and energy. The CPS boundary can be similarly determined as an increase in counts over a much larger range of energies. However, this boundary is not always obvious and so a judgement is made by the author based on all the criteria. Once the entry times were obtained, the GSM latitude and radial distance from the Earth (including the x- and z-components) were then obtained from the ephemeris data. Figure 4.1 presents a schematic to show the parameters in terms of the GSM co-ordinate system that is described in Appendix 1. The difference between the location of the PSBL and CPS gives an upper limit for the thickness of the PSBL.

A typical example from this statistical study is presented in Figure 4.2, with electron density from Hydra in panel 1, Hydra ion and electron spectrograms in panels 2 & 3, with CAMMICE DCR spectrogram and pitch angle data in panels 4 & 5 (see Chapter 5 for full description). The dashed red lines indicate the time of entry into the PSBL and CPS. This example is ideal, as the transition from the tail lobe to the PSBL is very clear. This took the form of an increase in the electron density and ion and electron count rates and energies, as

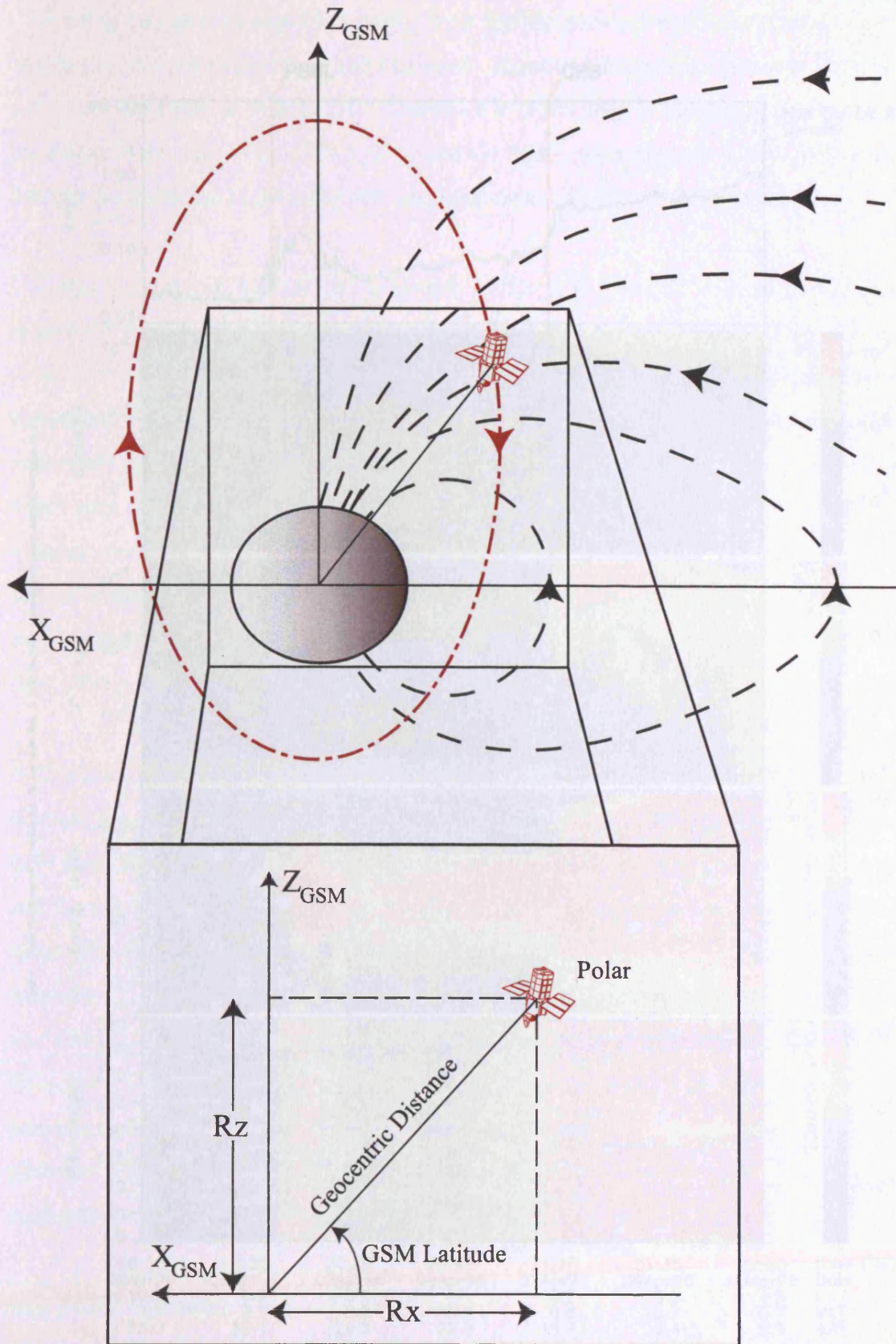


Figure 4.1: Schematic to show the GSM latitude and geocentric distance in a GSM co-ordinate system.

well as the observation of earthward and tailward ion beams in the DCR pitch angle data. The CPS entry can also be identified easily by a further increase in electron density and larger numbers of most energetic and electrons. However, there was a decrease after the initial entry into the PSBL.

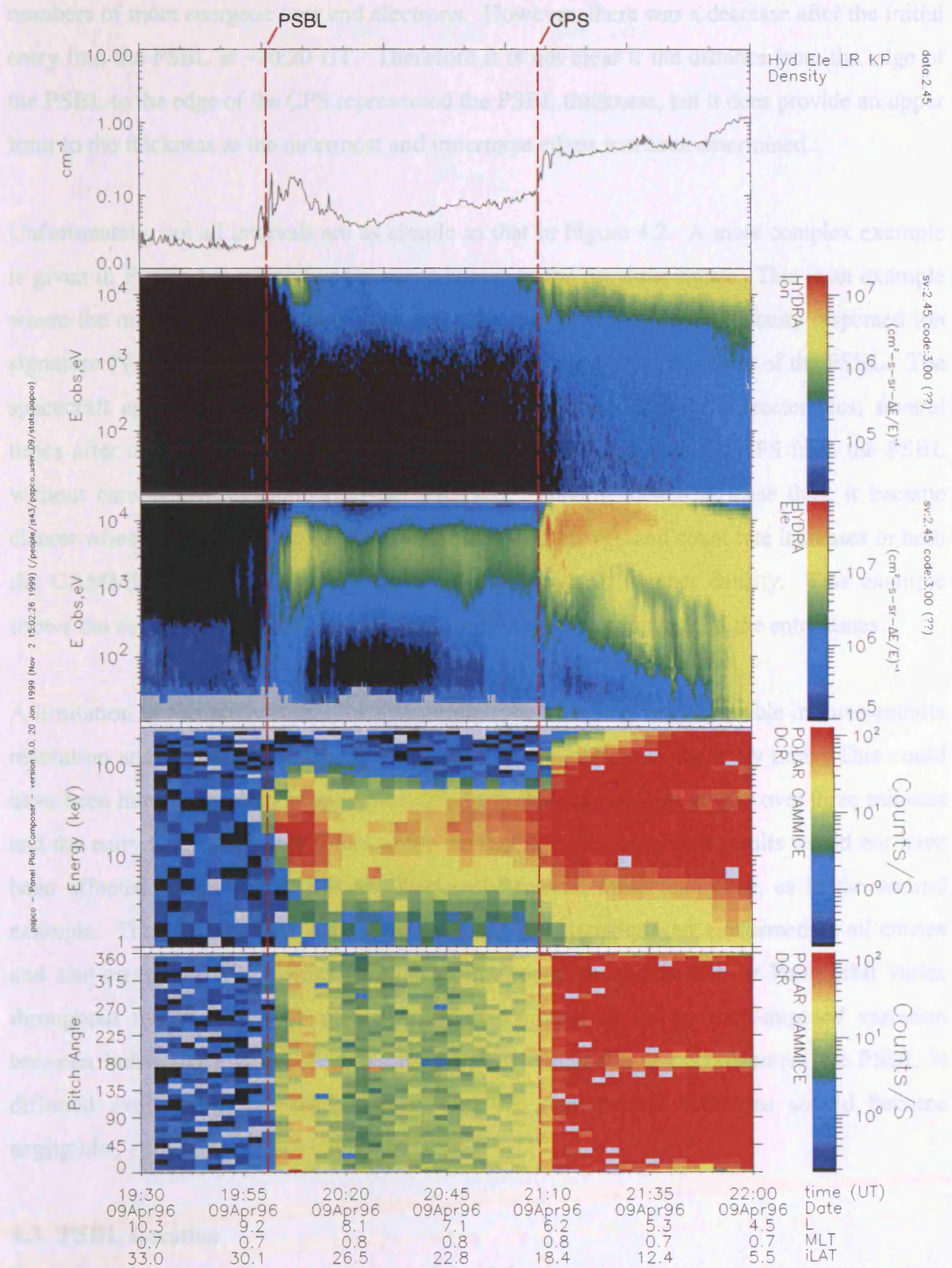


Figure 4.2: An example of a plot used to identify the PSBL and CPS entries.

entries as a function of latitude in the top panel and as a function of geographic distance in the bottom panel. The "summer" and "winter" values are separated into two G forest distributions represented by the light and dark shading. The mean of the whole sample and the means for

well as the observation of earthward and tailward ion beams in the DCR pitch angle data. The CPS entry can also be identified easily by a further increase in electron density and larger numbers of more energetic ions and electrons. However, there was a decrease after the initial entry into the PSBL at ~20:20 UT. Therefore it is not clear if the distance from the edge of the PSBL to the edge of the CPS represented the PSBL thickness, but it does provide an upper limit to the thickness as the outermost and innermost edges had been determined..

Unfortunately, not all intervals are as simple as that in Figure 4.2. A more complex example is given in Figure 4.3, which has the same layout as the previous figure. This is an example where the number density does not reach the 0.1 cm^{-3} threshold but a velocity dispersed ion signature (VDIS) was observed at ~09:20 UT, which is a typical signature of the PSBL. The spacecraft appeared to enter the PSBL, or plasma that had similar characteristics, several times after this initial entry and it was very difficult to distinguish the CPS from the PSBL without careful investigation of all the data sets. Having looked at these data, it became clearer when the CPS was actually entered identifying energy and count rate increases in both the CAMMICE and Hydra data, with a small increase in number density. This example shows the need for using more than one data set for the determination of the entry times.

A limitation of this study is that the spacecraft ephemeris was only available in three-minute resolution and so the ephemeris used was that immediately after the entry time. This could have been interpolated but, as the spacecraft position does not vary greatly over three minutes and the entry times were only found to the nearest minute, the overall results would not have been affected. Also, the PSBL was frequently entered more than once, as in the second example. Therefore the data were separated such that statistics were performed on all entries and also on initial PSBL entries only. The final point to note is that the Polar orbit varies throughout the year (see Chapter 3) such that there may be an orbit-imposed variation between individual events. That is, the point at which the spacecraft enters the PSBL is different every orbit, but with a large data set such orbital variations should become negligible.

4.3. PSBL Location

Having analysed the data as described above, the location statistics for the plasma sheet boundary layer are discussed in this section. Figure 4.4 presents the location of all PSBL entries as a function of latitude in the top panel and as a function of geocentric distance in the bottom panel. The 'summer' and 'winter' values are separated into two different distributions represented by the light and dark shading. The mean of the whole sample and the means for

popco - Panel Plot Composer - version 9.0, 20 Jan 1999 (Jan 25 12:49:14, 2000) (more)

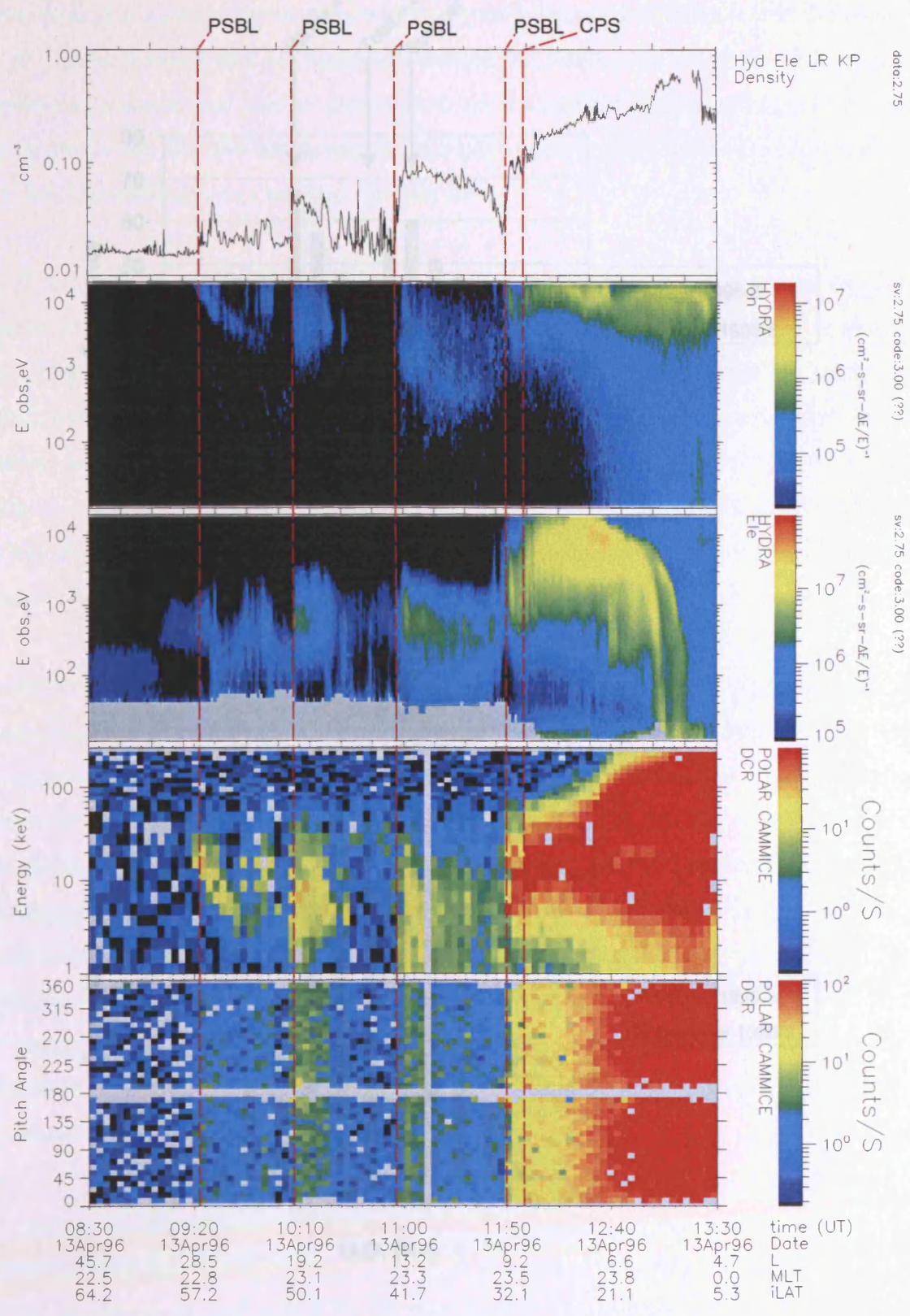


Figure 4.3: Another example of a plot used to identify the PSBL and CPS entries.

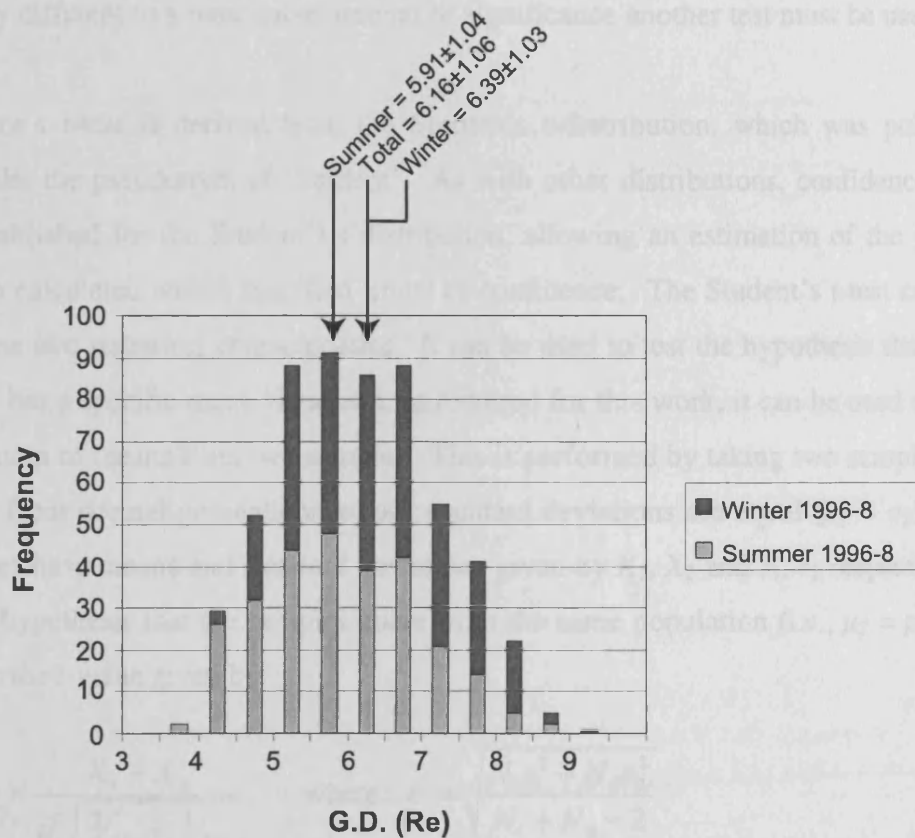
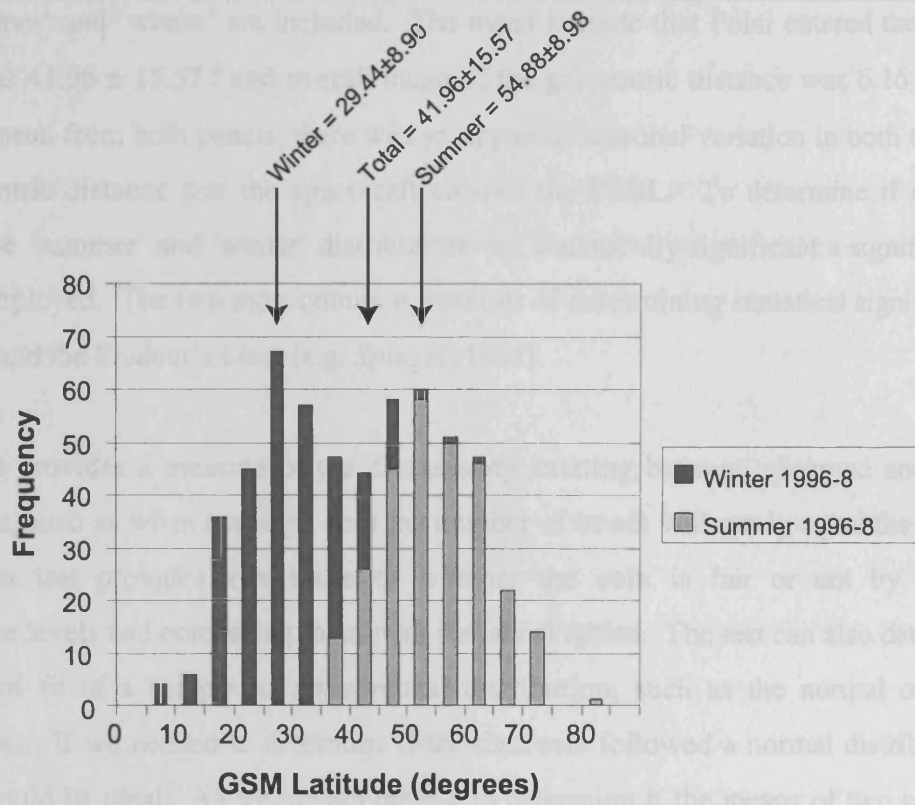


Figure 4.4: PSBL entry location in both latitude and geocentric distance (G.D.), with seasons also separated.

both 'summer' and 'winter' are included. The mean latitude that Polar entered the PSBL for all data was $41.96 \pm 15.57^\circ$ and overall mean of the geocentric distance was $6.16 \pm 1.06 R_E$. As can be seen from both panels, there was an apparent seasonal variation in both the latitude and geocentric distance that the spacecraft entered the PSBL. To determine if differences between the 'summer' and 'winter' distributions are statistically significant a significance test must be employed. The two most common methods of determining statistical significance are the χ^2 test and the Student's t-test [e.g. *Spiegel*, 1961].

The χ^2 test provides a measure of the discrepancy existing between observed and expected frequencies, such as when tossing a coin the number of heads will rarely equal the number of tails. This test provides a measure of whether the coin is fair or not by computing significance levels and comparing them with statistical tables. The test can also determine the goodness of fit of a sample to a theoretical distribution, such as the normal or binomial distributions. If we needed to determine if the data sets followed a normal distribution then this test would be ideal. As we are attempting to determine if the means of two samples are statistically different to a reasonable amount of significance another test must be used.

The Student's t-test is derived from the Student's t-distribution, which was published by Gosset under the pseudonym of 'Student'. As with other distributions, confidence intervals can be established for the Student's t-distribution, allowing an estimation of the population mean to be calculated within specified limits of confidence. The Student's t-test can be used to determine two statistical characteristics. It can be used to test the hypothesis that a normal population has a specific mean value and, as required for this work, it can be used to measure the differences of means from two samples. This is performed by taking two samples of sizes N_1 and N_2 from normal populations whose standard deviations are equal ($\sigma_1 = \sigma_2$). If these two samples have means and standard deviations given by X_1, X_2 and s_1, s_2 respectively, then to test the hypothesis that the samples come from the same population (i.e., $\mu_1 = \mu_2$ and $\sigma_1 = \sigma_2$), we use the t -value given by:

$$t = \frac{X_1 - X_2}{\sigma \sqrt{\frac{1}{N_1} + \frac{1}{N_2}}} \quad \text{where} \quad \sigma = \sqrt{\frac{N_1 s_1^2 + N_2 s_2^2}{N_1 + N_2 - 2}}$$

This value is then compared with the Student's t table for sample size and significance limits. Both 0.01 and 0.05 levels of significance are used as these provide a method of 'grading' the level of significance, with 0.01 indicating a 1 % chance of the t-value being outside the 'means are equal' distribution and 0.05 representing a 5% chance. If the means being equal is

found to be significant at the 0.01 level then the means are equal to a high degree of significance. If they are significant at the 0.05 level, but not the 0.01 level then the result is possibly significant and the means may be equal. If they are not significant at either level then the means are not equal. Next it must be decided if a one-tailed or two-tailed test is relevant. A one-tailed test is used to determine if the hypothesis that the means are equal is correct, or if one of the means is always larger/smaller. A two-tailed test is used to determine if the means are equal or not, and so a two-tailed test is relevant here. For a two-tailed test the 1 % chance can occur either side of the distribution (i.e., 0.5 % either side) and so the $t_{.995}$ score is used. Similarly for the 5 % chance (2.5 % either side), where the $t_{.975}$ score is used. For a sample size greater than 120, as in this study, the 0.01 level of significance for a two-tailed test gives $t_{.995} = 2.58$ and a 0.05 level of significance gives $t_{.975} = 1.96$. To determine if there is a statistically significant difference between the mean location for the 'summer' and 'winter' distributions, the hypothesis that the mean value during 'summer' and the mean value during 'winter' are equal is tested. If the t-value is larger than those quoted there is statistically significant difference. Table 4.2 presents the mean values and their calculated t-values.

Parameter	'Summer' Mean (\pm S.D.)	'Winter' Mean (\pm S.D.)	t-value
Latitude ($^{\circ}$)	54.88 \pm 8.98	29.44 \pm 8.90	33.669
Geocentric distance (R_E)	5.91 \pm 1.04	6.39 \pm 1.03	5.449

Table 4.2: The 'summer' and 'winter' means and t-values for all PSBL entries.

Such high t-values indicates that the above hypothesis can be rejected at both the 0.01 and 0.05 levels of significance. Therefore both the latitude and geocentric distance locations are statistically different between 'summer' and 'winter'.

As mentioned earlier, there were many orbits in which the spacecraft apparently encounters the PSBL more than once before entering the CPS. Therefore the location statistics were refined by using only the initial PSBL entry and the results are presented in Figure 4.5 in a format identical to that presented in the previous figure. This indicates that by only taking the initial encounter the total mean latitude was increased to $42.82 \pm 15.62^{\circ}$ and the total mean geocentric distance had only slightly decreased to $6.14 \pm 1.09 R_E$. The Student's t-test was once again employed to test the level of significance between the 'summer' and 'winter' means. This was performed in a manner identical to that described above. Table 4.3 presents

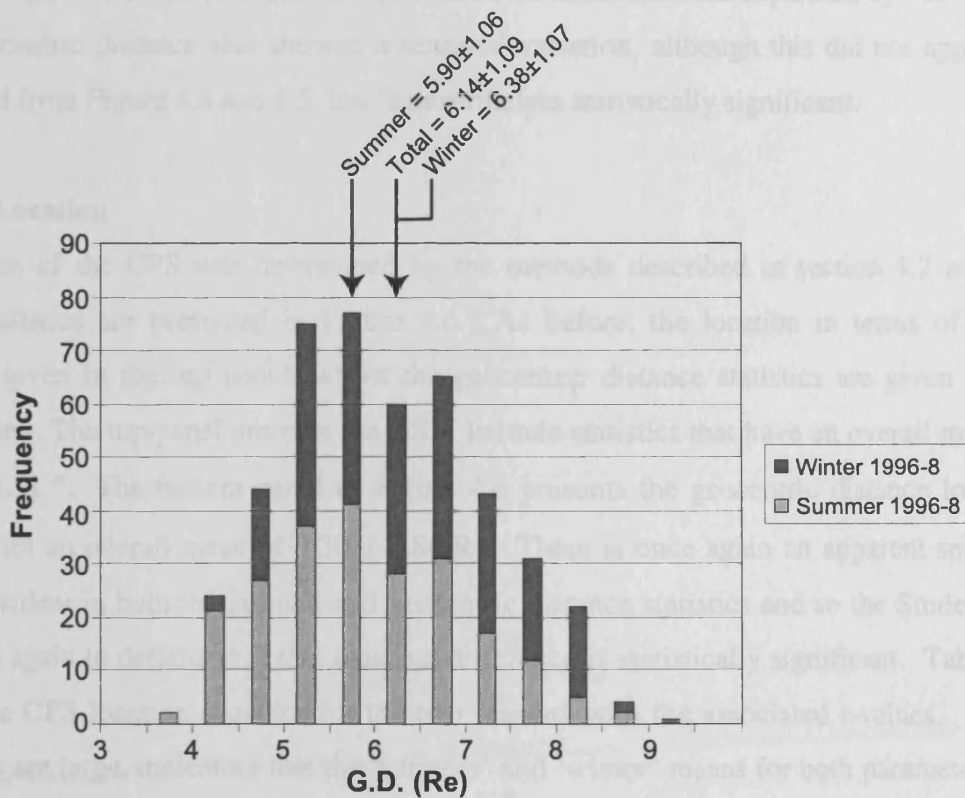
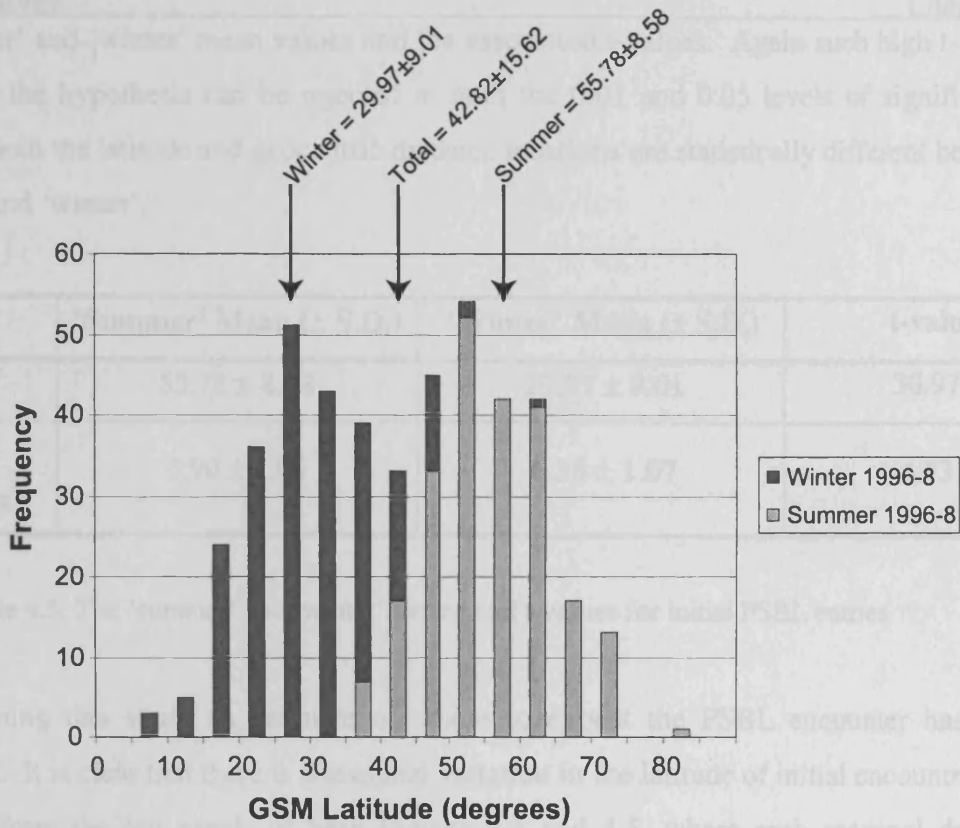


Figure 4.5: PSBL entry location for initial encounters in both latitude and geocentric distance (G.D.), with seasons also separated.

the 'summer' and 'winter' mean values and the associated t-values. Again such high t-values means that the hypothesis can be rejected at both the 0.01 and 0.05 levels of significance. Therefore both the latitude and geocentric distance locations are statistically different between 'summer' and 'winter'.

Parameter	'Summer' Mean (\pm S.D.)	'Winter' Mean (\pm S.D.)	t-value
Latitude ($^{\circ}$)	55.78 \pm 8.58	29.97 \pm 9.01	30.973
Geocentric distance (R_E)	5.90 \pm 1.06	6.38 \pm 1.07	4.731

Table 4.3: The 'summer' and 'winter' means and t-values for initial PSBL entries.

By performing this study an estimate of where to expect the PSBL encounter has been determined. It is clear that there is a seasonal variation in the latitude of initial encounter with the PSBL from the top panels of both Figures 4.4 and 4.5, where each seasonal data set appeared to have a normal distribution, but centred on mean latitudes separated by $\sim 25^{\circ}$. The orbital geocentric distance also showed a seasonal variation, although this did not appear as pronounced from Figure 4.4 and 4.5, but is nevertheless statistically significant.

4.4. CPS Location

The location of the CPS was determined by the methods described in section 4.2 and the location statistics are presented in Figure 4.6. As before, the location in terms of GSM latitude is given in the top panel, whilst the geocentric distance statistics are given in the bottom panel. The top panel presents the GSM latitude statistics that have an overall mean of $33.55 \pm 15.51^{\circ}$. The bottom panel of Figure 4.6 presents the geocentric distance location statistics with an overall mean of $5.30 \pm 0.86 R_E$. There is once again an apparent seasonal variation evident in both the latitude and geocentric distance statistics and so the Student's t-test is used again to determine if this seasonal difference is statistically significant. Table 4.4 presents the CPS location statistics for the two seasons with the associated t-values. Again the t-values are large, indicating that the 'summer' and 'winter' means for both parameters are significantly different at both the 0.01 and 0.05 levels. Another point to note is that there is a $\sim 25^{\circ}$ difference between summer and winter mean latitudes, which is the same difference as that observed in the PSBL location statistics.

Parameter	'Summer' Mean	'Winter' Mean (\pm S.D.)	F-value
Latitude (°)	46.73	20.48 \pm 8.51	33.679
Geocentric distance (Re)	5.30	5.07 \pm 0.86	5.976

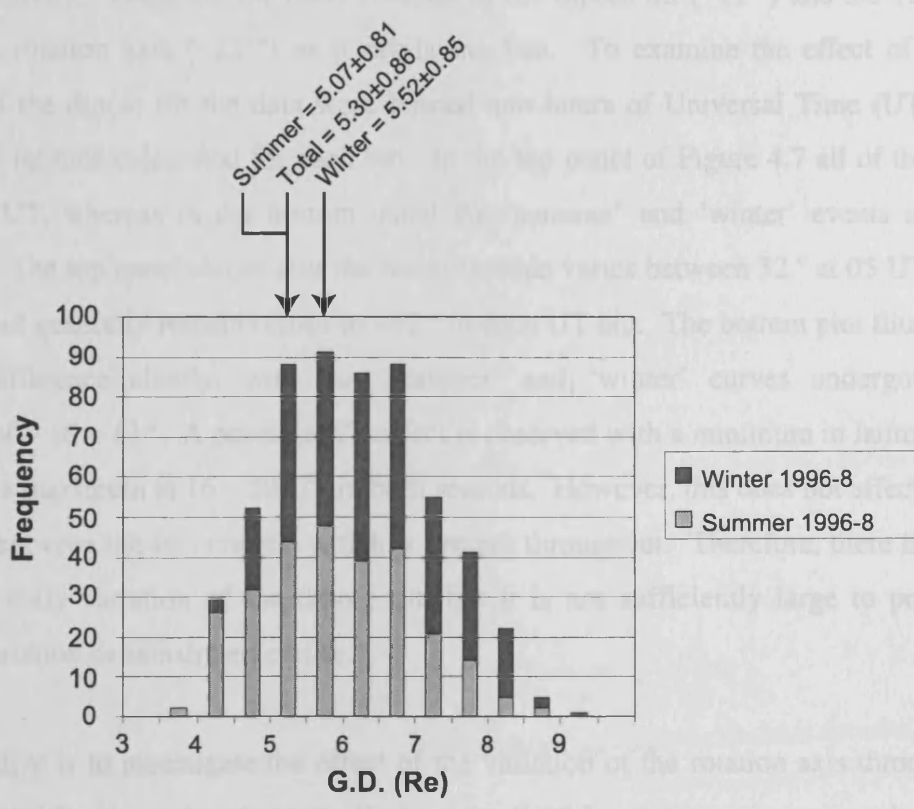
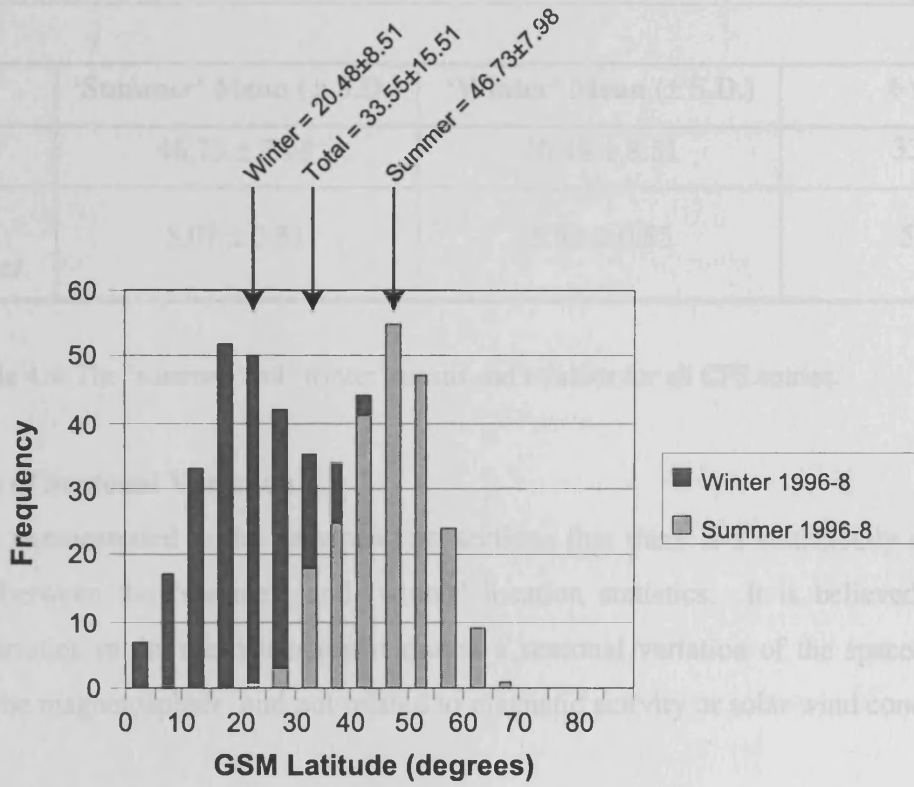


Figure 4.6: CPS entry location in both latitude and geocentric distance (G.D.), with seasons also separated.

Parameter	'Summer' Mean (\pm S.D.)	'Winter' Mean (\pm S.D.)	t-value
Latitude ($^{\circ}$)	46.73 \pm 7.98	20.48 \pm 8.51	33.679
Geocentric distance (R_E)	5.07 \pm 0.81	5.52 \pm 0.85	5.976

Table 4.4: The 'summer' and 'winter' means and t-values for all CPS entries.

4.5. Cause of Seasonal Variation

It has been demonstrated in the previous two sections that there is a statistically significant difference between the 'summer' and 'winter' location statistics. It is believed that this seasonal variation in the mean location is due to a seasonal variation of the spacecraft orbit relative to the magnetosphere, and not related to magnetic activity or solar wind conditions.

There are two factors that alter the magnetosphere tilt regardless of solar wind conditions or magnetic activity. These are the daily rotation of the dipole tilt ($\sim 11^{\circ}$) and the variation of the Earth's rotation axis ($\sim 25^{\circ}$) as it orbits the Sun. To examine the effect of the daily variation of the dipole tilt the data were binned into hours of Universal Time (UT) and the mean GSM latitude calculated for each bin. In the top panel of Figure 4.7 all of the data are binned by UT, whereas in the bottom panel the 'summer' and 'winter' events are binned separately. The top panel shows that the mean latitude varies between 32° at 05 UT and 49° at 19 UT, but generally remains close to $\sim 42^{\circ}$ in each UT bin. The bottom plot illustrates the seasonal difference clearly, with the 'summer' and 'winter' curves undergoing small variations of $\sim 10 - 12^{\circ}$. A possible UT effect is observed with a minimum in latitude at 04 - 08 UT and a maximum at 16 - 20 UT in both seasons. However, this does not affect the $\sim 25^{\circ}$ difference between the two curves, which is present throughout. Therefore, there is an effect due to the daily variation of the dipole tilt, but it is not sufficiently large to produce the seasonal variation demonstrated earlier.

The alternative is to investigate the effect of the variation of the rotation axis throughout the year. Figure 4.8 represents schematically how the Earth's rotation axis varies relative to the Sun over the Earth's orbit. As this statistical study is concerned with the Northern Hemisphere only, references to seasons will reflect that. Therefore, at summer solstice (22/6) the Earth's rotation axis is tilted Sunward, whilst at winter solstice it is tilted anti-Sunward. The study intervals are also marked on this diagram such that it is clear that during the 'summer' intervals the Earth's rotation axis will be initially tilted in the X-Z GSM plane

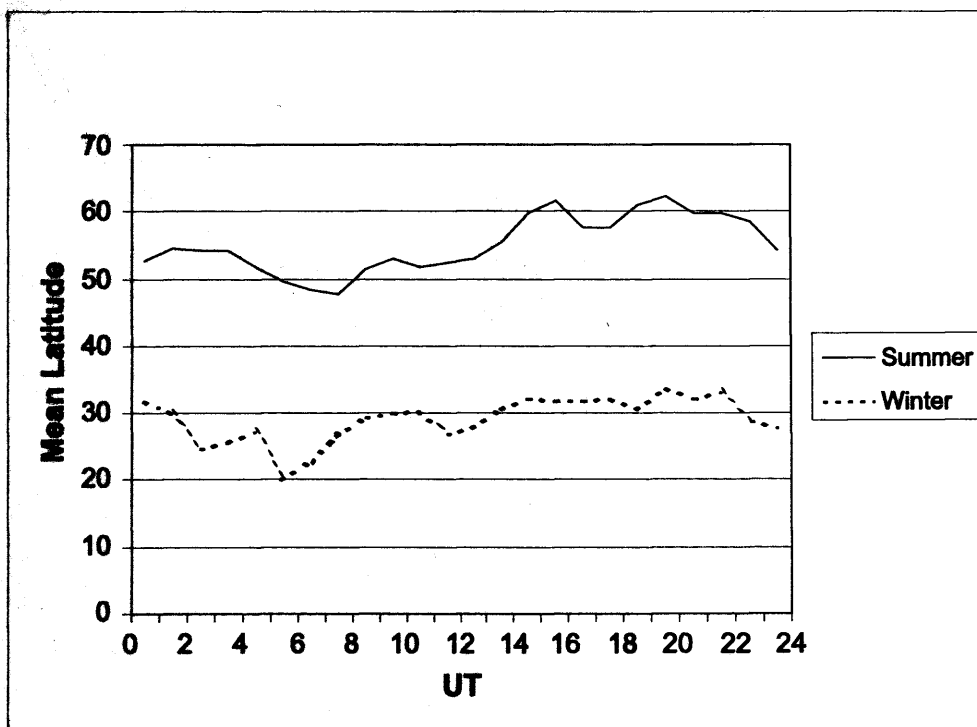
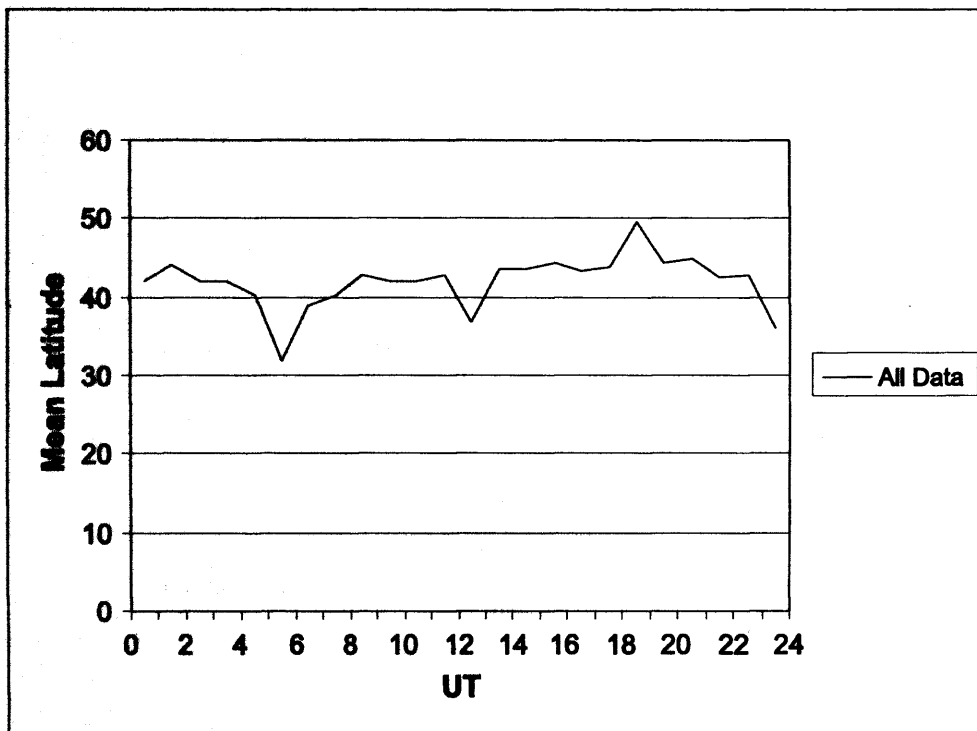
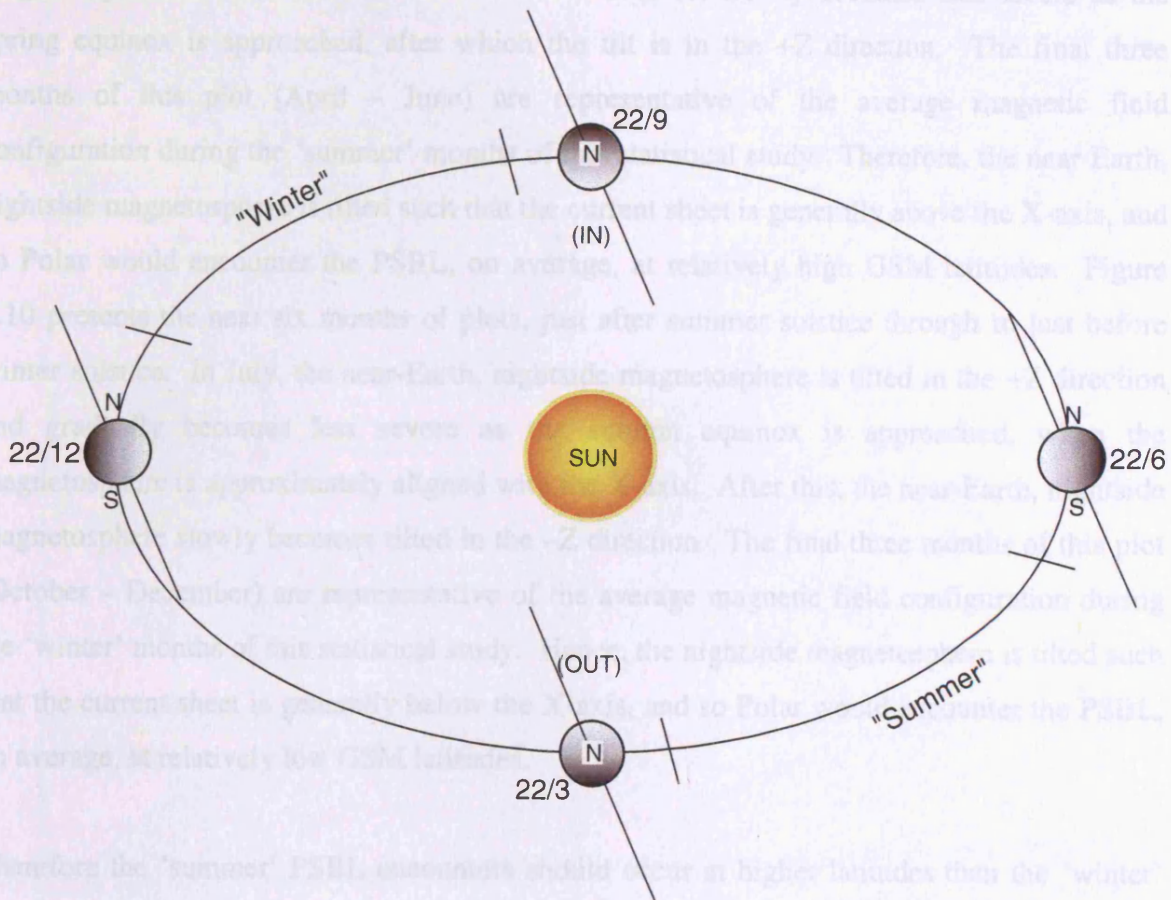


Figure 4.7: Data showing the UT dependence of the mean latitude of PSBL encounters for all data (top) and separated by season (bottom).

slightly towards the Sun, becoming more so as the orbit progresses. Conversely, in the 'winter' intervals the rotation axis will be initially tilted slightly away from the Sun, becoming more so as the orbit progresses. Therefore, on average, more of the near-Earth, nightside magnetosphere will be above (+Z) the X-axis in 'summer' and below (-Z) in 'winter'. To show this difference the Tsytarenko field model was used to plot model field configurations under average conditions throughout the year. In Figure 4.9 the Tsytarenko field is plotted on the first day of each of the first six months, from just after winter solstice to just before summer solstice, in the $X_{GSM} - Z_{GSM}$ plane. At the start of the year the near-Earth, nightside magnetosphere was tilted in the -Z direction. This tilt slowly becomes less severe as the spring equinox is approached, after which the tilt is in the +Z direction. The final three months of this plot (April - June) are representative of the average magnetic field configuration during the 'summer' months of this statistical study. Therefore, the near-Earth, nightside magnetosphere is tilted such that the current sheet is generally above the X-axis, and so Polar would encounter the PSBL, on average, at relatively high GSM latitudes. Figure 4.10 shows the near-Earth, nightside magnetosphere tilted in the -Z direction, and so Polar becomes less severe as the autumn equinox is approached. The magnetic field is approximately aligned with the X-axis. After this, the near-Earth, nightside magnetosphere slowly becomes tilted in the -Z direction. The final three months of this plot (October - December) are representative of the average magnetic field configuration during the 'winter' months of this statistical study. The nightside magnetosphere is tilted such that the current sheet is generally below the X-axis, and so Polar would encounter the PSBL, on average, at relatively low GSM latitudes.



Therefore the 'summer' PSBL encounters should occur at higher latitudes than the 'winter' encounters, as is the case with this statistical study. As the Tsytarenko magnetic field plots are made at a single UT the plots show the effect of the changing rotation axis (relative to the Sun) and not the effect of the diurnal dipole tilt variation. To illustrate this result further the PSBL latitude data were binned by month and year. The binned data are plotted as a solid line and show a periodic variation with the 'summer' months at the maxima and 'winter' months at minima, showing clearly the $\sim 23^\circ$ difference (Figure 4.11). Ideally all the months would be included, perhaps giving a plot such as the dashed line, which is a sine wave fitted such

Figure 4.8: Schematic to show the variation of the rotation axis over Earth orbit relative to the Sun

one of the reasons for this study is that the spacecraft must be close to local midnight (see section 4.1) the data are limited to those presented.

slightly towards the Sun, becoming more so as the orbit progresses. Conversely, in the 'winter' intervals the rotation axis will be initially tilted slightly away from the Sun, becoming more so as the orbit progresses. Therefore, on average, more of the near-Earth, nightside magnetosphere will be above (+Z) the X-axis in 'summer' and below (-Z) in 'winter'. To show this difference the Tsyganenko field model was used to plot model field configurations under average conditions throughout the year. In Figure 4.9 the Tsyganenko field is plotted on the first day of each of the first six months, from just after winter solstice to just before summer solstice, in the $X_{\text{GSM}} - Z_{\text{GSM}}$ plane. At the start of the year the near-Earth, nightside magnetosphere was tilted in the $-Z$ direction. This tilt slowly becomes less severe as the spring equinox is approached, after which the tilt is in the $+Z$ direction. The final three months of this plot (April – June) are representative of the average magnetic field configuration during the 'summer' months of this statistical study. Therefore, the near-Earth, nightside magnetosphere is tilted such that the current sheet is generally above the X-axis, and so Polar would encounter the PSBL, on average, at relatively high GSM latitudes. Figure 4.10 presents the next six months of plots, just after summer solstice through to just before winter solstice. In July, the near-Earth, nightside magnetosphere is tilted in the $+Z$ direction and gradually becomes less severe as the autumn equinox is approached, when the magnetosphere is approximately aligned with the X-axis. After this, the near-Earth, nightside magnetosphere slowly becomes tilted in the $-Z$ direction. The final three months of this plot (October – December) are representative of the average magnetic field configuration during the 'winter' months of this statistical study. Hence, the nightside magnetosphere is tilted such that the current sheet is generally below the X-axis, and so Polar would encounter the PSBL, on average, at relatively low GSM latitudes.

Therefore the 'summer' PSBL encounters should occur at higher latitudes than the 'winter' encounters, as is the case with this statistical study. As the Tsyganenko magnetic field plots are made at a single UT the plots show the effect of the changing rotation axis (relative to the Sun) and not the effect of the diurnal dipole tilt variation. To illustrate this result further the PSBL latitude data were binned by month and year. The binned data are plotted as a solid line and show a periodic variation with the 'summer' months at the maxima and 'winter' months at minima, showing clearly the $\sim 25^\circ$ difference (Figure 4.11). Ideally all the months would be included, perhaps giving a plot such as the dashed line, which is a sine wave fitted such that the maxima and minima are located at summer and winter solstices. However, as one of the restrictions on the study is that the spacecraft must be close to local midnight (see section 4.1), the data are limited to those presented.

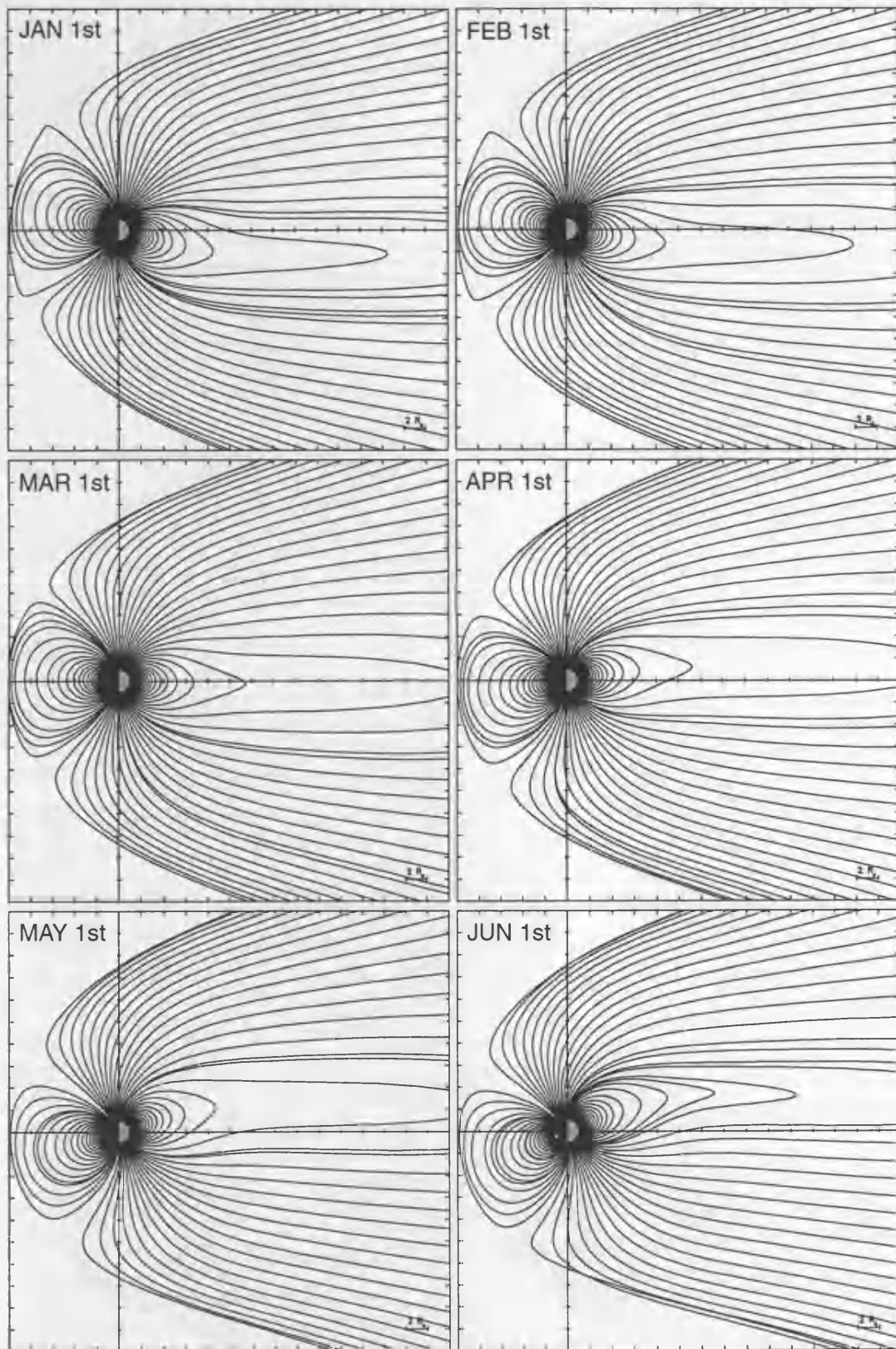


Figure 4.9: Tsyganenko 89 field model plotted on the 1st of January - June in the X-Z GSM plane. This shows the magnetospheric variation due to rotation of the Earth around the Sun.

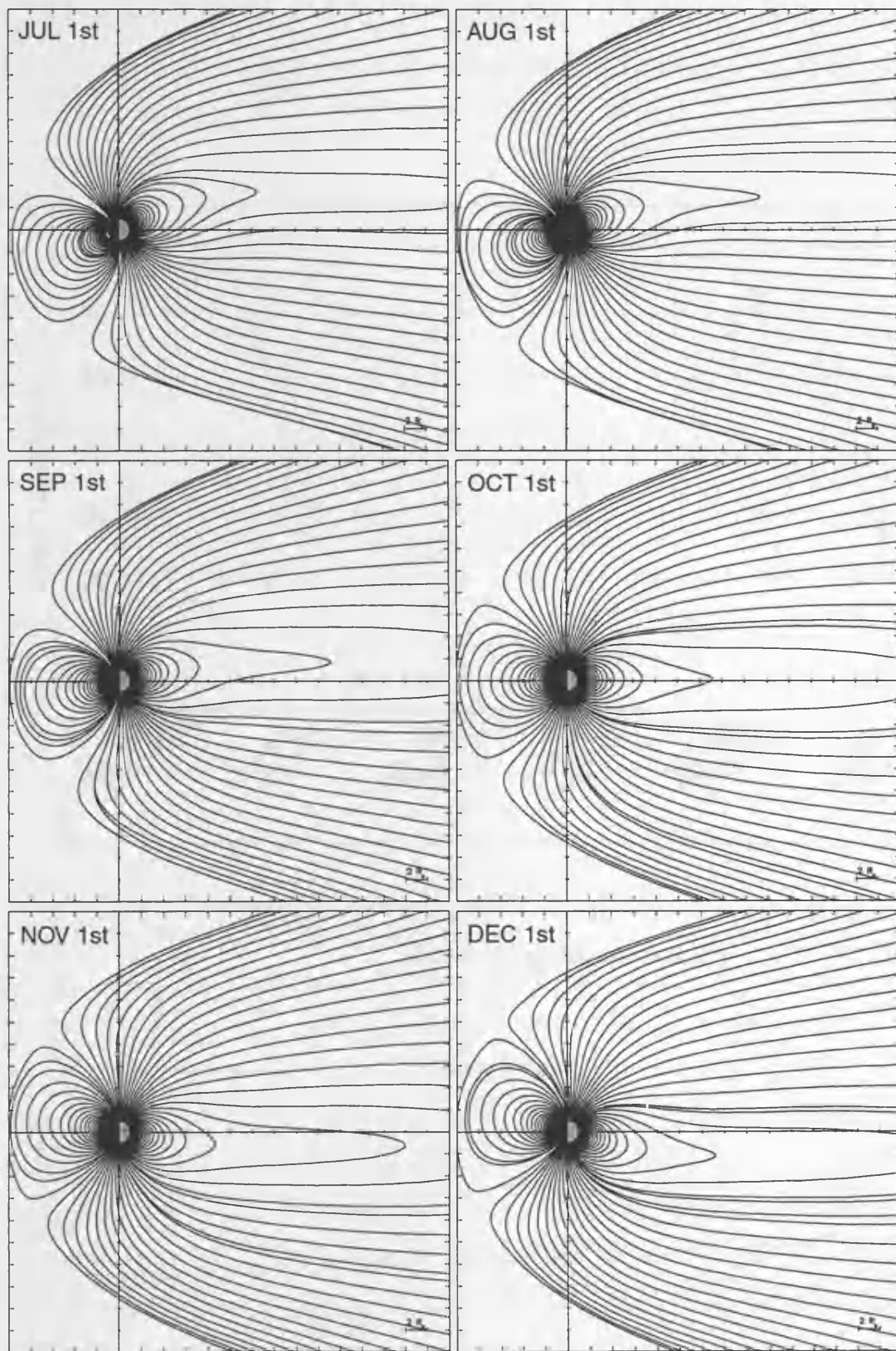
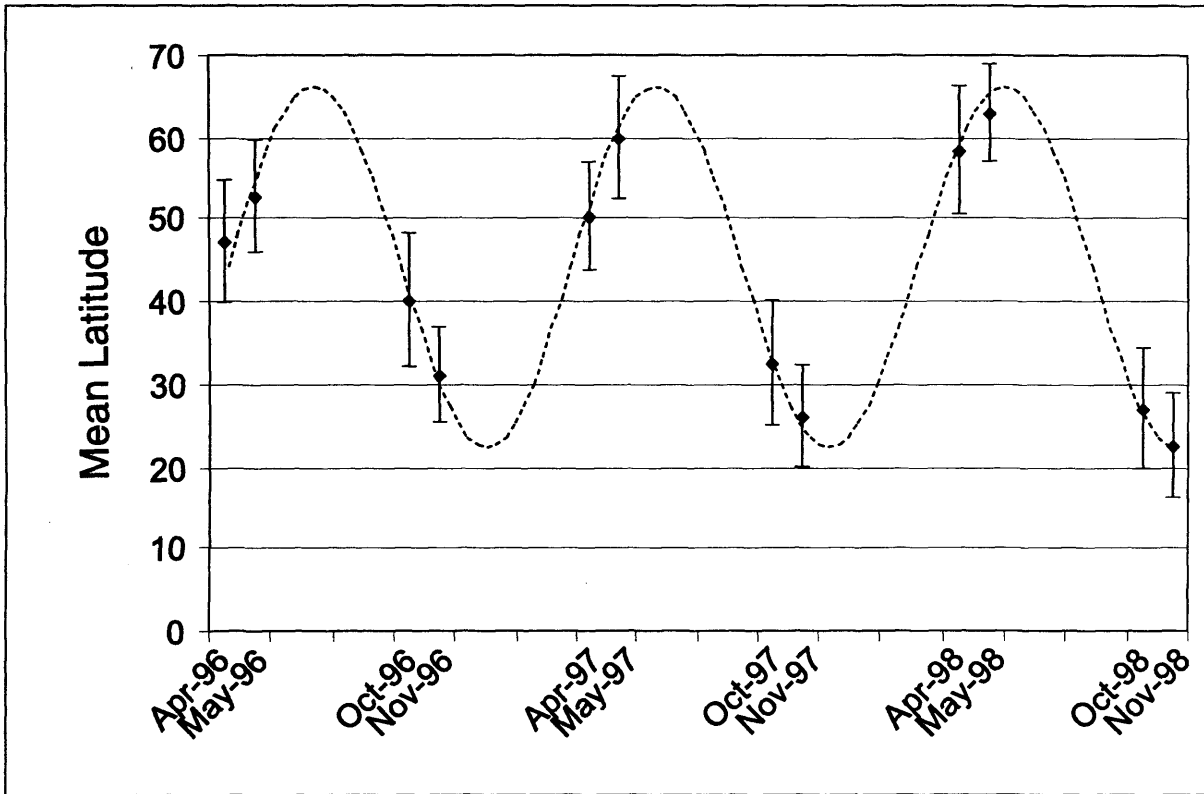


Figure 4.10: Tsyganenko 89 field model plotted on the 1st of July - December in the X-Z GSM plane. This shows the magnetospheric variation due to rotation of the Earth around the Sun.



Observations (Mean +/- S.D.)

 Possible trend

Figure 4.11: Data is binned by month and year. The solid line represents the observed data and the dashed line represents the expected pattern of results due to rotation axis variation.

The seasonal variation repeats with the $\sim 25^\circ$ difference, which can be explained by rotation axis variation as the dominant factor. Therefore the seasonal variation is similar to that observed during the solstices. The small, but statistically significant, variations in the geocentric distance statistics are representative of the different locations on the orbit that the spacecraft encounters the PSBL or CPS. Dipole tilt will also be relevant by spreading the latitude location distributions. Other factors such as solar wind and magnetic conditions may also spread the distributions. These effects are investigated in the following sections.

4.6. PSBL Thickness

The PSBL was first identified by *Lui et al.* [1977] and *DeCoster and Frank* [1979] who noticed that during plasma sheet expansions high-speed flows are mostly confined to a $1-2 R_E$ thick layer near the upper and lower boundaries of the plasma sheet. This region later became known as the PSBL. Therefore, over two decades ago there was an estimate of the thickness of the PSBL, albeit a general one. *Dandouras et al.* [1986b] produced a statistical average for the average width of the plasma sheet boundary layer of ~ 5000 km at distances downtail from $X \sim -10 - -25 R_E$. In this section the thickness of the PSBL will be found along the Polar orbit, and consequently a value of the vertical (Z_{GSM} direction) thickness at a specific range of X_{GSM} values.

As the location of both the PSBL and CPS had been found, the distance separating the two gives an upper limit to the thickness of the PSBL at that point along the orbit as the spacecraft frequently observes multiple PSBL entries. This may not be the exact thickness of the PSBL, and it may differ from previous definitions, but it will be referred to as such for the purpose of this work. This value will be a distance along Polar's orbit, which may not follow the Z-axis exactly. Therefore the X- and Z-components of this distance are also examined. The histograms of PSBL thickness statistics are presented in Figure 4.12. The top panel presents the thickness statistics in terms of orbital thickness (along orbit path – referred to as T); the middle panel gives the thickness in terms of the X-component (T_X), and the bottom panel in terms of the Z-component (T_Z). The data gave a mean orbital thickness of $1.27 \pm 0.84 R_E$, a mean X-component thickness of $0.07 \pm 0.39 R_E$ and a mean Z-component thickness of $1.22 \pm 0.81 R_E$. The Student's t-test is once again employed to determine if the seasonal means are significantly different. The seasonal mean values and the t-values for each of the panels are presented in Table 4.5. T and T_Z have low t-values such that the probability of the 'summer' and 'winter' means of these values being equal is significant at the 0.01 level. However the T_X means are not equal, as the t-value is larger than the calculated t-values quoted earlier.

Thickness	Summer Mean (± S.D.)	Winter Mean (± S.D.)	t-value
$T(\text{Re})$	1.21 ± 0.82	1.34 ± 0.85	1.672
$T_x(\text{Re})$	0.07 ± 0.39	-0.19 ± 0.28	17.672
$T_z(\text{Re})$	1.22 ± 0.81	1.17 ± 0.80	1.302

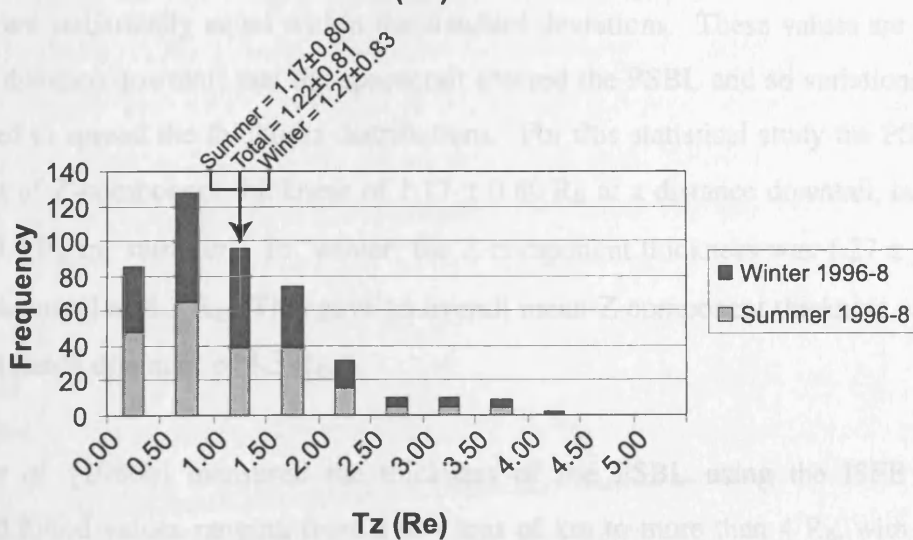
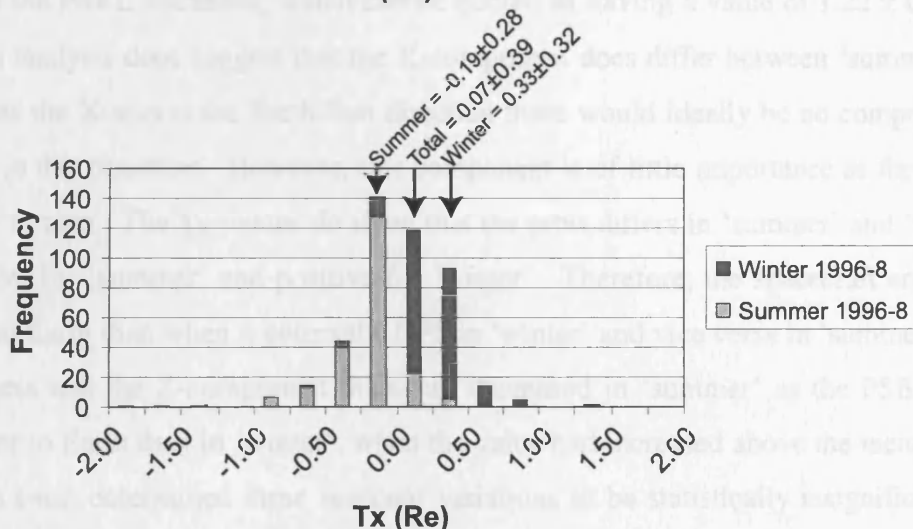
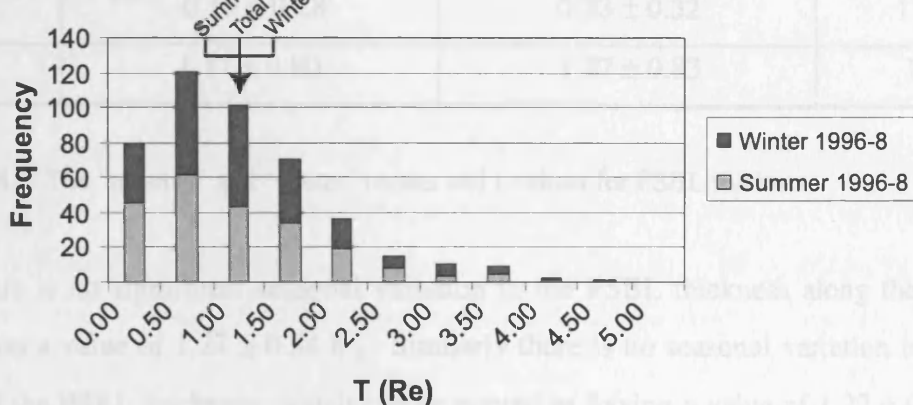


Figure 4.12: PSBL thickness histograms. The top panel presents the thickness by orbital radius, the second in terms of the X-component and the bottom in terms of Z-component.

'Thickness'	'Summer' Mean (\pm S.D.)	'Winter' Mean (\pm S.D.)	t-value
T (R_E)	1.21 ± 0.82	1.34 ± 0.85	1.672
T _X (R_E)	-0.19 ± 0.28	0.33 ± 0.32	17.872
T _Z (R_E)	1.17 ± 0.80	1.27 ± 0.83	1.302

Table 4.5: The 'summer' and 'winter' means and t-values for PSBL thickness.

Therefore there is no significant seasonal variation in the PSBL thickness along the orbital path, which has a value of $1.27 \pm 0.84 R_E$. Similarly there is no seasonal variation in the Z-component of the PSBL thickness, which can be quoted as having a value of $1.22 \pm 0.81 R_E$. The statistical analysis does suggest that the X-component does differ between 'summer' and 'winter', but as the X-axis is the Earth-Sun direction there would ideally be no component of the thickness in this direction. However, this component is of little importance as the overall mean is close to zero. The T_X values do show that the orbit differs in 'summer' and 'winter', as it is negative for 'summer' and positive for 'winter'. Therefore, the spacecraft enters the PSBL closer to Earth than when it enters the CPS in 'winter' and vice versa in 'summer'. The orbital thickness and the Z-component thickness decreased in 'summer' as the PSBL entry occurred closer to Earth than in 'winter', when the value had increased above the mean value. The Student's t-test determined these seasonal variations to be statistically insignificant and so the means are statistically equal within the standard deviations. These values are directly related to the distance downtail that the spacecraft entered the PSBL and so variations in this distance served to spread the thickness distributions. For this statistical study the PSBL had an upper limit of Z-component thickness of $1.17 \pm 0.80 R_E$ at a distance downtail, in the $-X$ direction, of $3.3 R_E$ in 'summer'. In 'winter' the Z-component thickness was $1.27 \pm 0.83 R_E$ at a distance downtail of $5.3 R_E$. This gave an overall mean Z-component thickness of $1.22 \pm 0.81 R_E$ at a distance downtail of $4.3 R_E$.

Dandouras et al. [1986b] measured the thickness of the PSBL using the ISEE 1 & 2 spacecraft and found values ranging from a few tens of km to more than $4 R_E$, with a mean value of ~ 5000 km, from distances downtail from $X \sim -10$ to $-25 R_E$. Therefore the values obtained in this study are slightly higher than in the previous work, but the measurements are still within the quoted range. As Polar is in a higher inclination orbit than the ISEE spacecraft there is less chance of any distortion in the X_{GSM} direction having an effect on the measurements and so provides a more accurate value, but at only limited values of X_{GSM} ,

whereas the ISEE spacecraft provided measurements from a larger range of downtail distances.

4.7. Effect of Magnetic Activity

The mean locations of the PSBL and CPS have been shown to be directly related to the variation of the rotational axis of the Earth relative to the Sun. As this thesis concentrates on features occurring during Polar passes through the PSBL this section determines the effect, if any, of geomagnetic activity on the location and thickness of the PSBL. To perform this study the ideal magnetic indices for comparison are AE and Dst. Dst is primarily used to monitor geomagnetic storms by monitoring the strength of the ring current [Dessler and Parker, 1959]. The auroral electrojet indices were defined by Davis and Sugiura [1966] to determine the strength of the auroral electrojets relatively uncontaminated by ring current effects and so are directly related to substorm activity. Unfortunately, at the time of submission, no final AE values are available for the intervals studied, with the only usable data being daily plots generated automatically. Therefore a substorm index (SSI) was devised. The PSBL entry time was found on the AE plot and a number ascribed to the event on substorm phase: (Q) quiet - no activity, (G) growth phase, (E) expansion phase and (R) recovery phase. If the activity was unclear then the event was not used for the SSI study. Figure 4.13 represents schematically how the SSI was determined from the AE plots.

Figure 4.14 presents the SSI variations with the PSBL latitude location. The top panel presents data from all entries into the PSBL and the associated SS Index. Although there is no obvious effect there are small variations as the growth (G) phase events were grouped at higher latitudes than the expansion (E) phase, whilst the quiet (Q) and recovery (R) phase events were more evenly distributed. The middle panel shows the data from the 'summer' entries and the bottom panel presents the 'winter' entries. These plots show the seasonal variation as described earlier as the 'summer' events were clustered around higher latitudes than the 'winter' events. The only effect that is clear from these data is that the Q events covered most of the latitude ranges, whilst G and E slightly more narrow latitudinal ranges. The R events also covered a large latitudinal range, but mainly at higher latitudes. The G events appeared to occur at slightly higher latitudes than the E events, but there are enough 'spurious' points to cast doubt on this presumption. It appears that there is little pattern to the SSI data, and hence the substorm phase at the time of entry only plays a minor role in the location of the PSBL, with other factors being more important. However, the work detailed later has shown that there is in fact an effect on the location of the PSBL during substorms,

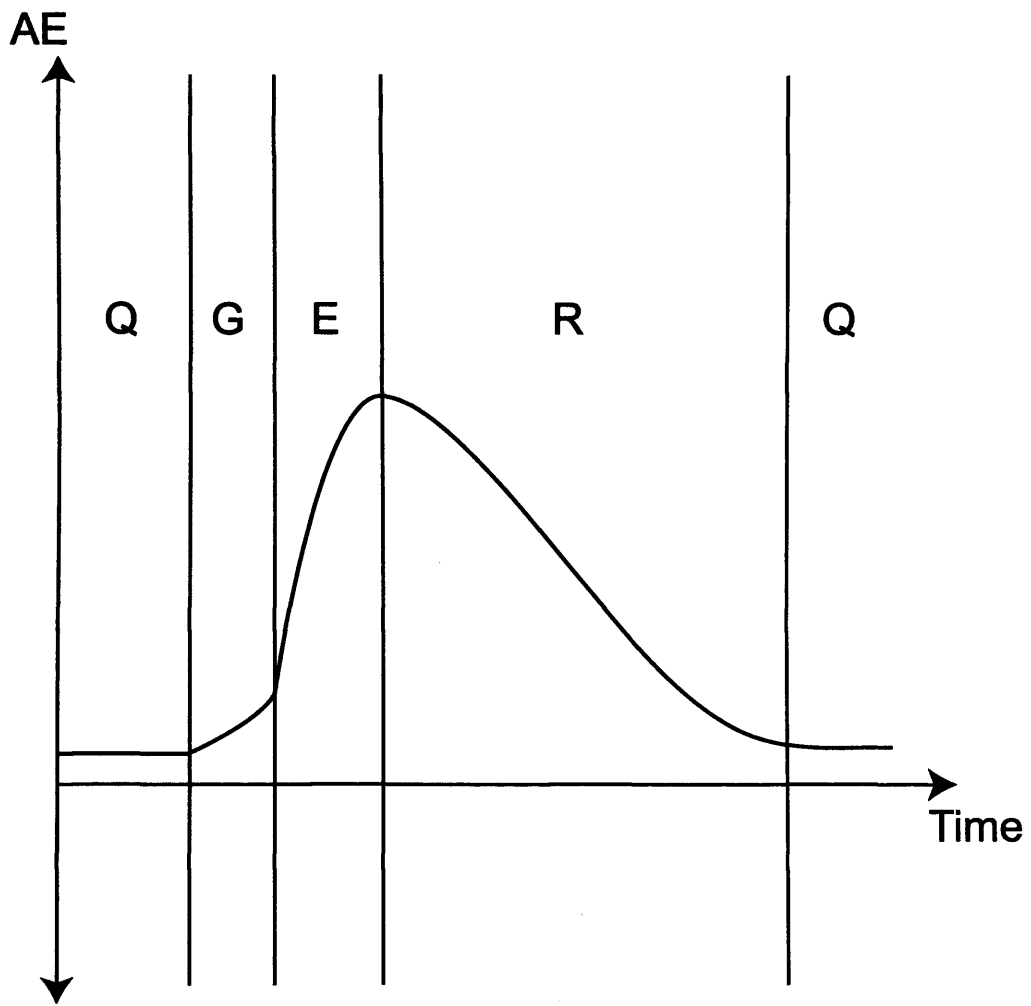


Figure 4.13: Schematic to show how the SubStorm Index (SSI) was devised using plots of AE.

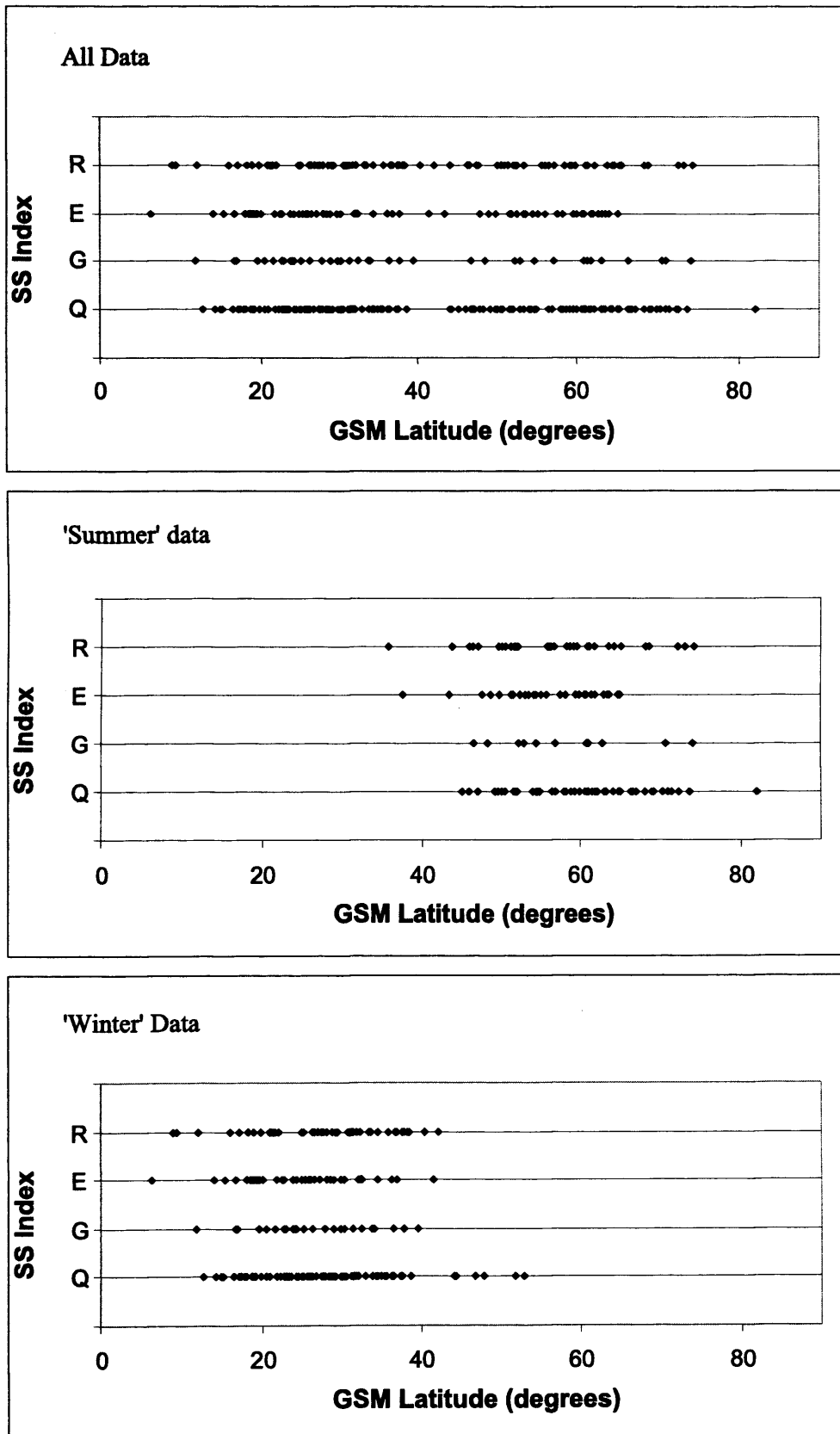


Figure 4.14: Geomagnetic substorm effects on the PSBL entry latitude. The top panel presents the effects of the SubStorm Index for all events, the second panel presents the 'Summer' effects and 'Winter' effects in the bottom panel.

which is not evident in this study, but perhaps this effect will become obvious when the final AE data becomes available.

The Dst values are available as hourly means so the value is chosen such that the PSBL entry time is included in the hour from which the Dst value is quoted. Figure 4.15 presents the PSBL entry latitudes compared with the Dst values, with all the entries shown in the top panel, the 'summer' entries in the middle panel and the 'winter' entries in the bottom panel. Linear correlation coefficients were calculated for each plot, but these showed little ($|R| < 0.2$) linear correlation. Therefore there was no definite connection between Dst and the PSBL latitude.

4.8. Effect of IMF B_z

IMF B_z is the north – south component of the solar wind magnetic field, and as such may have an effect on the location of the PSBL primarily due to dayside reconnection effects and hence substorm activity (see Chapter 1). The IMF B_z data used in this section were measured by the MFI on board the Wind satellite (see Chapter 3). To study any possible effect the location statistics were separated into two separate data sets, those during IMF B_z positive (northward) and those during IMF B_z negative (southward). The values of IMF B_z are found by subtracting a propagation delay from the PSBL entry times. This delay is an estimate of the propagation time of the solar wind from the spacecraft to the magnetopause. Figure 4.16 presents the initial encounter location statistics for cases where B_z was positive and Figure 4.17 presents the data for negative B_z . In both figures the top panel presents the GSM latitude and the bottom panel presents the geocentric distance statistics. The mean values for 'summer', 'winter' and 'All Data' are presented in Table 4.6. In order to determine if there is a statistically significant difference between the IMF B_z positive and negative values the Student's t-test has once again been employed. The calculated t-values are also included in Table 4.6.

When the calculated t-values are compared with the 0.01 level of significance for a two-tailed test ($t_{.995} = 2.58$) and a 0.05 level of significance ($t_{.975} = 1.96$) the latitude differences between positive and negative IMF B_z are found to be statistically significant for the 'winter' and 'all data' statistics, but not for 'summer'. The geocentric distance (G.D.) differences between positive and negative IMF B_z are found to be statistically insignificant for the 'winter' 'summer' and 'all data' statistics.

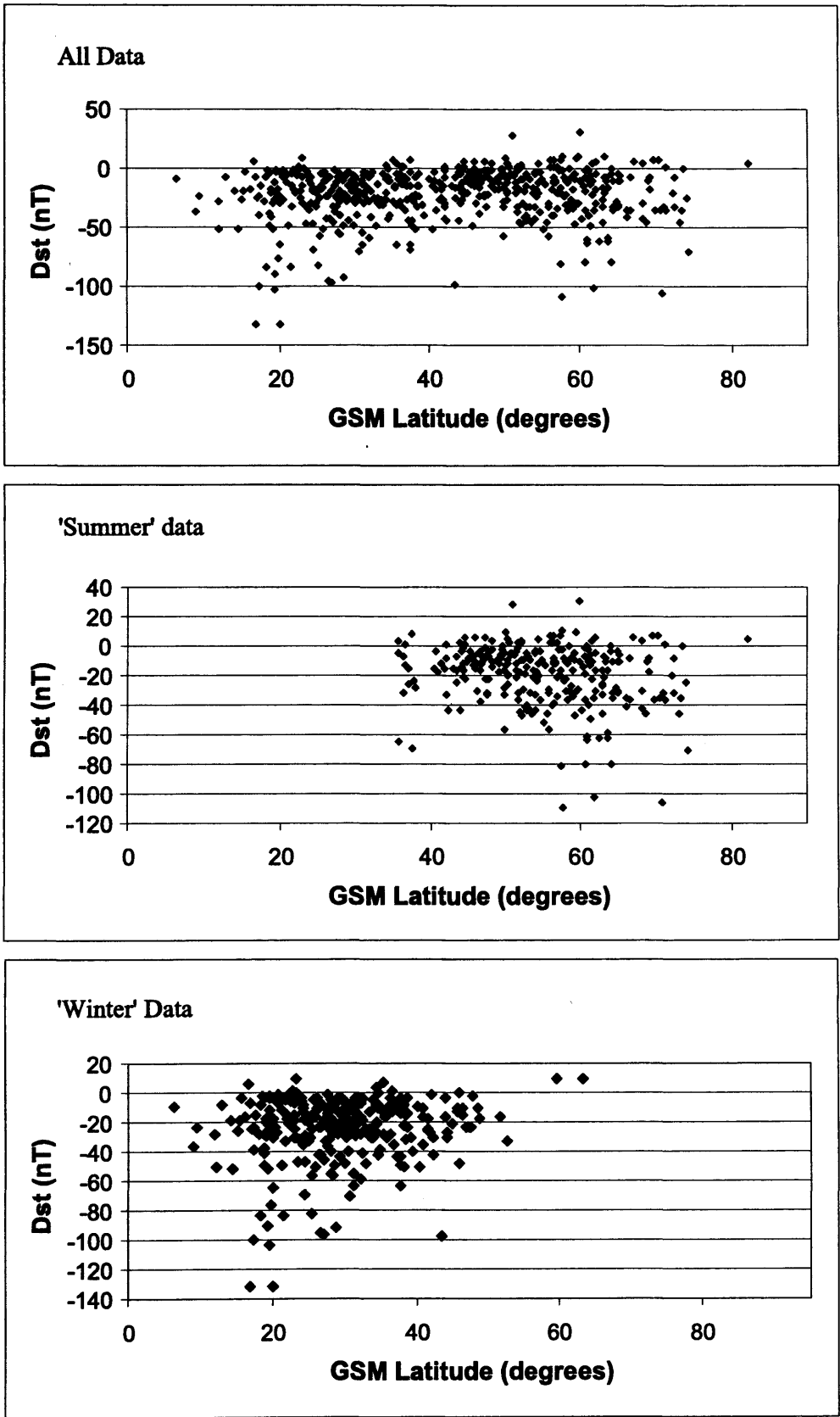


Figure 4.15: Dst effects on the PSBL entry latitude. The top panel presents the effects of Dst for all events, the second panel presents the 'Summer' events and the 'Winter' events are in the bottom panel.

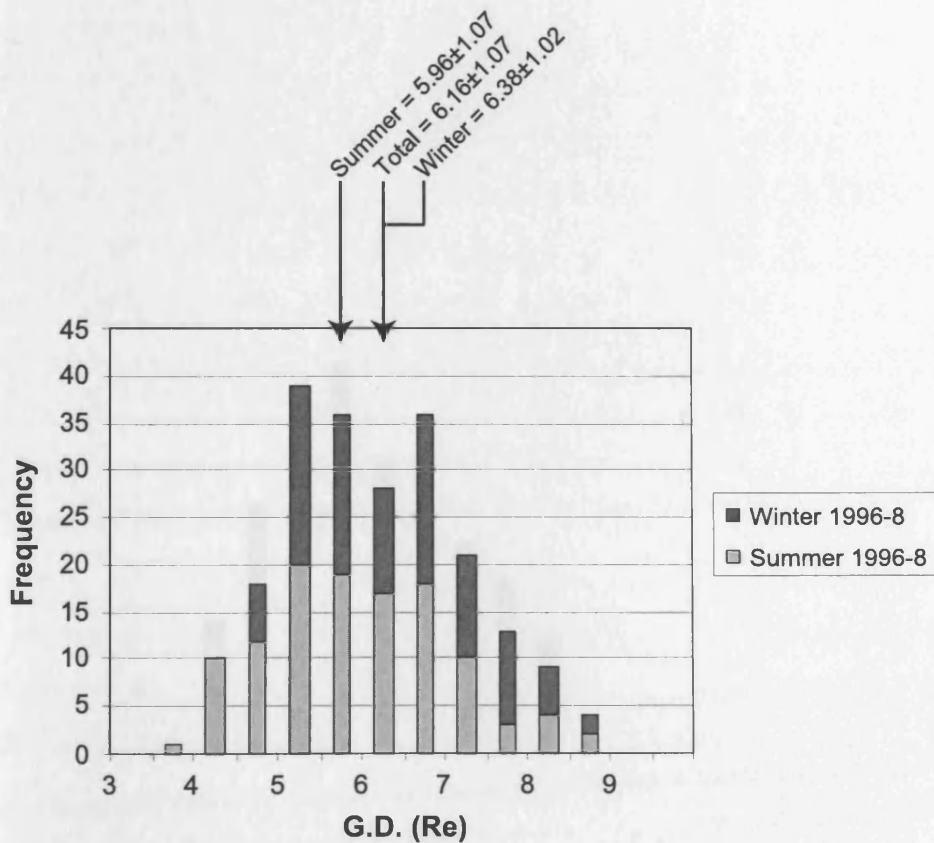
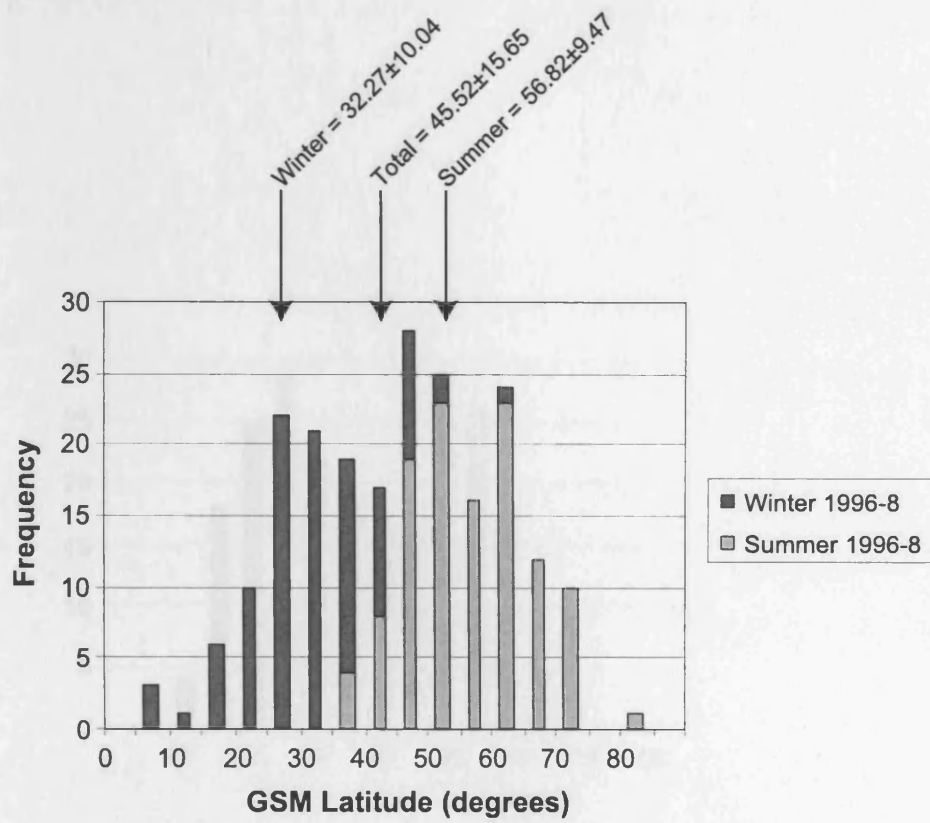


Figure 4.16: PSBL entry location in both latitude and geocentric distance (G.D.) for positive B_z , with seasons also separated.

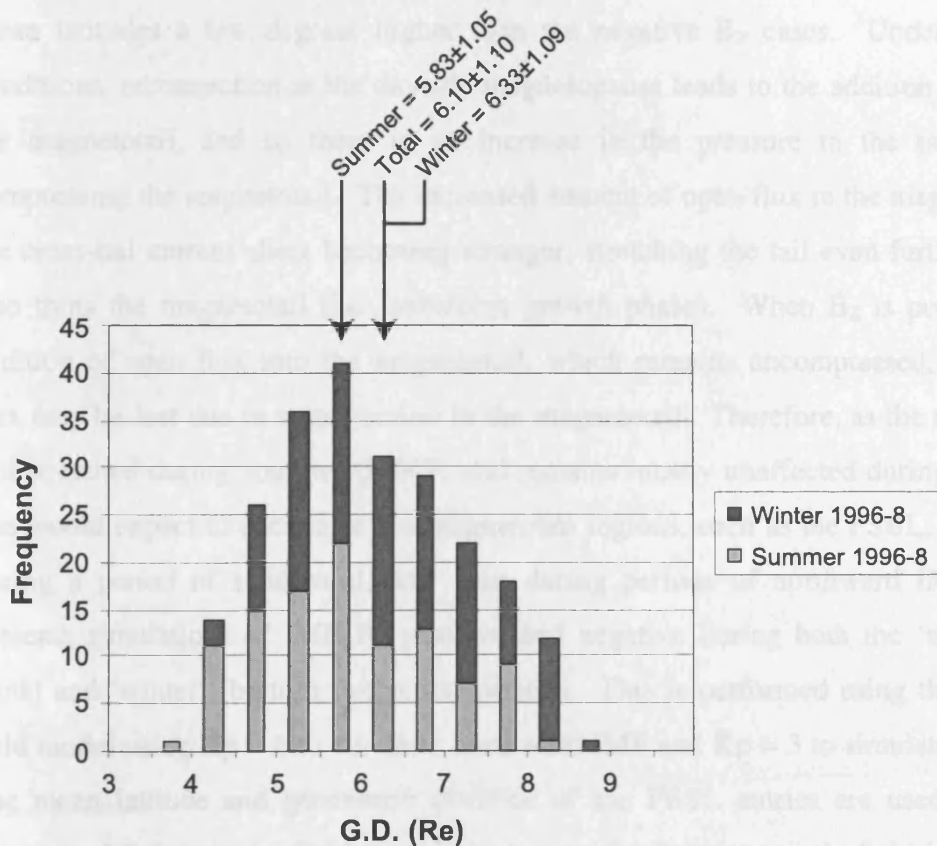
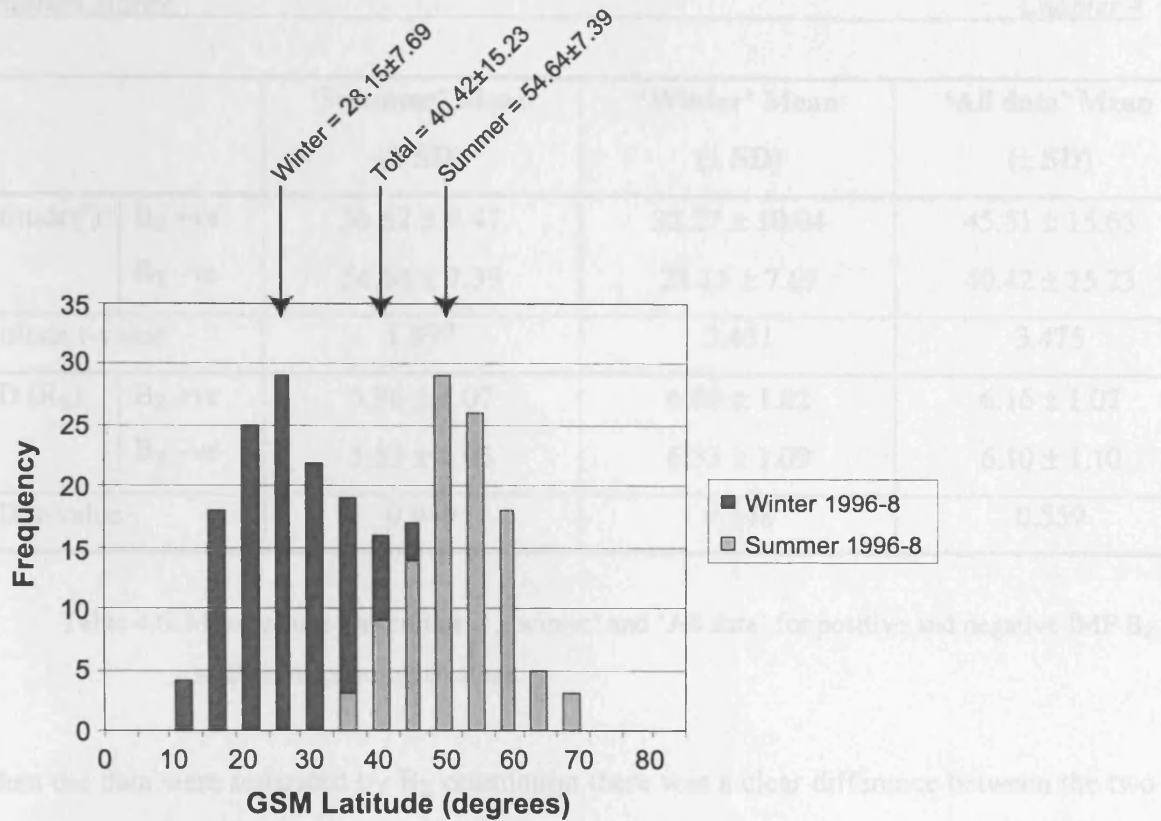


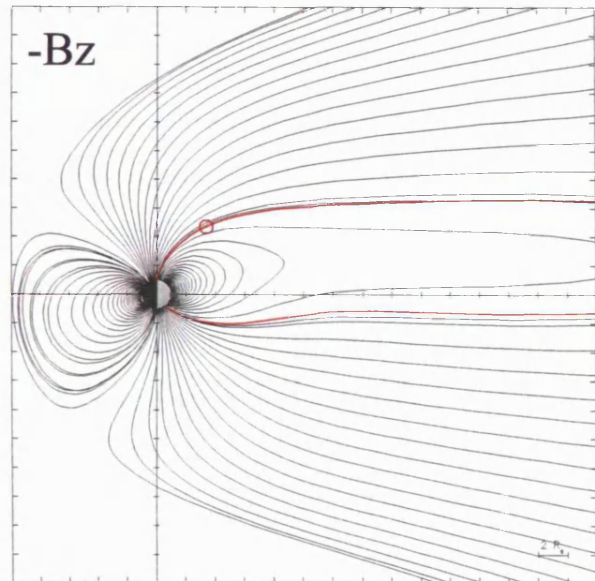
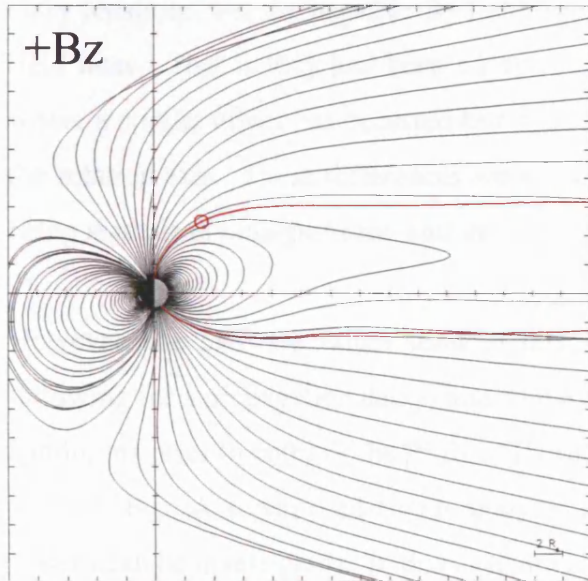
Figure 4.17: PSBL entry location in both latitude and geocentric distance (G.D.) for negative B_z , with seasons also separated.

		'Summer' Mean (\pm SD)	'Winter' Mean (\pm SD)	'All data' Mean (\pm SD)
Latitude($^{\circ}$)	B _Z +ve	56.82 \pm 9.47	32.27 \pm 10.04	45.51 \pm 15.65
	B _Z -ve	54.64 \pm 7.39	28.15 \pm 7.69	40.42 \pm 15.23
Latitude t-value		1.897	3.451	3.475
G.D.(R _E)	B _Z +ve	5.96 \pm 1.07	6.38 \pm 1.02	6.16 \pm 1.07
	B _Z -ve	5.83 \pm 1.05	6.33 \pm 1.09	6.10 \pm 1.10
G.D. t-value		0.949	0.348	0.559

Table 4.6: Mean values for 'summer', 'winter' and 'All data' for positive and negative IMF B_Z with corresponding t-values.

When the data were separated by B_Z orientation there was a clear difference between the two separate cases for both the 'winter' and overall latitude statistics, with the positive B_Z having mean latitudes a few degrees higher than the negative B_Z cases. Under southward IMF conditions, reconnection at the dayside magnetopause leads to the addition of open flux into the magnetotail, and so there is an increase in the pressure in the tail lobes, thereby compressing the magnetotail. The increased amount of open flux in the magnetotail results in the cross-tail current sheet becoming stronger, stretching the tail even further downtail, and also thins the magnetotail (i.e., substorm growth phase). When B_Z is positive there is no addition of open flux into the magnetotail, which remains uncompressed, and indeed open flux may be lost due to reconnection in the magnetotail. Therefore, as the tail is compressed and stretched during southward IMF, and remains mostly unaffected during northward IMF, one would expect to encounter the magnetotail regions, such as the PSBL, at lower latitudes during a period of southward IMF than during periods of northward IMF. Figure 4.18 presents simulations of IMF B_Z positive and negative during both the 'summer' (top two plots) and 'winter' (bottom two plots) periods. This is performed using the Tsyganenko 89 field model using K_p = 0 to simulate northward IMF and K_p = 3 to simulate southward IMF. The mean latitude and geocentric distance of the PSBL entries are used to calculate the location of Polar on the field models and trace the Polar magnetic field line. A red circle indicates the location of the spacecraft and the field line is traced in red. There are two features evident from these plots. The first is that the dayside has been eroded from the positive to negative cases. The second is that the nightside magnetic field lines are more compressed in the negative cases than in the positive cases. The Polar field line for the two

'Spring'



'Autumn'

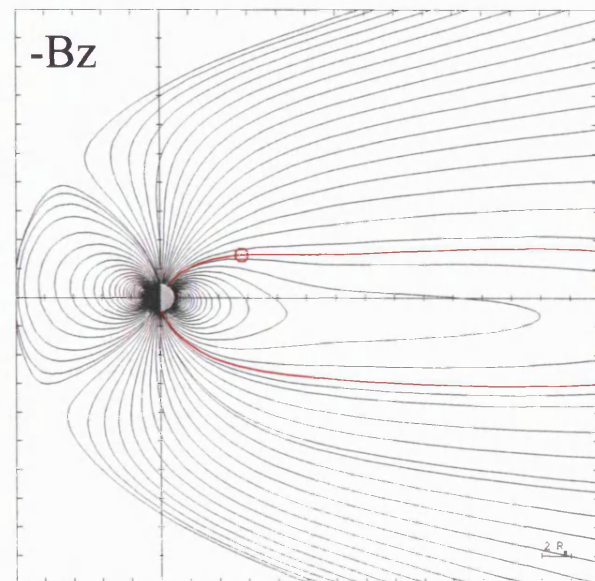
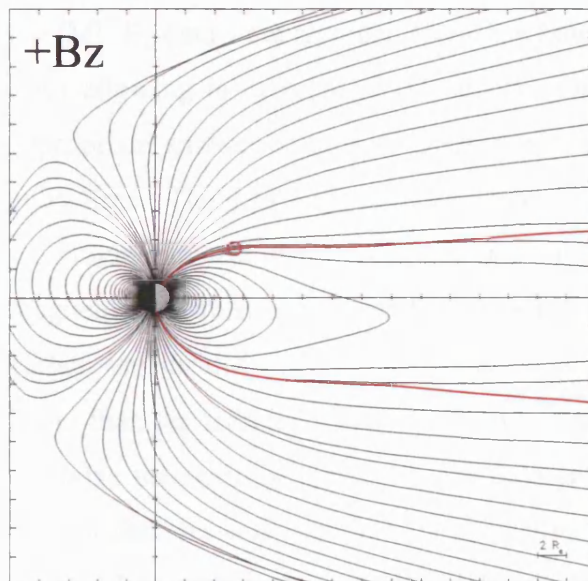
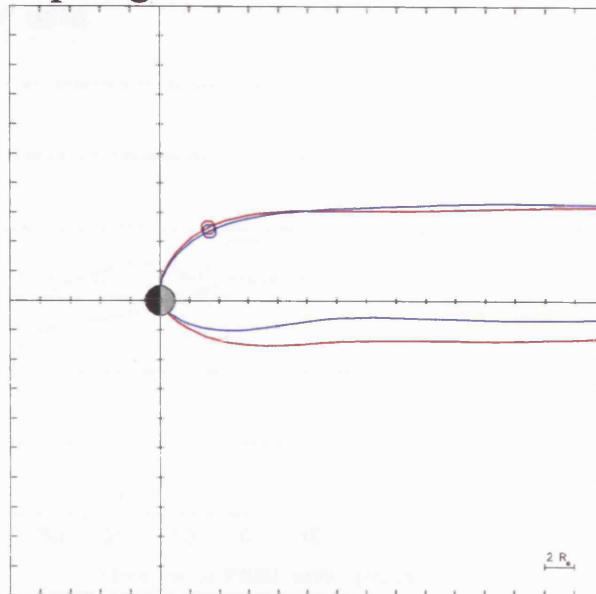


Figure 4.18: Tsyganenko 89 field model plotted in the X-Z GSM plane for the 1st May in the top two plots and 1st November in the bottom two plots during both IMF Bz positive and negative. Polar is on the field line marked in red.

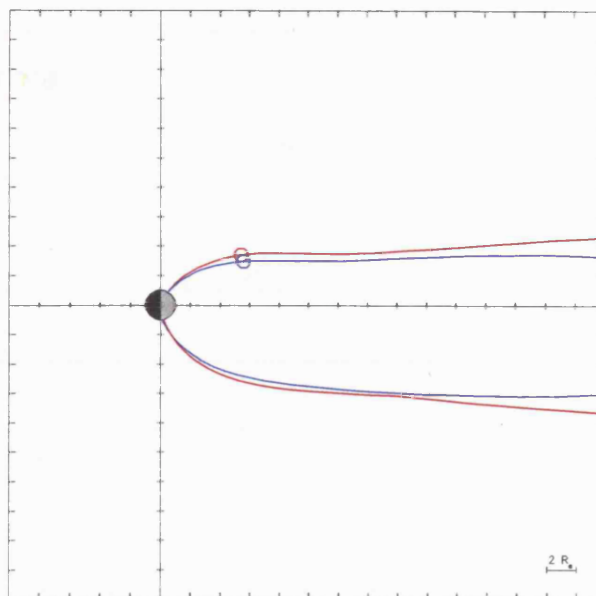
IMF orientations are directly compared in Figure 4.19. This figure comprises of the Polar field lines for both positive and negative IMF B_z superimposed upon each other during 'summer' and 'winter'. The positive B_z field lines are coloured red, whilst the negative B_z field lines are coloured blue. In 'summer' there was very little difference between the PSBL entry locations, but the negative B_z field lines were closer to the X-axis than the positive B_z field lines. That is they had been compressed. This was more evident in the 'winter' plot where a similar effect has occurred but with more obvious differences due to the variation in the rotation axis. These differences were shown in the statistics with the 'summer' variation being statistically insignificant, and the 'winter' differences being statistically significant.

However, the IMF B_z values used in this section were taken at the time of PSBL entry (allowing for a propagation delay) and so may not be indicative of the predominant solar wind conditions prior to entry of the PSBL. Therefore a superposed-epoch analysis was performed on IMF B_z . A superposed-epoch analysis is a method by which the average effects on a system can be investigated. In this case, it is not always as important to know the actual value of IMF B_z as it is to know the predominant direction of the IMF both leading up to, during and after the event in question. To do this the PSBL entry time and latitude were noted, and the IMF B_z data were recorded from one hour before through to one hour after the entry time (also allowing for a propagation delay). One hour was chosen because it was deemed an appropriate amount of time to determine the prevailing IMF conditions with respect to the entry time. The data were separated into the 'summer' and 'winter' entries and then binned by latitude to test the hypothesis that southward IMF would compress and stretch the magnetotail, whilst northward IMF would not. The latitude bins were determined by the earlier statistical means for PSBL entry, with 'low-latitude' entries occurring at latitudes lower than the seasonal mean value, and 'high-latitude' entries occurring at latitudes equal to or above the seasonal mean. A test data set was also included as a control data set. This control data set was obtained by collecting two hundred sets of two hours of IMF B_z at random from within the statistical database (one hundred for each season). For each of these data sets the IMF B_z data were noted every five minutes and the mean calculated for each of these time bins. The data produced the results presented in Figure 4.20, which shows the various bins and test data as three time series of coloured lines plotted against IMF B_z for both 'summer' and 'winter'. As the mean would be affected by extreme values of B_z , the median was also calculated and plotted. Whilst there were some minor differences between the mean and median plots, the overall pattern of the data were unaffected, indicating that no extreme conditions were observed during the study interval.

'Spring'



'Autumn'



- +Bz
- -Bz
- Polar

Figure 4.19: Tsyganenko 89 field model plotted in the X - Z GSM plane for the 1st May in the top plot and 1st November in the bottom plot. The red lines indicate the field line Polar is occupying during northward IMF with the blue line indicating southward IMF.

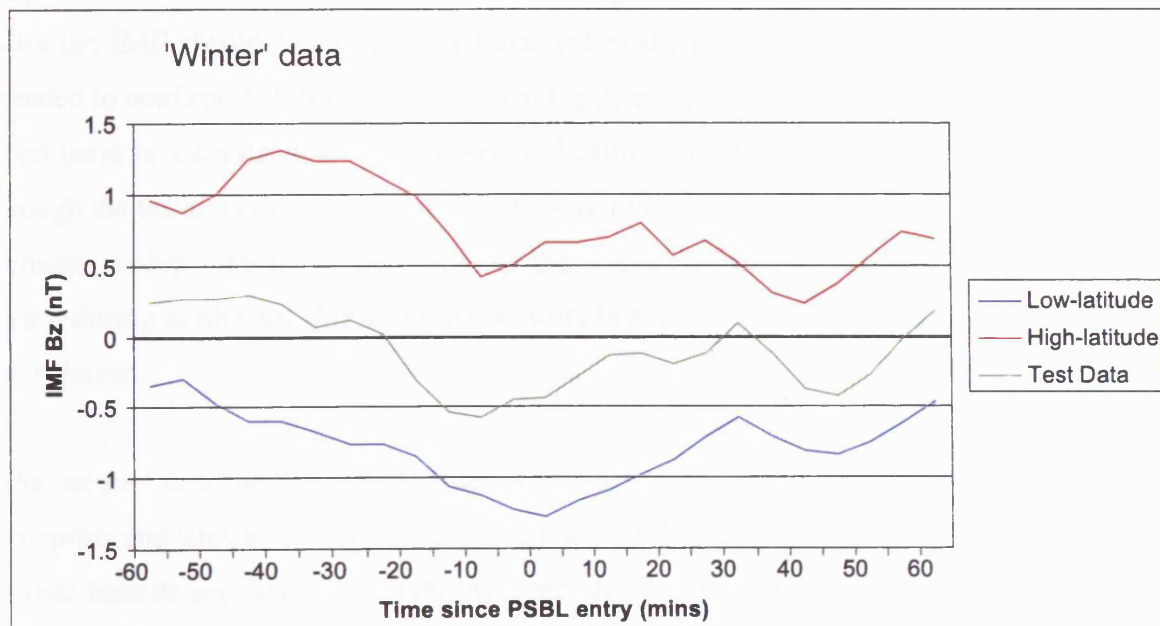
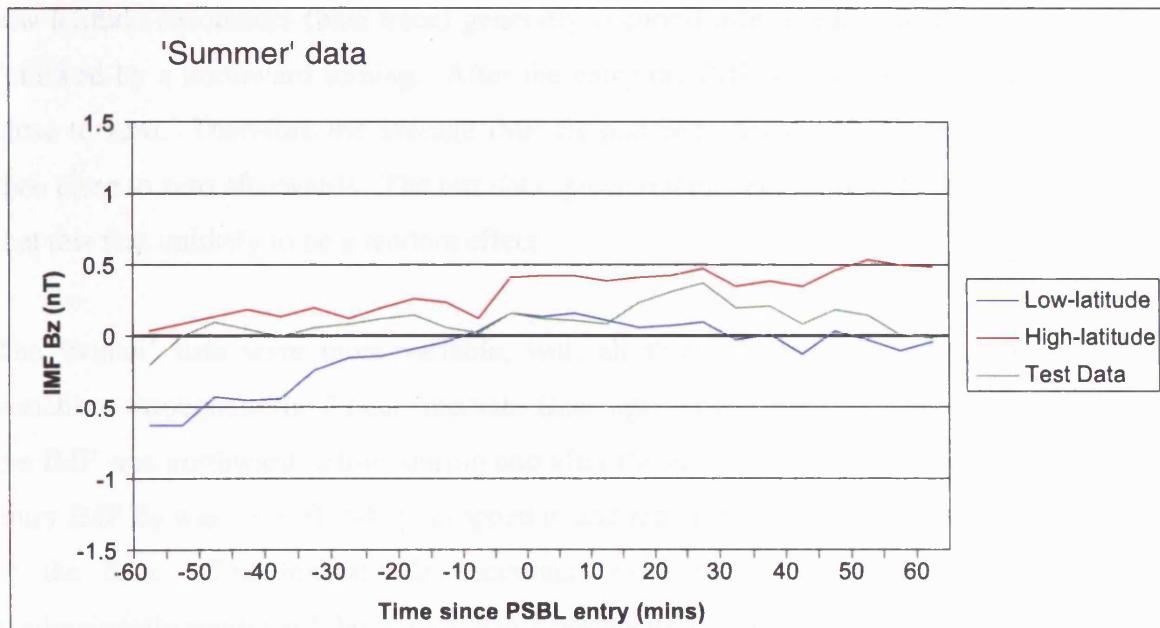


Figure 4.20: Superposed-Epoch analysis of IMF Bz for one hour before and after PSBL entry time in two latitude bins for each season. Test data are also included for a control data set.

The 'summer' data plot showed that the high-latitude (red trace) encounters occurred, on average, after the IMF had been northward for the preceding hour and that the entries also occurred during northward IMF, which remained northwards after the entry. However, the low-latitude encounters (blue trace) generally occurred after predominantly southward IMF, followed by a northward turning. After the entry the IMF was variable, with a mean value close to zero. Therefore the average IMF B_z had been negative before the encounters and then close to zero afterwards. The test data (green trace) were mostly close to zero, indicating that this was unlikely to be a random effect.

The 'winter' data were more variable, with all three traces undergoing more significant variations throughout the 2 hour interval. Once again the high-latitude entries occurred when the IMF was northward before, during and after the entry. However, ~40 minutes before the entry IMF B_z was ~-1.3 nT, which dropped to and remained close to ~-0.5 nT for the remainder of the data. The low-latitude encounters once again occurred after the IMF was predominantly southward, but rather than a northward turning close to the entry time, IMF B_z decreased further, dropping from ~ -0.3 nT to ~ -1.3 nT. After the entry time there was an apparent recovery of the IMF, with B_z increasing to ~ -0.7 nT. There is no clear explanation why the IMF should 'recover' after Polar enters the PSBL, and a much expanded study is needed to confirm that this is, in fact, an accurate result. In fact, if the test-data are examined then there is a similar feature observed, indicating that this may be a random factor. Even though the test-data do undergo significant variations throughout the interval, the trace always remains within ~-0.6 nT of zero, and so the overall result that the high-latitude encounters occur during northward IMF and the low-latitude encounters occur during southward IMF can be believed.

The 'winter' data suggest that the hypothesis was correct and that southward IMF does indeed compress and stretch the magnetotail, causing the PSBL to occur at lower-latitudes, whilst the higher-latitude encounters occur during intervals of northward IMF when this alteration of the magnetotail does not occur. The 'summer' data are not so clear, but there is still initially southward IMF during the low-latitude encounters and continual northward IMF during the high-latitude encounters. An expansion of the data set to include other years (1999 onwards) and other spacecraft data could clarify this result and conclusively prove this hypothesis.

4.9. Effect of Solar Wind Dynamic Pressure

The final parameter investigated for an effect on the PSBL location was the solar wind dynamic pressure, the idea being that a sudden increase (or decrease) could force a reconfiguration of the whole magnetosphere, thereby altering the PSBL location.

To consider this effect a superposed-epoch analysis was performed once again, this time using dynamic pressure data from the SWE (see Chapter 3) on-board the Wind spacecraft. The same process as that described in the previous section was carried out, but using the dynamic pressure measurements rather than IMF B_z . These data produced the plots presented in Figure 4.21, with the coloured traces representing the high- and low-latitude data as before. Although there are small variations in each of the traces over the two hours of data, each trace remains within 0.1 nPa of an average value. The most significant variation seen in these data are not along one of the traces, but are between the traces. This is the difference between the high- and low-latitude traces in both the 'summer' and 'winter' data. In the 'summer' data the high-latitude (red) trace is centred on ~ 2.1 nPa, whilst the low-latitude (blue) trace is centred on ~ 2.3 nPa. Therefore there was a $\sim 10\%$ increase in solar wind dynamic pressure from when the PSBL was located at low-latitude to when it was located at high-latitude. Similarly, in the 'winter' data the high-latitude trace is centred on ~ 2.05 nPa, whilst the low-latitude trace is centred on ~ 2.15 nPa. Therefore there was a $\sim 5\%$ increase in solar wind dynamic pressure from when the PSBL was located at low-latitude to when it was located at high-latitude. From these data it is clear that during both seasons the low-latitude PSBL entries occurred when the solar wind dynamic pressure was larger than during the high-latitude encounters. This suggests that an increase in the solar wind dynamic pressure reconfigures the magnetosphere such that the nightside plasma regions are shifted closer to the ecliptic plane. As with the previous section further data are required to confirm this statement, both from Polar and from other spacecraft.

4.10. Other Parameters

Parameters other than those described above were also tested for an effect on the PSBL location. These included the Kp magnetic index and the Polar Cap (PC) index. The variation of these indices produced no obvious effects on the location of the PSBL, and so the plots have not been included here.

The location of the plasma sheet boundary layer was investigated by Polar observations in April, May, and June.

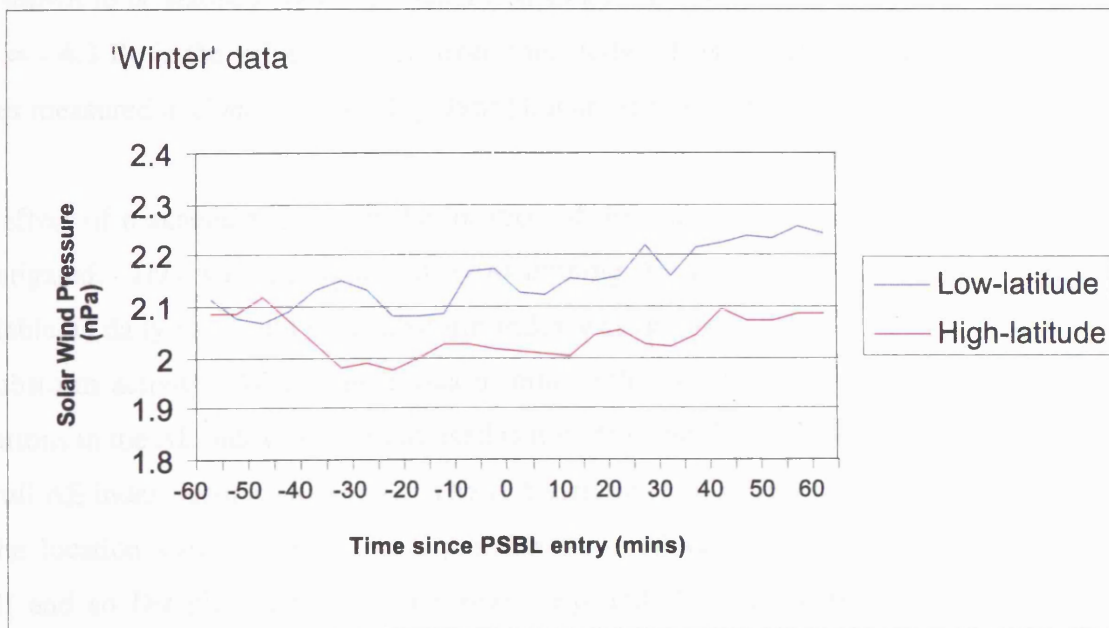
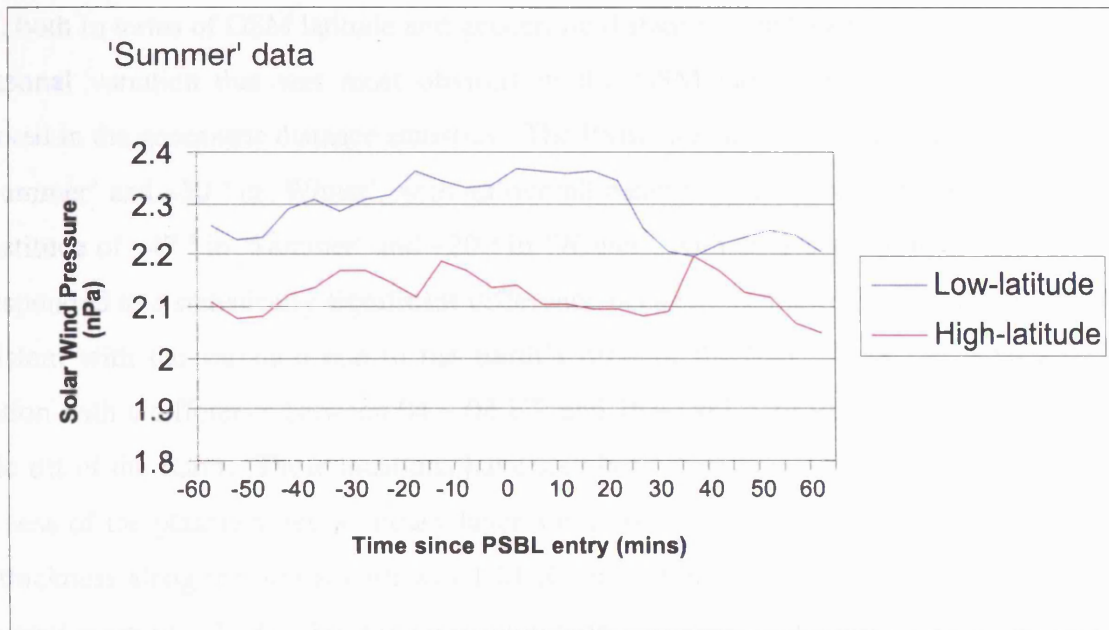


Figure 4.21: Superposed-Epoch analysis of solar wind dynamic pressure for one hour before and after PSBL entry time in two latitude bins for both seasons.

4.11. Summary

The location of the plasma sheet boundary layer and central plasma sheet have been investigated by Polar observations in April, May, October and November 1996, 1997 and 1998, both in terms of GSM latitude and geocentric distance. The location was found to have a seasonal variation that was most obvious in the GSM latitude statistics, but was also observed in the geocentric distance statistics. The PSBL was to be found at a latitude of $\sim 55^\circ$ in 'Summer' and $\sim 30^\circ$ in 'Winter', with an overall mean of $\sim 42^\circ$. The CPS was to be found at a latitude of $\sim 47^\circ$ in 'Summer' and $\sim 20^\circ$ in 'Winter', with an overall mean of $\sim 34^\circ$. This corresponded to a statistically significant difference between 'Summer' and 'Winter' of $\sim 25^\circ$, consistent with the variation due to the Earth's orbit of the Sun. There was also a daily variation with a difference between 04 – 08 UT and 16 – 20 UT of $\sim 11^\circ$, consistent with the dipole tilt of the Earth. These locations have also been used to derive the upper limit of the thickness of the plasma sheet boundary layer along the orbit path and in the Z_{GSM} direction. The thickness along the orbital path was $1.21 R_E$ in 'Summer' and $1.34 R_E$ in 'Winter', with an overall mean of $1.27 R_E$. The thickness along the Z_{GSM} direction was $1.17 R_E$ in 'Summer' and $1.27 R_E$ in 'Winter', with an overall mean of $1.22 R_E$. However, this seasonal variation was shown to be statistically insignificant and so a Z-component thickness of $1.22 \pm 0.81 R_E$ at $X = -4.3 R_E$ is the value obtained from this study. This value is slightly larger than the values measured in *Dandouras et al.* [1986b] but are still within the range given.

The effect of magnetic activity on the location of the plasma sheet boundary layer was then investigated. This was accomplished by examining AE and Dst. The AE index was only available as daily plots, and so a substorm index was devised by ascribing each event a level of substorm activity. Whilst there was a minor effect on the location statistics caused by variations in the AE index the method used is not ideal and the study should be repeated when the full AE index becomes available. The Dst variation was observed to induce a small effect on the location statistics, including a possible seasonal variation, but the correlations were small and so Dst plays only a minor role. K_p and PC indices were also examined but produced no discernible variations in the location statistics. It appeared that magnetic activity causes some small variations in the location of the plasma sheet boundary layer, but cannot explain the major variations.

Finally, solar wind control of the location statistics was investigated by examination of IMF B_z and dynamic pressure data from the Wind spacecraft. The data were separated into positive and negative IMF B_z and a significant variation was found. This variation was further investigated by performing a superposed-epoch analysis on the IMF B_z . It was found

that entries during periods of predominantly northward IMF occurred at lower latitudes than those during predominantly southward IMF. This was because dayside reconnection is at a maximum during southward IMF, and so the increased tail lobe pressure compresses the magnetotail, resulting in the plasma sheet boundary layer being located at lower latitudes. The final parameter examined was the solar wind dynamic pressure. Once again a superposed-epoch analysis was performed, and it was found that low-latitude PSBL entries occurred during slightly higher solar wind dynamic pressure than the high-latitude encounters.

The location of the plasma sheet boundary layer and central plasma sheet proved to be highly variable, with the main cause of this variation being the variation of the Earth's rotation axis relative to the Sun. Magnetic activity was found to have only a minor effect, but the orientation of the IMF and, to a lesser degree, the solar wind dynamic pressure also proved to be significant. Ideally this study would use data from all periods in the year, and so the full seasonal variation could be determined. Unfortunately, Polar is only able to perform such a study for a limited period each year due to orbital constraints. This is but one improvement that could be made to this study, another has already been mentioned, but even within these limitations this study has shown a significant orbital effect, and some solar wind control on the location of the plasma sheet boundary layer and central plasma sheet.

Chapter 5

Investigation of substorm-associated features in the plasma sheet observed by the Polar satellite: 9th April 1996 case study

5.1. Introduction

This chapter reports a case study of Polar observations of the plasma sheet (CPS and PSBL) during a period of substorm activity. The aim of this study is to develop an understanding of the plasma flows in this region and investigate their relationship with the various phases of substorm activity. The connection between the in-situ plasma flows and any auroral intensifications are also investigated. To identify potential intervals of interest, the times of Polar passes over the Scandinavian sector in the interval 18:00 – 02:00 UT were logged. Ground-based magnetometer data from the IMAGE and SAMNET arrays were then searched for evidence of substorm activity, e.g. Pi2 pulsations and enhanced electrojets (see Chapter 2). All geomagnetic events were noted and any possible substorm events were then verified by investigating the LANL data from the SOPA (Synchronous Orbit Plasma Analyser) instrument. These geosynchronous data were used to find evidence of dispersionless particle dropouts and/or injections (see Chapter 2). Therefore, a list of substorm events had been compiled, one of which was selected for this chapter.

5.2. The Interval – 9th April 1996

The interval under discussion ran from 19:30 – 22:00 UT on 9th April 1996 when the spacecraft was on an inbound pass through the nightside magnetosphere (Figure 5.1a). The orbital footprint (Figure 5.1b) was mapped into the ionosphere using the Tsyganenko 89 magnetic field model for the appropriate Kp values (2+ and 3-). Polar passed over Novaya Zemlya from 19:30 – 21:00 UT and then over Scandinavia after ~21:30 UT, at magnetic local times of ~00:45 MLT. Also presented in Figure 5.1b are the locations of selected magnetometer stations of IMAGE and SAMNET from which data are used in this study.

5.3. Observations

5.3.1. Ground Magnetometer Networks

As this is a substorm study, ground magnetic activity must be present during the interval. To determine the presence of substorm signatures ground magnetometer data from the IMAGE and SAMNET networks were examined for some of the many onset-associated signatures such as Pi2 pulsations and magnetic bays. The magnetometer stations cover a magnetic local time range of $MLT = UT$ to $MLT = UT + 2$ hours and are situated ~ 1 – 2 hours to the west of

(a) 96 100 APR 9 06:00:00.000 to 96 101 APR 10 00:00:00.000

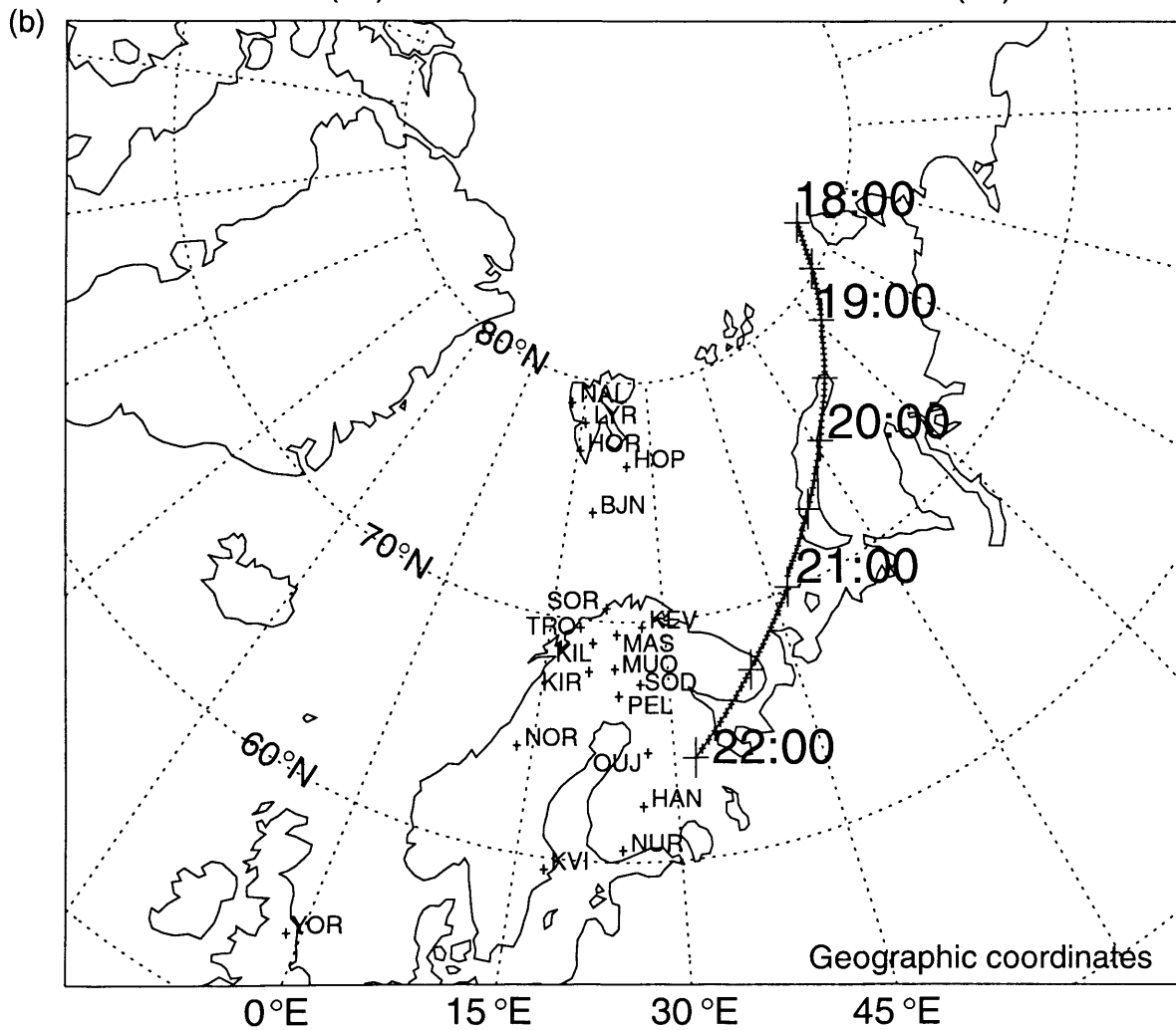
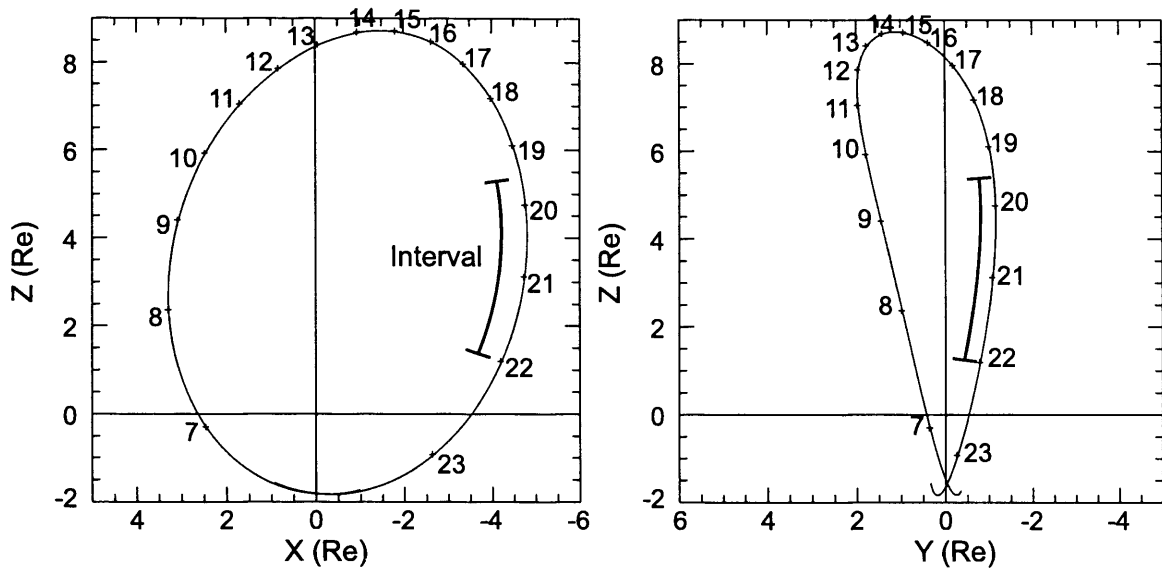


Figure 5.1: Polar's orbit during this interval. (a) The spacecraft orbit in both the X-Z and Y-Z GSM planes. (b) The spacecraft footprint mapped into the ionosphere using the Tsyganenko 89 model for the appropriate Kp values, with the location of the magnetometers used in this study also included.

the spacecraft footprint (Figure 5.1b). Although the interval runs from 19:30 – 22:00 UT the ground magnetometer data were examined from 18:15 UT to determine any activity that occurred earlier, thereby placing the spacecraft observations in context. The data are generally referred to in XYZ co-ordinates (geographic north, east and vertically down), whilst some data may be in HDZ co-ordinates (magnetic north, east and vertically down). Appendix 1 describes the co-ordinate systems in more detail. For ease of presentation, the magnetometer stations were separated into three groups; mid-latitude, auroral-latitude and high latitude. The mid-latitude stations spanned 50 – 65 °N, with the auroral-latitude stations comprising of the remaining mainland stations and the high-latitude stations comprising the Svalbard and Bear Island stations. Figure 5.2 presents mid-latitude X-component data that have been filtered with a bandpass of 20 – 200 seconds to show Pi2 pulsations. In this interval, Pi2 pulsations observed at the mid-latitude magnetometer stations have been marked with vertical red lines at the following times: 18:22, 18:38, 18:58, 19:17, 19:32, 19:44, 20:17 and 21:10 UT.

The mid-latitude data are also used to locate the substorm current wedge (SCW) as described in Chapter 2. In certain circumstances the SCW can be observed in the auroral latitude stations, but these stations are more commonly used to identify the location of the enhanced electrojets (also described in Chapter 2). The unfiltered high-latitude magnetometer data are used to identify any high-latitude features such as periods when the electrojet system has moved poleward and any other signatures that may occur in this region.

Figure 5.3 presents the unfiltered mid-latitude X-component data and Figure 5.4 presents the unfiltered mid-latitude Y-component data. At 18:22 UT there were weak, positive X-component deflections at mid-latitude, particularly at OIJ, with stronger positive deflections seen in the mid-latitude Y-component. These data suggest that OIJ was close to the longitude of the upward-directed FAC of the SCW. The auroral-latitude data are presented in Figures 5.5 (X-component) and 5.6 (Z-component) and the high-latitude data are presented in Figures 5.7 (X-component) and 5.8 (Z-component). These data show negative X-component deflections from SOR to KIR, and both positive and negative deflections in the Z-component, with the change from positive to negative occurring close to KIL (69.05 °N). These measurements suggest that an enhanced westward electrojet was centred at latitude of ~ 69 °N.

The next Pi2 pulsation occurred at 18:38 UT. The mid-latitude data (Figures 5.3 & 5.4) showed positive X-component deflections as far west as NOR, with OIJ at maximum and YOR experiencing very little deflection. The Y-component showed positive deflections, with

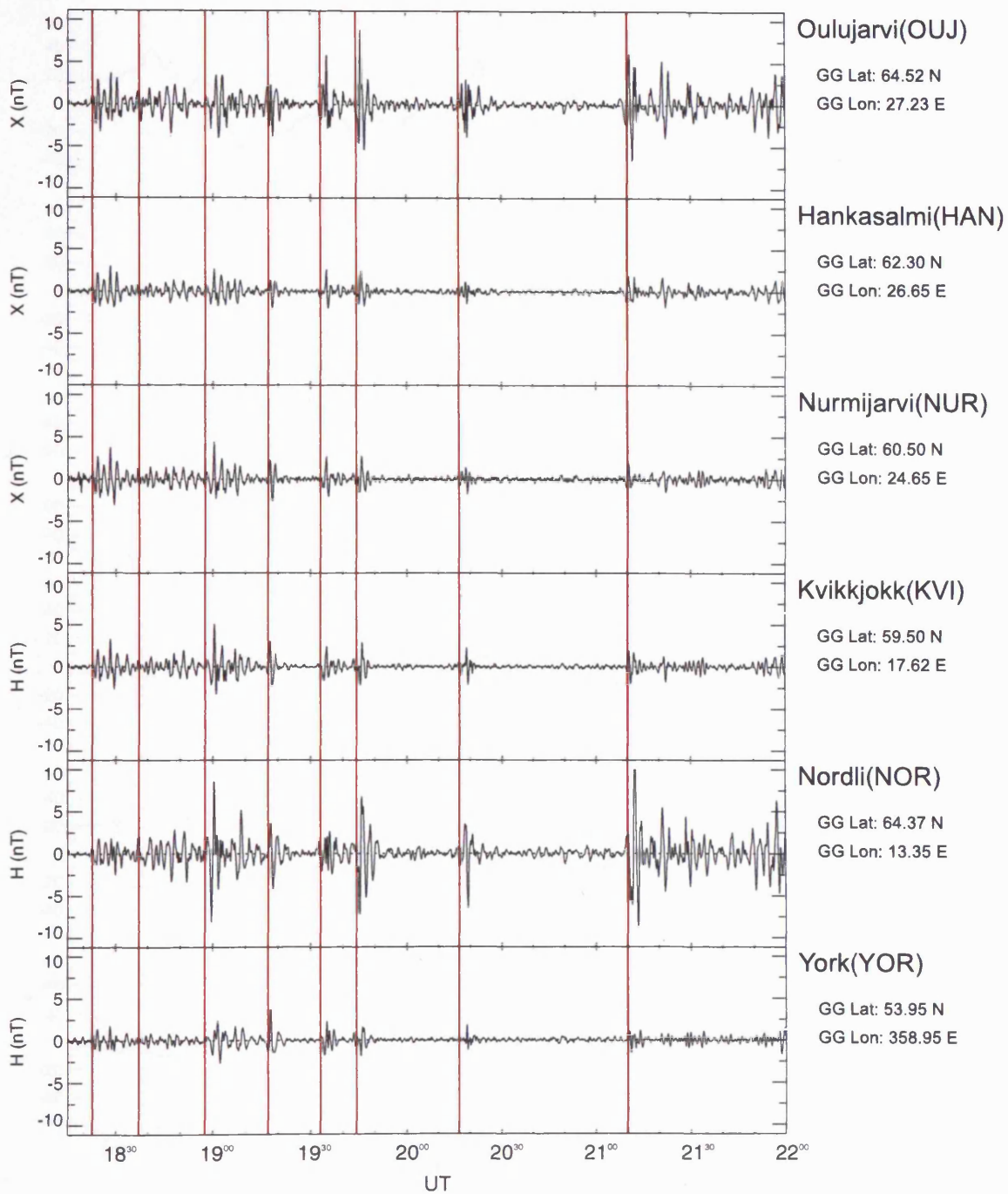


Figure 5.2: Filtered mid-latitude X/H component ground magnetometer data from 09/04/96.

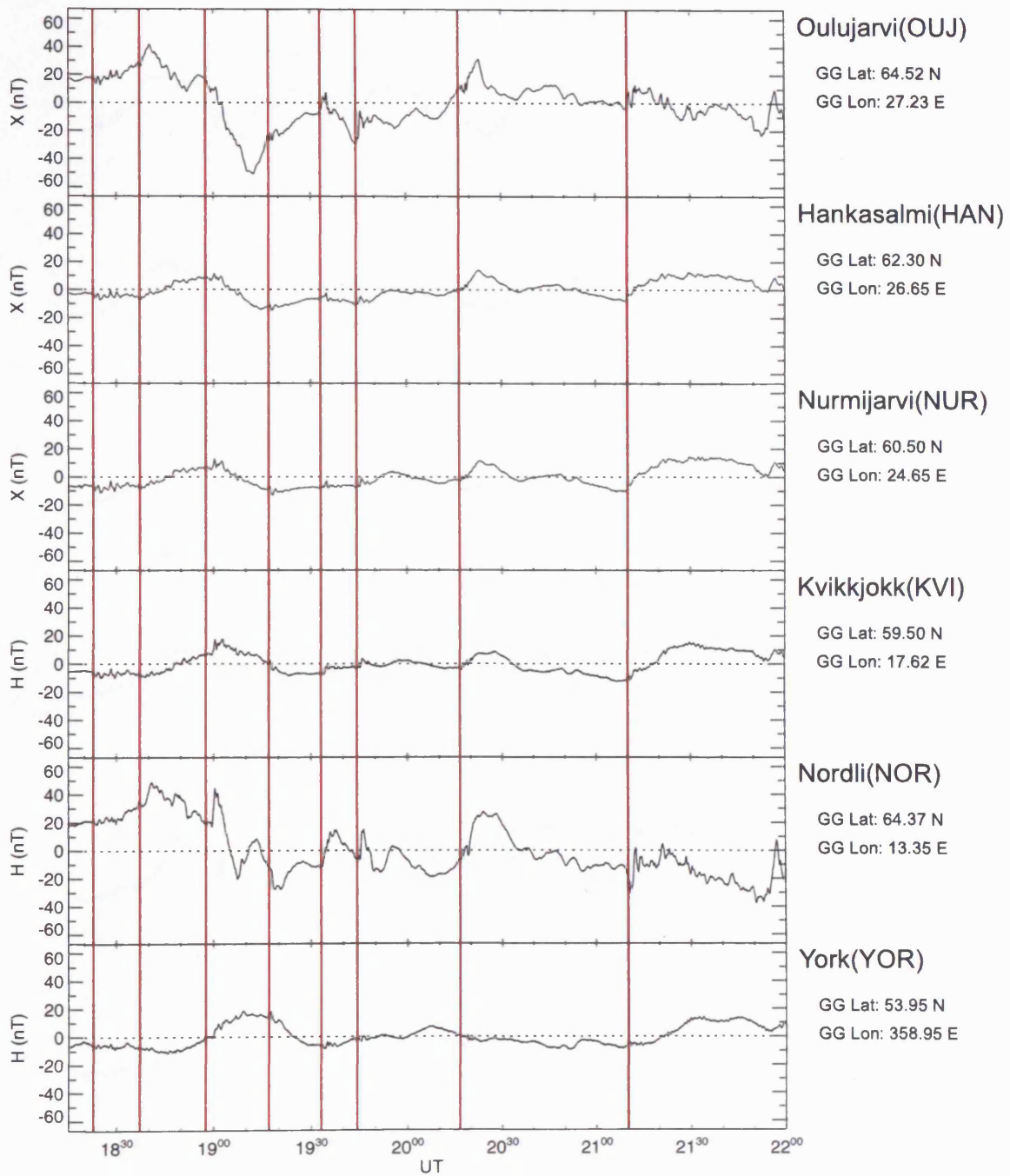


Figure 5.3: Mid-latitude X/H component ground magnetometer data from IMAGE and SAMNET on 09/04/96.

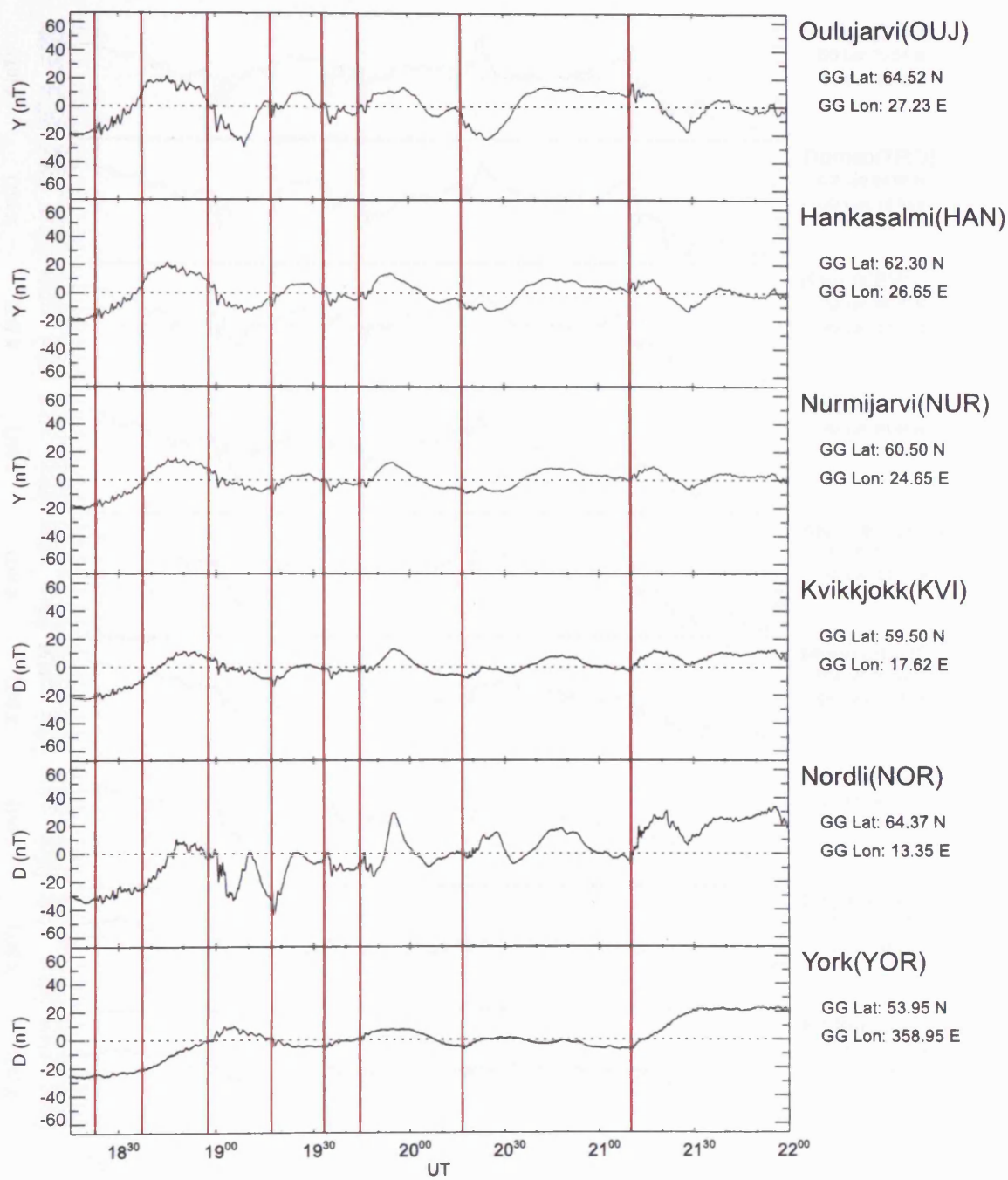


Figure 5.4: Mid-latitude Y/D component ground magnetometer data from IMAGE and SAMNET on 09/04/96.

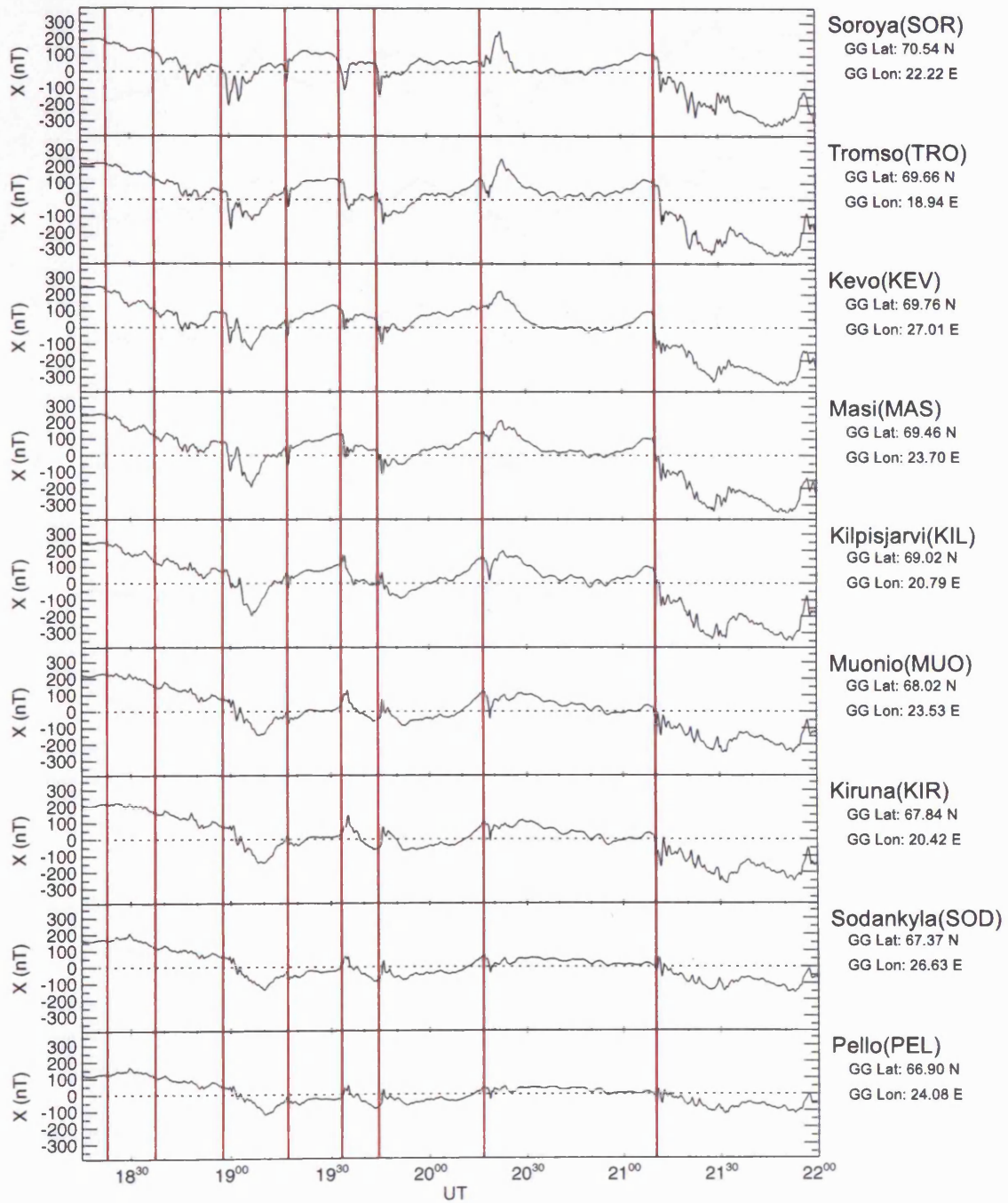


Figure 5.5: Auroral-latitude X component ground magnetometer data from IMAGE on 09/04/96.



Figure 5.6: Auroral-latitude Z component ground magnetometer data from IMAGE on 09/04/96.

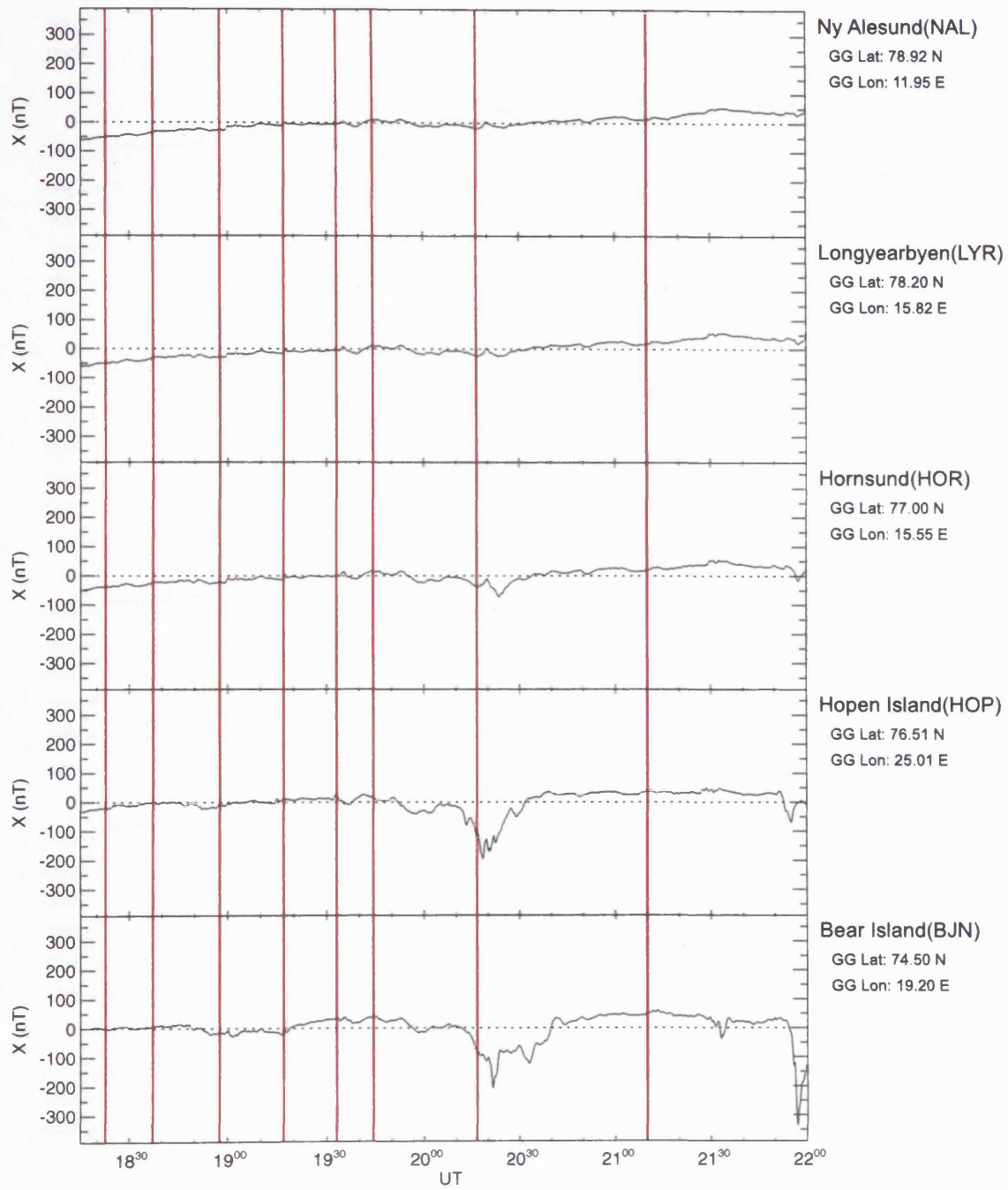


Figure 5.7: High-latitude X component ground magnetometer data from IMAGE on 09/04/96.

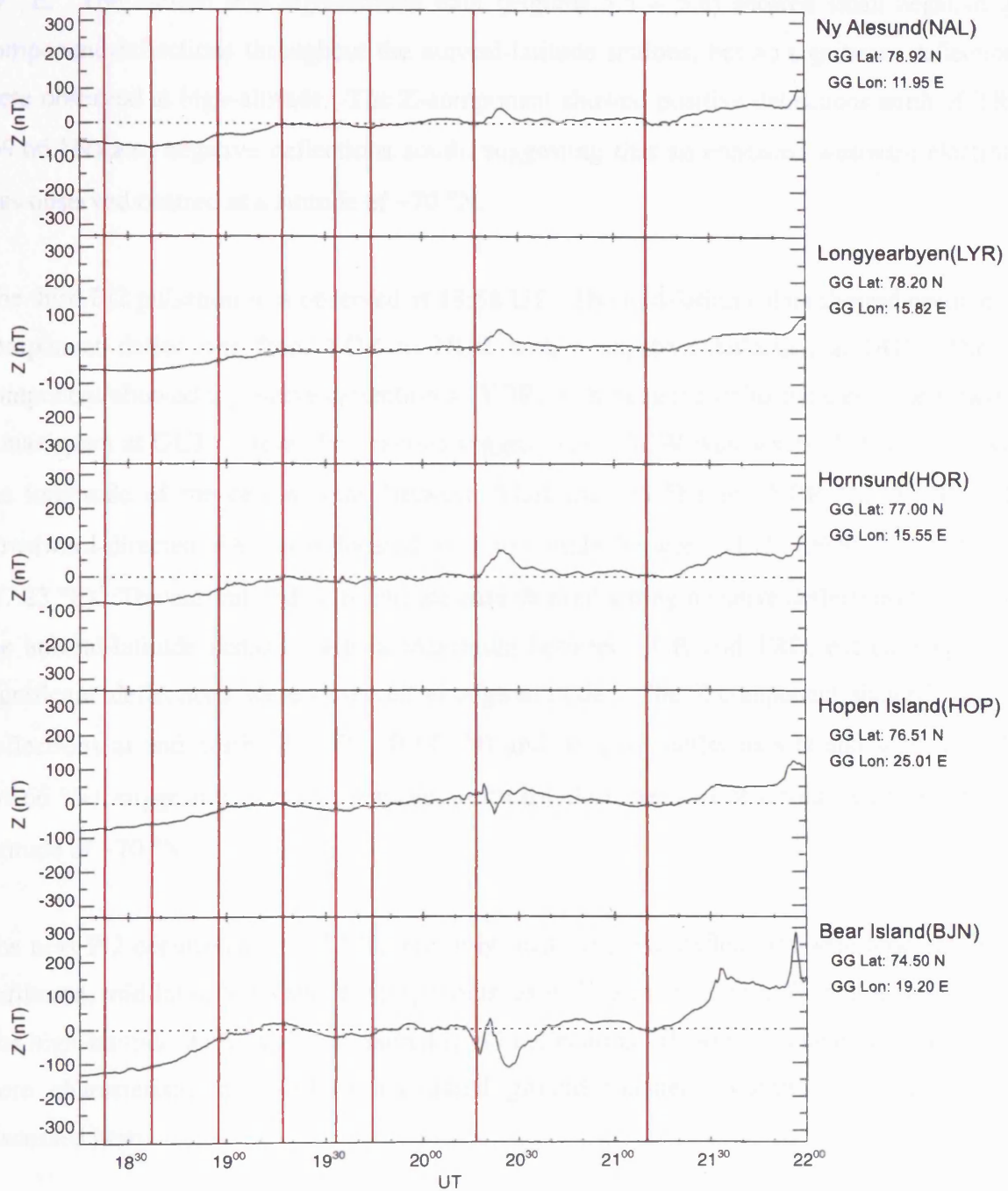


Figure 5.8: High-latitude Z component ground magnetometer data from IMAGE on 09/04/96.

a maximum noted between YOR and NOR and very little deflection at OUI. These observations suggest that a SCW was observed at this time that covered all the mid-latitude stations. The longitude of the centre of the SCW was close to OUI (27.23 °E), and YOR and NOR experienced the effects of the upward-directed FAC, which was located at a longitude of ~7 °E. The auroral and high-latitude data (Figures 5.5 – 5.8) showed small negative X-component deflections throughout the auroral-latitude stations, but no significant deflections were observed at high-altitude. The Z-component showed positive deflections north of TRO (69.66 °N) and negative deflections south, suggesting that an enhanced westward electrojet was observed centred at a latitude of ~70 °N.

The third Pi2 pulsation was observed at 18:58 UT. The mid-latitude data showed positive X-component deflections from YOR to NUR with a negative deflection at OUI. The Y-component showed a positive deflection at YOR, with negative deflections elsewhere having a maximum at OUI. These observations suggest that a SCW was observed at this time with the longitude of the centre being between YOR (358.95 °E) and NOR (13.35 °N). The downward-directed FAC was located at a longitude between HAN (26.65 °E) and OUI (27.23 °E). The auroral and high-latitude data showed strong negative deflections throughout the auroral-latitude stations, with a maximum between SOR and TRO, but once again no significant deflections were observed at high-altitude. The Z-component showed positive deflections at and north of SOR (70.54 °N) and negative deflections at and south of TRO (69.66 °N), suggesting that an enhanced westward electrojet was observed, again centred at a latitude of ~70 °N.

The next Pi2 occurred at 19:17 UT, but only small negative deflections were observed in the unfiltered, mid-latitude X- and Y-components, as well as in the auroral X- and Z-components. The high-latitude stations also measured small deflections. However, none of these variations were characteristic of substorm-associated ground magnetic variations and so are not discussed here.

At 19:32 UT another Pi2 pulsation was identified that did produce significant deflections. The mid-latitude data showed small positive X-component deflections and small positive Y-component deflections east of KVI (17.62 °E), and small negative Y-component deflections west of KVI. These data suggest that all the stations are within the longitudinal limits of the SCW, with the centre being close to the longitude of KVI at ~18 °E. The upward-directed FAC could be located close to the longitude of YOR and the downward-directed FAC could

be located close to the longitude of OIJ, but these are the most westerly and easterly stations, and so the FACs are not well determined. The auroral and high-latitude X-component data showed positive deflections at lower-latitude stations, then negative deflections at MAS (69.46 °N) and above, with a maximum negative deflection at SOR. The auroral and high-latitude Z-component data showed negative deflections becoming less strong towards high-latitude such that there is only a small negative deflection at SOR and very small positive deflections in the high-latitude stations. This suggests that an eastward electrojet was observed in the lower-latitude stations, with an enhanced westward electrojet seen north of MAS and centred at a latitude close to SOR.

The last Pi2 pulsation of this initial packet of wave activity occurred at 19:44 UT. The mid-latitude X-component magnetograms showed small positive deflections except at YOR where there is no deflection, with the Y-component showing positive deflections throughout. This indicated that all stations except YOR were inside the SCW, with the centre close to or east of OIJ (27.23 °E). The auroral and high-latitude stations observed very similar X-component deviations to those at 19:32 UT with positive deflections at the lower-latitude stations, then negative deflections at MAS and above, with a maximum negative deflection at SOR. However, at this time the Z-component data showed negative deflections at and south of TRO, and positive deflections at and north of SOR, placing the centre of the enhanced westward electrojet at a latitude of ~70 °N.

The extensive magnetic bays in Figures 5.3 – 5.8 indicated a series of auroral electrojets, initially centred near MAS (69.46 °N) at 18:22 UT. The electrojet activity then expanded polewards until the centre of activity was located in the region of SOR (70.54 °N) at 19:44 UT. However, at no time during the period did the electrojet move to latitudes of 74.5 °N (BJN). Therefore a period of substorm activity was observed, with the expansion phase onset occurring at 18:22 UT, with several further intensifications, and the activity decreasing after 19:44 UT.

The next significant electrojet signature during this interval began at 20:12 UT. In the high-latitude X-component data negative deflections were observed at HOR (77.00 °N), HOP (76.51 °N) and a large (~150 nT) negative deflection at BJN all of which began at this time. Also, some of the lower-latitude stations measured a small positive X-deflection at this time. The Z-component showed a small positive deflection at HOR, very little deviation at HOP and negative deflections elsewhere, placing the centre of the enhanced westward electrojet close to HOP. Shortly afterwards, a Pi2 pulsation was observed at 20:17 UT, when the X-component

underwent a further decrease at the high-latitude stations, but SOR observed a small positive deflection followed by another much larger positive deflection. The remaining stations observed a small negative deflection followed by a small positive deflection. In the auroral and high-latitude Z-component data there were small positive deflections observed at all stations. This electrojet activity had decayed at all stations by ~ 20:35 UT. The mid-latitude data showed positive X-component deflections at all stations except YOR, with the Y-component undergoing no significant deflection at YOR, a large positive deflection at NOR, smaller positive deflections at KVI and NUR, a small negative deflection at HAN and a large negative deflection at OUJ. These observations suggest that the mid-latitude stations observed a SCW, the centre of which was located at a longitude between HAN (26.65 °E) and NUR (24.65 °E). The downward-directed FAC was close to the longitude of OUJ (27.23 °E) and the upward-directed FAC was possibly between YOR (358.95 °E) and NOR (13.35 °E), although it is difficult to be certain as YOR is at much lower latitudes than the other stations.

At 21:10 UT, a Pi2 pulsation was observed at mid-latitude. The mid-latitude magnetograms experienced small positive X-component deflections at this time. All mid-latitude stations west of HAN observed positive Y-component deflections and all stations east of HAN observed negative deflections, whilst HAN itself did not observe any significant deviations. Therefore a SCW was detected at mid-latitude centred at a longitude close to that of HAN (26.65 °E). NOR experienced that maximum positive Y-deflection and so the upward-directed FAC was located close to this station at a longitude of ~13 °E. OUJ was closest to the downward-directed FAC, but did not undergo a large deflection suggesting that the FAC was still some distance away. The auroral and high-latitude magnetograms underwent large negative deflections in the X-component from MUO (68.02 °N) to KEV (69.76 °N), with maximum deviation at KEV. TRO (69.66 °N) and SOR did not observe this deflection until 21:11 UT, suggesting a poleward propagation of the current. The Z-component data showed a change in sign of deflections also at KEV. These data place the enhanced electrojet centred close to KEV, at latitude ~ 70 °N.

There are further signatures of ground magnetic activity, but these are not relevant to this study, which is concerned mainly with substorm activity whilst Polar is located in or close to the plasma sheet. Therefore it is shown later that the last relevant packet of magnetic activity occurred at 21:10 UT.

5.3.2. LANL Geosynchronous spacecraft

The next data set to be examined show the LANL geosynchronous spacecraft (Chapter 3) particle fluxes. Unfortunately one of the spacecraft, 1990-095, was unable to collect any proton data throughout the interval. Due to the position of the spacecraft (Figure 5.9) this is a problem, as this is the only spacecraft consistently in the dusk sector where any dispersed proton injections would be seen (due to gradient curvature drift – see Chapter 2). The remaining two spacecraft are ideally situated to observe any electron flux variations as they span the post-midnight sector. The electron flux data for all three spacecraft are presented in Figure 5.10, with the proton data for 1991-080 and 1994-084 in Figure 5.11. The vertical red lines indicate when the Pi2 pulsations were observed by the ground magnetometers. The LANL data shows a series of injections and flux dropouts that are summarised in Table 5.1. The position of the injection region is determined by the amount of dispersion apparent in the injections, which translates to a distance from the spacecraft as mentioned in Chapter 2.

Pi2 (UT)	1991-080	1994-084	Position of injection region
18:22	Electron and proton injections.	Electron flux dropout and injections seen.	Close to 1991-080
18:38	Faint electron injection.	Strong near-dispersionless electron injection.	Close to 1994-084
18:58	Dispersed electron injection.	Dispersed electron injection.	Pre-midnight sector
19:17	None.	None.	N/A
19:32	None.	None.	N/A
19:44	Dispersed electron injection.	Dispersed electron injection.	Pre-midnight sector
20:17	Very small trace of possible electron injection.	Small flux dropout followed by dispersed injection.	Unknown
21:10	Electron flux dropout at 21:09, followed by small dispersionless injection.	Dispersed electron injection at 21:12.	Close to 1991-080

Table 5.1: Summary of LANL geosynchronous particle flux data.

5.3.3. Polar Ultra-Violet Imager (UVI)

LBHL images from the Polar Ultra-Violet Imager (UVI) are used to relate the global auroral disturbances associated with the substorm activity with the in-situ features observed by the spacecraft. In order to relate directly the in-situ and remotely sensed observations, the spacecraft footprint was mapped down to the ionosphere as described in section 5.2 and

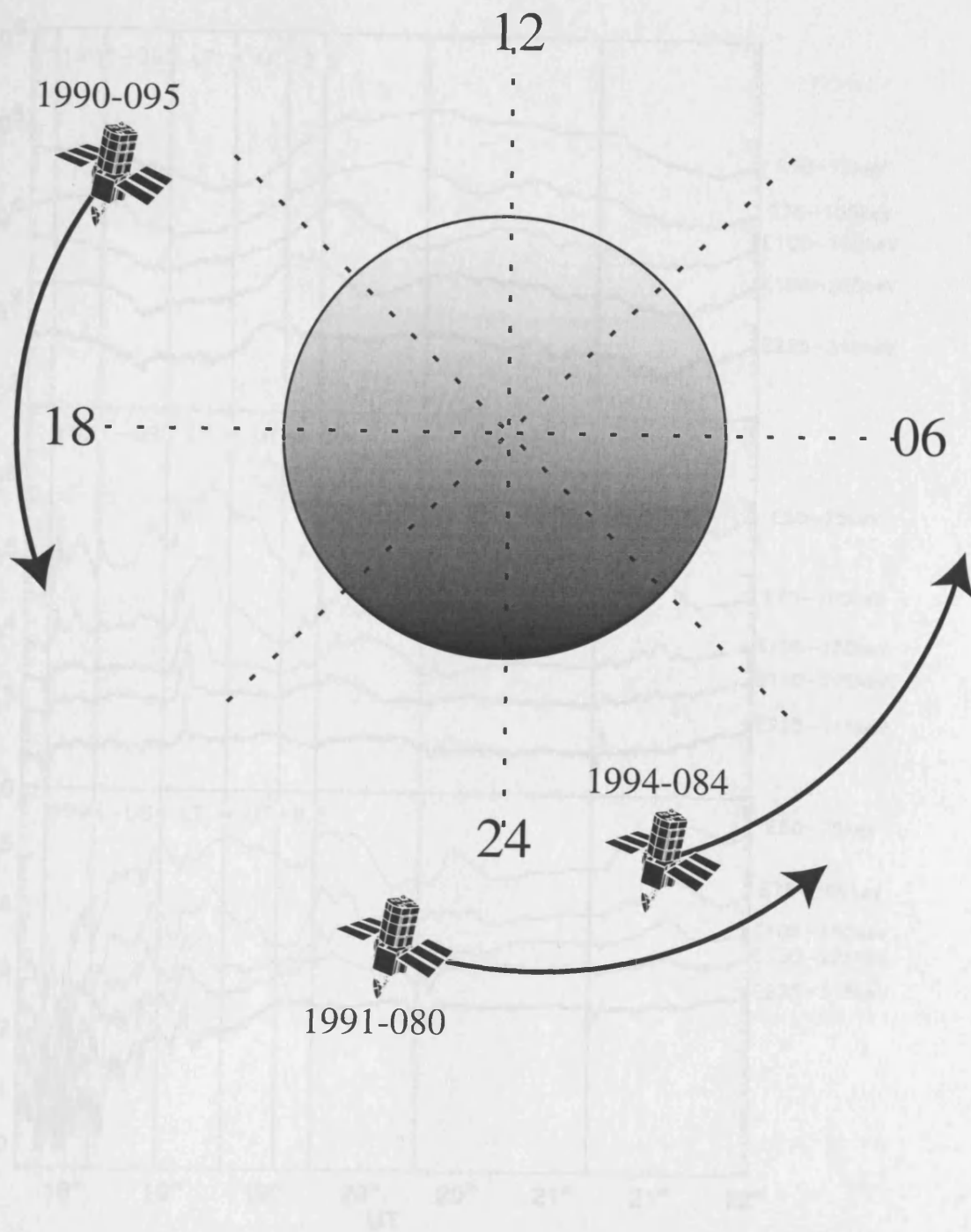


Figure 5.9: Schematic to show the approximate MLT location of the LANL spacecraft during this interval (18:15 - 22:00 UT).

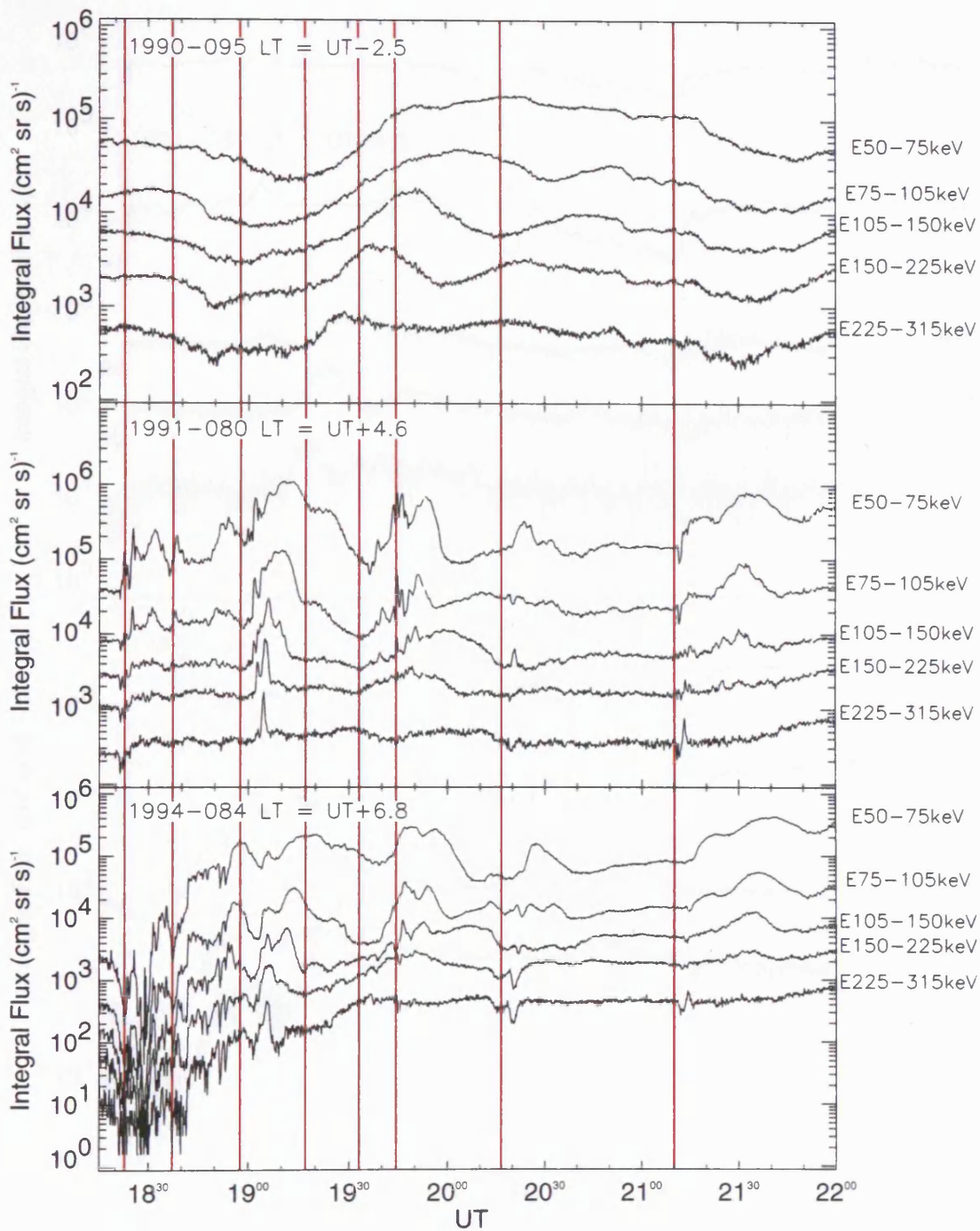


Figure 5.10: Geosynchronous electron flux data for the three LANL spacecraft in various energy channels.

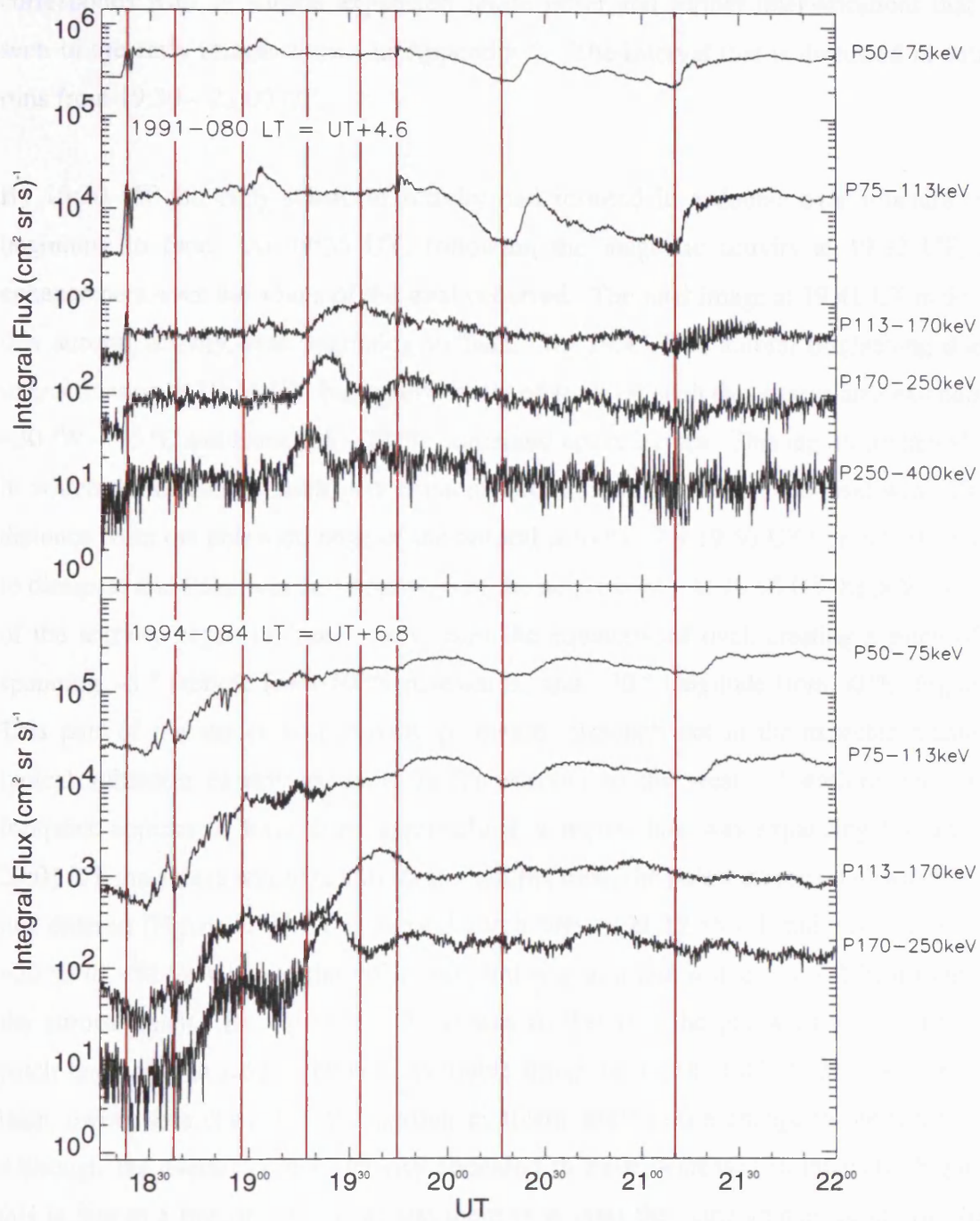


Figure 5.11: Geosynchronous proton flux data for the LANL spacecraft 1991-080 and 1994-084 in various energy channels.

plotted on the UVI images as a black and white cross. The UVI images from this interval can be found in Appendix 2, with certain relevant images included in the chapter itself. At the start of this interval Polar was over the polar cap (see orbit plot – Figure 5.1a), and so in a good position for auroral imaging. The early magnetic activity shown in the previous section corresponds with an auroral expansion phase onset and further intensifications that can be seen in the early images shown in Appendix 2. The interval that is discussed in detail here runs from 19:30 – 22:00 UT.

By 19:30 UT the early substorm activity had resulted in a double oval structure that was beginning to fade. At 19:35 UT, following the magnetic activity at 19:32 UT, another enhancement over the whole of the oval occurred. The next image at 19:41 UT indicates that this auroral activity, was beginning to fade. By 19:45 UT, auroral brightening due to the intensification at 19:44 UT, had again enhanced the oval such that a large area extending from $\sim 30^\circ\text{W} - 75^\circ\text{E}$ and from $\sim 65 - 73^\circ\text{N}$ contained active aurora. This region contained the area in which the enhanced electrojets existed. At this time, the Polar footprint was still a short distance from the poleward edge of the auroral activity. By 19:50 UT this activity had begun to dissipate and Polar was still poleward of the active oval. At 19:55 UT the poleward portion of the activity began to ‘peel’ away from the equatorward oval, creating a patch of aurora spanning $\sim 5^\circ$ latitude from 70°N polewards, and $\sim 30^\circ$ longitude from 30°E (Figure 5.12). This part of the aurora was moving poleward, although not in the expected manner for a typical substorm expansion, such as the activity to the west. Therefore, the spacecraft footprint appears to have been approaching a region that was expanding towards it. By 20:01 UT the aurora had begun to form a double oval, the poleward region of which Polar had just entered (Figure 5.13). The auroral patch present at 19:55 UT had now moved to cover $\sim 20^\circ\text{E}$ to $\sim 50^\circ\text{E}$, whereas the Polar footprint was in a less active area ~ 1 hour to the east of the auroral patch. By 20:06 UT, Polar was further into the poleward arc, with the auroral patch beginning to fade. The next available image occurred at 20:16 UT, about ten minutes later, owing to a change in the despun platform angle and a change in the filter sequence. Although the overall auroral activity appeared to have decreased in intensity (Figure 5.14), this is due to a line-of-sight error and there is at least the same amount of activity (personal communication, M. Brittner, 1999). By this time, the spacecraft footprint had entered the gap between the poleward and equatorward arcs in the double oval. Therefore, the spacecraft mapped to a relatively quiet region of the aurora. This remained the case in the next image (20:23 UT), but there was a major enhancement duskward of the spacecraft footprint, which covered a large area spanning $\sim 10^\circ$ latitude and $\sim 45^\circ$ longitude between Norway and Svalbard. This enhancement followed the fluctuations in the ground magnetic field at high

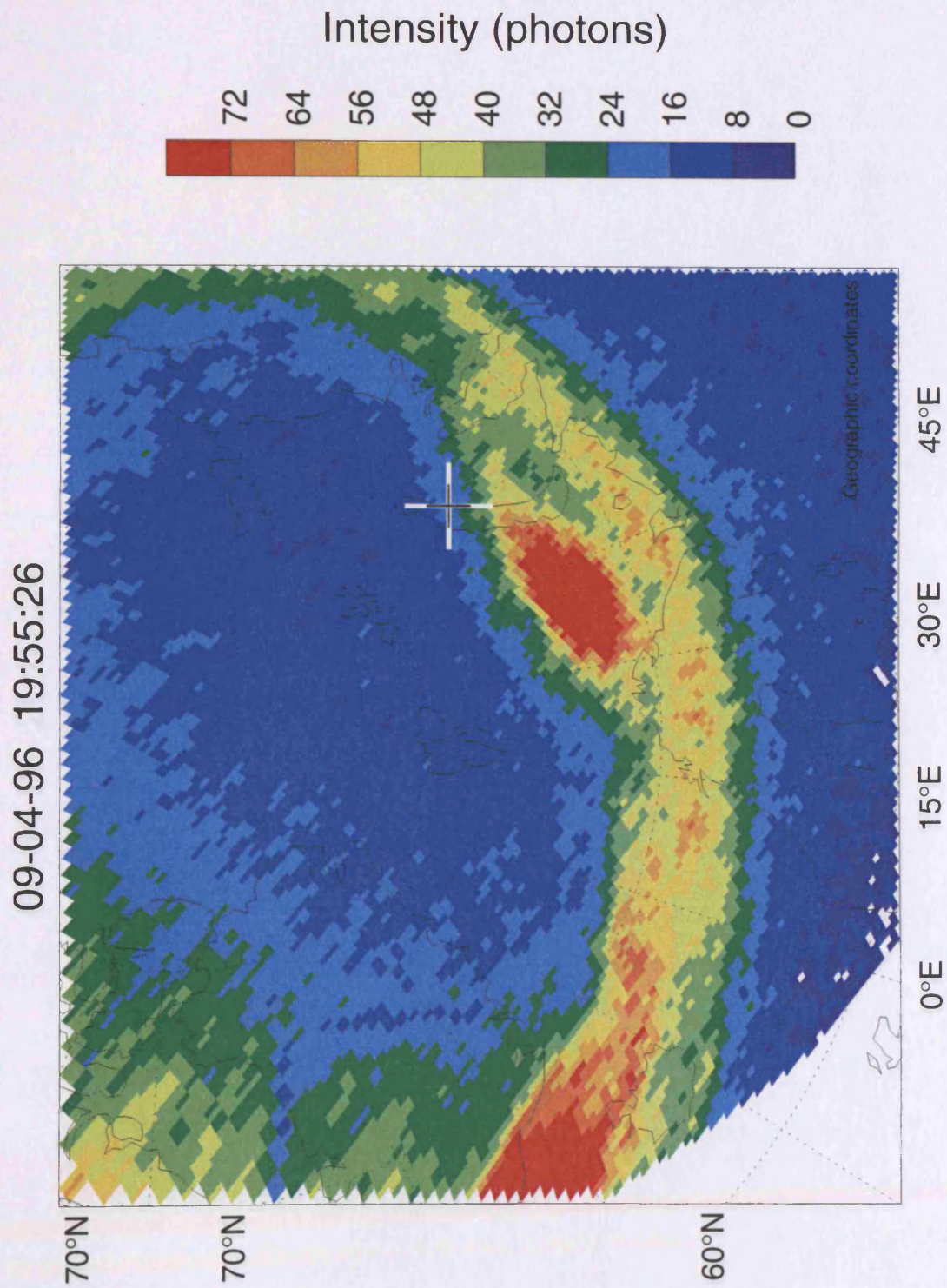


Figure 5.12: Polar UVI image taken on 9th April 1996 at 19:55 UT. Polar's footprint is indicated by the black and white cross.

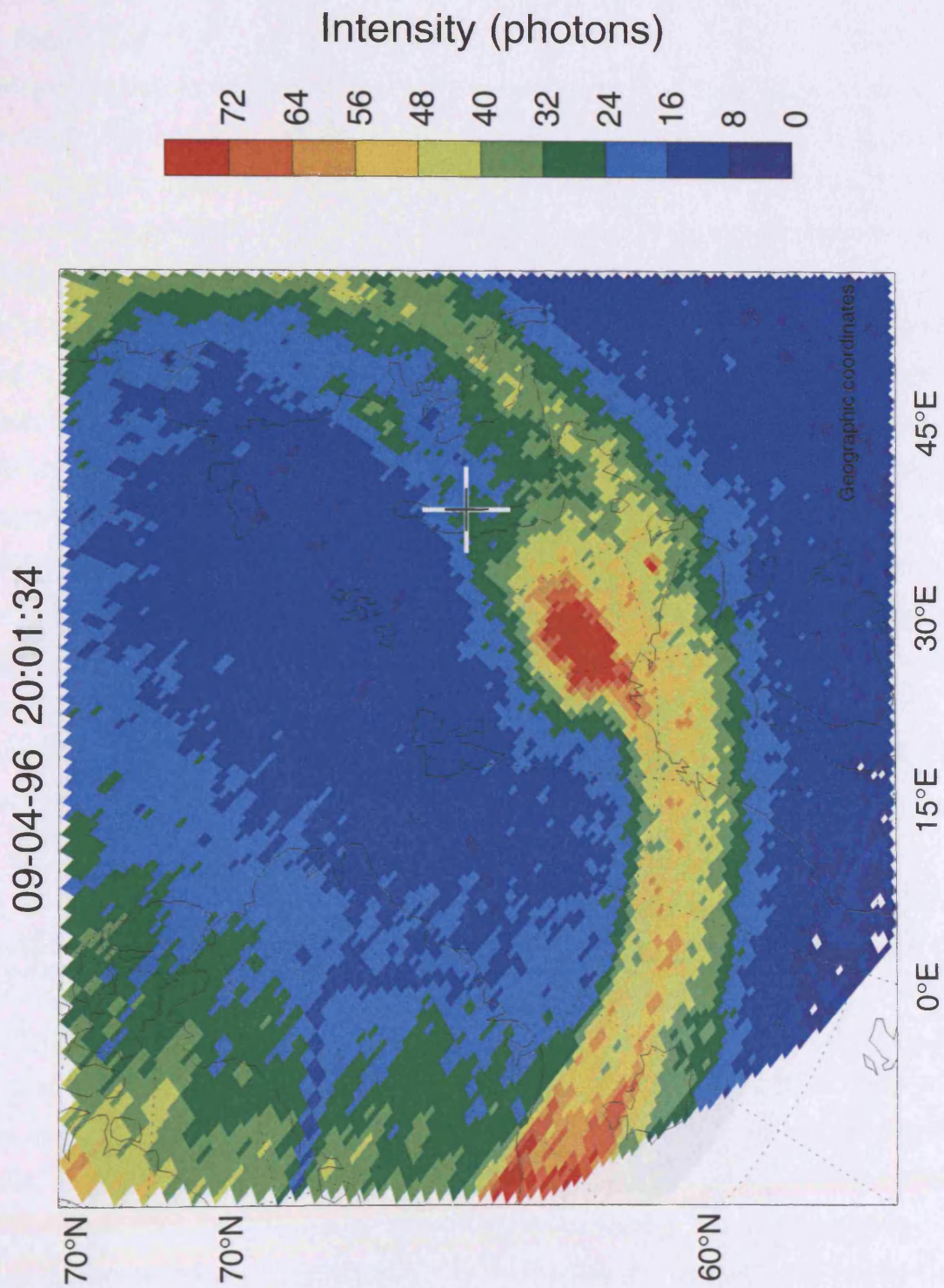


Figure 5.13: Polar UVI image taken on 9th April 1996 at 20:01 UT. Polar's footprint is indicated by the black and white cross.

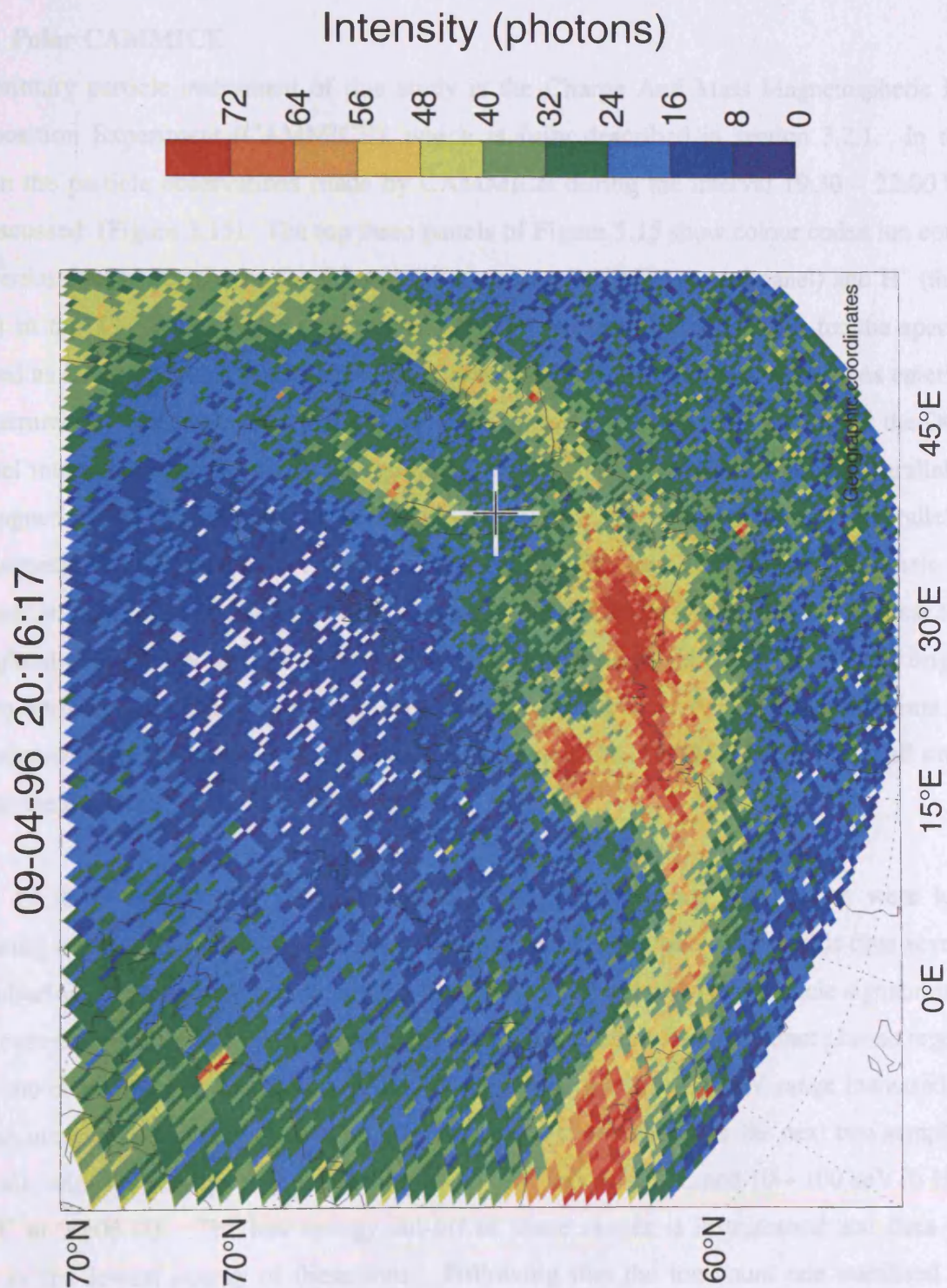


Figure 5.14: Polar UVI image taken on 9th April 1996 at 20:16 UT. Polar's footprint is indicated by the black and white cross.

and auroral latitudes, and the Pi2 pulsation observed at mid-latitude at 20:17 UT. By the final image at 20:36 UT the intensification had almost dissipated. Unfortunately this marks the end of the images as the instrument was then shielded before the spacecraft entered the Radiation Belts.

5.3.4. Polar CAMMICE

The primary particle instrument of this study is the Charge And Mass Magnetospheric Ion Composition Experiment (CAMMICE), which is fully described in section 3.2.1. In this section the particle observations made by CAMMICE during the interval 19:30 – 22:00 UT are discussed (Figure 5.15). The top three panels of Figure 5.15 show colour coded ion count rate versus energy per charge for O^+ and O^{++} (top panel), He^{++} (second panel) and H^+ (third panel) in the 1 – 240 keV/e energy range. Panel 4 presents the same data for the species labelled as DCR (Double Coincidence Rate), which effectively measures all the ions entering the instrument (see Chapter 3). The bottom panel shows pitch angle information for the DCR channel integrated over the whole energy range, with 0° representing the direction parallel to the magnetic field, termed field-aligned in this thesis, and the 180° direction is anti-parallel to the magnetic field, termed field-opposed in this thesis. The ions shown in the top panels are representative of both ionospheric ($O^{+/++}$) and solar wind sources (He^{++}), and so it is clear that throughout this interval there were fewer ions of ionospheric origin than of solar wind origin, but the dominant ion is H^+ , which can originate at either source. As the integration time for each scan is relatively long (197.5 s), in the discussion of the CAMMICE data below all times refer to the start time of the integration period.

From 19:30 until 19:58 UT particle counts in all energy bands and species were low, indicating that the spacecraft was on open field lines in the tail lobe. During this time several Pi2 pulsations were observed, indicating substorm activity, but no in-situ particle signatures of these events were detected. At 19:58 UT the spacecraft entered a new, distinct plasma regime when the count rates in the DCR and He^{++} channels in the 20 – 50 keV range increased by over an order of magnitude. The count rate continued to increase over the next two sampling intervals, with the energy range expanding to 1 – 100 keV in DCR, and 10 – 100 keV in He^{++} and H^+ at 20:06 UT. The low energy cut-off of these ranges is instrumental and does not relate to the lowest energy of these ions. Following this the ion count rate stabilised for another three sampling intervals before decreasing to a level that was still much higher than the tail lobe, which had been observed before 19:58 UT. This lower count rate lasted only two sampling intervals before, at 20:25 UT, the ion count rate began to increase again, whilst remaining at a level much reduced from the initial PSBL encounter. At 21:08 UT there was a

significant increase in the DCR, H⁺ and He⁺⁺ count rates in the energy range 10 - 50 keV. At 21:11 UT, there was a much larger intensification in all the ion species presented in Figure 5.15.

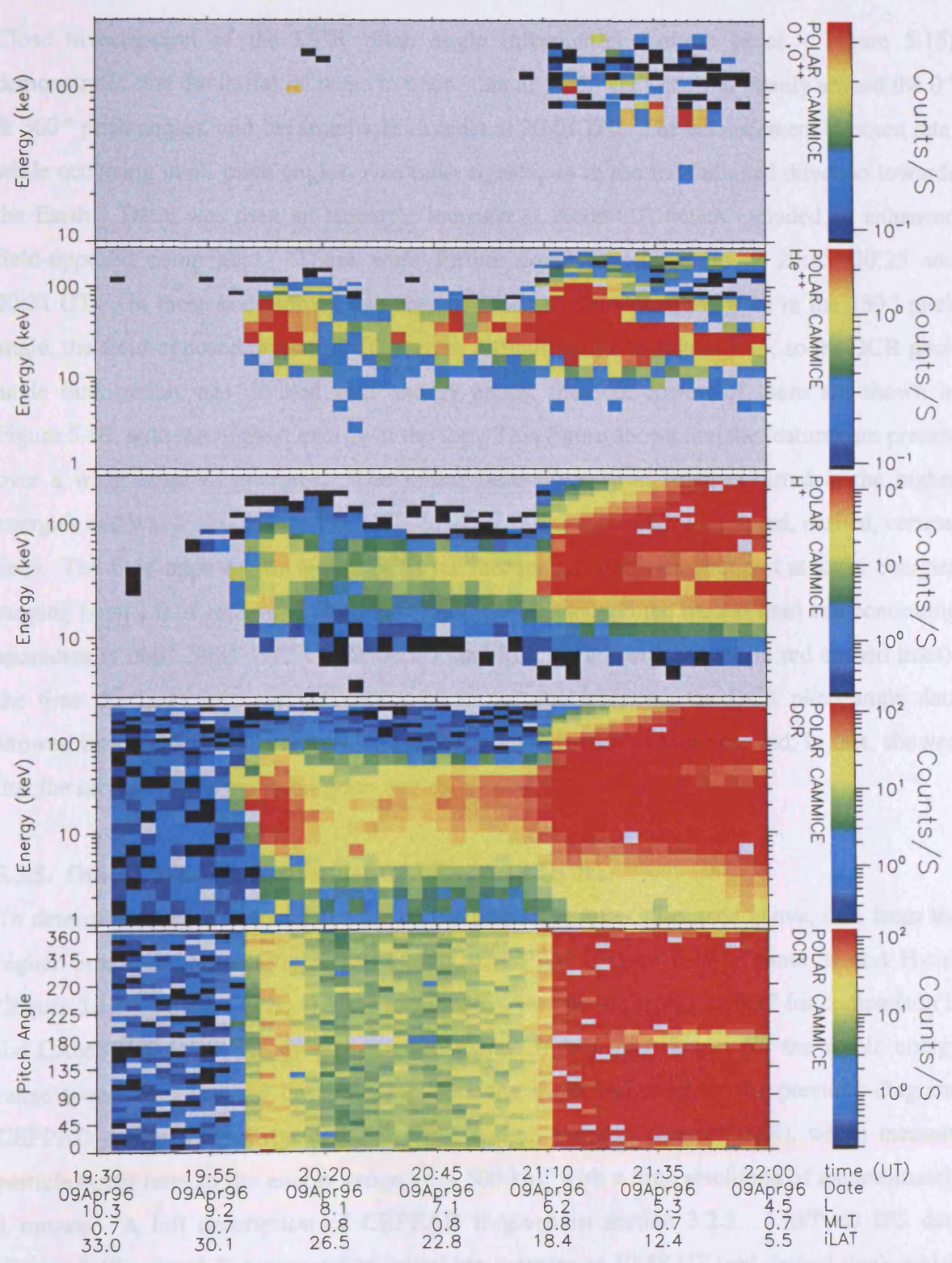


Figure 5.15: A CAMMICE plot of five panels. The top three panels show colour-coded ion counts versus energy per charge from 1 - 240 keV/Q for the various species labelled. The bottom two panels show energy per charge and pitch angle data for DCR.

significant increase in the DCR, H^+ and He^{++} count rates in the energy range 10 – 50 keV. At 21:11 UT, there was a much larger intensification in all the ion species presented in Figure 5.15.

Close investigation of the DCR pitch angle information (bottom panel – Figure 5.15) demonstrates that the initial increase in count rate at 19:58 UT occurred mainly around the 0° & 360° pitch angles, and became more distinct at 20:01 UT. The enhancement in count rate, while occurring in all pitch angles, was most significant in the field-aligned direction towards the Earth. There was then an isotropic increase at 20:06 UT, which included an enhanced field-opposed component. There were further count rate increases at 20:15, 20:25 and 20:31 UT. On these occasions, however, the plasma intensifications were in the 180° pitch angle, the field-opposed direction. These are difficult to see in Figure 5.15, so the DCR pitch angle distribution was divided into energy bands, the four lowest of these are shown in Figure 5.16, with the highest energy at the top. This figure shows that the features are present over a wide range of energies. The initial field-aligned ion beam occurred at the higher energies and was most clear in the 13.2 – 31 keV range at 19:58 UT (first red, dashed, vertical line). The field-opposed ion beams occurred throughout, but were strongest at lower energies ranging from 1.0 to 13.2 keV, beginning at 20:06 UT (second red dashed line) and continuing sporadically until 20:31 UT. At 21:08 UT and 21:11 UT (third and fourth red dashed lines), the time the large increase was observed in the spectrograms, the DCR pitch angle data showed little evidence of field-aligned or opposed count rate variations, and, in fact, showed that the increase occurred in all pitch angles.

5.3.5. Other Particle instruments: CEPPAD and Hydra

To determine a more accurate timing of the plasma features discussed above, data from the higher time-resolution particle instruments, CEPPAD (Figure 5.17 – panel 3) and Hydra (Figure 5.17 – panels 1, 2 & 4) were examined. Also shown in Figure 5.17 for comparison is the CAMMICE DCR energy spectrogram (panel 5) and pitch angles for the whole energy range (panel 6). The red dashed lines mark the times indicated on the previous diagram. CEPPAD consists of an ion detector (IPS) and an electron detector (IES), which measure particle count rates in the energy range 20 – 500 keV with a time resolution of approximately 1 minute. A full description of CEPPAD is given in section 3.2.3. CEPPAD IPS data (Figure 5.17 – panel 3) measured an initial ion increase at 19:58 UT (red dashed line), which was followed by a further increase in both the count rate and average energy of the ions at 20:03 UT, approximately the same time as the Earthward ion beam. A subsequent increase in counts in the 20 – 50 keV energy range occurred at 20:06 UT, the same time as the isotropic

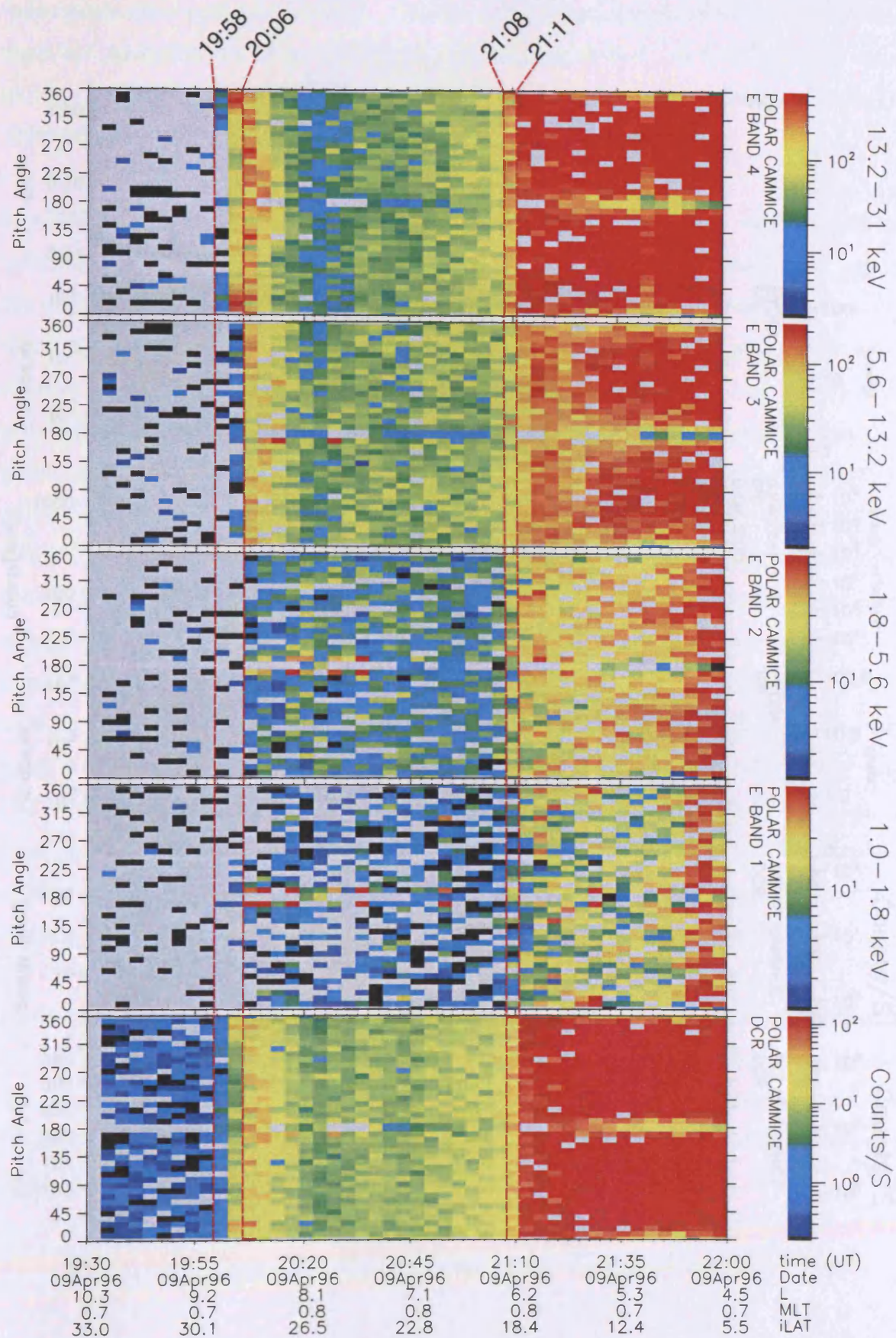


Figure 5.16: Data from CAMMICE DCR channel. The panels are CAMMICE DCR pitch angle data split into a series of energy bands to distinguish the field-aligned and field-opposed ion beams. The red lines indicate features identified in the text.

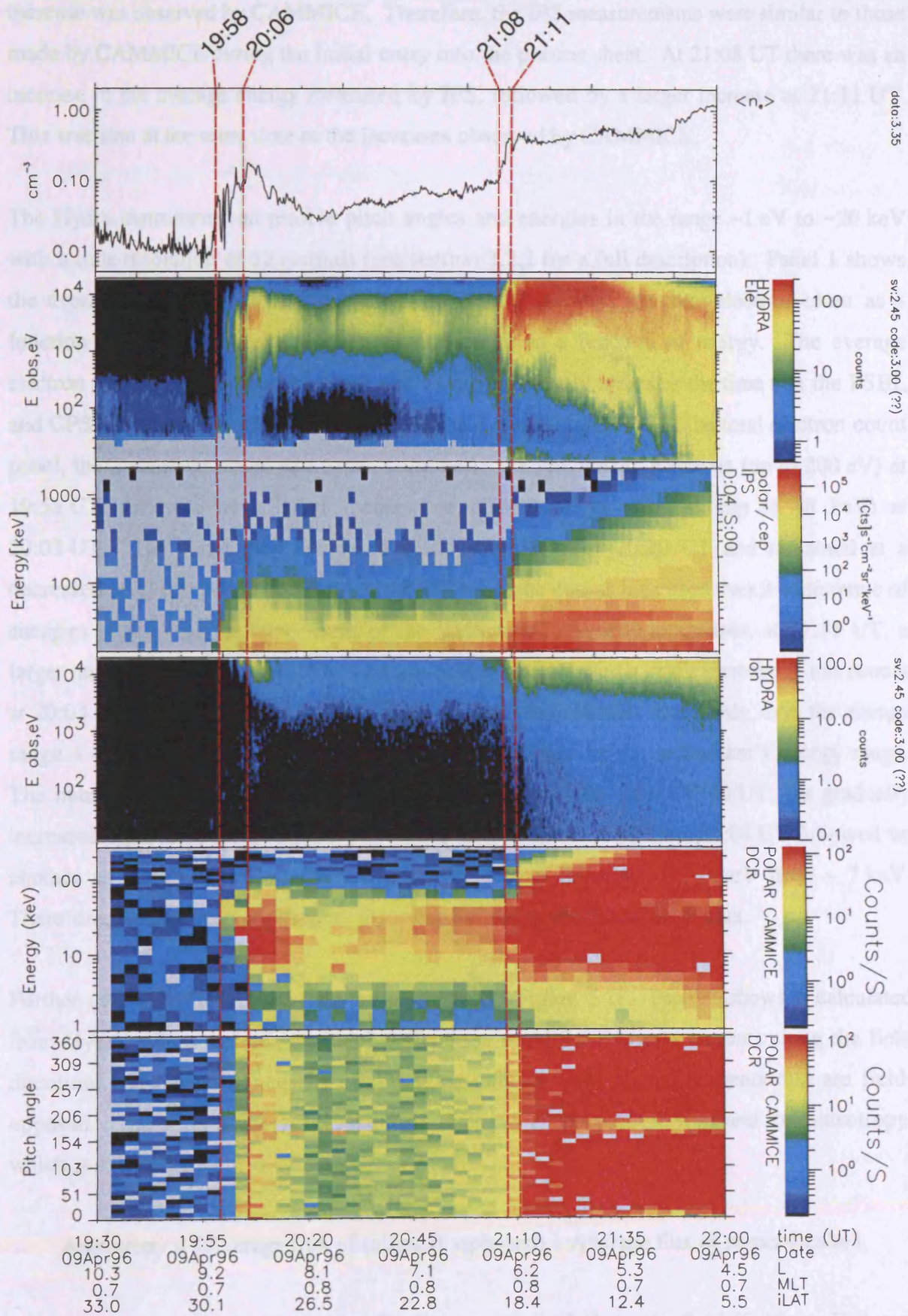


Figure 5.17: Data from each of the particle instruments used in this study. The top panel shows average electron number density data from Hydra. The second and fourth panels show electron and ion spectrograms also from Hydra. CEPPAD IPS data are shown in the third. The bottom two panels are DCR plots from CAMMICE as before.

increase was observed by CAMMICE. Therefore, the IPS measurements were similar to those made by CAMMICE during the initial entry into the plasma sheet. At 21:08 UT there was an increase in the average energy measured by IPS, followed by a larger increase at 21:11 UT. This was also at the same time as the increases observed by CAMMICE.

The Hydra instrument can resolve pitch angles and energies in the range ~ 1 eV to ~ 20 keV with a time resolution of 12 seconds (see section 3.2.2 for a full description). Panel 1 shows the average electron number density, whilst panel 2 presents the total electron count as a function of energy and panel 4 the total ion count as a function of energy. The average electron number density has been included as it most clearly indicates the time that the PSBL and CPS are entered via the increase in this value (see Chapter 4). In the total electron count panel, the instrument observed a small increase in the low energy electrons (up to 200 eV) at 19:58 UT, followed by a larger increase of higher energy electrons (up to 10 keV) at 20:03 UT. The count then decreased at all energies after 20:20 UT and remained at a decreased level from 20:20 UT until 21:08 UT when the counts increased over a wide range of energies (100 eV to the upper limit of the instrument). Shortly afterwards, at 21:11 UT, a larger increase was observed. The total ion counts also showed a small increase in ion counts at 20:03 UT. This was eclipsed by a larger increase immediately afterwards, over the energy range 4 – 20 keV, the upper limit of which was imposed by the instrument's energy range. The number of ions then decreased to significantly lower levels by 20:20 UT, but gradually increased once more from $\sim 20:30$ UT. There was an increase again at 21:08 UT followed by another at 21:11 UT. Here, the lower energy cut-off decreased to ~ 2 keV from ~ 7 keV. Therefore, Hydra observations were also very similar to the CAMMICE data.

Further analysis of the Hydra data are presented in Figure 5.18. Panel 1 shows J_{\parallel} calculated from Hydra, where the red (positive) deflections show field aligned currents along the field direction, and the blue (negative) deflections indicate field aligned currents that are field-opposed. The second and fifth panels of Figure 5.18 present electron and ion anisotropy, which is calculated as:

$$\text{Anisotropy} = \{ \text{Average flux of (aligned, opposed)} - \text{Average flux of perpendicular} \}$$

In these panels yellow/red indicates distributions peaked along the field (field parallel) and blue/purple indicates distributions peaked perpendicular to the field (field perpendicular). The third and sixth panels Figure 5.18 present electron and ion skew, which is calculated as:

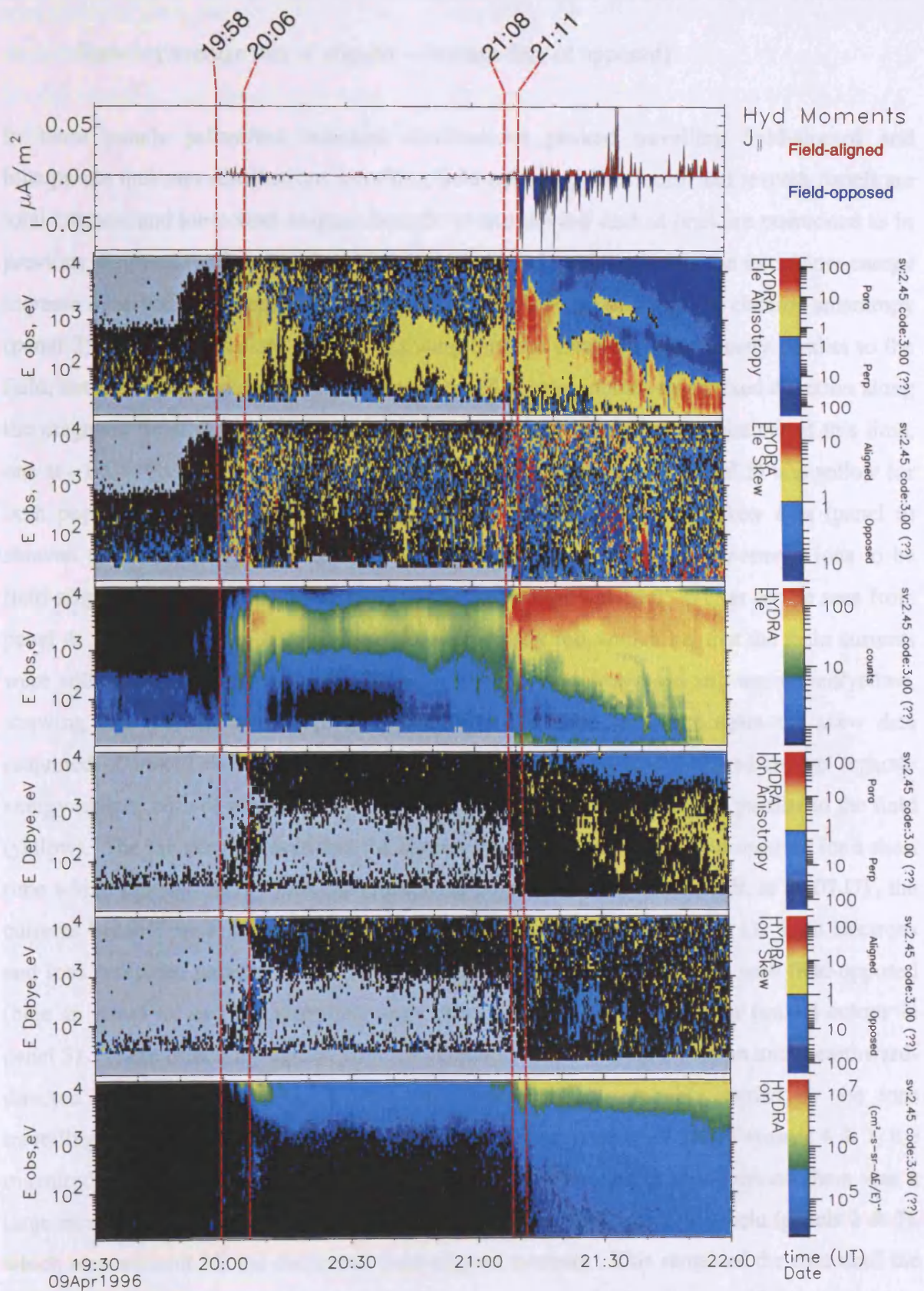


Figure 5.18: Hydra composite plot showing field-parallel currents from Hydra at the top. There are also electron and ion anisotropy, skew and spectrograms. The Hydra currents show the currents in both the field-aligned (red) and field-opposed (blue) directions.

$$\text{Skew} = \{ \text{Average flux of aligned} - \text{Average flux of opposed} \}$$

In these panels yellow/red indicates distributions peaked travelling field-aligned and blue/purple indicates distributions travelling field-opposed. The fourth and seventh panels are total electron and ion counts as described above and the red dashed lines are positioned as in previous diagrams. All panels show the low number of particles before the initial low-energy increase observed by Hydra, which occurred at 19:58 UT. At this time the electron anisotropy (panel 2) was mainly red and yellow, showing that the electrons were mostly parallel to the field, but the electron skew (panel 3) was of mixed colour, indicating a mixed direction along the magnetic field. The ion data showed there to be two small ion populations at this time, one at $\sim 100 - 1000$ eV and one at $\sim 5 - 10$ keV. The ion anisotropy (panel 5) was yellow for both populations, indicating that were parallel to the field. The ion skew data (panel 6) showed the lower-energy ions to be field-opposed (blue) and the higher-energy ions to be field-aligned (yellow). The higher-energy increase occurred at 20:03 UT, as can be seen from panel 4. At this time the J_{\parallel} data (panel 1) were mostly red, indicating that the main currents were still field-aligned. Also at this time the electron anisotropy was still mainly red/yellow, showing that the electrons were still parallel to the field, but once again the skew data remained of mixed colour, indicating mixed direction. The ions occurred in two separate energy ranges, both of which, from the ion anisotropy (panel 5), remained parallel to the field (yellow). The ion skew showed that the higher-energy ions remained field-opposed for a short time whilst the low-energy ions remained field-aligned. Shortly afterwards, at 20:07 UT, the currents became predominantly field-opposed (blue and negative in panel 1). Both electrons and ions remained parallel to the field (panels 2 & 5), but the ions were now field-opposed (blue in panel 6) and the electrons were once again mixed in direction (mixed colour in panel 3). These directions agreed with the direction of the currents, with an initial earthward-directed current, followed by a tailward-directed current probably carried by the ions travelling in those directions. As the particle counts decreased at 20:20 UT (panels 4 & 7) the magnitude of the currents also decreased (panel 1). Throughout this decrease there was a large increase in the proportion of particles directed perpendicular to the field (panels 2 & 5), which may account for the decreased field-aligned currents. This remained the case until the increase at 21:08 UT, when there were few currents recorded by Hydra, with mixed particle directions. At 21:11 UT, the time of the larger increase, strong currents were measured in both directions (panel 1), the larger being the tailward-directed currents (blue). The electron anisotropy (panel 2) showed a sudden increase in the field-aligned direction (red) over the whole energy range, which began to decrease soon afterwards. The ions had both parallel and

perpendicular directed populations (panel 5), but the perpendicular particles (blue) were more numerous and of higher energy. Note that the total electron increase observed by Hydra had no low energy cut-off (panel 4), but the total ion increase had a low-energy cut-off at ~3 keV, with the exception being the low energy field-opposed ions (panel 7).

5.3.6. Polar Magnetic Field Experiment (MFE)

The magnetic field measured by the Polar Magnetic Fields Experiment (MFE) is presented in Figure 5.19. This figure presents the data in GSM co-ordinates, B_x , B_y and B_z , with the inclination, I , of the magnetic field (positive in the $-Z$ direction) and the right ascension, RA (positive in the $+Y$ direction) in the bottom two panels. These were calculated using the following formulae:

$$I = \tan^{-1}\left(\frac{-B_z}{B_x}\right) \quad \& \quad RA = \tan^{-1}\left(\frac{B_y}{B_x}\right)$$

At the start of this interval, B_x was positive (140 nT), and gradually rose to a peak of 200 nT at 21:08 UT. After a drop in the field it resumed a steady rise until ~21:35 UT when it reached 190 nT. It then began to drop quite sharply back to 140 nT by the end of the interval. For most of this interval B_y varied between 15 nT and 40 nT, the exceptions being from 21:08 – 21:20 UT, and after 21:45 UT. B_z began the interval with a negative field (-50 nT) but gradually increased, becoming positive at ~20:50 UT. The field continued to rise, reaching 270 nT by the end of the interval.

In this interval, there were two periods of significant variation in the magnetic field. The first disturbance began at 19:58 UT and continued until 20:26 UT. The second began at 21:08 UT and lasted until 21:20 UT. Close examination of the B_x data showed many small negative deflections during the first period, the largest of these being at 20:06 UT, with a deflection of ~5 nT. During the second period, the next significant variation in B_x occurred at 21:08 UT, when there was a 16 nT negative deflection. This was followed by a 14 nT negative deflection at 21:11 UT, giving a total deflection of 30 nT over a 4-minute interval. The x-component then slowly returned to a stable configuration.

The first major deflection in B_y occurred at 19:58 UT with a 5 nT negative deflection, followed by a 13 nT positive deflection immediately afterwards. Another negative deflection occurred at 20:06 UT, this time of 15 nT, again followed by a sharp increase, this time of 21 nT at 20:11 UT. This pattern of negative then positive deflections continued, but the magnitude of the variations decreased until there was little deflection by 20:26 UT. Although

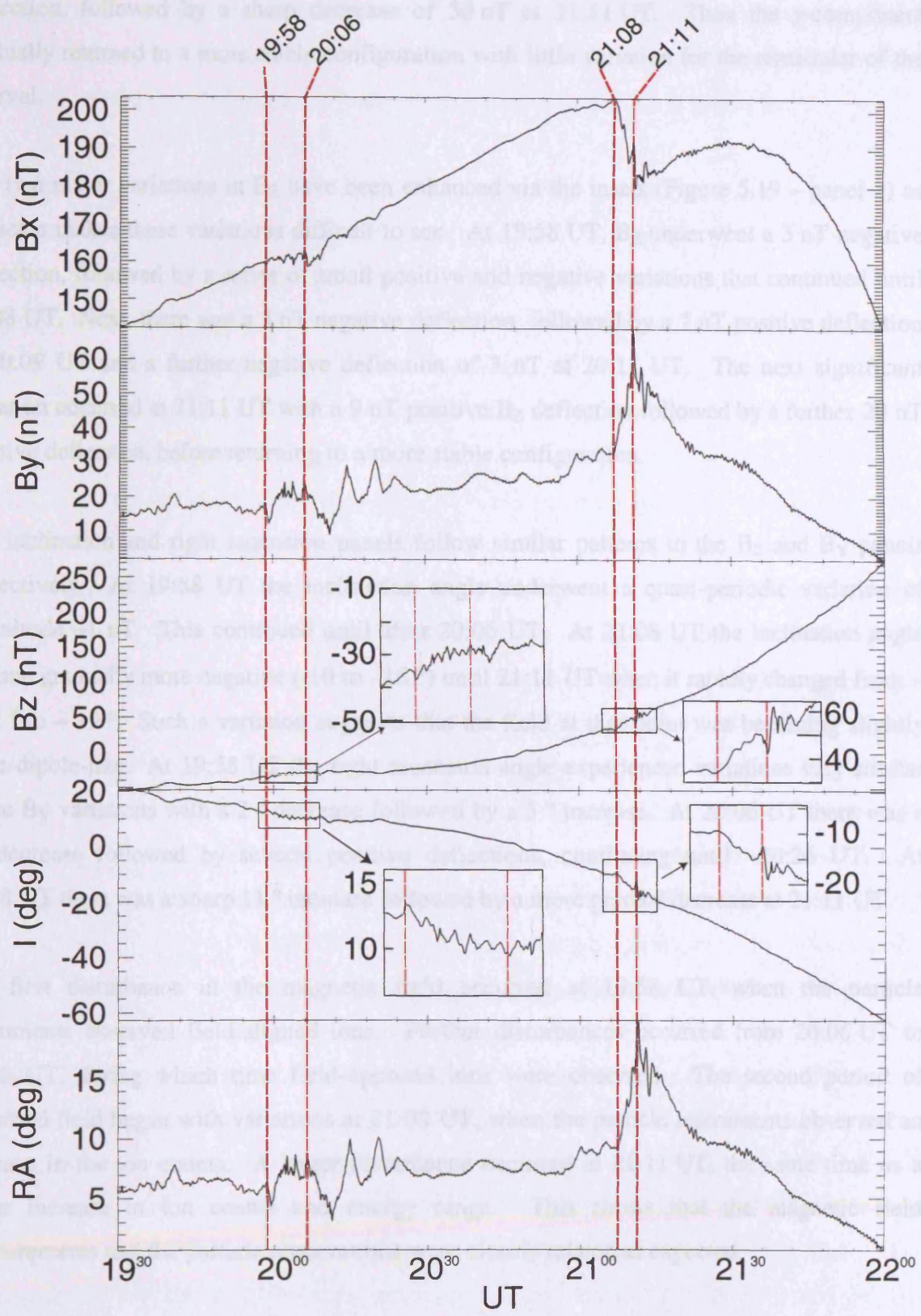


Figure 5.19: In situ magnetospheric magnetic field data taken by MFE on Polar. The top three panels are B_x , B_y and B_z in GSM co-ordinates, with the inclination, I , and right ascension, RA , in the bottom two panels.

there was a variation at 20:57 UT, there are no corresponding signatures in the other data sets. Therefore the next relevant deflection in B_Y occurred at 21:08 UT with a 42 nT positive deflection, followed by a sharp decrease of 30 nT at 21:11 UT. Then the y-component gradually returned to a more stable configuration with little variation for the remainder of the interval.

The two major variations in B_Z have been enhanced via the insets (Figure 5.19 – panel 3) as the scale makes these variations difficult to see. At 19:58 UT, B_Z underwent a 3 nT negative deflection, followed by a series of small positive and negative variations that continued until 20:08 UT. Next, there was a 5 nT negative deflection, followed by a 7 nT positive deflection at 20:09 UT and a further negative deflection of 3 nT at 20:11 UT. The next significant variation occurred at 21:11 UT with a 9 nT positive B_Z deflection followed by a further 20 nT positive deflection, before returning to a more stable configuration.

The inclination and right ascension panels follow similar patterns to the B_Z and B_Y panels respectively. At 19:58 UT the inclination angle underwent a quasi-periodic variation of magnitude ~ 1 nT. This continued until after 20:06 UT. At 21:08 UT the inclination angle became gradually more negative (-10 to -15°) until 21:11 UT when it rapidly changed from $\sim -12^\circ$ to -19° . Such a variation suggests that the field at that point was becoming slightly more dipole-like. At 19:58 UT the right ascension angle experienced variations very similar to the B_Y variations with a 2° decrease followed by a 5° increase. At 20:06 UT there was a 5° decrease followed by several positive deflections, continuing until $\sim 20:26$ UT. At 21:08 UT there was a sharp 11° increase followed by a more gradual decrease at 21:11 UT.

The first disturbance in the magnetic field occurred at 19:58 UT, when the particle instruments observed field-aligned ions. Further disturbances occurred from 20:06 UT to 20:26 UT, during which time field-opposed ions were observed. The second period of disturbed field began with variations at 21:08 UT, when the particle instruments observed an increase in the ion counts. A larger disturbance occurred at 21:11 UT, the same time as a larger increase in ion counts and energy range. This shows that the magnetic field measurements and the particle observations were closely related as expected.

5.4. Discussion

Throughout this interval there is considerable substorm activity, characterised by signatures seen both on the ground and in space. The particle data provide information on the plasma flows and region changes that may be related to the substorm activity. These data are placed in the context of the substorm phase by the other data sets as described in Chapter 3.

At the start of this interval there was a well-established period of substorm activity, as identified by the ground magnetometer disturbances shown in Figures 5.2 – 5.8, culminating in the Pi2 pulsation observed at 19:44 UT. There were also particle injections observed at geosynchronous orbit by the LANL spacecraft and auroral activity observed by UVI. During this time, Polar was located above the polar cap on open field lines, as indicated by the low plasma density and the spacecraft footprint position on the UVI images. The spacecraft footprint entered the poleward edge of the auroral oval some time between the 19:55 UT and 20:01 UT images during the late expansion or early recovery phase of the substorm. At 19:58 UT Polar entered a plasma regime distinct from that observed earlier, which manifested itself as a small increase in the particle count rates at energies from 10 – 50 keV. Within one sampling interval, CAMMICE began to observe a series of field-aligned and field-opposed beams in the DCR data. Such counterstreaming ion beams at the edge of the plasma sheet are known to be more intense during the recovery phase [Lui *et al.*, 1983; Baumjohann *et al.*, 1990]. Examination of the particle data suggests that this new region was the PSBL. As the spacecraft entered the PSBL, CAMMICE observed an earthward travelling beam in the energy range 13 – 31 keV, followed shortly afterwards by a series of tailward-directed ion beams. One possible cause of such a signature is that the earthward travelling beam was mirrored close to Earth. If this was the case, the time taken for the returning beam to appear can be estimated. Due to the ~3 minute time resolution of CAMMICE, it is difficult to identify the exact time when the returning beam was first observed, but it was two scans after the earthward beam was first observed. Therefore, the time between the earthward and tailward ion beams must be at least 197 s. Assuming the distance travelled along the field line by the ions is equal to the spacecraft's altitude, the ions would be travelling a distance of ~14 R_E . If the ion beam is assumed to be composed of protons of energy ranging from 1 – 100 keV then the time taken for the protons to return to the spacecraft varies from ~20 s to ~3 minutes. This would indicate that the delay between the observed ion beams is too large for any but the lowest energy ions. By using CEPPAD and in particular, Hydra, the timing of the first earthward and tailward beams can be determined more accurately than with CAMMICE. The earthward beam is assumed to be composed of the higher-energy (~10 keV) field-aligned ions shown in Figure 5.18 (panel 6), but these were not observed until 20:03 UT. The tailward

beam is assumed to be composed of the higher-energy field-opposed ions that were first seen at 20:07 UT and the lower-energy (up to 1 keV) field-opposed ions that were first seen at 20:04 UT. As there is no loss of energy during a mirror process, the returning ion beam would have to consist of the higher energy ions, giving a mirror time of four minutes, which is too long for 10 keV protons. Therefore, from all three instruments, the delay between the observed ion beams is too large to be explained only by a mirroring process. Another problem with this idea is that only relatively high-energy ions are observed flowing earthwards, but ions from a much larger range of energies are observed flowing tailwards. Therefore there were ions of a certain energy flowing tailward, but not earthward, indicating a source closer to Earth. The most likely source is ion upflow from the auroral region of the ionosphere [e.g. Lu *et al.*, 1992]. Many satellite observations have shown these upflows to produce ions of 10 eV up to 10 keV, covering the energy range of the tailward travelling ions observed in this case study. However, the upflowing ions would be of ionospheric origin, and so would be mainly H^+ , O^+ and He^+ . The CAMMICE data only shows the tailward ion beams in DCR, and not in any of the other species (data not shown). There was some evidence of the tailward travelling ion beams in the Hydra data occurring at energies below the threshold of CAMMICE. Therefore the ions must be of ionospheric origin as ionospheric outflow is the only reasonable mechanism to produce them.

A second point concerning the beams is the association with the in-situ magnetic field. As the spacecraft entered the PSBL at 19:58 UT MFE observed fluctuations in an otherwise stable field (Figure 5.19). These fluctuations occurred primarily in B_Y , with smaller fluctuations in the other components. When the particle instruments observed the field-aligned ion beams, MFE observed a series of variations in B_Y and in the right ascension angle. To gauge the relationship between the different data sets Figure 5.20 has been constructed, which covers the interval 19:50 to 20:50 UT. This presents the currents from Hydra in the top panel, in-situ magnetic field in the next three panels, CAMMICE DCR energy bands in the next four panels and CEPPAD IPS and Hydra total ion data in the bottom 2 panels. Red lines on the diagram denote times of particular interest indicated in earlier diagrams; the first when significant ion count rates were initially observed at 19:58 UT and the second when the tailward flowing ion beams began at 20:06 UT. The initial magnetic deflection at 19:58 UT was negative in both the y- and z-components. Following this there was a series of quasi-periodic oscillations in these two components which ceased at $\sim 20:06$ UT (Figure 5.20 – panels 3 & 4). The Hydra currents (panel 1) indicate a series of field-aligned currents during this time, whilst CAMMICE observed field-aligned ion beams, which are the likely current carriers in the Earth's rest frame. After 20:06 UT, the Hydra currents indicated a series of field-opposed

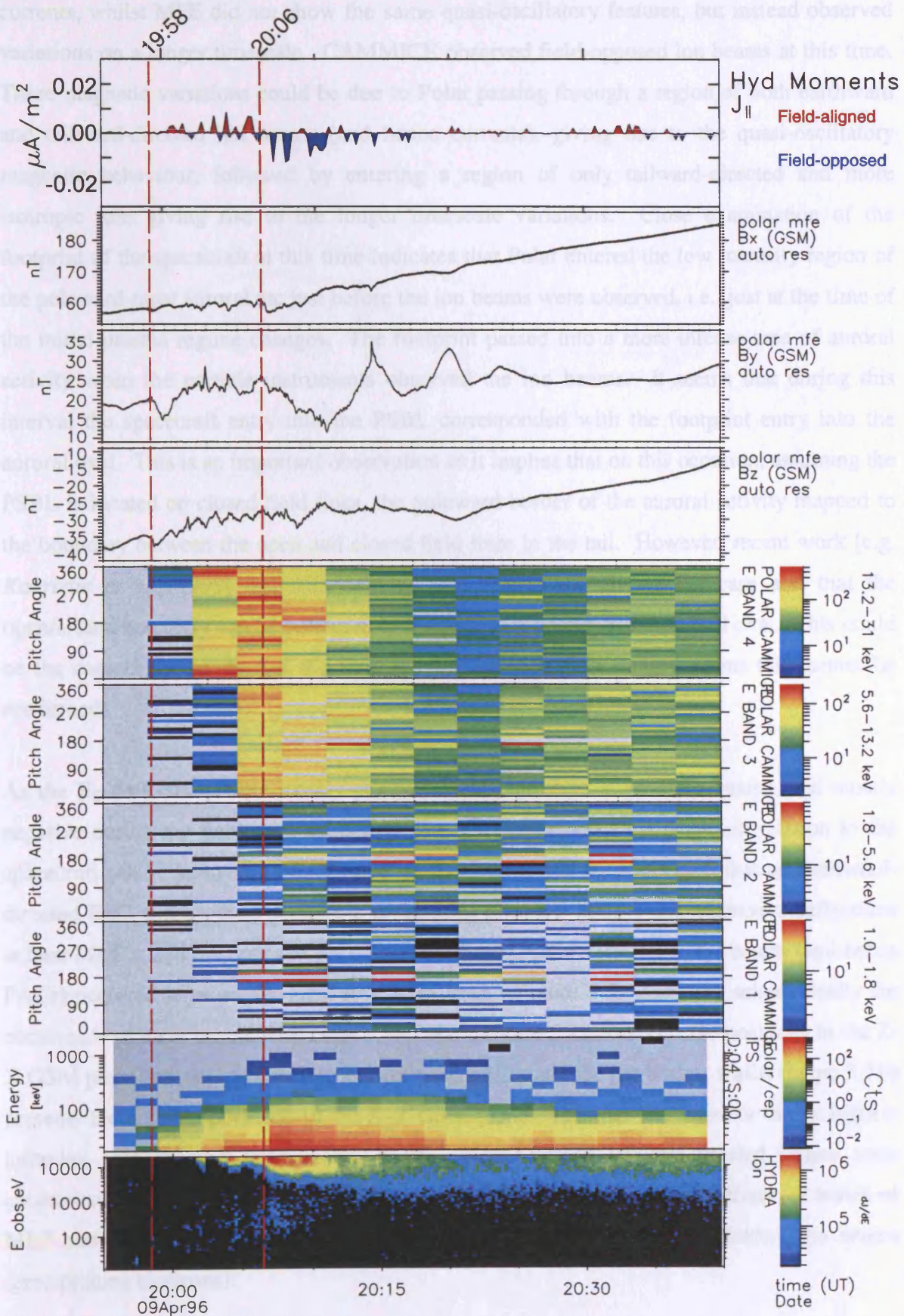


Figure 5.20: An expanded plot showing Hydra currents in the first panel, data from MFE in panels 2 - 4, CAMMICE DCR in energy slices in the next four panels, with CEPPAD IPS data and Hydra ion data in the bottom two panels.

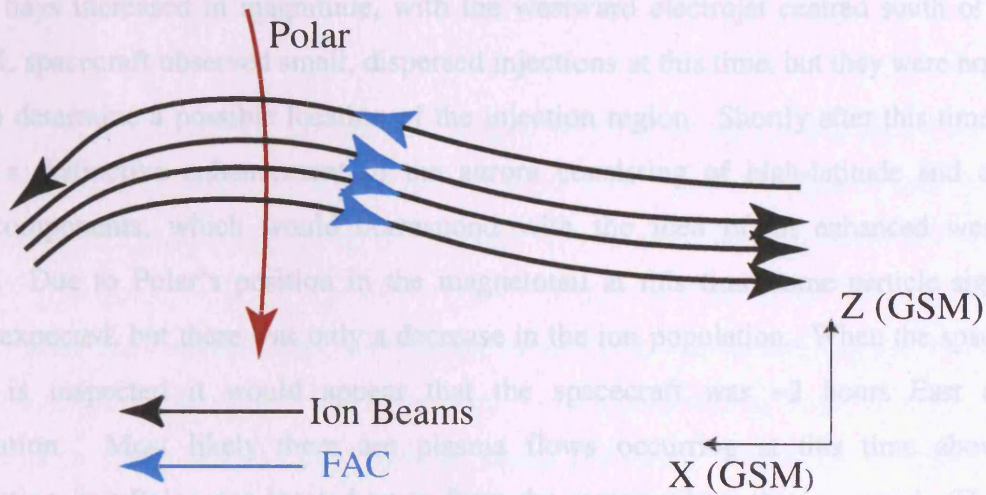
currents, whilst MFE did not show the same quasi-oscillatory features, but instead observed variations on a longer timescale. CAMMICE observed field-opposed ion beams at this time. These magnetic variations could be due to Polar passing through a region of both earthward and tailward-directed ion beams (and hence currents), giving rise to the quasi-oscillatory magnetic behaviour, followed by entering a region of only tailward-directed and more isotropic ions giving rise to the longer timescale variations. Close examination of the footprint of the spacecraft at this time indicates that Polar entered the low intensity region of the poleward-most auroral arc just before the ion beams were observed, i.e., just at the time of the initial plasma regime changes. The footprint passed into a more intense area of auroral activity when the particle instruments observed the ion beams. It seems that during this interval the spacecraft entry into the PSBL corresponded with the footprint entry into the auroral oval. This is an important observation as it implies that on this occasion, assuming the PSBL is located on closed field lines, the poleward border of the auroral activity mapped to the boundary between the open and closed field lines in the tail. However, recent work [e.g. *Kauristie et al.*, 1999] has demonstrated that this is not always the case and that the open/closed boundary can be poleward of the poleward border of the auroral oval. This could be the case in this study, but the time interval between UVI images means this cannot be confirmed.

As the B_z deflections were mostly positive during the field-aligned ion beams, and mostly negative during the field-opposed beams, the MLT location of the beams in relation to the spacecraft can be inferred. A FAC sheet gives an extended B_y effect such that an earthward-directed FAC will produce positive z deflections at earlier MLT's and negative z deflections at later MLT's, and the opposite for tailward-directed FACs. Therefore, the beams (and hence FACs) occurred at an earlier local time than Polar. Figure 5.21 illustrates schematically the occurrence of these beams with respect to Polar. Figure 5.21a presents the positions in the Z-X GSM plane and also relationship between the FAC's and the ion beams, whilst Figure 5.21b presents the possible positions in the X-Y GSM plane. The first ion beam, or that at highest latitudes, was directed towards the Earth. Next, several tailward-directed beams were encountered at lower latitudes. The UVI images show intense auroral activity ~2 hours of MLT earlier than Polar, in agreement with the location of the tailward-directed ion beams (precipitating electrons).

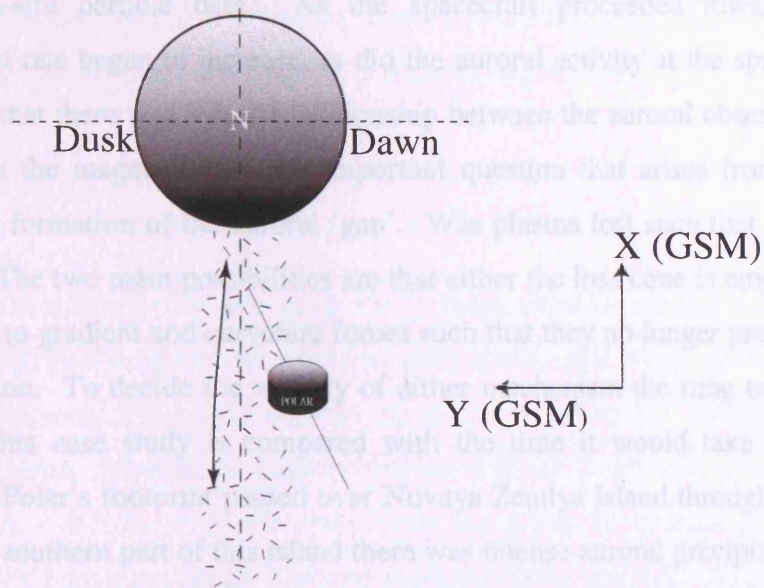
The next magnetic activity is first observed as an onset in the high latitude ground magnetometers at 20:12 UT. The high-latitude ground magnetometer data suggests that electrojet signatures were observed, with negative magnetic bays measured in the high-latitude

X-component data, and positive deflections seen at lower-latitude. Such variations suggest that by 20:17 UT a pre-existing westward electrojet existed at high-latitude centred close to HOP, and an eastward electrojet was centred close to SOR at lower-latitude. Coincident with the P12 injection at 20:17 UT, the IMAGE data show enhancement of both electrojets as the ion beams increased in magnitude, with the westward electrojet centred south of SOR.

(a)



(b)



 Approx. location of counterstreaming beams

Figure 5.21: A schematic showing the approximate positions of the field-parallel ion beams on the edge of the PSBL in relation to the spacecraft. (a) shows the positions in the X - Z plane and also shows the FAC connection. (b) shows the positions in the X - Y plane and indicates that the ion beams are observed at an earlier local time than Polar.

X-component data, and positive deflections seen at lower-latitude. Such variations suggest that by 20:17 UT a pre-existing westward electrojet existed at high-latitude centred close to HOP, and an eastward electrojet was centred close to SOR at lower-latitude. Coincident with the Pi2 pulsation at 20:17 UT, the IMAGE data show enhancement of both electrojets as the magnetic bays increased in magnitude, with the westward electrojet centred south of SOR. The LANL spacecraft observed small, dispersed injections at this time, but they were not clear enough to determine a possible location of the injection region. Shortly after this time, UVI observed a distinctive enhancement in the aurora consisting of high-latitude and auroral latitude components, which would correspond with the idea of an enhanced westward electrojet. Due to Polar's position in the magnetotail at this time some particle signature might be expected, but there was only a decrease in the ion population. When the spacecraft footprint is inspected it would appear that the spacecraft was ~2 hours East of the intensification. Most likely there are plasma flows occurring at this time above the intensification, but Polar was located away from the region where they occurred. The UVI data shows that Polar had actually left the latitude of the poleward-most arc, and was now in a 'gap' between the poleward- and equatorward-most arcs. This explains why an ion decrease was observed in the in-situ particle data. As the spacecraft proceeded towards the equatorward arc, the count rate began to increase, as did the auroral activity at the spacecraft footprint. It seems likely that there was a direct relationship between the auroral observations and the ion population in the magnetotail. One important question that arises from these observations concerns the formation of the auroral 'gap'. Was plasma lost such that the gap appeared and if so why? The two main possibilities are that either the loss cone is emptied or that the particles drift due to gradient and curvature forces such that they no longer precipitate into the same auroral region. To decide the validity of either mechanism the time taken for the region to empty in this case study is compared with the time it would take via the mechanisms in question. Polar's footprint passed over Novaya Zemlya Island throughout the UVI images, and over the southern part of this island there was intense auroral precipitation at 19:45 UT that had disappeared by 20:01 UT. Thus, the loss cone must have been emptied in less than 16 minutes. From *Roederer* [1970] and *Lyons and Williams* [1984], the minimum lifetime of a particle population is given via the strong diffusion limit as:

$$\tau_m = \frac{4LR_\xi}{2.2v \sin^2 \alpha_{LC}}$$

where L is the L-shell ($9 R_E$), R_E is radius of Earth (6371 km), v is velocity of particles and α_{LC} is the atmospheric loss cone angle at the equator and is given by:

$$\alpha_{LC} = \sin^{-1} \left[\left(\frac{B_0}{B_{100}} \right)^{\frac{1}{2}} \right] = \sin^{-1} \left[\left(\frac{\sim 300}{\sim 50000} \right)^{\frac{1}{2}} \right] \approx 4^\circ$$

where B_0 is the equatorial field strength and B_{100} is the field strength at 100 km on the $L = 9$ field line. By using approximate values of 300 & 50000 nT, the atmospheric loss cone was found to be $\sim 4^\circ$. The average energy of precipitating electrons resulting in the UV aurora is 5 – 10 keV [Germany *et al.*, 1997], which gives a minimum lifetime for electrons of $\sim 6 - 9$ minutes. Thus the electrons could be removed in this way, thereby creating the auroral gap. This does not explain, however, why there were no ions observed by Polar, as the ions take several hours to empty the flux tube through strong diffusion. Therefore, we consider the alternative of the drifting plasma, which requires that the amount of drift of auroral particles must be approximated. From the 19:45 and 20:01 UT auroral images, the eastward edge of the intense (red) aurora moved from $\sim 65^\circ E$ to $45^\circ E$. Therefore there was a 20° movement in 16 minutes. To simplify the calculation, drift speeds in a dipole field [Parks, 1991] are used as an approximation. From this work the drift period in minutes is given by:

$$T_D = \frac{43.8}{LE}$$

where L is the L-Shell and E is the particle energy in MeV. If the particles are taken to be 1 – 10 keV electrons and 5 – 100 keV ions then the electrons drift at 0.07 to 0.74 %/minute and the ions drift at 0.37 to 7.40 %/minute. Thus in 16 minutes the electrons can drift 1 – 12° east and the ions can drift 6 – 120° west. Therefore, it seems that the drift can explain the absence of ions, but only some of the electrons will drift away from the region in question. In fact, looking at the in-situ particle data from Hydra it would seem that there was a more significant decrease in the number of ions than the number of electrons. The most likely explanation is a combination of both processes results in the production of the auroral gap and large decrease in the number of ions detected, with the drift motion affecting the in-situ measurements and the loss into the atmosphere (through the loss cone) responsible for the auroral observations.

The final points to be discussed are the observations made at 21:08 UT. At this time there was a disturbance in the magnetic field measured by Polar with a negative B_x deflection, a positive B_y deflection and little B_z variation. The LANL spacecraft observed a dispersionless injection at the 1991 – 080 spacecraft, indicating that the injection region was close to this

spacecraft. The mid-latitude magnetometer stations observed a Pi2 pulsation at 21:10 UT. This corresponded with magnetic bays seen in the unfiltered data that indicated a classic substorm signature, with the electrojet centred at Kevo (KEV) and moving polewards. At this time, the Polar footprint mapped close to the latitude of the electrojet, but approximately one hour to the east of the magnetometer stations. If data from a quiet day is examined, we can see that it is usual to see a count rate and energy increase as the spacecraft enters the lower latitude regions. However, the signature observed by CAMMICE would appear to be a temporal variation superimposed on this background spatial variation, as quiet day data show a much smaller increase in ions at a similar region. The Polar MFE variations at this time took the form of a negative deflection in B_x with a positive deflection in B_z . If a dipolarisation of the tail field were occurring at this point then the inclination of the field would increase. At 21:08 UT, before the deflection is observed, the inclination of the field was -12° . At 21:11 UT, just after the deflection, the inclination was -19° . Due to the sign convention this decrease in the inclination suggests that the 7° reconfiguration at the location of Polar, which was relatively close to Earth, was the result of a 'dipolarisation' of the magnetotail field, a sign of an expansion phase onset (see Chapter 2). From the background data sets, the temporal variation observed by the particle instruments at 21:10 UT must be due to the particle injection that occurs at substorm expansion phase onset. Therefore a dipolarisation, a plasma injection, enhanced electrojets and Pi2 pulsations had occurred. There were two other onsets that can be confirmed by the background data sets, but they occurred after Polar had entered a low-latitude region of the nightside magnetosphere where the presence of energetic particles masks any possible signatures.

5.5. Summary

Throughout this substorm interval two interesting periods have been found. The first was a period when the spacecraft entered the region of closed magnetic field lines in the geomagnetic tail during which good auroral imager coverage, magnetic field and particle data were available. In the second period only particle and magnetic field data were available to study the expansion phase onset that occurred as the spacecraft entered the CPS.

The spacecraft encounter with an increased ion population, consistent with the PSBL, coincided with the movement of the spacecraft footprint across the poleward boundary of the auroral oval. Immediately after entering this region counterstreaming ion beams, characteristic of the PSBL, were observed by the particle instruments, with both MFE and Hydra currents showing that these beams were closely connected to field-aligned currents. The auroral oval at this time exhibited a double oval configuration and the footprint of the

PSBL was coincident with the poleward-most arc. Therefore there was an apparent mapping of the poleward boundary of the auroral oval to the boundary between open and closed field lines in this case. There was, however, a six minute gap between UVI LBHI images from 19:55 – 20:01 UT, so the exact time of entry into the auroral oval could be up to three minutes later, which would correspond to an open/closed field line boundary poleward of the auroral zone. When the spacecraft footprint left the poleward arc and entered the gap between the poleward and equatorward arcs, the in-situ particle count rate decreased. This occurred just after the ground magnetometers indicated an electrojet enhancement, whilst the UVI data demonstrated enhanced auroral activity to the west of the spacecraft footprint.

The final period of activity occurred when Polar was deep in the PSBL and was approaching the central plasma sheet (CPS). At this time, the UVI had been shielded to avoid damage and so there were no images available. There was one major expansion phase onset at 21:10 UT, confirmed by a number of signatures, such as a clear Pi2 pulsation and a westward electrojet centred on Kevo, at latitude similar to Polar. There was also a fairly large change in the orientation of the magnetic field (7°) seen by MFE on Polar, consistent with dipolarisation, confirming the onset timing of this substorm as between 21:10 and 21:11 UT. Finally, CAMMICE observed a small ion increase prior to onset, which was then followed, at the time of the onset, by a much larger increase in the ion count rate and energies. The other particle instruments confirmed that this small initial increase did not correspond with the expansion phase onset timing and also observed the larger increase. Therefore, Polar was travelling through the PSBL (characterised by the presence of counterstreaming ion beams) until 21:08 UT, when the spacecraft entered the CPS. At 21:11 UT, just after the entry into the CPS, the spacecraft observed a large particle increase, corresponding to a particle injection at expansion phase onset. There are further onsets in this final period, but Polar was at sufficiently low latitudes that any particle signatures were obscured by the energetic particles of the CPS and radiation belts.

This case study demonstrates the need for context data such as UVI images and magnetometer networks in studying dynamic changes in the magnetotail measured in-situ by a spacecraft such as Polar. From the UVI data it is clear that the spacecraft observations began in an area of open field lines. Polar then passed into the poleward arc of a double-oval aurora that had developed as a result of earlier substorm activity. Entering this double oval, the spacecraft observed a series of counterstreaming ion beams, a signature of the PSBL. When Polar exited this poleward arc and entered the gap between the poleward and equatorward arcs, the in-situ particle data registered a relatively low count rate despite the evidence for further activity to

the West of the spacecraft. The low count rate continued until the spacecraft entered the CPS at 21:08 UT and observed the plasma injection associated with expansion phase onset. Although there are no UVI images available at this time, the location of the poleward edge of the equatorward arc in the final image occurred at $\sim 69^\circ\text{N}$. As the footprint of the spacecraft was at $69.3 - 68.9^\circ\text{N}$ from 21:06 - 21:12 UT, it would be reasonable to say that the encounter with the CPS from the particle data is concurrent with the spacecraft footprint's encounter with the poleward edge of the equatorward arc.

CHAPTER 6

Pseudobreakup and Substorm effects on the high latitude plasma sheet:

17th May 1996 case study

6.1. Introduction

The previous chapter reported details of plasma flows in both the CPS and PSBL during different phases of substorm activity. This chapter presents another case study during a similar orbit identified by the same selection process as the previous interval. However, during this interval, 20:00 – 22:30 UT on 17th May 1996, the spacecraft enters the plasma sheet briefly, but exits shortly afterwards, before re-entering some time later. The background data sets suggest that pseudobreakups are occurring during this time and may be responsible for the initial entry into the plasma sheet. Multiple entries into the plasma sheet are not unusual, and many can be found in the Polar data.

6.2. The Interval – 17th May 1996

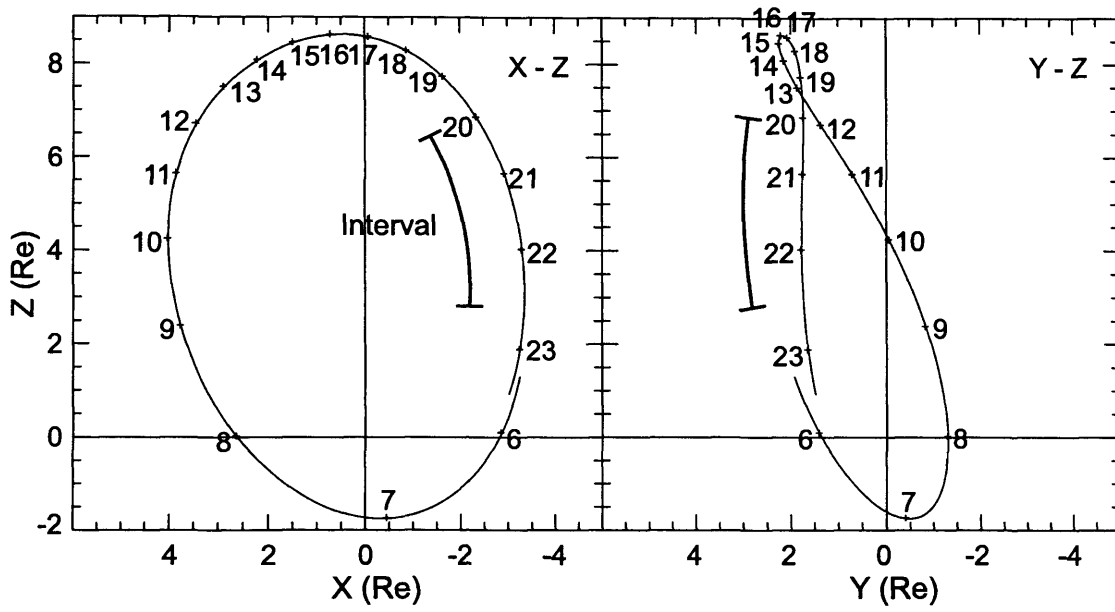
The interval under discussion ran from 20:00 – 22:30 UT on 17th May 1996. Figure 6.1a presents Polar's orbit in both the X-Z and Y-Z GSM planes and Figure 6.1b presents the orbital footprint. The spacecraft was on an in-bound pass through the nightside magnetosphere. The orbital footprint was mapped into the ionosphere by use of the Tsyganenko 89 magnetic field model for the appropriate Kp value (2-). Polar passed over Svalbard just before the interval began, and travelled towards Iceland, which was passed at about 22:15 UT. This placed the spacecraft close to the Scandinavian sector before local midnight. Also presented in Figure 6.1b are the locations of the magnetometer stations from the IMAGE, SAMNET and Greenland magnetometer networks from which data are used in this study.

6.3. Observations

6.3.1. Solar Wind Conditions

To determine if any dayside reconnection occurred during this interval the solar wind conditions were investigated via data from the Wind spacecraft. Data from the Magnetic Field Instrument (MFI – see Chapter 3) for this interval are shown in Figure 6.2. This figure presents IMF B_x , B_y and B_z , all in GSM co-ordinates (see Appendix 1). As Wind was located at (+88, -39, -2.5) R_E there was a resulting ~20 minute delay to the magnetopause. As this case study is associated with substorm activity the z-component is the most relevant as this determines when dayside reconnection begins, and hence when the magnetotail begins to

a)



b)

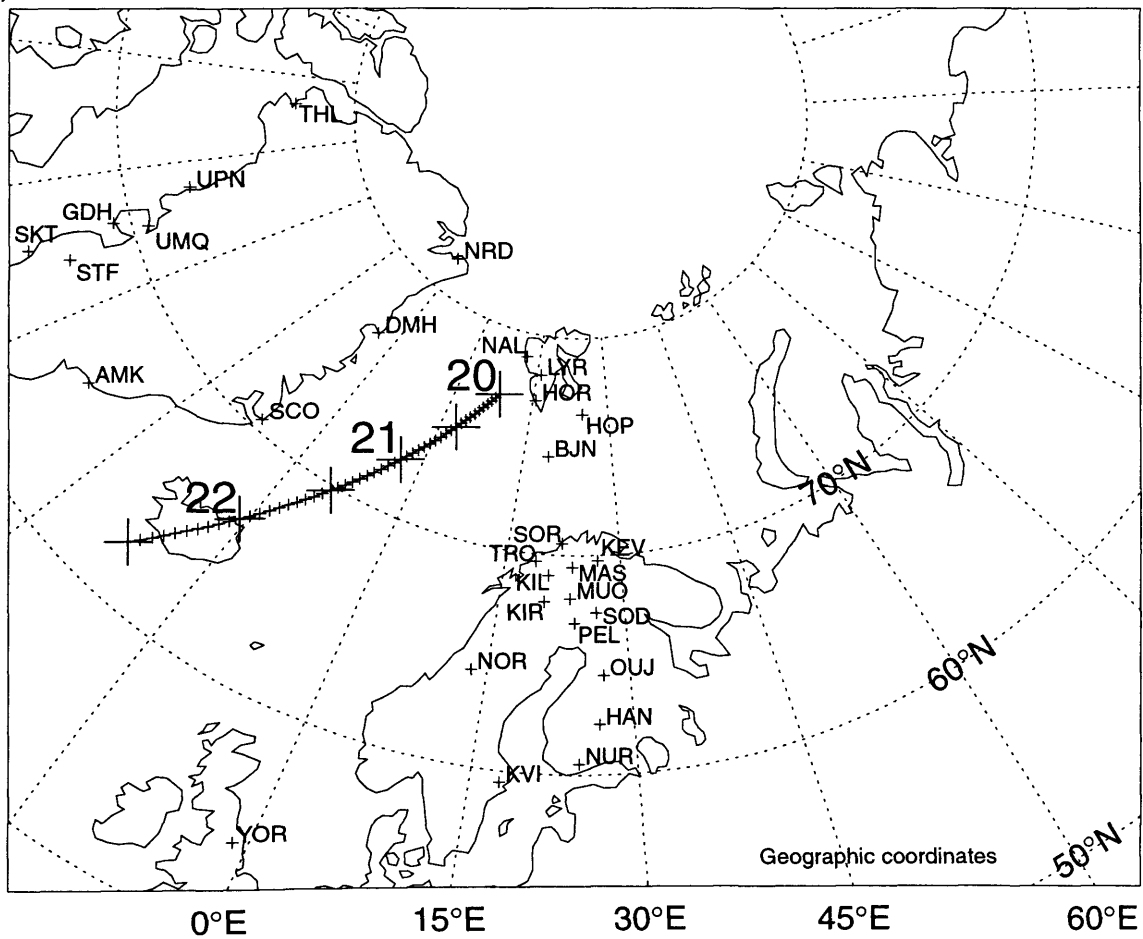


Figure 6.1: The Polar orbit. (a) Polar's orbit in the X-Z and Y-Z GSM planes (b) the orbital footprint mapped down to 100 km by using the Tsyganenko model.

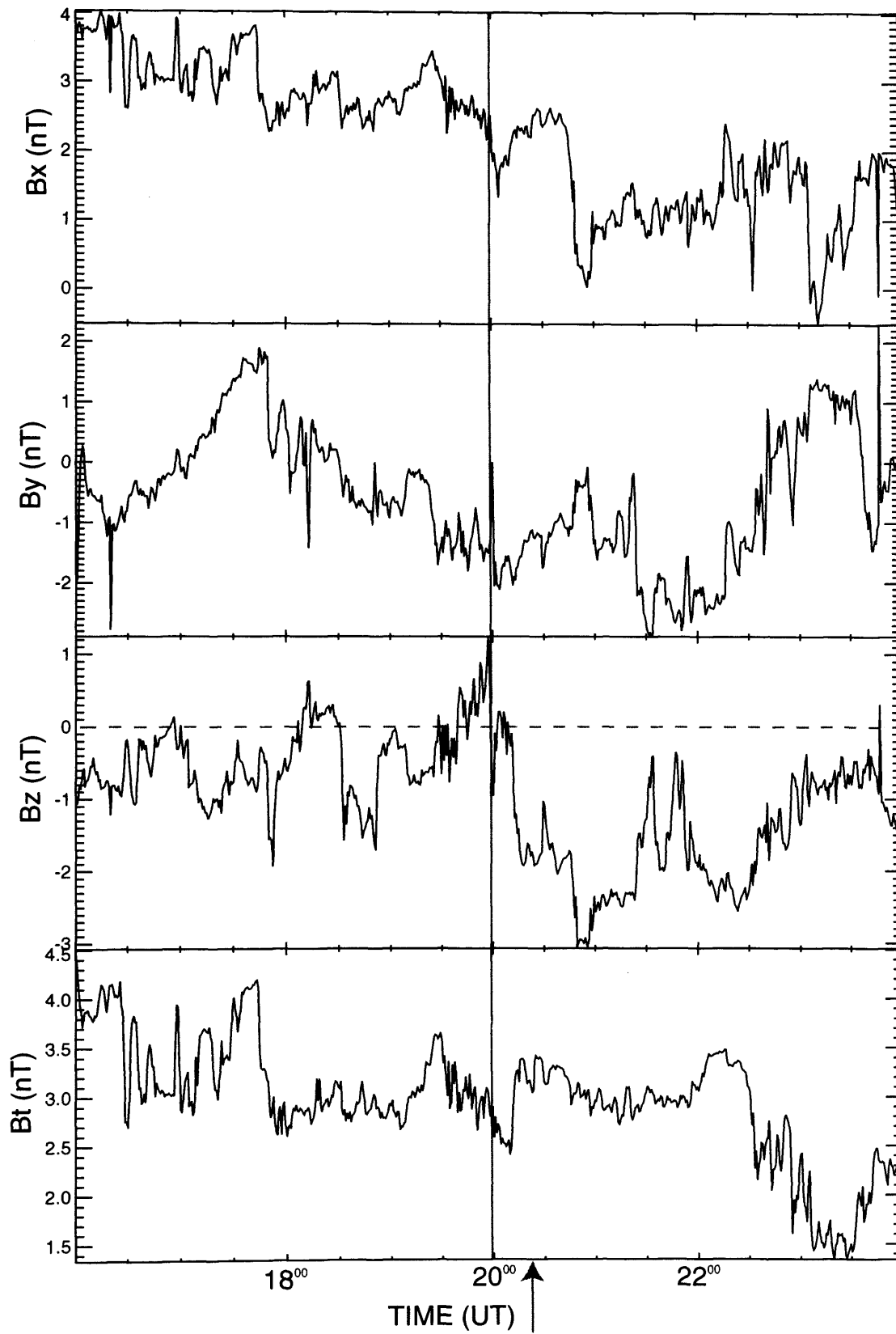


Figure 6.2: Solar Wind magnetic field data measured at the Wind spacecraft. Wind is at $(88, -39, -2.5)$ Re, and so there is a delay of ~ 20 minutes.

be loaded (Growth Phase). Briefly, IMF B_X remained positive throughout the interval, varying from 3.5 down to 0 nT. IMF B_Y remained negative for most of the interval, varying between 0 and -3 nT. IMF B_Z was negative (southward) from $\sim 19:20$ UT (taking account of a ~ 20 minutes delay from the Wind spacecraft to the magnetopause) until $\sim 20:00$ UT, when there was a northward turning (B_Z became positive). This remained the case until $\sim 20:20$ UT when the IMF turned southwards, and remained predominantly southwards for the remainder of the interval. The time of this southward turning at the spacecraft is located by a blue, vertical line, and by a blue arrow at the time at the magnetopause.

6.3.2. Ground Magnetometer Networks

As in the previous chapter substorm activity is a prerequisite for this case study and so ground magnetometer data from the IMAGE, SAMNET and Greenland networks are examined for some of the many expansion phase onset-associated signatures such as Pi2 pulsations and magnetic bays. As in the previous chapter the data are referred to in XYZ co-ordinates, whilst the data may be in HDZ co-ordinates (see Appendix 1). In this interval Pi2 pulsations were observed at the mid-latitude magnetometer stations at the following times: 20:13, 20:39, 20:48, 21:00 and 21:46 UT (see Figure 6.3 for filtered mid-latitude X-component data). These data have been filtered with a bandpass of 20 – 200 seconds and the Pi2 signatures have been marked with a red line. This interval comprises of an isolated Pi2 at 20:13 UT, followed by a group of three Pi2 pulsations at 20:39, 20:48 and 21:00 UT, with a final Pi2 pulsation concluding the activity at 21:46 UT.

As in the previous chapter the European ground magnetometers were separated into three groups, mid-latitude, auroral latitude and high-latitude (see Chapter 5 for details). The unfiltered mid-latitude data are used to locate the substorm current wedge (SCW) as described in Chapter 2. In certain circumstances, in particular if the electrojet part is at higher than usual latitudes, the SCW can be observed in the auroral latitude stations, but these stations are more commonly used to identify the location of the enhanced auroral electrojets (also described in Chapter 2). The unfiltered high-latitude magnetometer data are used to identify any high-latitude features such as periods when the electrojet system has moved poleward and any other signatures that may occur in this region. The Greenland magnetometers are at similar latitudes to the auroral and high-latitude IMAGE stations, and so can be used in a similar way. They are also a good indicator of any poleward expansion, due to the good high-latitude coverage, and westward expansion, due to the stations' westerly locations.

Figure 6.4 presents the unfiltered mid-latitude X-component data and Figure 6.5 presents the Y-component. In these data the P12 pulsations are also seen as periodic variations in the magnetic field. The relevant features, however, are the larger scale variations observed, usually immediately after the P12 pulsations. At 20:13 UT (first red line) the mid-latitude X-component underwent small positive deflections at all stations with small negative deflections in the Y-component at all stations except YOR, which was being remotely

operated. The largest positive deflection was observed at OUI, with a maximum deflection of +1.5 nT. The largest negative deflection was observed at YOR, with a maximum deflection of -0.5 nT. At 20:48 UT (third red line) a significant negative deflection was observed at all stations, with a maximum deflection of -1.5 nT at OUI. At 21:13 UT (fourth red line) a significant positive deflection was observed at all stations, with a maximum deflection of +1.5 nT at OUI. At 21:58 UT (fifth red line) a significant positive deflection was observed at all stations, with a maximum deflection of +1.5 nT at OUI.

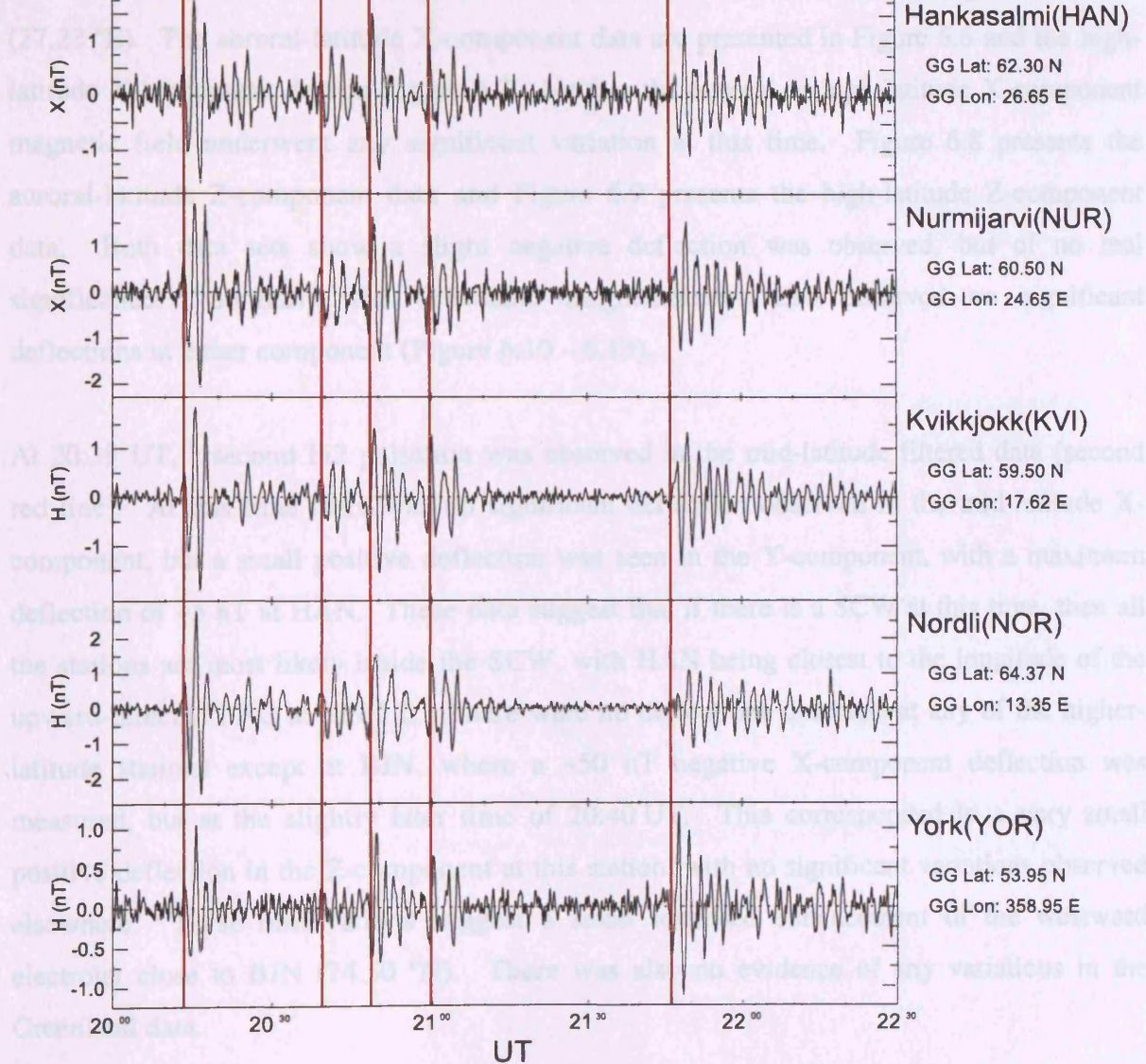


Figure 6.3: Filtered mid-latitude X/H component ground magnetometer data from 17/5/96.

The next P12 pulsation was observed at 20:48 UT (third red line). At this time, all the mid-latitude stations underwent a positive X-deflection, with a maximum deflection of +1.5 nT at OUI, and a minimum deflection of -0.5 nT at YOR. The largest positive deflection was observed at OUI, with a maximum deflection of +1.5 nT. The largest negative deflection was observed at YOR, with a maximum deflection of -0.5 nT. At 21:13 UT (fourth red line) a significant positive deflection was observed at all stations, with a maximum deflection of +1.5 nT at OUI. At 21:58 UT (fifth red line) a significant positive deflection was observed at all stations, with a maximum deflection of +1.5 nT at OUI.

Figure 6.4 presents the unfiltered mid-latitude X-component data and Figure 6.5 presents the Y-component. In these data the Pi2 pulsations are also seen as periodic variations in the magnetic field. The relevant features, however, are the larger scale variations observed, usually immediately after the Pi2 pulsations. At 20:13 UT (first red line) the mid-latitude X-component underwent small positive deflections at all stations, with small negative deflections in the Y-component at all stations except YOR, which observed very little deviation. The largest of these negative deflections occurred at OUI with a magnitude of ~ 8 nT. These data suggest a SCW was being remotely observed, centred at a longitude close to that of YOR (358.95°E), with a downward-directed FAC close to the longitude of OUI (27.23°E). The auroral-latitude X-component data are presented in Figure 6.6 and the high-latitude X-component data in Figure 6.7. Neither the auroral or high-latitude X-component magnetic field underwent any significant variation at this time. Figure 6.8 presents the auroral-latitude Z-component data and Figure 6.9 presents the high-latitude Z-component data. Both data sets show a slight negative deflection was observed, but of no real significance. Similarly, the Greenland magnetometers also observed no significant deflections in either component (Figure 6.10 – 6.13).

At 20:39 UT, a second Pi2 pulsation was observed in the mid-latitude filtered data (second red line). At this time there was no significant deflection observed in the mid-latitude X-component, but a small positive deflection was seen in the Y-component, with a maximum deflection of ~ 5 nT at HAN. These data suggest that if there is a SCW at this time, then all the stations are most likely inside the SCW, with HAN being closest to the longitude of the upward-directed FAC at $\sim 27^\circ\text{E}$. There were no deflections observed at any of the higher-latitude stations except at BJN, where a ~ 50 nT negative X-component deflection was measured, but at the slightly later time of 20:40 UT. This corresponded to a very small positive deflection in the Z-component at this station, with no significant variations observed elsewhere. These observations suggest a small localised enhancement of the westward electrojet close to BJN (74.50°N). There was also no evidence of any variations in the Greenland data.

The next Pi2 pulsation was observed at 20:48 UT (third red line). At this time, all the mid-latitude stations underwent a positive X-deflection, with a maximum deflection of ~ 8 nT at OUI, but of only ~ 2 nT at YOR. The Y-component underwent positive deflections in the west, from YOR to HAN, with the maximum deflection of ~ 9 nT occurring close to NOR, and no significant deflection at OUI. Therefore a SCW system was observed, the centre of which occurred at longitude close to OUI (27.23°E), and an upward-directed FAC close to

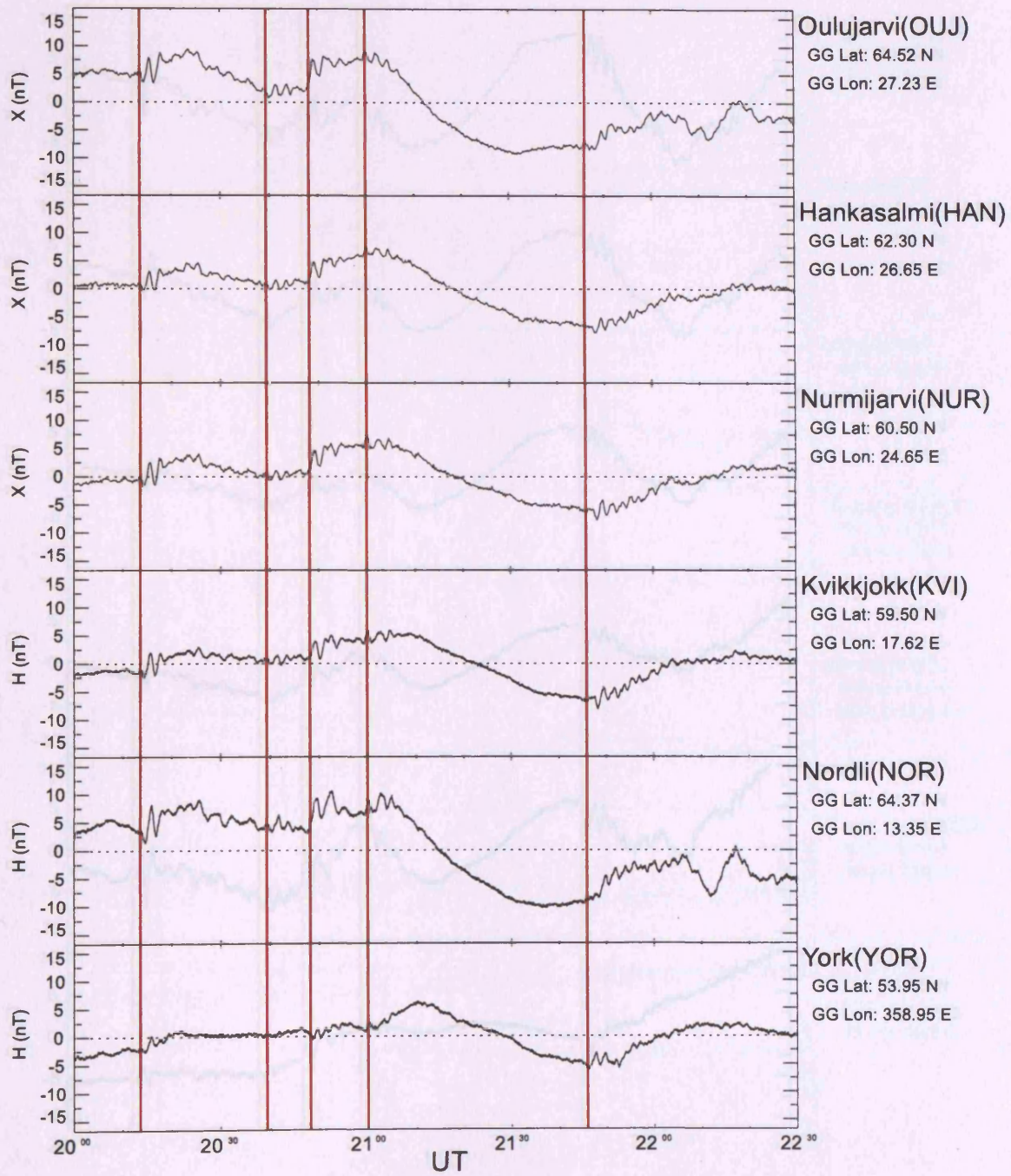


Figure 6.4: Mid-latitude X/H component ground magnetometer data from IMAGE and SAMNET on 17/5/96.

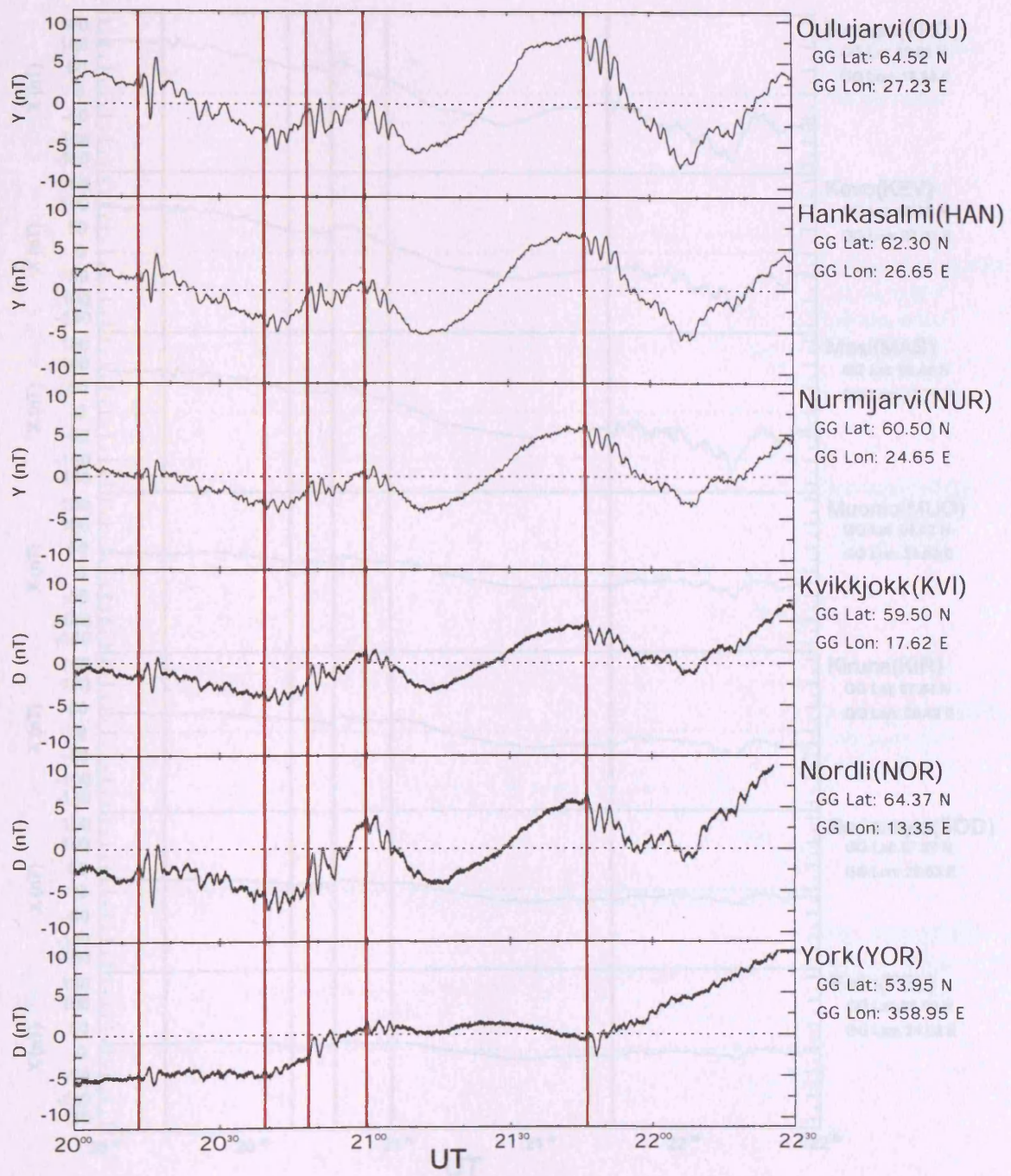


Figure 6.5: Mid-latitude Y/D component ground magnetometer data from IMAGE and SAMNET on 17/5/96.

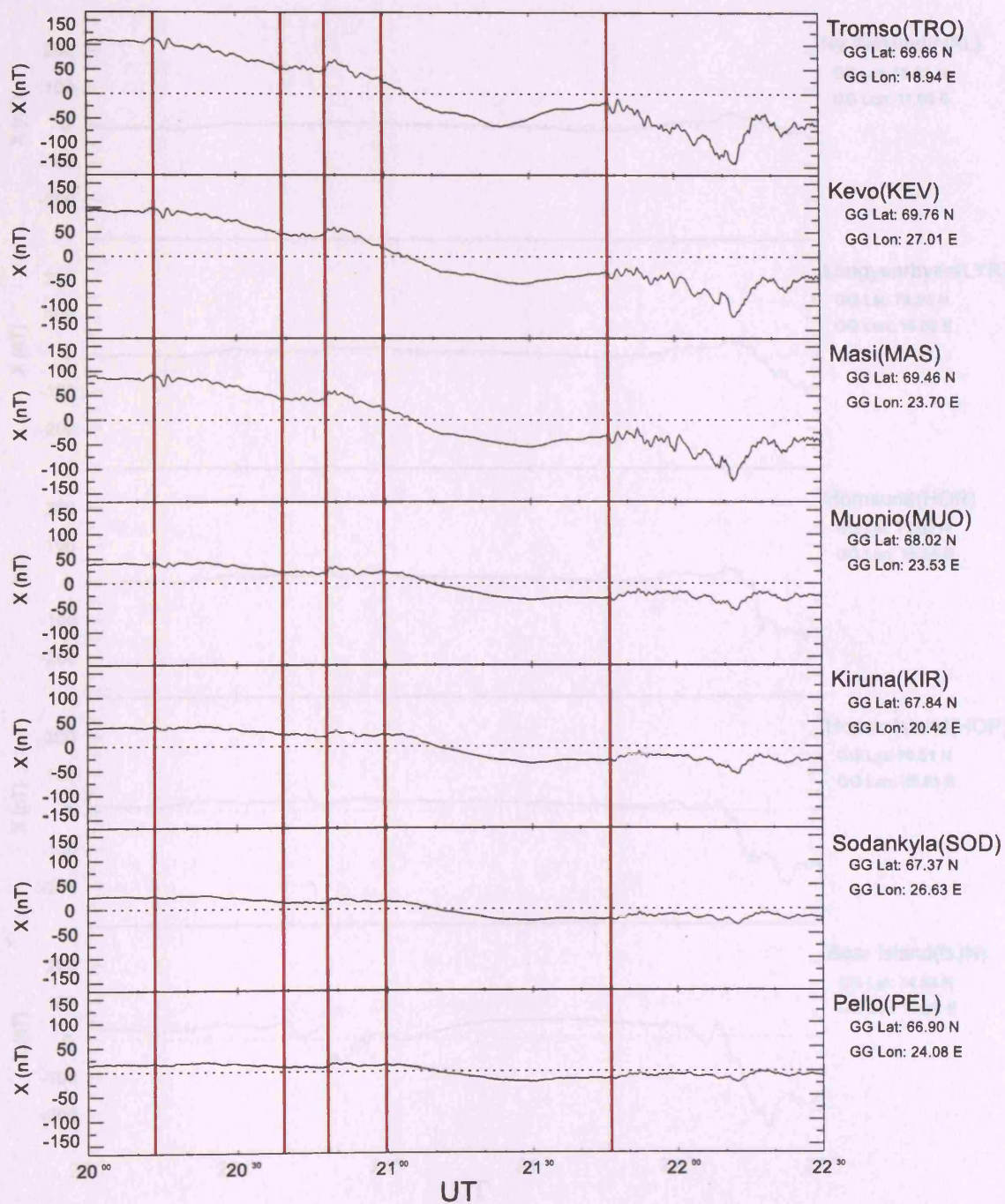


Figure 6.6: Auroral-latitude X-component ground magnetometer data from IMAGE on 17/5/96.

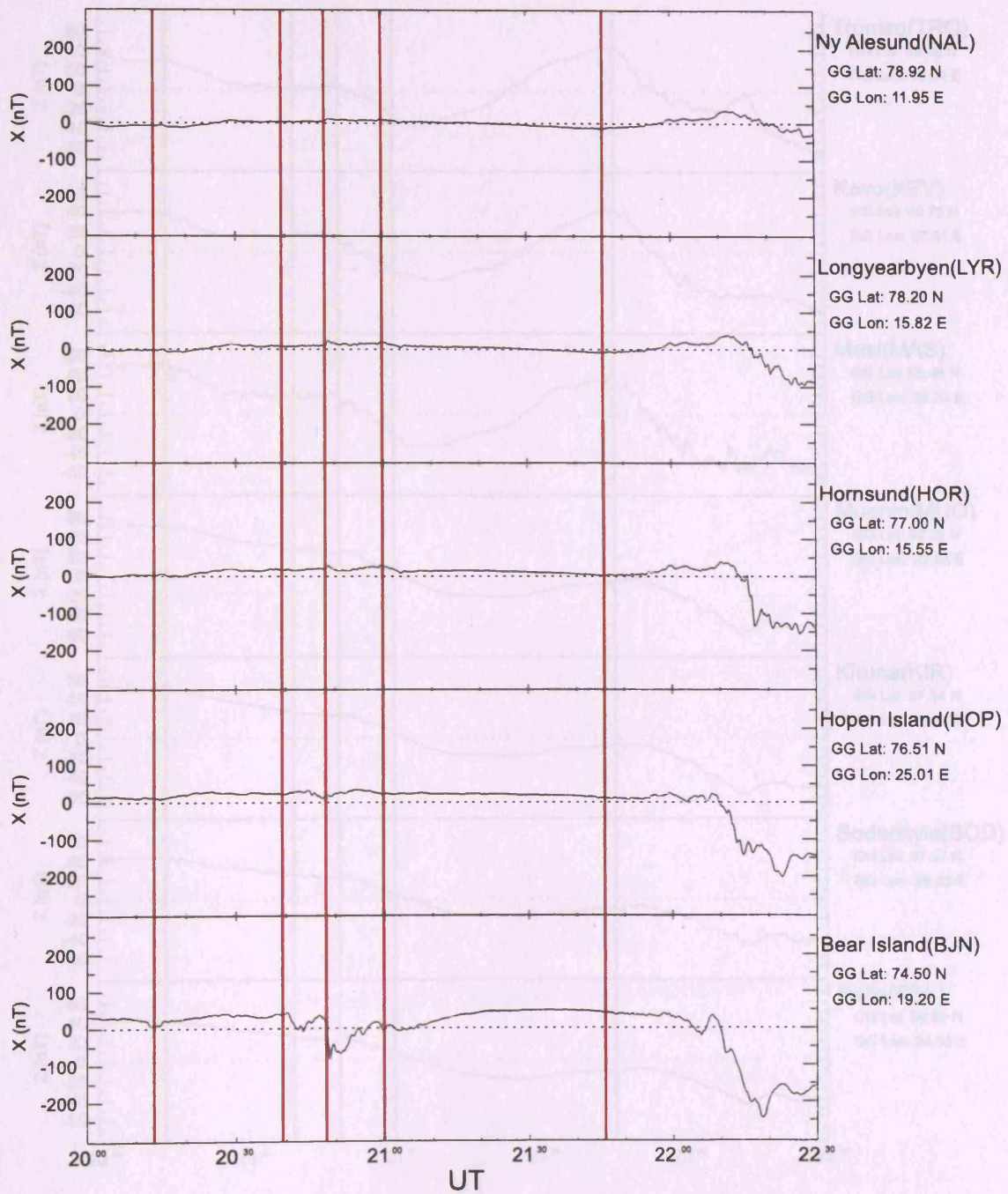


Figure 6.7: High-latitude X-component ground magnetometer data from IMAGE on 17/5/96.

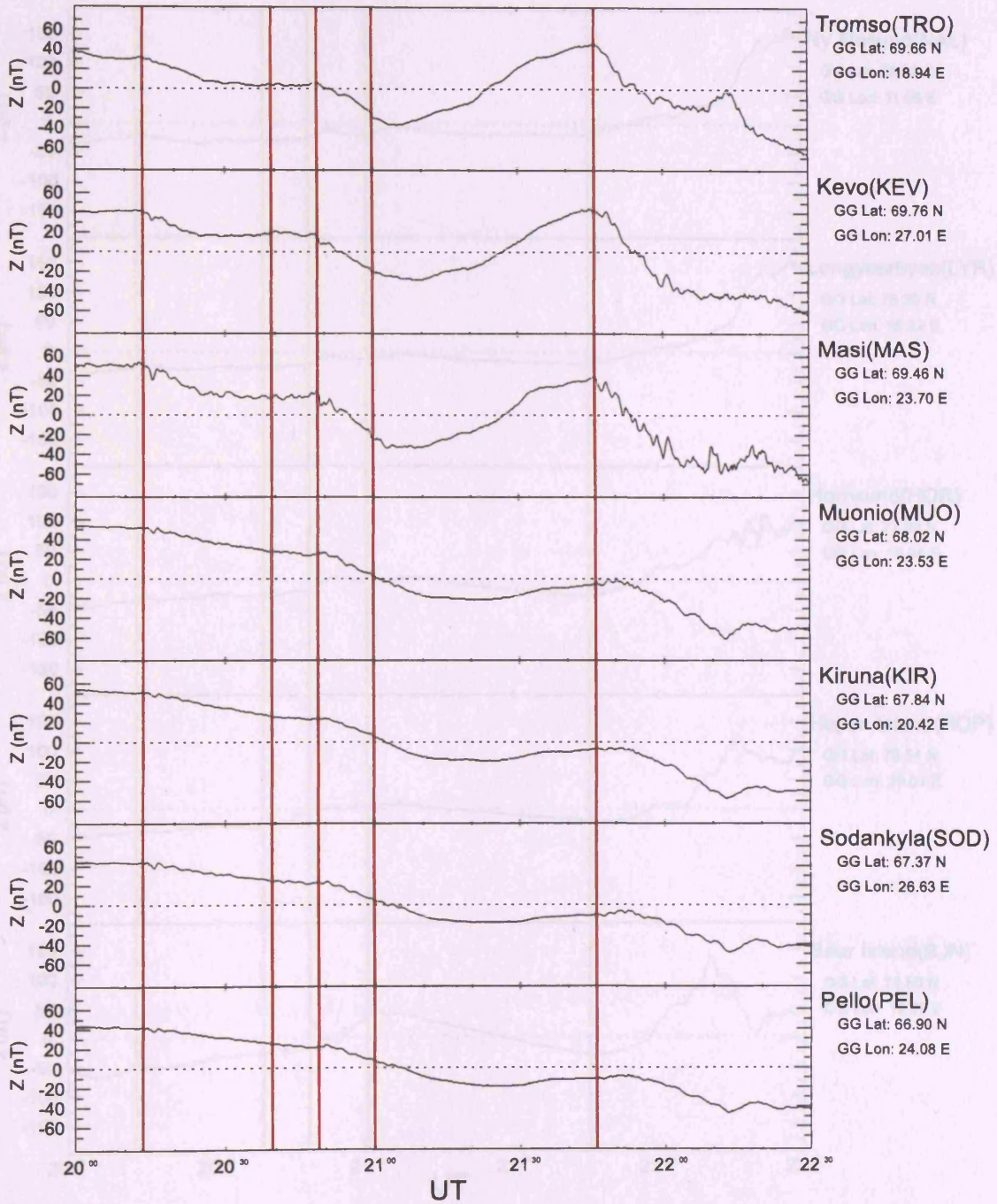


Figure 6.8: Auroral-latitude Z-component ground magnetometer data from IMAGE on 17/5/96.

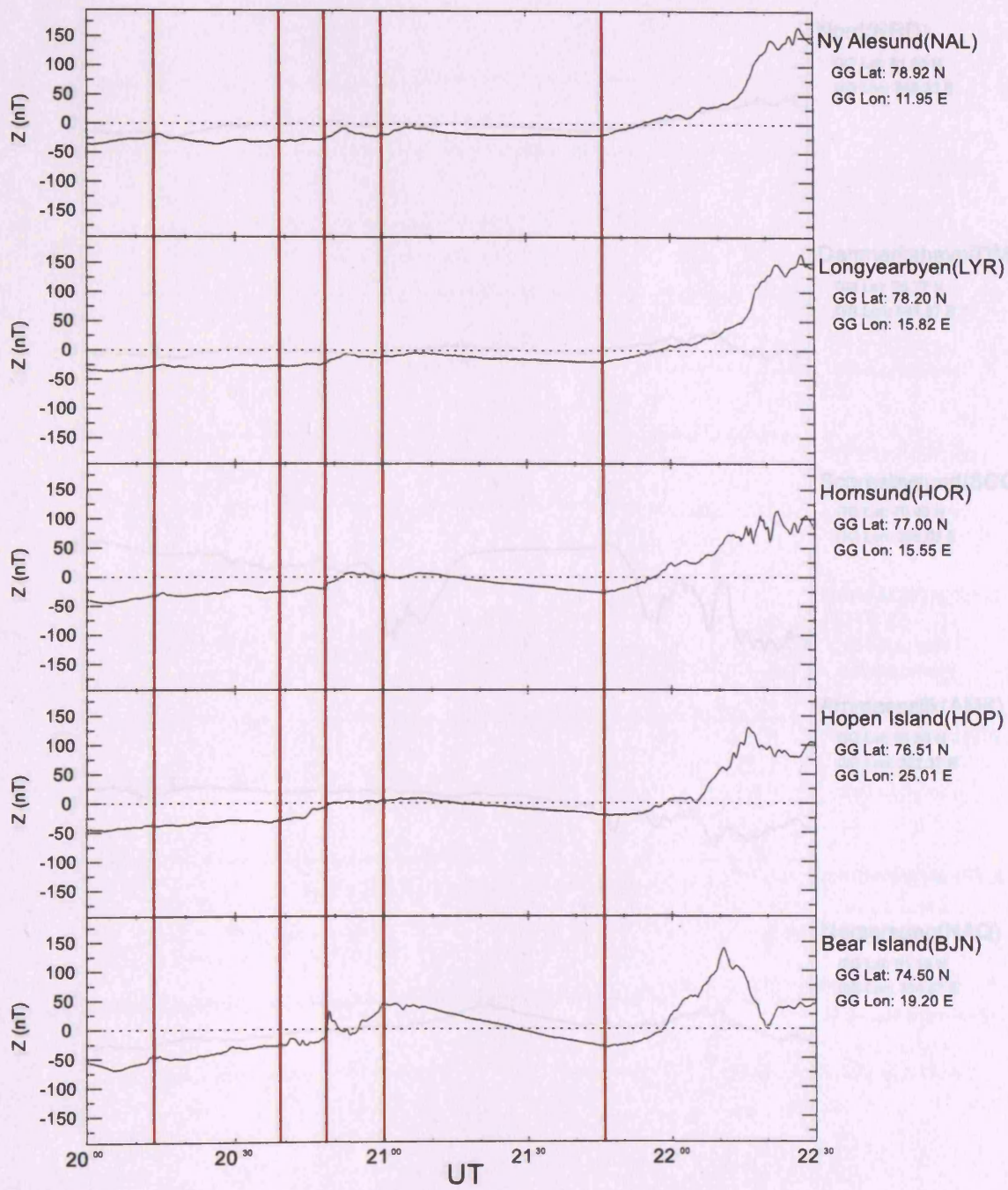


Figure 6.9: High-latitude Z-component ground magnetometer data from IMAGE on 17/5/96.

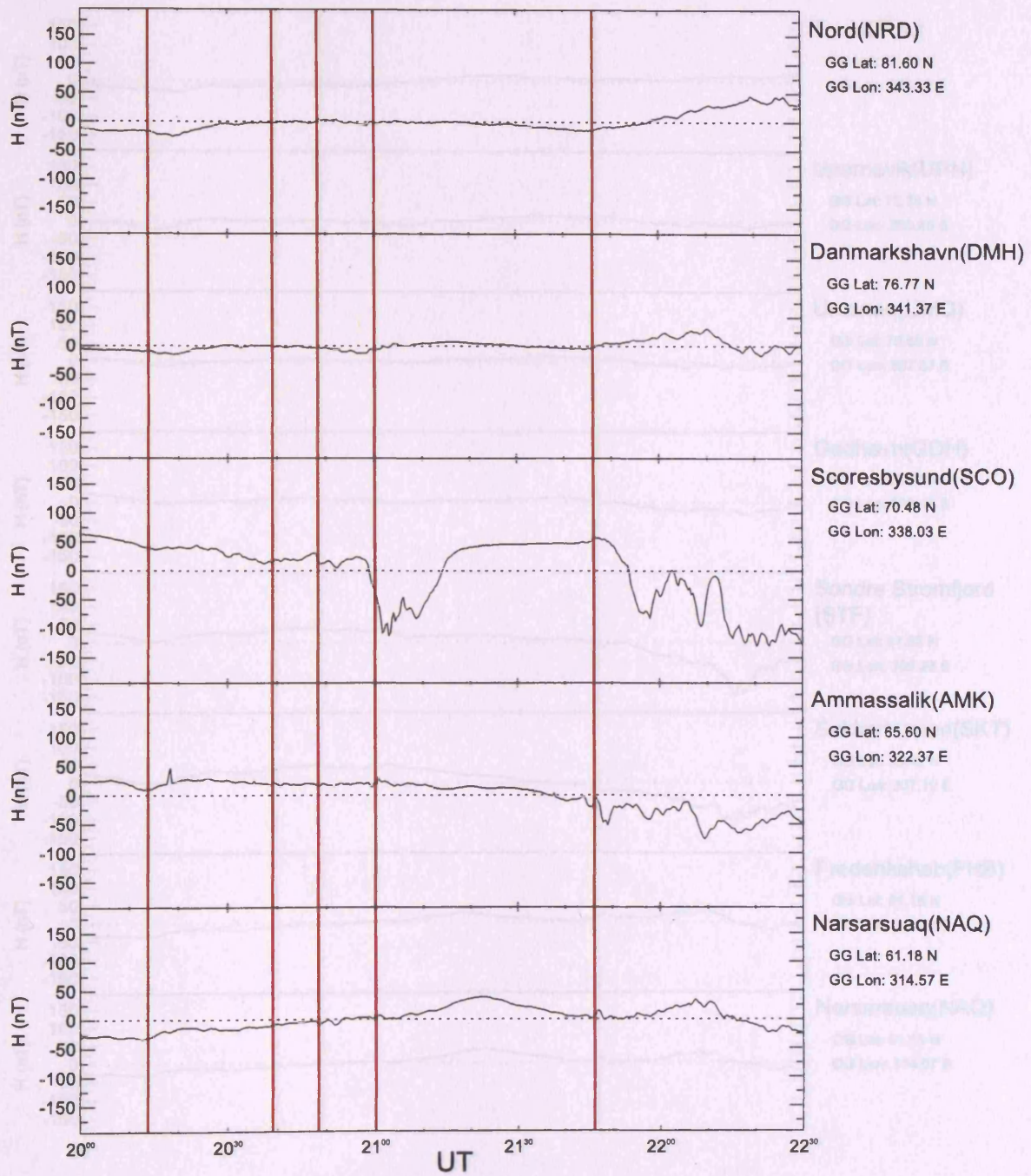


Figure 6.10: Greenland-East X-component ground magnetometer data on 17/5/96.

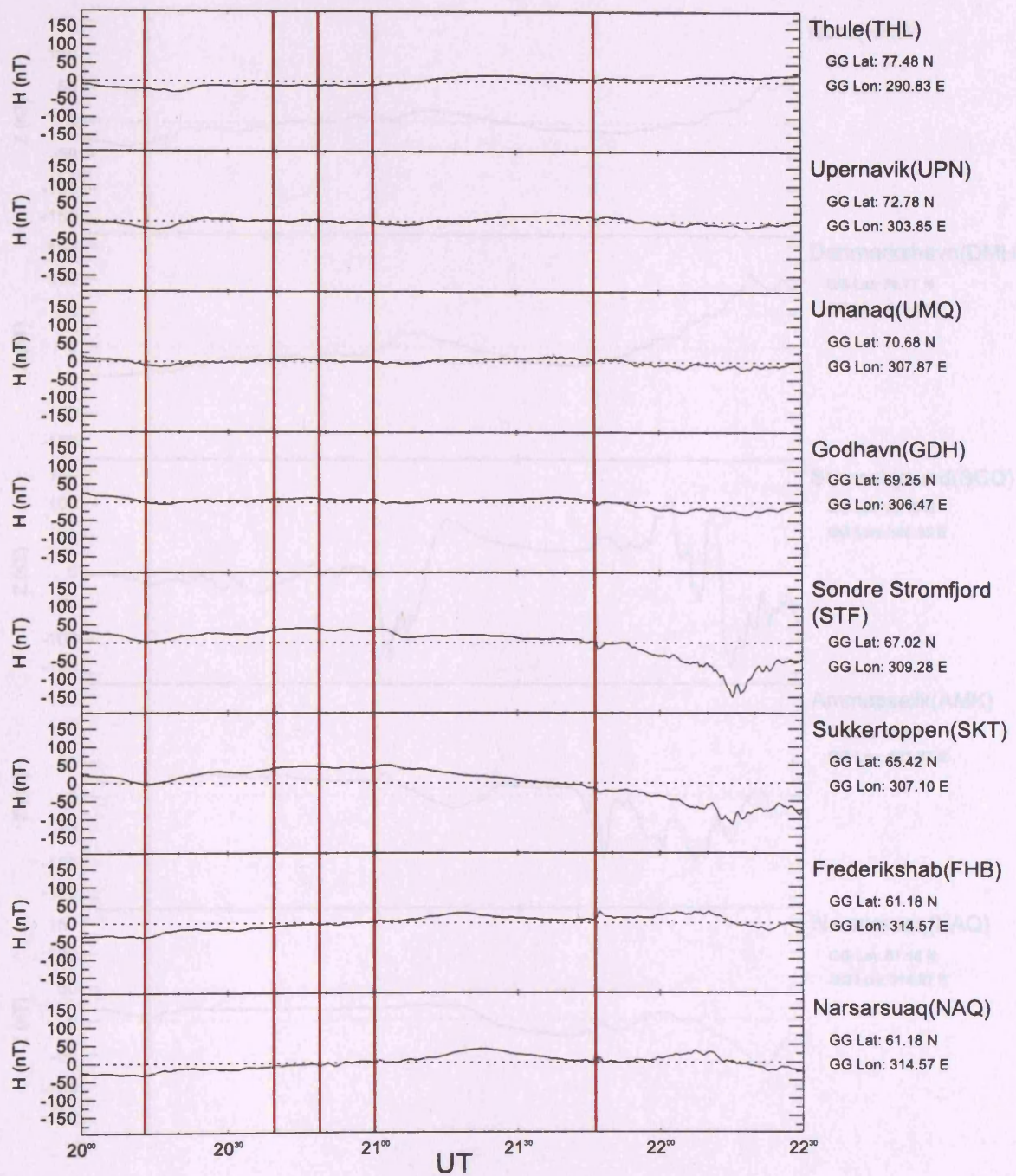


Figure 6.11: Greenland-West X-component ground magnetometer data on 17/5/96.

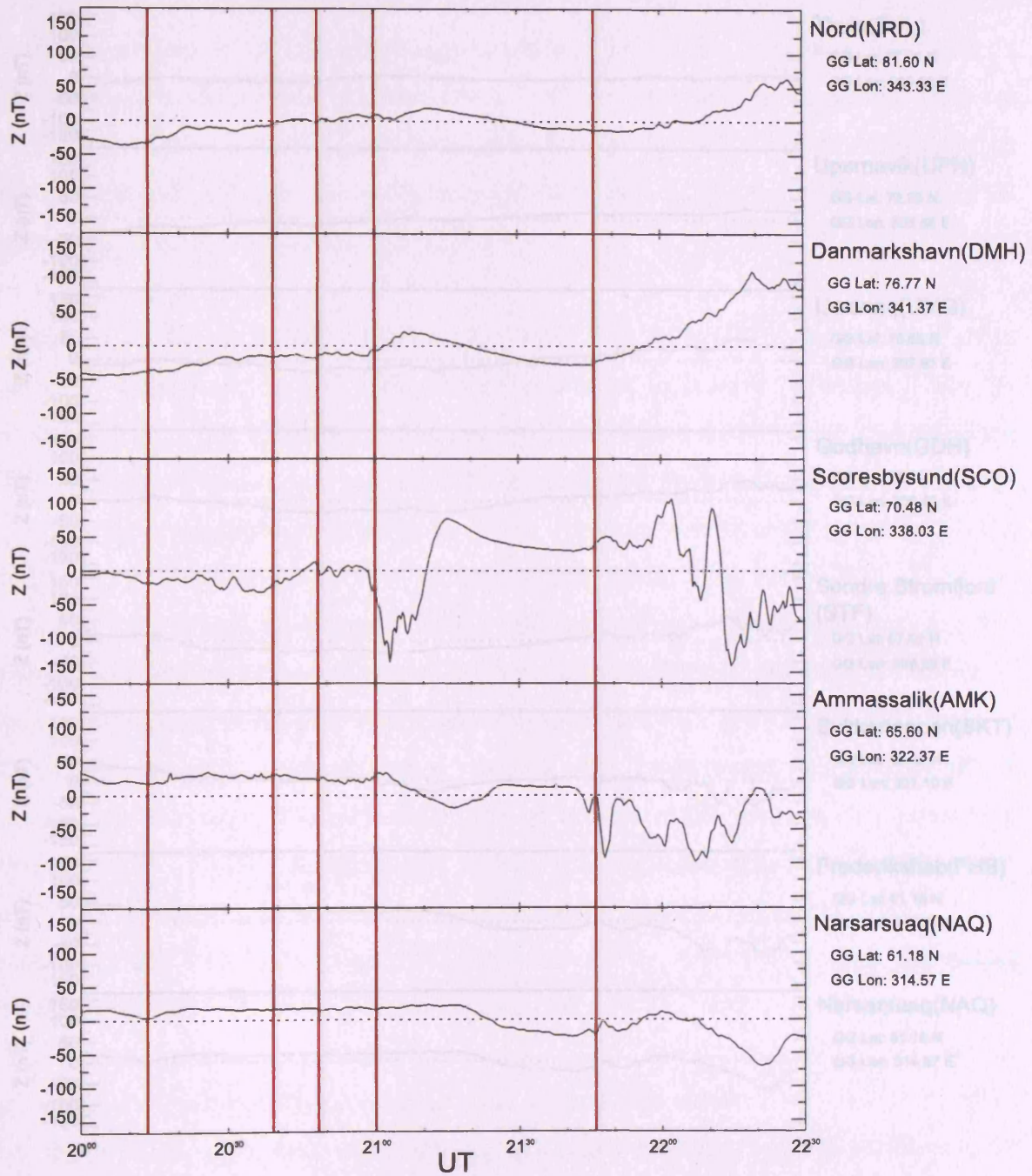


Figure 6.12: Greenland-East Z-component ground magnetometer data on 17/5/96.

the longitude of NOR (13.35 °E). At this time, only one of the higher-latitude stations, BJN, observed a large, negative ~120 nT X-component deflection (Figures 6.6 & 6.7), whereas the high-latitude stations remained undisturbed and the auroral-latitude stations experienced a small negative X-deflection. The Z-component variations followed a similar trend, with the auroral-latitude stations observing small negative deflections, and the high-latitude stations undergoing positive deflections. The largest deflection once again occurred at BJN, where a ~50 nT positive deflection was measured. These observations suggest a localised enhancement of the westward electrojet close to BJN (74.50 °N). The Greenland stations again experienced no significant deflections in either the X- (Figures 6.10 & 6.11) or Z- (Figures 6.12 & 6.13) components at this time.

At the time of the fourth Pi2 pulsation, 21:00 UT, the mid-latitude stations experienced negative X-deflections, except YOR, which measured a positive deflection. The Y-component echoed this difference, with negative deflections measured at all stations except YOR, where little variation was recorded. NOR underwent the largest negative deflection of ~8 nT. These observations suggest that the SCW was centred close to the longitude of YOR (358.95 °E), with the downward FAC occurring close to the longitude of NOR (13.35 °E). The higher-latitude stations observed very small, gradual deflections around this time, but nothing suggesting an enhanced electrojet. The Greenland-West stations also showed no large variations, and of the Greenland-East stations (Figures 6.10 & 6.12) only SCO observed a X-component negative magnetic bay of ~140 nT. The Z-component variations were more widespread. Once again, the main deflection occurred at SCO and was also negative, of magnitude ~150 nT. The stations south of SCO also showed negative deflections, but of much reduced magnitude, whilst the stations north of SCO measured small positive variations. These observations suggest that the centre of the westward electrojet was located at a latitude between SCO and DMH, but much closer to SCO (70.48 °N).

The clearest Pi2 pulsation that was observed at mid-latitude occurred at 21:46 UT (fifth red line). At this time, all of the mid-latitude stations measured positive X-deflections, with the maximum deflections occurring at YOR and NOR (~9 nT). The Y-component data followed a different trend, with all stations observing a negative deflection, except YOR that measured a positive deflection. The largest deflections occurred at OUJ (-16 nT) and YOR (+10 nT). These observations suggest that the SCW was centred between YOR and NOR at a longitude between 358.95 °E and 13.35 °E (~7 °E). The other mid-latitude stations were all located at longitudes within the SCW, with the downward FAC close to or east of OUJ. At the auroral-latitude stations the X-component underwent a gradual negative deflection, seen at stations

from MAS up to and including TRO, with TRO experiencing the largest deflection of ~ 130 nT. The high-latitude stations were subjected to no variations at this time, but showed a large negative deflection at 22:09 UT. The Z-component also underwent deflections at this time, with negative deflections seen at the auroral-latitude stations and positive deflections seen at high-latitude. At 22:09 UT the high latitude Z-component is somewhat different. Both BJN and HOP observed negative deflections, with HOR, LYR and NAL measuring positive deflections. These observations suggest that at 21:46 UT the enhanced westward electrojet was centred at a latitude between TRO (69.66°N) and BJN (74.50°N). However, the centre of the enhancement moved north, until by 22:09 UT the centre of the electrojet was now between HOP (76.51°N) and HOR (77.00°N). The Greenland-East stations also observed magnetic fluctuations at 21:46 UT in the form of a large (~ 140 nT) negative bay at SCO and a small negative deflection at AMK. The Z-component data showed negative deflections south of SCO, which measured only a small positive deflection, and stronger positive deflections northwards. However, a short time later, the SCO deflections became negative, whilst the stations northward of SCO continued to measure positive deflections. The Greenland-West magnetometers showed very little at 21:46 UT, but began to show an X-deflection at $\sim 22:00$ UT at STF and the stations further south. Similarly, the Z-component did not show any significant variations until after the Pi2 pulsation occurred. The deflections then took the form of negative deflections in the stations south of STF, with positive deflections observed north of this station. These observations suggest that the activity observed by the Scandinavian magnetometers was also experienced by the stations on the east coast of Greenland, specifically SCO, which is at very similar latitudes to the IMAGE stations. Specifically, an enhanced westward electrojet was observed by the Greenland East stations, centred very close to SCO (70.48°N). As the Greenland West stations do not observe any variations until $\sim 22:00$ UT, the activity did not expand that far west for some 15 minutes, when it was observed by the western stations, with the electrojet centred between STF and FHB at a latitude of $\sim 66^\circ\text{N}$. Therefore, the final packet of activity is seen to expand both polewards and westwards, which is typical of the substorm expansion phase. Of the five Pi2 pulsations that occur during the interval, only the last has magnetic signatures typical of the expansion phase.

6.3.3. Polar Ultra-Violet Imager (UVI)

As in Chapter 5, the Polar UVI is used in this study to allow the in-situ magnetospheric observations to be placed in context with the substorm auroral activity in the ionosphere. There is significant magnetic variability during this interval to suggest some substorm activity. In order to relate directly the in-situ and remotely sensed observations, the spacecraft

footprint is mapped down to the ionosphere as described earlier and plotted on the UVI images as a black and white cross. The UVI images from the whole interval can be found in Appendix 3 whilst certain relevant images will be included in this chapter. As mentioned earlier the different filters and integration rates provide a LBHI (36 s) image approximately every 6 minutes, although data gaps do occur due to instrument realignment.

At 20:01 UT, a patch of aurora covered an area from 7 °W to 15 °E, and spanning perhaps 2 or 3 ° latitude around 70 °N. This small patch had completely died away by 20:07 UT. The next image at 20:13 UT indicates another patch, covering an area from 0 – 30 °E and poleward of the previous patch. This region had almost dissipated by 20:19 UT when another patch began to form in the west, which was fully developed by 20:25 UT. This patch, spanning 0 – 22 °W, was still around the 70 °N latitude before it began to disperse, such that only a small amount of auroral luminosity existed by 20:31 UT. The remaining luminosity intensified slightly at 20:38 UT, but a larger intensification occurred at 20:44 UT (Figure 6.14), which was much more widespread and of greater magnitude. This new area was slightly polewards of the pre-existing arc, and to the East, covering an area from 15 – 30 °E. By 20:49 UT (Figure 6.15) the two separate features had become connected so the active patch now covered 30 °W – 30 °E. This is also the time that the spacecraft footprint entered this poleward-most arc. This new active area began to fade almost immediately, until little activity remained by 20:55 UT. At 21:01 UT there was a much more intense brightening covering the 0 – 30 °W area (Figure 6.16). However, this auroral activity was also relatively short-lived, and had faded by 21:07 UT. These two intensifications had both been short-lived, quite localised and had undergone no apparent significant poleward expansion and it seems likely that these features can be attributed to pseudobreakups. The next series of images (21:13 – 21:41 UT) shows that there was very little activity during this period, but that the auroral oval moved equatorwards. This equatorward motion continued until the spacecraft footprint appears to exit the oval at 21:35 UT. By 21:41 UT there is even less activity with the spacecraft footprint being polewards of a quiet region. This equatorward motion is difficult to judge from the existing images and so Figure 6.17 has been produced. This is a ‘keogram’ of the UVI data taken along the 22:30 MLT meridian and, as such, presents the location of the auroral activity along one line of MLT as a function of magnetic latitude and UT. Although data are shown for the whole interval, the period of 20:49 – 21:41 UT is discussed first. Initially the auroral activity covered magnetic latitudes of 67.5 – 73.5 °. As time progressed this activity dissipated until there was coverage of only 67.5 – 70.0 ° at 21:13 UT. At this time Polar’s footprint was still located within the auroral oval. The active aurora then moved equatorwards such that the auroral luminosity was now ~1 ° lower at 21:19 UT, but Polar’s footprint still remained inside

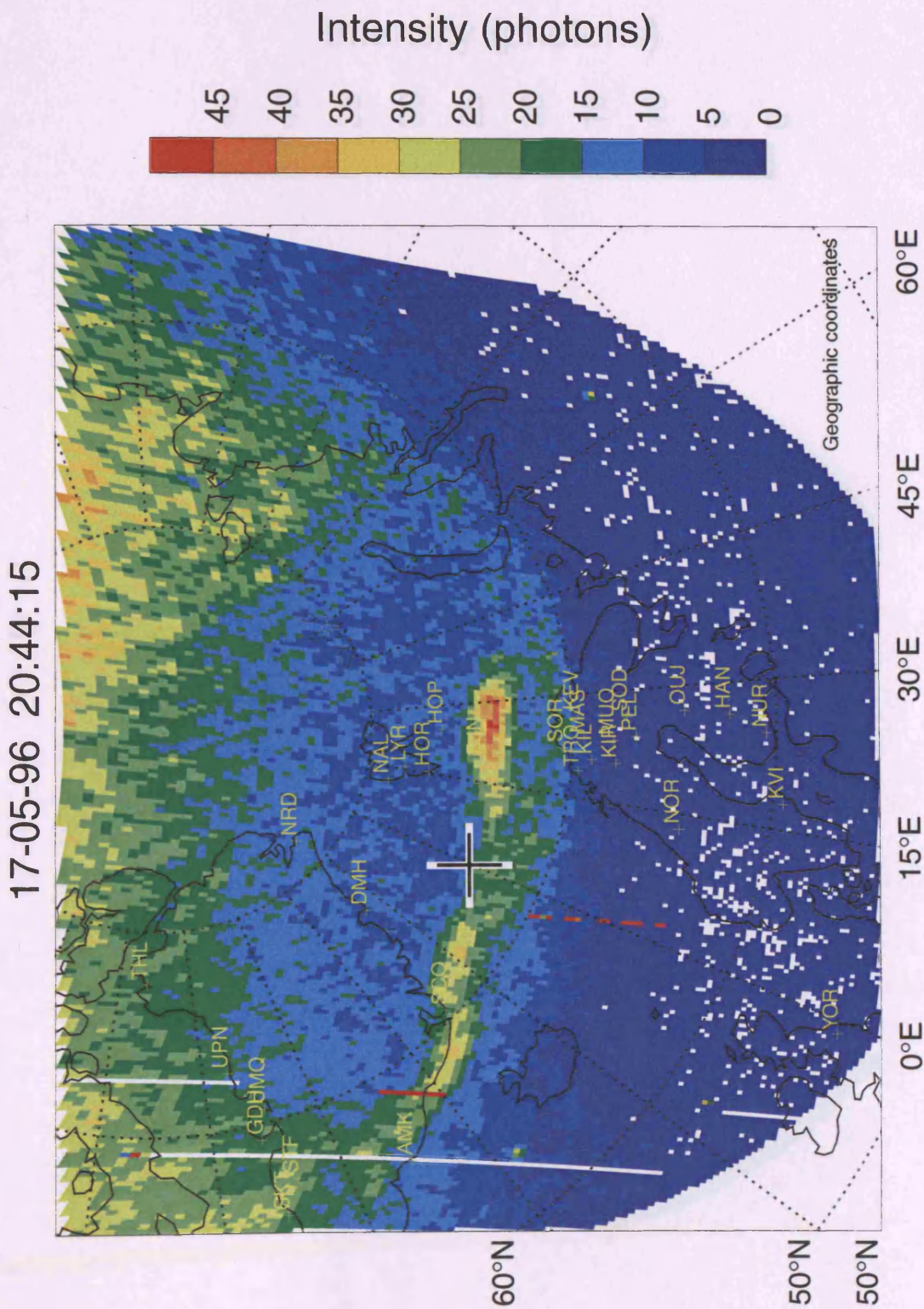


Figure 6.14 An image from UVI taken at 20:44 UT on 17/5/96.

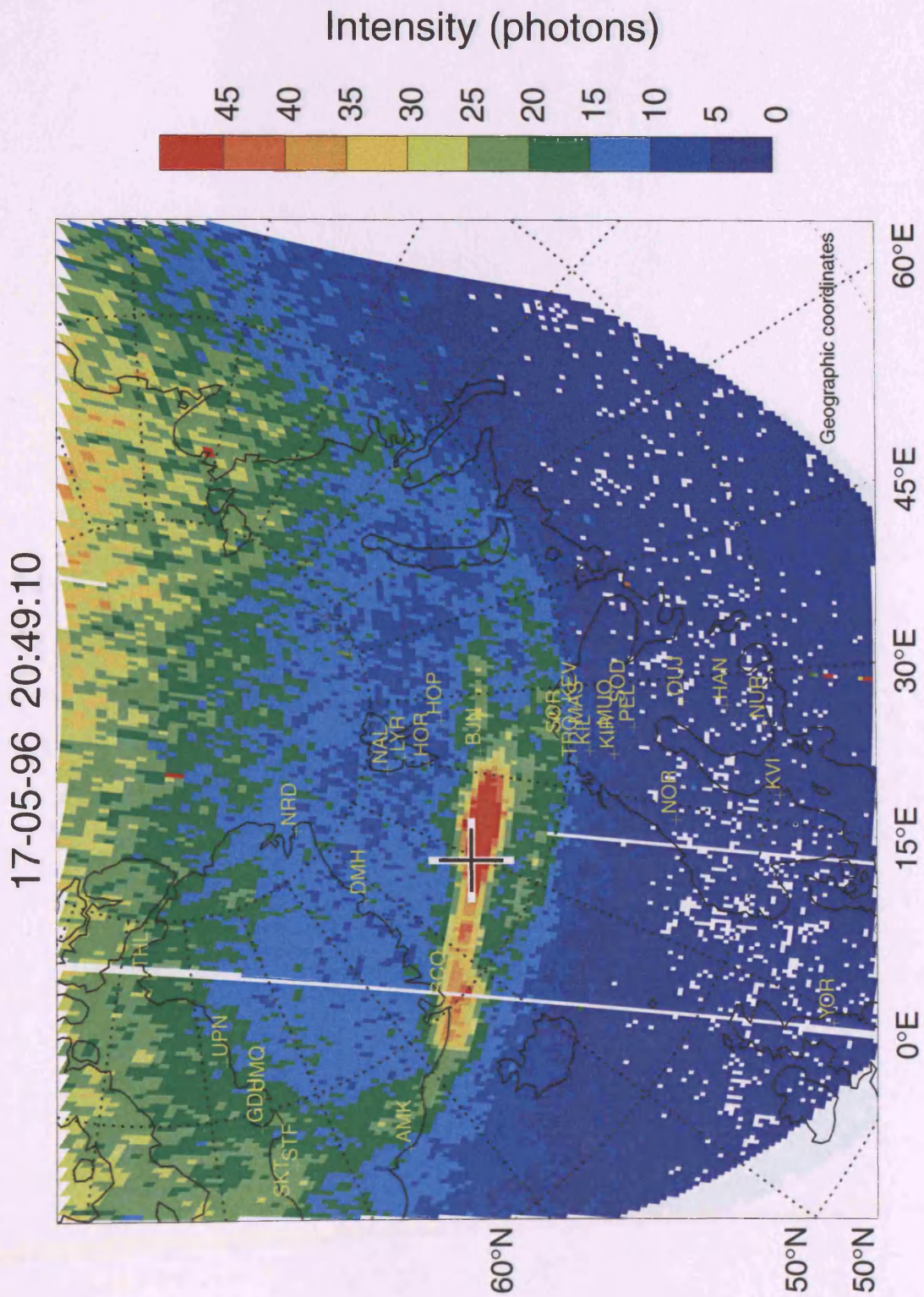


Figure 6.15: An image from UVI taken at 20:49 UT on 17/5/96.

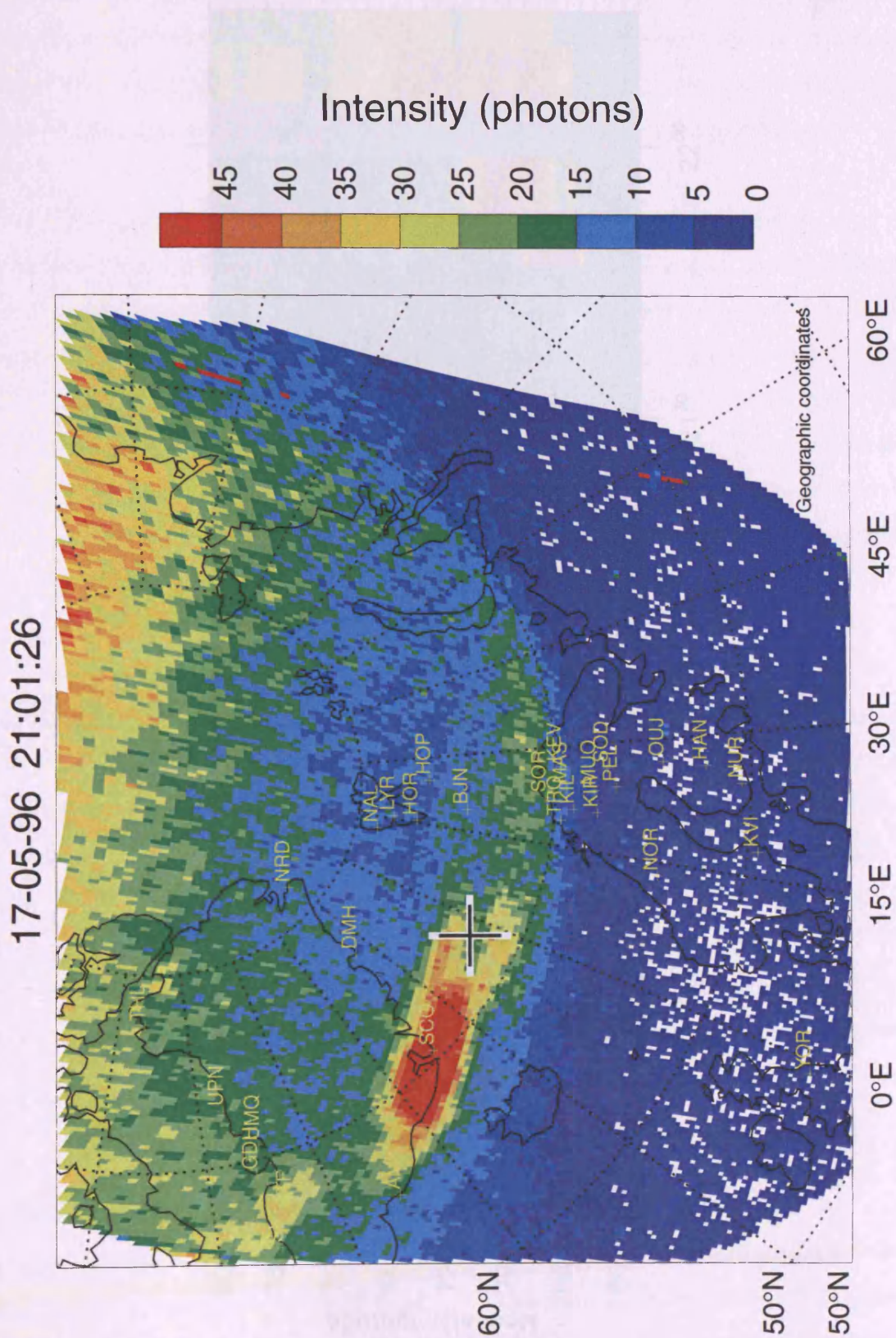


Figure 6.16: An image from UVI taken at 21:01 UT on 17/5/96.

the oval. This was followed by a decrease in the auroral activity such that the auroral luminosity dropped to near background levels. At 21:57 UT, following this there was a further expansion of the auroral oval moving to magnetic latitudes of 56.5–57.0°. The equatorward motion was only ~1° this approach.

At 21:47 UT (Figure 6.17) the auroral oval moved to magnetic latitudes of 56.5–57.0°. The equatorward motion was only ~1° this approach.

At 21:53 UT, such that the auroral oval moved to magnetic latitudes of 56.5–57.0°. The equatorward motion was only ~1° this approach.

There is also a significant expansion of the auroral oval. This is accompanied by a decrease in the auroral activity such that the auroral luminosity dropped to near background levels.

At 21:57 UT, following this there was a further expansion of the auroral oval moving to magnetic latitudes of 56.5–57.0°. The equatorward motion was only ~1° this approach.

At 21:53 UT, such that the auroral oval moved to magnetic latitudes of 56.5–57.0°. The equatorward motion was only ~1° this approach.

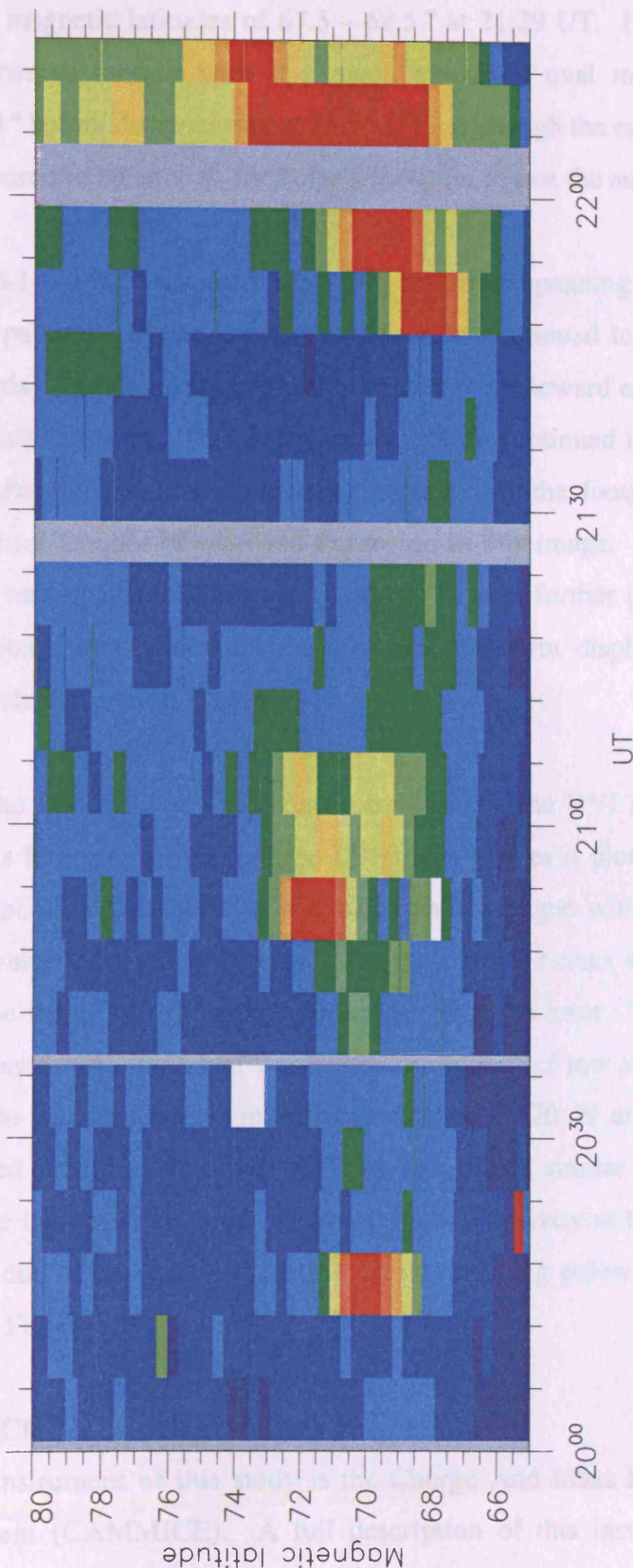


Figure 6.17: A keogram of UVI data taken along the 22:30 MLT meridian to show the motion of the auroral oval throughout the interval.

the oval. This was followed by a decrease in the auroral activity such that the auroral luminosity dropped to magnetic latitudes of $67.5 - 68.5^\circ$ at 21:29 UT. Following this there was a further equatorwards motion with this much quietened oval moving to magnetic latitudes of $66.5 - 67.0^\circ$ before disappearing at 21:35 UT. Although the equatorwards motion was only $\sim 1^\circ$ this appeared to be enough for Polar's footprint to exit the auroral oval.

At 21:47 UT (Figure 6.18) a new auroral brightening occurred, spanning a much larger area than previous auroral patches. This auroral intensification continued to spread, expanding polewards and eastwards. The poleward expansion caused the poleward edge of the aurora to move over the spacecraft footprint. This poleward expansion continued in the next image at 21:53 UT, such that the arc had now completely passed over the footprint (Figure 6.19). There is also a significant amount of eastward expansion in this image. This intensification continued in the final two images at 22:05 and 22:11 UT, with further poleward expansion accompanied by westward expansion; a classic auroral substorm display. The poleward expansion can also be clearly seen in Figure 6.17.

Figure 6.20 presents the UVI data in a different format. Here the UVI intensity (as photon flux) at the spacecraft's footprint for each of the LBHI 36 s images is plotted as a function of time. To do this the pixel at the footprint was taken and averaged with the surrounding 8 pixels, giving a mean value and associated error. The mean value occurs where the horizontal stroke is placed and the length of the vertical stroke indicates the error. The plot shows that before 20:44 UT the spacecraft's footprint was located in regions of low auroral activity. The footprint then began to observe higher intensities, peaking at 20:49 and 21:01 UT. The intensity then decreased such that by 21:41 UT it was at a level similar to the initial value. Another sharp increase indicates the onset of strong auroral activity at the footprint, which once again decreases, due on this occasion to the activity moving polewards away from the spacecraft as shown in Figure 6.19.

6.3.4. Polar CAMMICE

The primary particle instrument of this study is the Charge And Mass Magnetospheric Ion Composition Experiment (CAMMICE). A full description of this instrument is given in Chapter 3. The particle observations made by CAMMICE during the interval are presented in Figure 6.21, where the top three panels present colour-coded ion count rate versus energy per charge for O^+ and O^{++} (top panel), He^{++} (second panel), H^+ (third panel) and DCR (fourth panel) in the $\sim 1 - 200$ keV/q energy range. As described earlier, DCR represents approximately all the ions entering the instrument. The bottom panel shows pitch angle

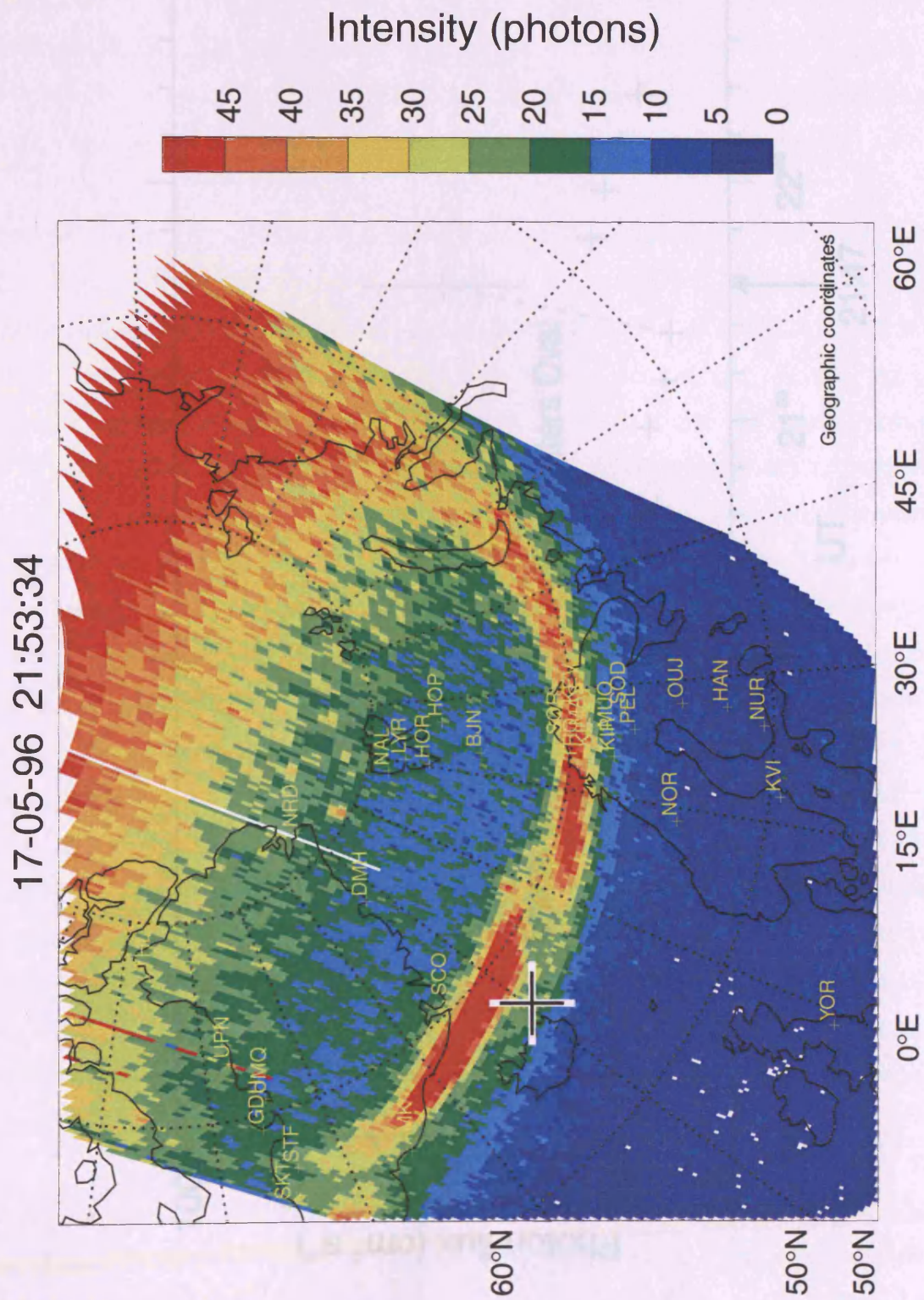


Figure 6.19: An image from UVI taken at 21:53 UT on 17/5/96.

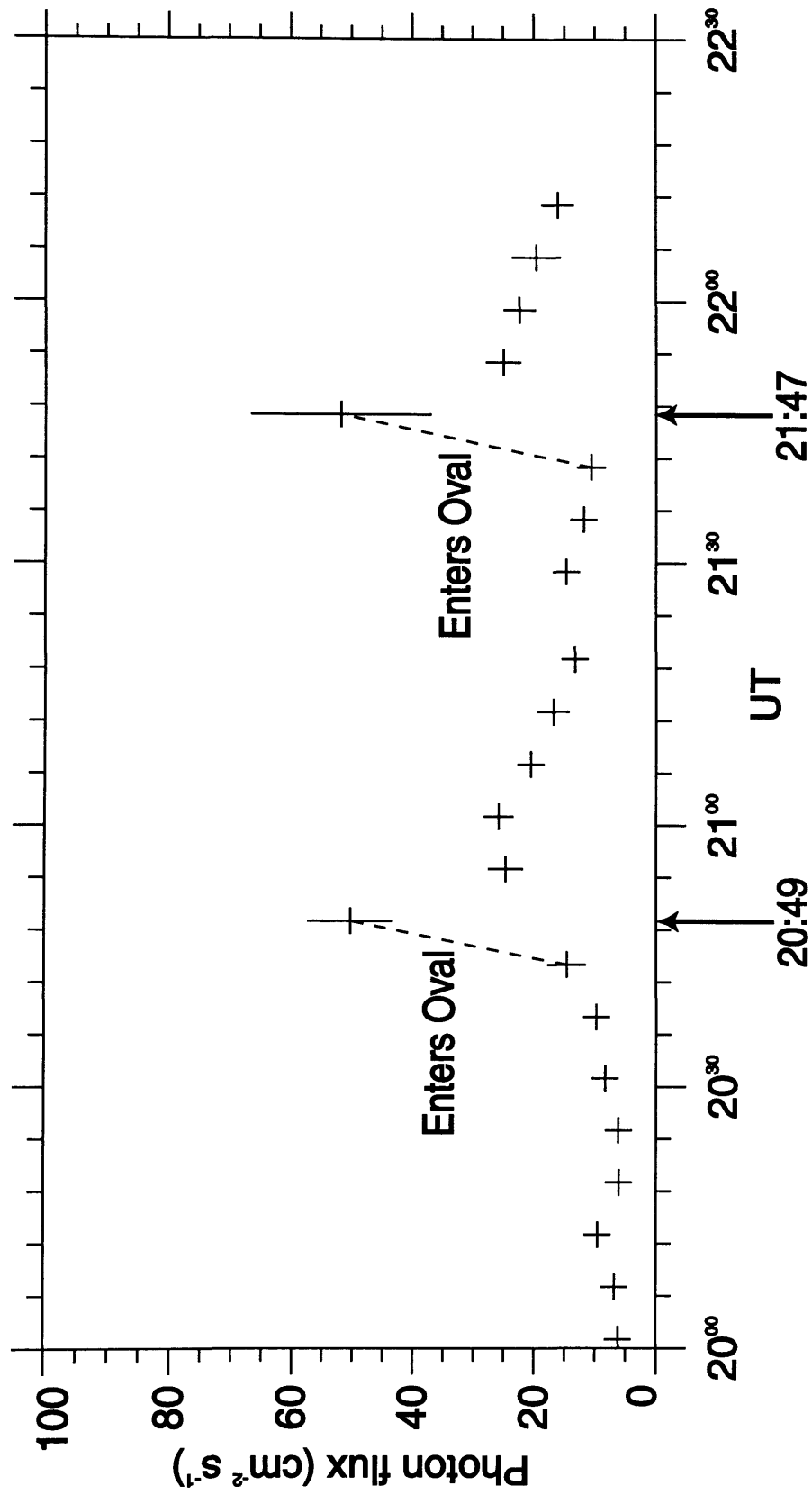


Figure 6.20: Plot of UVI intensities along the spacecraft's footprint.

information for DCR with 0° (and 360°) representing the direction parallel to the magnetic field, termed field-aligned in this chapter, and 180° representing the direction antiparallel to the magnetic field, termed field-opposed. The ions shown are representative of both ionospheric (O^+/O^{++}) and solar wind sources (He^{++}). Throughout this interval there are fewer ions of ionospheric origin than of solar wind origin, but the dominant ion is H^+ which can come from either source. As the integration time for each scan is relatively long (197.5 s), all times discussed below refer to the start time of the integration period as in Chapter 5.

The interval begins with CAMMICE observing very low particle counts in all energy bands, indicating that the spacecraft was on open field lines in the tail lobe. This remains the case until 20:49 UT (first red arrow), the start of the first sample after the third Pi2 pulsation was observed in the mid-latitude magnetometer data during the interval. At this time the instrument observed an increase in ion count rate for the DCR, H^+ and He^{++} species primarily in the 10 – 100 keV energy range. The DCR pitch angle data (bottom panel) indicates that a small field-opposed ion beam was also observed at this time. This is more clear in the energy range, pitch angle data (Figure 6.22). This figure presents the DCR pitch angle data separated into four energy bands, with red arrows marked as in Figure 6.21. This first ion beam lasted only one sampling interval (197.5 seconds), but occurred over three energy ranges spanning 1 – 13 keV. The count rate was further enhanced at 21:01 UT (second red arrow), around the 10 – 100 keV energy range in the DCR panels (Figure 6.21), which is coincident with the first sample after the fourth Pi2 pulsation had been observed. The energy range of these enhancements began to drop over the next 30 minutes, until the ion count rate and energy drop to levels associated with the tail lobes or open field lines by 21:37 UT. Once again, field-opposed ion beams were in evidence (Figure 6.22). This time, a longer-lived ion beam, 20:58 – 21:10 UT, was observed mostly over two energy ranges spanning 1- 5.6 keV. This was followed by a weak, field-opposed ion beam at 21:26 – 21:30 UT in the energy range 1.8 – 5.6 keV, which was in turn followed by the count rate returning to background values as described above.

The count rate increased isotropically at 21:44 UT (Figure 6.21 – third red arrow) between ~20 – 50 keV in DCR, H^+ and He^{++} . Another field-opposed ion beam was observed just afterwards at 21:47 UT in the energy range 1 – 13.2 keV (Figure 6.22). This slightly preceded a much larger ion increase in both counts and energy at ~21:55 UT, once more in both DCR and He^{++} . These variations occurred at approximately the same time as the fifth Pi2 pulsation observed by the mid-latitude magnetometer stations during the interval at

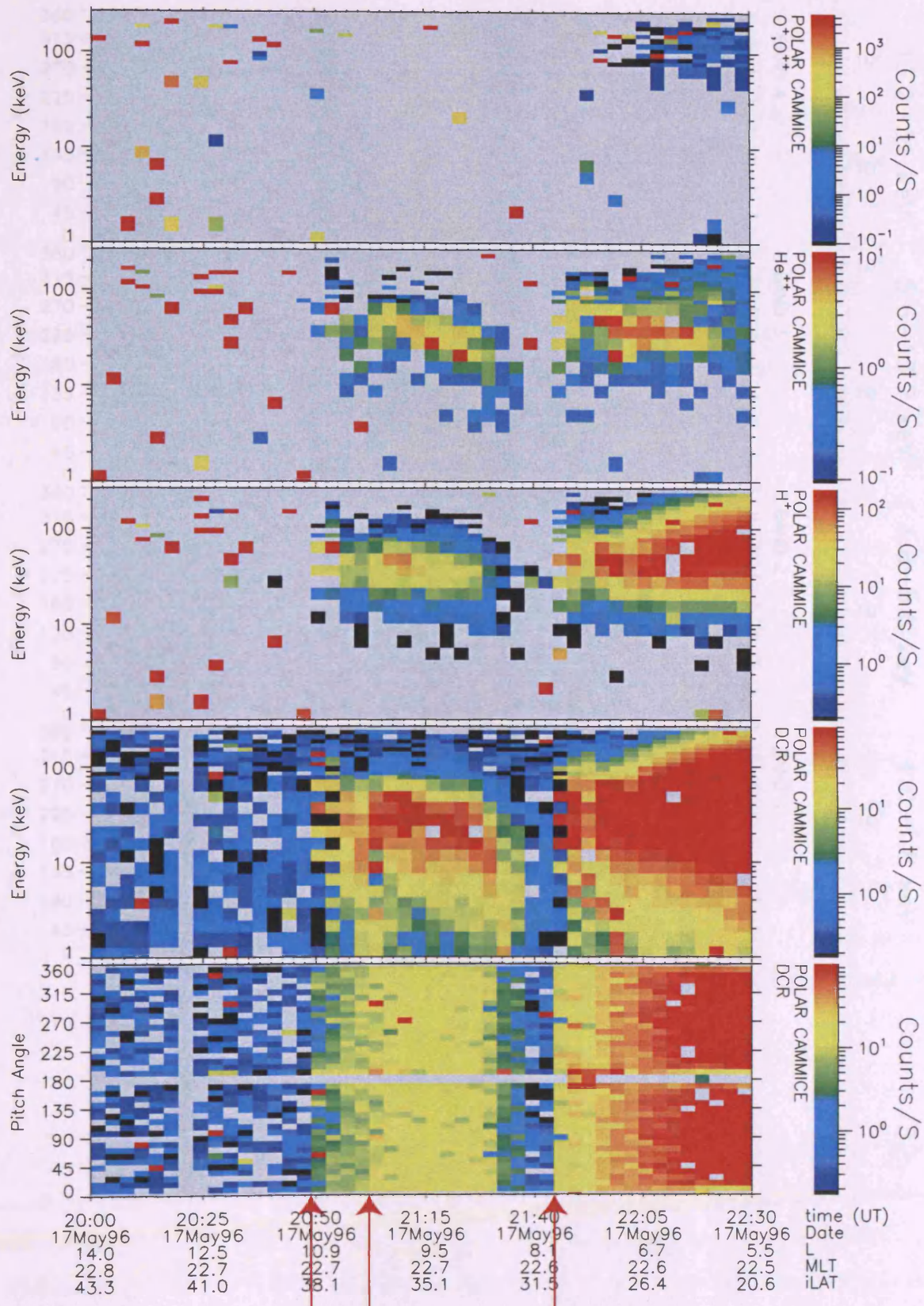


Figure 6.21: CAMMICE particle data showing colour-coded ion counts versus energy per charge for the various species in the top four panels, and the pitch angle in the bottom panel.

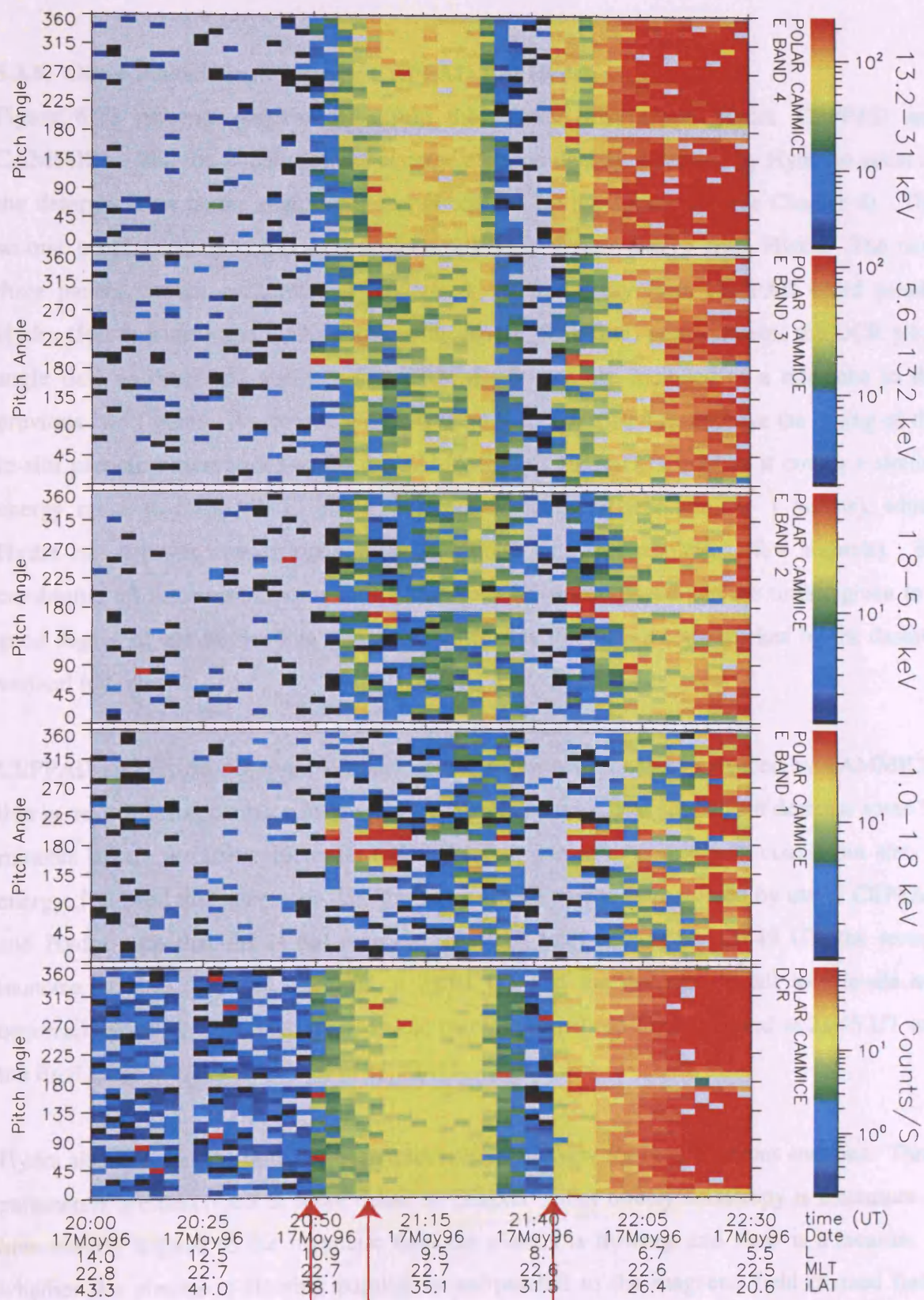


Figure 6.22: CAMMICE particle data showing colour-coded ion counts versus pitch angle separated into energy bins in the top four panels, with the plot for all energies in the bottom panel.

21:46 UT. The spacecraft then descended into the low latitude regions of the magnetosphere until the end of the interval.

6.3.5. Other Particle instruments: CEPPAD and Hydra

Figure 6.23 presents particle data from the particle instruments Hydra, CEPPAD and CAMMICE. The top panel presents average electron density measured by Hydra to assist in the determination of the region currently occupied by the spacecraft (see Chapter 4). The second panel presents colour-coded electron counts versus energy from Hydra. The next three panels present colour-coded ion counts versus energy from CEPPAD (third panel), Hydra (fourth panel) and CAMMICE (fifth panel). The final panel presents the DCR pitch angle data as described above. The CAMMICE data are included as a reference to the previous two figures. As before, CEPPAD and Hydra are used to improve the timing of the in-situ particle observations made by CAMMICE. CEPPAD is used as it covers a similar energy range to CAMMICE, but with improved temporal resolution (~ 1 minute), whilst Hydra has a lower energy range, but very good temporal resolution (few seconds). By combining all three instruments the features can be characterised and the timing given to a good degree of accuracy. The revised times for the three events are marked by the dashed, vertical red lines.

CEPPAD and Hydra observed similar particle features to those experienced by CAMMICE, that is, an initial ion increase followed by a further increase and subsequent decrease some 30 minutes later. A further increase and still larger increase, not only in counts but also in energy, followed this decrease. The timings of these events were refined by use of CEPPAD and Hydra such that the initial increase (first red line) occurred at 20:49 UT, the second increase (second red line) occurred at 21:01 UT and the decrease to tail lobe levels had occurred by 20:36 UT. The next particle increase (third red line) occurred at 21:45 UT and the final, large increase occurred at 21:53 UT.

Hydra also has the ability to measure anisotropy and skew for both electrons and ions. These parameters are described in more detail in Chapter 5, but briefly anisotropy is a measure of how closely aligned to the magnetic field the plasma is flowing, and skew is a measure of whether the plasma is flowing parallel or antiparallel to the magnetic field (termed field-aligned and field-opposed). These data can be found in Figure 6.24, which presents electron anisotropy, skew and counts data in the top three panels, and similarly for ions in the bottom three panels.

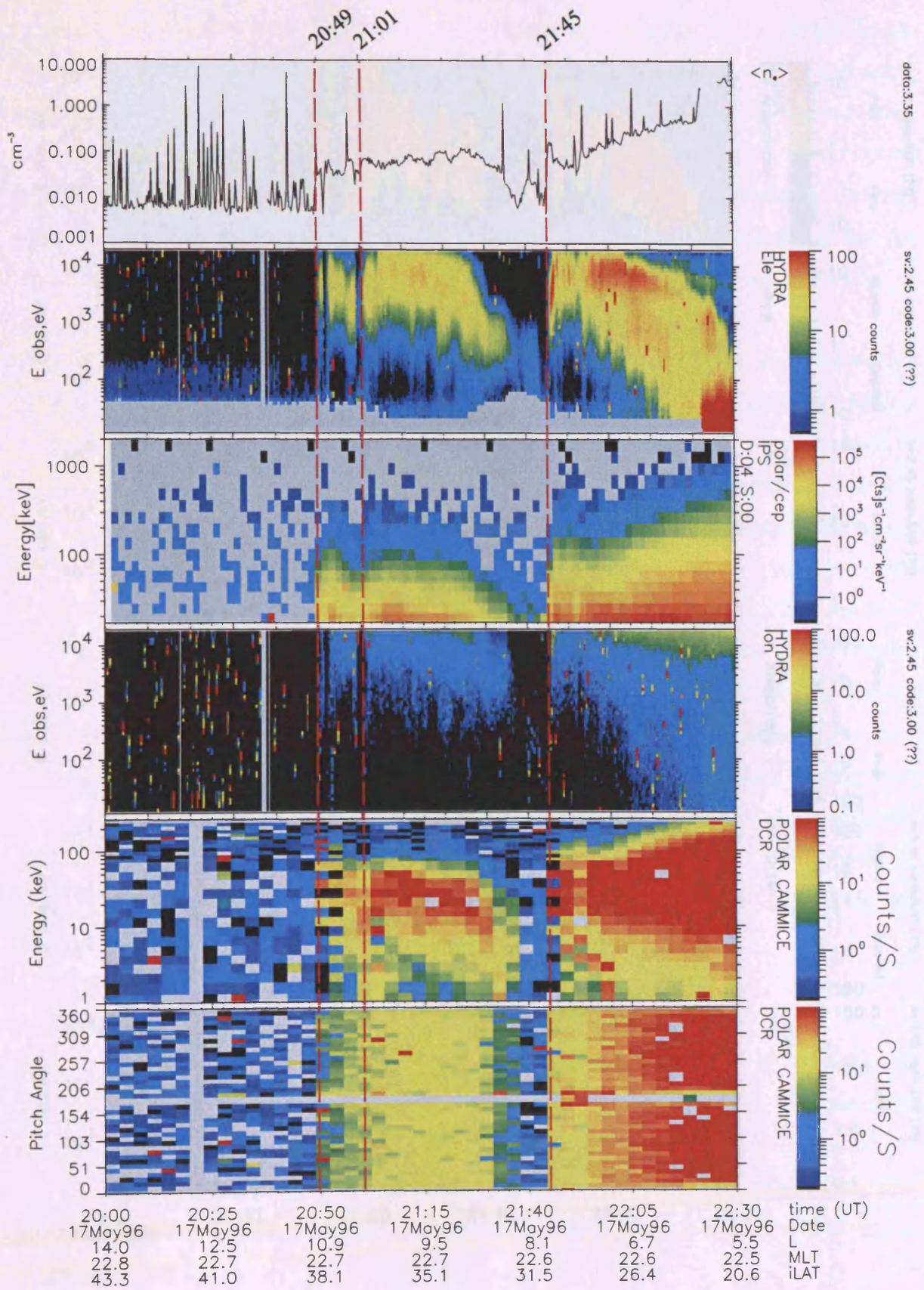


Figure 6.23: Particle data from CAMMICE, Hydra and CEPPAD showing counts versus energy for the ions in the bottom four panels, and the average electron density in the top panel.

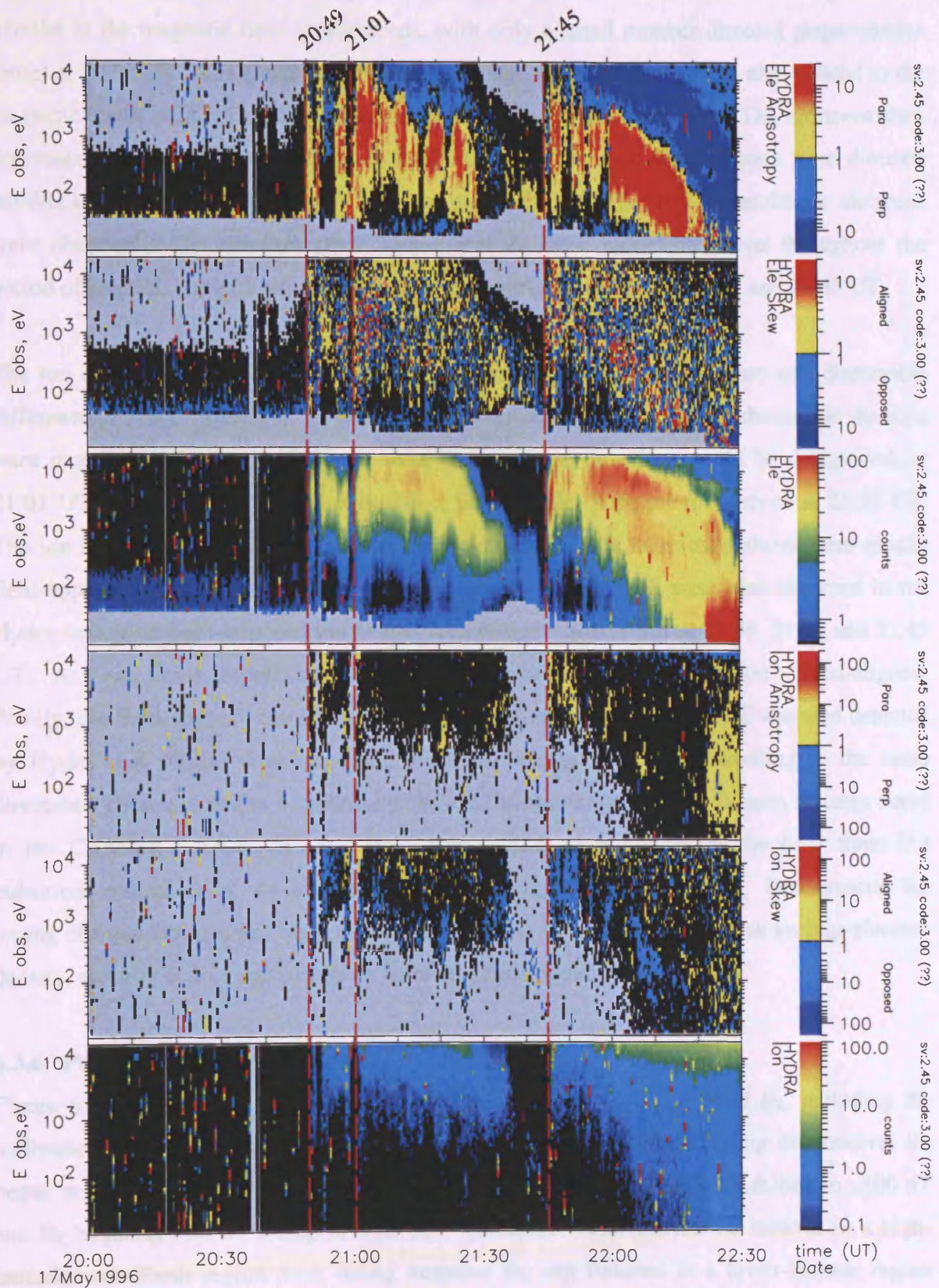


Figure 6.24: Particle data from Hydra showing counts, skew and anisotropy versus energy for both ions and electrons.

There are two... magnetic field variations observed by the IMF instrument during this interval. To make the variations more clear Figure 6.26 has been produced, which presents the three components and the magnitude of the magnetic field as

At 20:49 UT the electron anisotropy (panel 1) shows that the electrons were mainly directed parallel to the magnetic field (yellow/red), with only a small number directed perpendicular (blue) at 20:54 UT. The electrons at the further increase at 21:01 UT were also parallel to the magnetic field, with no parallel component occurring until 21:08 UT. The electrons then decreased before the next increase at 21:45 UT. Once again the electrons were directed parallel to the magnetic field and it was not until 21:53 UT that any perpendicular electrons were observed. The electron skew data (panel 2) show mixed directions throughout the period of interest, but with enhanced field-aligned direction at 20:49, 21:01 and 21:45 UT.

The ion counts were not as numerous as the electron counts, but there are still discernible differences in their direction. At 20:49 UT the ion anisotropy (panel 4) shows that the ions were mostly parallel to the field, as were those, whose directions could be determined, at 21:01 UT and 21:45 UT. There was also a field-parallel population observed at 21:29 UT. The ion skew data (panel 5) show that the field-parallel ions mentioned above were mostly field-opposed. Therefore the main features seen by CAMMICE were also observed in the Hydra data, with field-opposed ion beams seen in both instruments at 20:49, 21:01 and 21:45 UT. At these times the electrons were travelling in the opposite direction – field-aligned. Finally, the field-opposed ion beam observed by CAMMICE at ~21:30 UT was also detected by Hydra at a similar time, covering a similar energy range and travelling in the same direction. Therefore, the two secondary particle instruments observed the main features noted in the CAMMICE DCR, H^+ and He^{++} data, which corresponded to the final three Pi2 pulsations measured by the mid-latitude ground magnetometer stations. Furthermore, the timing of these features has been improved and other characteristics, such as average electron density, electron counts and direction, have also been added.

6.3.6. Polar Magnetic Field Experiment (MFE)

Figure 6.25 presents the MFE data in GSM co-ordinates as B_x , B_y and B_z , including the inclination, I , and the right ascension, RA , of the magnetic field. During this interval B_x began at +100 nT and increased steadily to +270 nT, B_y began at -40 nT falling to -100 nT and B_z began at -90 nT rising to +52 nT. Therefore, Polar started the interval in a high-latitude, near-Earth region with strong negative B_z and finished in a lower-latitude region with positive B_z .

There are two significant periods of magnetic field variations observed by the MFE instrument during this interval. To make the variations more clear Figure 6.26 has been produced, which presents the three components and the magnitude of the magnetic field as

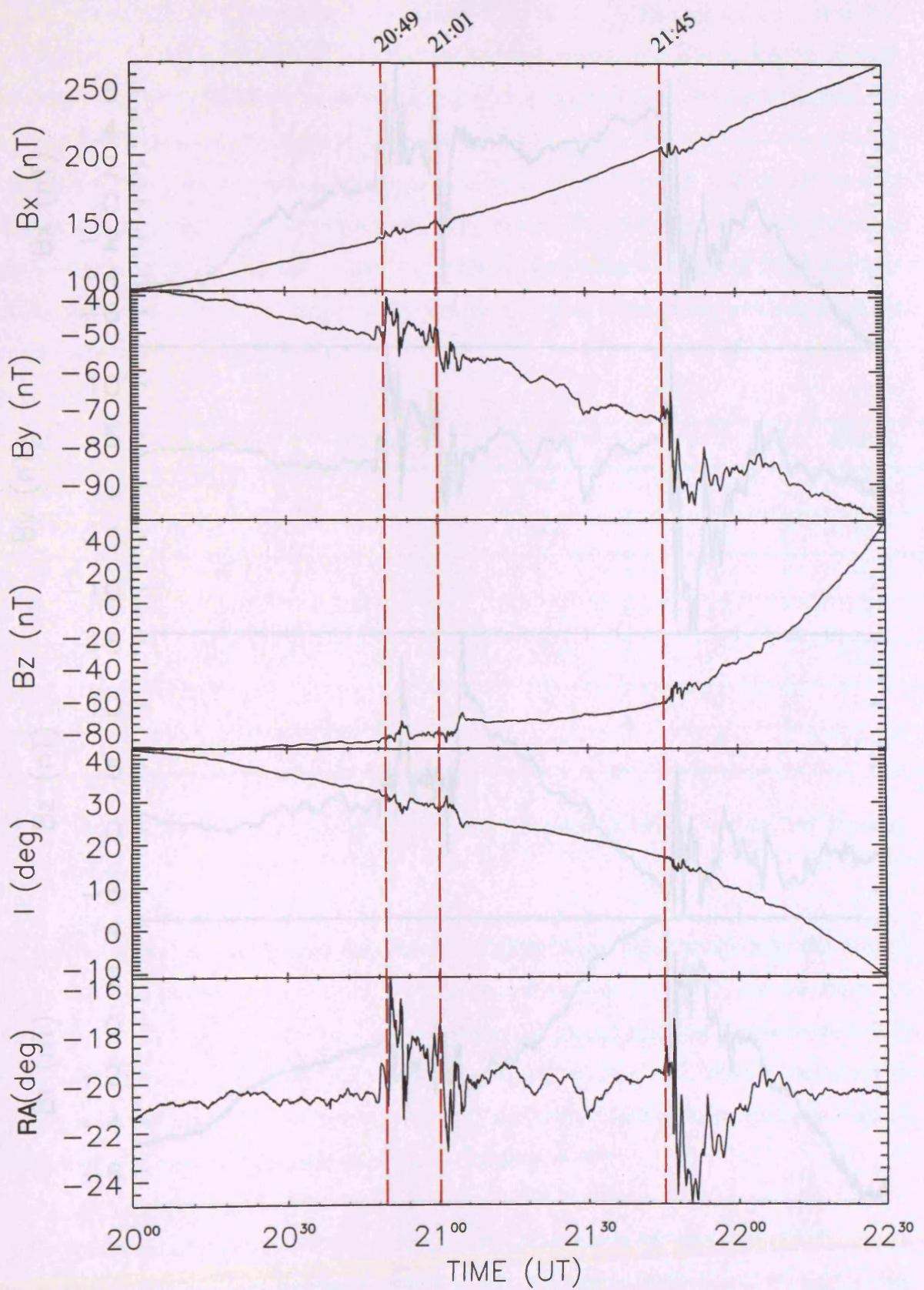


Figure 6.25: MFE data in GSM co-ordinates with inclination angle (I) and right ascension (RA).

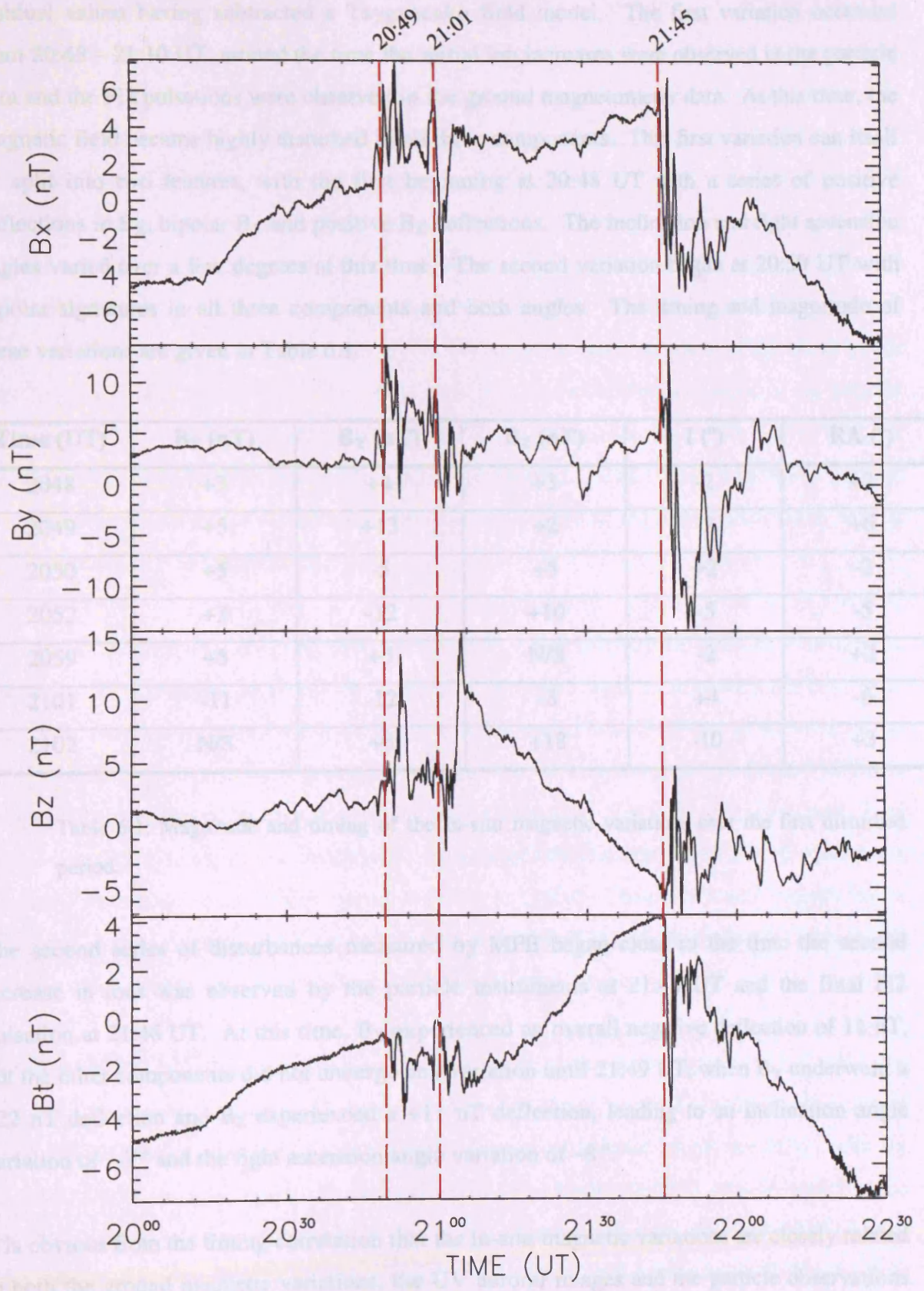


Figure 6.26: MFE residual data after subtracting a Tysganenko 89 field model.

residual values having subtracted a Tsyganenko field model. The first variation occurred from 20:48 – 21:10 UT, around the time the initial ion increases were observed in the particle data and the Pi2 pulsations were observed in the ground magnetometer data. At this time, the magnetic field became highly disturbed in all three components. This first variation can itself be split into two features, with the first beginning at 20:48 UT with a series of positive deflections in B_x , bipolar B_y and positive B_z deflections. The inclination and right ascension angles varied over a few degrees at this time. The second variation began at 20:59 UT with bipolar signatures in all three components and both angles. The timing and magnitude of these variations are given in Table 6.1.

Time (UT)	B_x (nT)	B_y (nT)	B_z (nT)	I (°)	RA (°)
2048	+3	+4	+3	-2	+2
2049	+5	+13	+2	-2	+6
2050	+5	-5	+5	+2	-2
2052	+3	-12	+10	-5	-5
2059	+5	+5	N/S	-2	+2
2101	-11	-12	-8	+4	-6
2102	N/S	+8	+18	-10	+3

Table 6.1: Magnitude and timing of the in-situ magnetic variations over the first disturbed period.

The second series of disturbances measured by MFE began close to the time the second increase in ions was observed by the particle instruments at 21:45 UT and the final Pi2 pulsation at 21:46 UT. At this time, B_x experienced an overall negative deflection of 11 nT, but the other components did not undergo any variation until 21:49 UT, when B_y underwent a -22 nT deflection and B_z experienced a +11 nT deflection, leading to an inclination angle variation of -3° and the right ascension angle variation of -8° .

It is obvious from the timing correlation that the in-situ magnetic variations are closely related to both the ground magnetic variations, the UV auroral images and the particle observations made by Polar. Possible connections between these features will be discussed in the following sections.

6.4. Discussion

The interval begins with a series of Pi2 pulsations observed in the SAMNET magnetometer data, the first of which occurred at 20:13 UT. At this time the mid-latitude magnetometers observed what could have been a SCW centred close to longitude of YOR with a downward-directed FAC close to the longitude of OUI. The other magnetometers observed only small deflections, with no electrojet signatures in evidence. A second Pi2 pulsation occurred at 20:39 UT, but, with the exception of magnetic bay at BJN, no other ground signatures were observed. The next Pi2 occurred at 20:47 UT, and the mid-latitude stations observed a SCW centred at longitude close to OUI and an upward-directed FAC close to the longitude of NOR. An enhanced westward electrojet was observed just south of the latitude of BJN, with the auroral stations observing the eastward electrojet, but there were no significant deflections observed by the Greenland stations. This feature was more localised than would be expected for an enhanced electrojet caused by an expansion phase onset, and so may be attributed to a pseudobreakup.

The next Pi2 pulsation was observed at 21:00 UT. The mid-latitude stations were able to place the SCW centred close to the longitude of York, with a downward-directed FAC occurring close to the longitude of NOR. It is clear that this activity was to the west of the 20:49 UT activity, and so the Greenland stations were of use. At this time the IMAGE data showed little evidence of an enhanced electrojet system. Similarly, the Greenland West stations recorded no significant variations. The Greenland East station at SCO showed large magnetic variations, with smaller variations seen at DMH. These variations suggest that a westward electrojet was centred at a latitude just south of SCO, but once again the feature was very localised, and so also appeared to be also due to pseudobreakup.

The clearest Pi2 pulsation that was observed during this interval occurred at 21:46 UT. The mid-latitude stations' observations suggest that the SCW was centred at a longitude between YOR and NOR. The other mid-latitude stations were all located within the SCW, with the downward-directed FAC close to or east of OUI. The higher-latitude data showed that the westward electrojet was enhanced at 21:46 UT, centred between TRO and BJN. The electrojet then moved northwards until it was centred close to the latitudes of HOP and HOR by 22:09 UT. The Greenland measurements suggest that the enhanced westward electrojet was initially located close to the latitude of SCO and had not reached any of the Greenland-West stations. By 22:09 UT the electrojet had expanded westwards as the Greenland-West stations experienced the effects of the current system, placing the centre at a latitude between STF and GDH. The centre of the electrojet system had also expanded polewards as the

Greenland-East stations observed the centre further north than earlier, now between SCO and DMH. The difference between the two latitudes of the electrojet may be attributed to the difference between geographic and magnetic co-ordinates. That is, the active oval was centred close to magnetic North, whilst the co-ordinate system used was centred on geographic North. With both westwards and polewards expansion occurring after this Pi2 pulsation this feature appeared to be a substorm expansion phase onset.

These magnetic fluctuations are closely related to the series of auroral intensifications observed by the UVI. The first Pi2 pulsation occurred at 20:13 UT, the same time as a small patch of active aurora appeared. This small patch did not develop further, and faded very quickly, before a new intensification occurred at 20:25 UT west of the original brightening. This was also a very short-lived patch, fading in about 10 minutes. Note that there is some evidence that there was an enhancement in the Pi2 wave activity just before 20:25 UT (Figure 6.3), which is most clearly seen in the data from KVI. The second Pi2 pulsation occurred at 20:39 UT, when UVI observed a very slight increase in the auroral luminosity, but again in a very localised region. The third Pi2 pulsation occurred at 20:47 UT, just as the spacecraft footprint entered a recently intensified poleward arc. This new active patch, though more extensive than the earlier auroral forms, was still relatively localised and had almost completely faded by 20:55 UT. This was in agreement with the magnetic variations that were also very localised. Such a localised patch of activity is indicative of pseudobreakup. The first image available after the fourth Pi2 pulsation was at 21:01 UT. This showed a new brightening to the west of the spacecraft footprint, over Southeast Greenland. As it is, this enhancement also faded quickly, disappearing completely by 21:13 UT. This auroral enhancement was also very localised and failed to expand significantly, also indicated by the localised ground perturbations at SCO and DMH. Again the data indicated that the variations were characteristic of a pseudobreakup. The oval was still visible due to a very small amount of auroral precipitation and the spacecraft footprint was still inside this arc. The auroral oval was subsequently seen to move equatorwards such that the spacecraft exited the oval at 21:35 UT. A decrease in the auroral luminosity appeared in the oval at the same position as the spacecraft footprint as well. The low auroral luminosity continued through until the 21:47 UT image when an intensification engulfed the spacecraft footprint. This intensification did not fade in a short time, like the earlier features, but expanded over the next images, until there was auroral activity covering a large area ($\sim 60^\circ$ longitude and $\sim 5^\circ$ latitude) by 22:05 UT. This intensification was clearly related to the fifth and final Pi2 pulsation observed by the ground magnetometers at 21:46 UT. The magnetometers also observed classic substorm signatures, such as magnetic bays. The magnetic data suggested

the westward electrojet initially occurred in the region where the intensifications began, but then moved northwards, as does the auroral activity. The ground magnetic data also showed the electrojet moving westwards over Greenland, as was seen in the final images of this interval. Such a series of events is typical of an expansion phase onset with both westward and poleward expansion.

The auroral activity between 20:44 and 20:49 UT occurred whilst the spacecraft footprint was passing into the poleward-most arc in the auroral zone and so must have passed through the open/closed field-line boundary at approximately the same time. At the start of this interval the spacecraft was on field lines characteristic of the tail lobes, which appeared to map to the Polar Cap and, as expected, very few ions were observed. The CAMMICE data show the first significant ion population was encountered at 20:49 UT, the first sample after the Pi2 and close to the time of an image showing an auroral intensification. The energy and number of ions suggest that the spacecraft had crossed onto closed field lines, specifically Polar had entered the plasma sheet. The presence of the tailward-directed ion beams suggests that the region was the plasma sheet boundary layer, PSBL (see Chapter 2). CEPPAD confirms this timing of 20:49 UT for the entry into the PSBL, but Hydra observed PSBL ions at 20:50 UT. This was because the ions that were being measured were velocity dispersed, with the more energetic ions being observed first. Therefore the lower energy ions, which are measured by Hydra, would be observed a small time after the initial encounter with the PSBL. At 21:01 UT, the time of further ground magnetic and auroral disturbances, the ion count rate increased around the 10 – 100 keV energy range in both the CAMMICE and CEPPAD data, and there was an increase in the higher energies of Hydra as well. This energetic plasma gradually decreased in energy and counts over the next thirty five minutes, until the count rates were as low as the initial measurements. Just before this happens, CAMMICE observed a small field-opposed ion beam. As was mentioned earlier, these ion beams characteristically appear on the edge of the PSBL. It seems that the spacecraft was leaving the PSBL and re-entering tail lobe plasma. Another ion increase followed at 21:45 UT, observed in both CAMMICE and CEPPAD, which occurs over the 20 – 50 keV energy range. Once again field-opposed ion beams are observed, before a much larger ion increase was noted at 21:53 UT over a wider energy range. Therefore, it seems that the spacecraft had once again entered the PSBL, but passed rapidly through it into the central plasma sheet (CPS) in a matter of some eight minutes.

The final data set to be examined is the in-situ magnetic field measured by MFE. Once again there are two main disturbances in this interval. The first variation is measured in all three

components and occurs at 20:48 – 21:10 UT, close to the time when the higher-energy ions are observed CAMMICE and CEPPAD and the Pi2 pulsations are measured by the ground magnetometers. From 20:48 – 21:00 UT MFE observed a series of positive deflections in B_x , bipolar variations in B_y and positive deflections in B_z . Figures 6.27 and 6.28 have been produced so that the MFE observations can be directly compared with the CAMMICE observations. Figure 6.27 presents B_x , B_y and B_z data from MFE in the top three panels and CAMMICE energy binned pitch angle data in the bottom four panels (as in Figure 6.22) over the time interval 20:25 – 21:45 UT, covering the first entry into the PSBL. Over the period of 20:48 – 21:10 UT CAMMICE observed some field-opposed ion beams, at ~20:49 UT and ~21:01 UT. As FAC's are closely related to ion beams MFE should detect FAC signatures. In Chapter 2 (section 2.5) FAC's are described to induce variations in the B_y component of the magnetic field in the magnetosphere, and so affect the right ascension angle. At 20:49 UT the first of the field-opposed ion beams was observed, and MFE underwent a bipolar deflection in B_y , with +17 nT followed by -17 nT net deflections. This led to a $+8^\circ / -7^\circ$ change in the right ascension, indicating the presence of a FAC directed tailwards, supported by the presence of the field-opposed ion beam. At 20:59 – 21:02 UT MFE observed another bipolar signature in B_y , with deflections of +5 and -12 nT this time, giving a right ascension variation of $+2^\circ / -6^\circ$. Therefore another tailward-directed FAC was observed at the same time that CAMMICE observed a field-opposed ion beam. At both of these times the inclination of the field underwent small variations. Just after 20:49 UT there was a 2° increase in the inclination, followed by a 5° decrease at 20:52 UT. At 21:01 UT there was a 4° increase followed shortly afterwards by a 10° decrease. The minor variations during this period do little to affect the plasma regime that Polar was passing through.

As the interval progresses the UV auroral images show that the auroral oval was moving equatorwards, which would suggest that magnetic flux was being added to the tail lobes. A possible consequence is that the high-latitude edge of the PSBL moves towards the equatorial plane. If the residual MFE B_z data are inspected there was a gradual decrease in this component. As this is the residual field one would expect it to remain close to zero. Such a decrease in the z-component of the field implies that the field lines were moving towards the equatorial plane. As the plasma is frozen into the magnetic field this also implies a motion of the outer edge of the plasma sheet towards the equatorial plane. This motion of the plasma sheet implies a compression/stretching of the magnetotail. The IMF B_z component had been predominantly southwards since ~20:20 UT (including propagation delay). Therefore enhanced dayside reconnection loaded the nightside magnetotail, resulting in increased tail lobe pressure and an increase in the cross-tail current, leading to compression and stretching

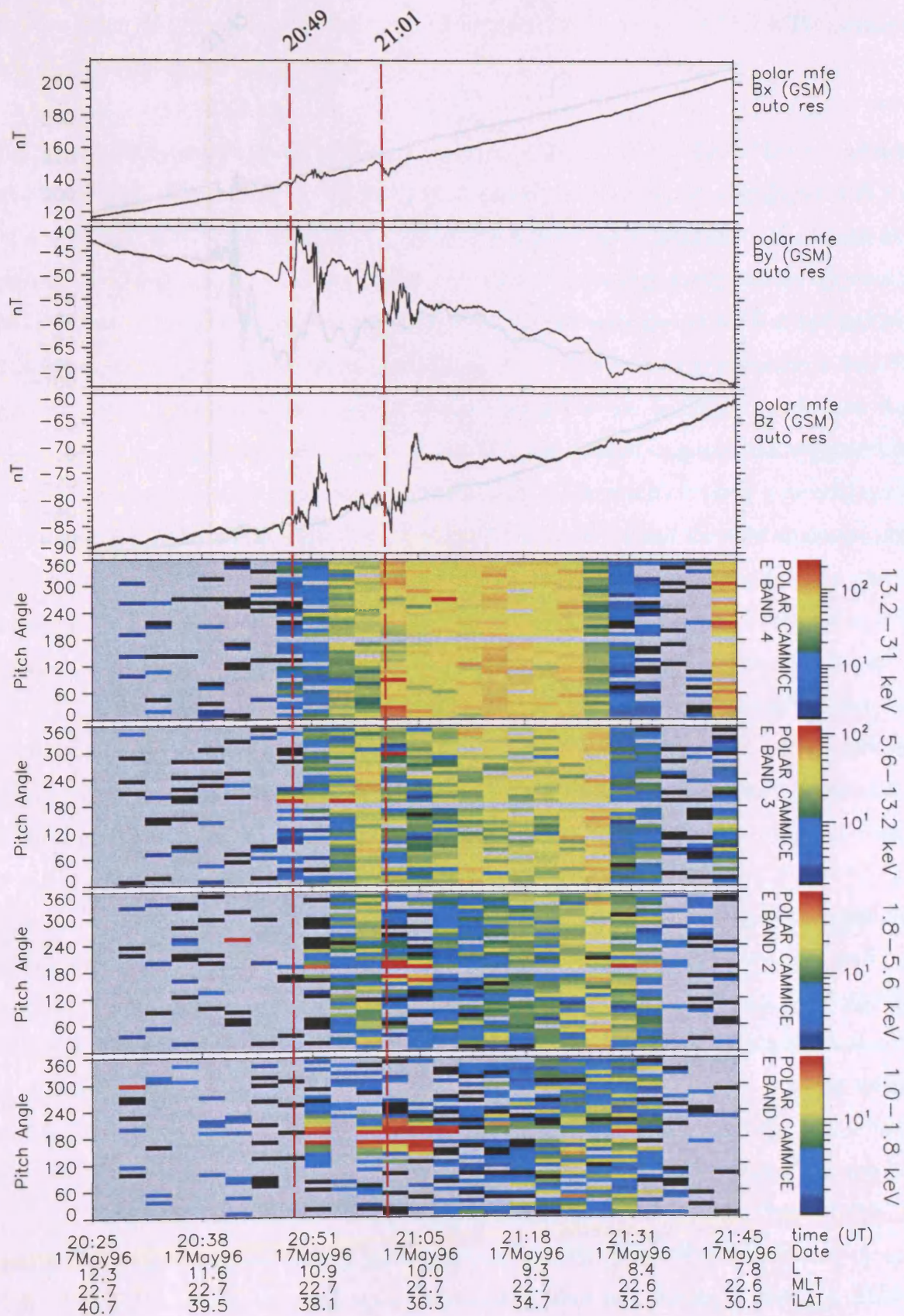


Figure 6.27: Particle pitch angle data from CAMMICE and in situ magnetic field data from MFE to compare the ion beams and magnetic field variations.

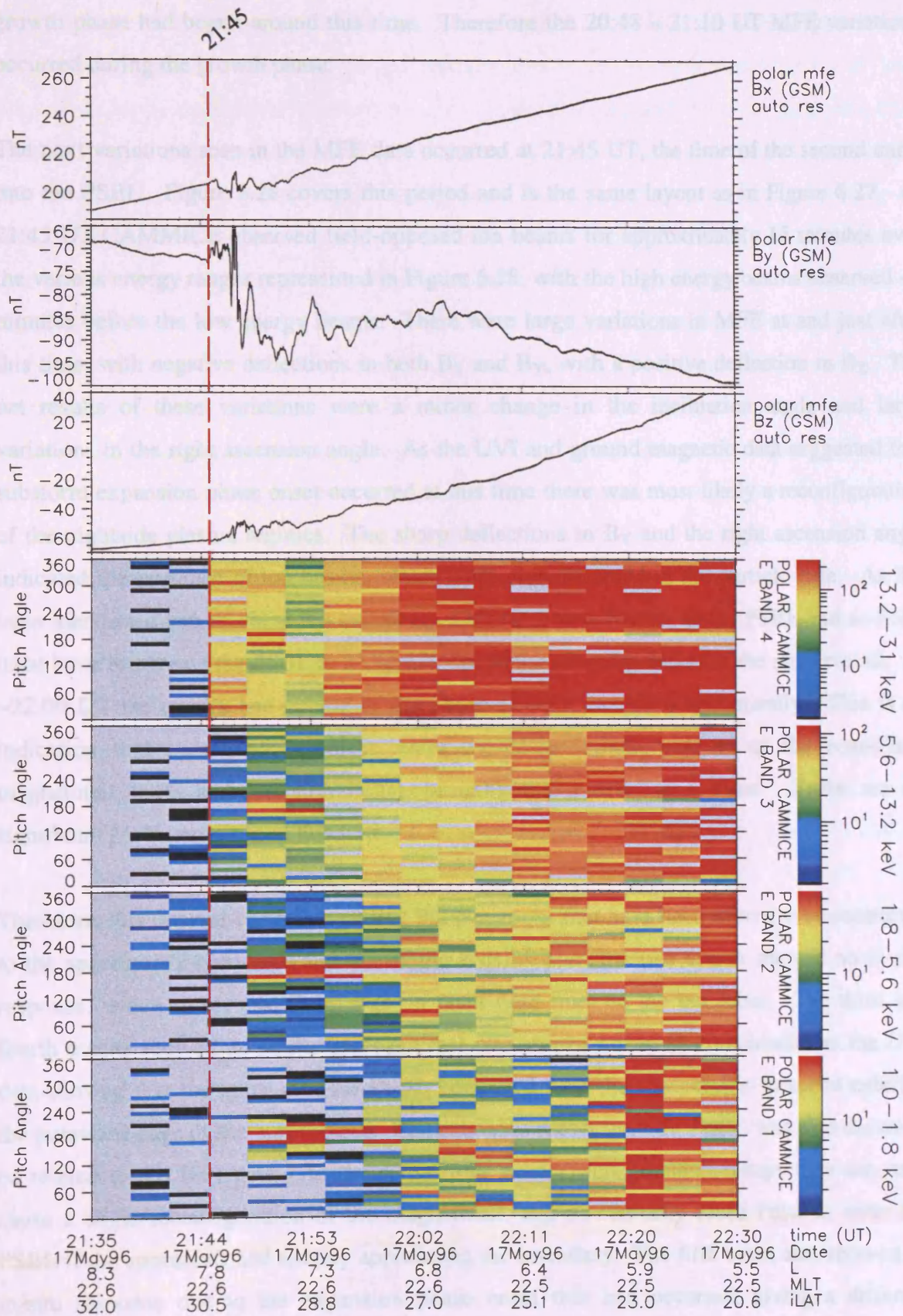


Figure 6.28: Particle pitch angle data from CAMMICE and in situ magnetic field data from MFE to compare the ion beams and magnetic field variations.

of the near-Earth magnetotail (see Chapters 1, 2 & 4). All these factors suggest that substorm growth phase had begun around this time. Therefore the 20:48 – 21:10 UT MFE variations occurred during the growth phase.

The next variations seen in the MFE data occurred at 21:45 UT, the time of the second entry into the PSBL. Figure 6.28 covers this period and is the same layout as in Figure 6.27. At 21:45 UT CAMMICE observed field-opposed ion beams for approximately 15 minutes over the various energy ranges represented in Figure 6.28, with the high energy beams observed ~3 minutes before the low energy beams. There were large variations in MFE at and just after this time, with negative deflections in both B_x and B_y , with a positive deflection in B_z . The net results of these variations were a minor change in the inclination angle and large variations in the right ascension angle. As the UVI and ground magnetic data suggested that substorm expansion phase onset occurred at this time there was most likely a reconfiguration of the nightside plasma regimes. The sharp deflections in B_y and the right ascension angle indicated the presence of ion beams, which were also observed in the particle data. As has been mentioned before, these ion beams are a characteristic feature of the PSBL and so Polar must have re-entered the PSBL at 21:45 UT due to the reconfiguration of the magnetotail. At ~22:00 UT the energy and counts of the observed ions increased dramatically. This is an indication that Polar had begun to enter the lower-latitude regions of the near-Earth magnetotail (CPS and radiation belts), bringing the interval to a close. There are no significant MFE variations at this time.

Therefore, this interval comprises of five Pi2 pulsations that have been shown to be connected to the spacecraft's entry into and out of the PSBL. The first two events showed no in-situ response, which is because Polar was on open field lines in the tail lobes. The third and fourth events showed an in-situ response that was shown not to be coincidental as the UVI data showed that the entry into the PSBL coincided with the spacecraft's footprint entering the poleward edge of the auroral oval. The subsequent exit from the PSBL was also shown to be related to the UVI data. As these first four events were pseudobreakups they can only cause a slight reconfiguration of the magnetotail, and so can only cause Polar to enter the PSBL if the spacecraft had already approached the boundary. The fifth event also showed an in-situ response due to the expansion phase onset that had occurred, giving a different signature to that observed in the previous four.

6.5. Summary

This interval, whilst having some qualities in common with the case discussed in Chapter 5, contains some unusual features, presenting both in-situ and ground observations of both pseudobreakup and expansion phase onset. The interval began with Polar on open field lines in the tail lobe. This remained the case until 20:49 UT when the in-situ particle instruments observed increased numbers of higher energy particles. Many of these particles were aligned along the field lines (directed away from Earth), and such field-aligned beams are a characteristic signature of the outer edge of the plasma sheet, the PSBL. At this time, and shortly afterwards, the ground magnetometer and UVI data suggested that some localised, short lived features were being observed in the ionosphere. These features have short-lived, localised auroral intensifications and localised variations in the ground magnetic field, including Pi2-like signatures, indicating that these were pseudobreakups. As Polar entered the PSBL at this time there appears to be either a connection between the two or it was entirely coincidental. Assuming there was a connection then the pseudobreakup caused slight reconfigurations in the local magnetic field lines, causing the PSBL to move over Polar. This was further compounded by the second pseudobreakup at 21:01 UT. A combination of the spacecraft's orbital motion and the pseudobreakup caused Polar to move deeper into the PSBL. As the magnetotail was still being loaded (and hence compressed and stretched) the lack of any further activity caused the PSBL to move back over Polar by 21:35 UT. This can be seen in both the particle data as a return to tail lobe particle levels and also in the UVI images as motion of the auroral oval back over the spacecraft footprint. Further evidence includes the small field-opposed ion beam observed by CAMMICE at 21:26 UT. This indicates that the outer edge of the PSBL had been encountered again. There was now a short gap until significant ion counts were observed again.

The final period began with Polar once again encountering the PSBL, now at the time of an expansion phase onset. Once again a reconfiguration of the magnetotail has caused the PSBL to move over the spacecraft. This is most evident in the ground magnetometer data and in two of the UVI images (Figures 6.18 & 6.19). The ground magnetometer data showed a substorm electrojet being enhanced and then moving polewards and westwards. The UVI images showed that a previously quiet oval moved rapidly over the spacecraft footprint, which remained relatively motionless. As the auroral oval is closely associated with the PSBL this corresponded to motion of the PSBL over Polar. As the magnetic activity continued the poleward motion continued, and hence the PSBL motion also continued. Therefore the spacecraft crossed the PSBL in a short time and rapidly entered the CPS and radiation belts. The auroral and magnetic variations continued as the substorm progressed,

but Polar had entered the low-latitude regions now, and so was in the wrong region to study any substorm effects.

There are very few studies comparing direct observation of the plasma sheet with auroral images and ground magnetic field data. There are none that show not only pseudobreakup causing near-Earth magnetospheric variations (resulting in the PSBL moving back and forth across the spacecraft) but also relates this to the auroral motion across the spacecraft footprint and ground activity. As Polar is relatively close to Earth the footprint can be mapped down into the ionosphere with a fair degree of accuracy. This mapping allows the in-situ observations to be directly compared with the auroral and ground magnetic observations, and so the pseudobreakups can be classified as causing a small reconfiguration of the near-Earth plasma sheet, a Pi2 pulsation, a short-lived, localised auroral intensification and a very localised, ground X-component, magnetic bay.

CHAPTER 7

Summary

7.1. Introduction

The aim of this thesis was to investigate the effect of geomagnetic substorm activity on the high-latitude plasma sheet. This has been performed first by examining the average characteristics of the plasma sheet by means of a statistical study, and secondly by the investigation of two case studies. The statistical study was based around particle measurements made in-situ by Polar whilst the case studies also used various background data sets. The statistical study not only provided the average location of the PSBL and CPS, but also discovered more widespread variations due to various factors, allowing the two case studies to be examined objectively. Although magnetospheric substorms have been studied in great detail throughout the years there are still many questions left unanswered and it is hoped that this study has aided in furthering the understanding of this fascinating research topic.

7.2. Summary of Results

The first data chapter presented a statistical study of the plasma sheet boundary layer and central plasma sheet. The location of the plasma sheet boundary layer and central plasma sheet have been investigated by Polar observations in April, May, October and November 1996, 1997 and 1998, both in terms of GSM latitude and geocentric distance. The location was found to have a seasonal variation that was most obvious in the GSM latitude statistics, but was also observed in the geocentric distance statistics. The PSBL was to be found at a latitude of $\sim 55^\circ$ in 'Spring' and $\sim 30^\circ$ in 'Autumn', with an overall mean of $\sim 42^\circ$. The CPS was to be found at a latitude of $\sim 47^\circ$ in 'Spring' and $\sim 20^\circ$ in 'Autumn', with an overall mean of $\sim 34^\circ$. This corresponded to a statistically significant difference between 'Spring' and 'Autumn' of $\sim 25^\circ$, consistent with the variation due to the Earth's orbit of the Sun. There was also a daily variation with a difference between 04 – 08 UT and 16 – 20 UT of $\sim 11^\circ$, consistent with the dipole tilt of the Earth. These locations have also been used to derive the upper limit of the thickness of the plasma sheet boundary layer along the orbit path and in the Z_{GSM} direction. The thickness along the orbital path was $1.21 R_E$ in 'Spring' and $1.34 R_E$ in 'Autumn', with an overall mean of $1.27 R_E$. The thickness along the Z_{GSM} direction was $1.17 R_E$ in 'Spring' and $1.27 R_E$ in 'Autumn', with an overall mean of $1.22 R_E$. However, this seasonal variation was shown to be statistically insignificant and so a Z-component thickness of $1.22 \pm 0.81 R_E$ at $X = -4.3 R_E$ is the value obtained from this study. This value is slightly larger than the values measured in *Dandouras et al.* [1986] but are still within the range given

in the earlier work. The larger values measured in this study may be a result of different definitions of the thickness of the PSBL.

The effect of magnetic activity on the location of the plasma sheet boundary layer was then investigated. This was accomplished by examining AE and Dst. The AE index was only available as daily plots, and so a substorm index was devised by ascribing each event a level of substorm activity. Whilst there was a minor effect on the location statistics caused by variations in the substorm index the method used is not ideal and the study should be repeated when the full AE index becomes available. The Dst variation was observed to induce a small effect on the location statistics, including a possible seasonal variation, but the correlations were small and so Dst plays only a minor role. Kp and PC indices were also examined but produced no discernible variations in the location statistics. It appeared that magnetic activity causes some small variations in the location of the plasma sheet boundary layer, but cannot explain the major variations.

Finally, solar wind control of the location statistics was investigated by examination of IMF B_z and dynamic pressure data from the Wind spacecraft. The data were separated into positive and negative IMF B_z and a significant variation was found. This variation was further investigated by performing a superposed-epoch analysis on the IMF B_z . It was found that entries during periods of predominantly northward IMF occurred at lower latitudes than those during predominantly southward IMF. This was because dayside reconnection is at a maximum during southward IMF, and so the increased tail lobe pressure compresses the magnetotail, which is also stretched due to the increase in the cross-tail current, resulting in the plasma sheet boundary layer being located at lower latitudes. The final parameter examined was the solar wind dynamic pressure. Once again a superposed-epoch analysis was performed, but this time no obvious effect was found.

The location of the plasma sheet boundary layer and central plasma sheet proved to be highly variable, with the main cause being the variation of the Earth's rotation axis relative to the Sun. Magnetic activity was found to have only a minor effect, but the orientation of the IMF also proved to be significant. Although limited by orbital constraints this study has shown a significant Earth orbital effect, and some solar wind control on the location of the plasma sheet boundary layer and central plasma sheet.

The second data chapter details a case study on 9th April 1996 running from 19:30 – 22:00 UT. This was examined using CAMMICE as the primary instrument, with Hydra and

CEPPAD as secondary in-situ particle instruments. These observations were placed in context of the substorm phase by utilising observations from UVI, MFE, the LANL geosynchronous satellites and various ground magnetometers. Throughout this substorm interval two interesting periods were found. The first was a period when the spacecraft entered the region of closed magnetic field lines in the geomagnetic tail during which good auroral imager coverage, magnetic field and particle data were available. In the second period only particle and magnetic field data were available to study the expansion phase onset that occurred as the spacecraft entered the CPS.

The spacecraft encounter with an increased ion population, consistent with the PSBL, coincided with the movement of the spacecraft footprint across the poleward boundary of the auroral oval. Immediately after entering this region counterstreaming ion beams, characteristic of the PSBL, were observed by the particle instruments, with both MFE and Hydra currents showing that these beams were closely connected to field-aligned currents. The auroral oval at this time exhibited a double oval configuration and the footprint of the PSBL was coincident with the poleward-most arc. Therefore there was an apparent mapping of the poleward boundary of the auroral oval to the boundary between open and closed field lines in this case. There was, however, a six minute gap between UVI LBHI images from 19:55 – 20:01 UT, so the exact time of entry into the auroral oval could be up to three minutes later, which would correspond to an open/closed field line boundary poleward of the auroral zone. When the spacecraft footprint left the poleward arc and entered the gap between the poleward and equatorward arcs, the in-situ particle count rate decreased. This occurred just after the ground magnetometers indicated an electrojet enhancement, whilst the UVI data demonstrated enhanced auroral activity to the west of the spacecraft footprint.

The final period of activity occurred when Polar was deep in the PSBL and was approaching the central plasma sheet (CPS). At this time, the UVI had been shielded and so there were no images available. There was one major expansion phase onset at 21:10 UT, confirmed by a number of signatures, such as a clear Pi2 pulsation and a westward electrojet centred on KEV, at latitude similar to Polar. There was also a fairly large change in the orientation of the magnetic field (7°) seen by MFE on Polar, consistent with dipolarisation, confirming the onset timing of this substorm as between 21:10 and 21:11 UT. Finally, CAMMICE observed a small ion increase prior to onset, which was then followed, at the time of the onset, by a much larger increase in the ion count rate and energies. The other particle instruments confirmed that this small initial increase did not correspond with the expansion phase onset timing and also observed the larger increase. Therefore, Polar was travelling through the

PSBL (characterised by the presence of counterstreaming ion beams) until 21:08 UT, when the spacecraft entered the CPS. At 21:11 UT, just after the entry into the CPS, the spacecraft observed a large particle increase, corresponding to a particle injection at expansion phase onset. There are further onsets in this final period, but Polar was at sufficiently low latitudes that any particle signatures were obscured by the energetic particles of the CPS and radiation belts.

This case study demonstrates the need for context data such as UVI images and magnetometer networks in studying dynamic changes in the magnetotail measured in-situ by a spacecraft such as Polar. From the UVI data it is clear that the spacecraft observations began in an area of open field lines. Polar then passed into the poleward arc of a double-oval aurora that had developed as a result of earlier substorm activity. Entering this double oval, the spacecraft observed a series of counterstreaming ion beams, a signature of the PSBL. When Polar exited this poleward arc and entered the gap between the poleward and equatorward arcs, the in-situ particle data registered a relatively low count rate despite the evidence for further activity to the West of the spacecraft. The low count rate continued until the spacecraft entered the CPS at 21:08 UT and observed the plasma injection associated with expansion phase onset. Although there are no UVI images available at this time, the location of the poleward edge of the equatorward arc in the final image occurred at $\sim 69^\circ\text{N}$. The footprint of the spacecraft was at $69.3 - 68.9^\circ\text{N}$ from 21:06 - 21:12 UT. It would be reasonable to say that the encounter with the CPS from the particle data is concurrent with the spacecraft footprint's encounter with the poleward edge of the equatorward arc.

The final data chapter details a second case study that was studied in a similar manner to that described for the first case study. This interval, whilst having some qualities in common with the case discussed in Chapter 5, contains some unusual features, presenting both in-situ and ground observations of both pseudobreakup and expansion phase onset. The interval began with Polar on open field lines in the tail lobe. This remained the case until 20:49 UT when the in-situ particle instruments observed increased numbers of higher energy particles. Many of these particles were aligned along the field lines (directed away from Earth), indicating that Polar had entered the PSBL. At this time, and shortly afterwards, the ground magnetometer and UVI data suggested that some localised, short lived features were being observed in the ionosphere. These features have short-lived, localised auroral intensifications and localised variations in the ground magnetic field, including Pi2-like signatures and so appear to be pseudobreakups. As Polar entered the PSBL at this time there appears to be either a connection between the two or it was entirely coincidental. Assuming there was a connection

then the pseudobreakup caused slight reconfigurations in the local magnetic field lines, causing the PSBL to move over Polar. This was further compounded by the second pseudobreakup at 21:01 UT. A combination of the spacecraft's orbital motion and the pseudobreakup caused Polar to move deeper into the PSBL. As the magnetotail was still being loaded (and hence compressed and stretched) the lack of any further activity caused the PSBL to move back over Polar by 21:35 UT. This can be seen in both the particle data as a return to tail lobe particle levels and also in the UVI images as motion of the auroral oval back over the spacecraft footprint. Further evidence includes the small field-opposed ion beam observed by CAMMICE at 21:26 UT. This indicates that the outer edge of the PSBL had been encountered again. There was now a short gap until significant ion counts were observed again.

The final period began with Polar once again encountering the PSBL, now at the time of an expansion phase onset. Once again a reconfiguration of the magnetotail has caused the PSBL to move over the spacecraft. This is most evident in the ground magnetometer data and in two of the UVI images (Figures 6.18 & 6.19). The ground magnetometer data showed a substorm electrojet being enhanced and then moving polewards and westwards. The UVI images showed that a previously quiet oval moved rapidly over the spacecraft footprint, which remained relatively motionless. As the auroral oval is closely associated with the PSBL this corresponded to motion of the PSBL over Polar. As the magnetic activity continued the poleward motion continued, and hence the PSBL motion also continued. Therefore the spacecraft crossed the PSBL in a short time and rapidly entered the CPS and radiation belts. The auroral and magnetic variations continued as the substorm progressed, but Polar had entered the low-latitude regions now, and so was in the wrong region to study any substorm effects.

There are very few studies comparing direct observation of the plasma sheet with auroral images and ground magnetic field data. There are none that show not only pseudobreakup causing near-Earth magnetospheric variations (resulting in the PSBL moving back and forth across the spacecraft) but also relates this to the auroral motion across the spacecraft footprint and ground activity. As Polar is relatively close to Earth the footprint can be mapped down into the ionosphere with a fair degree of accuracy. This mapping allows the in-situ observations to be directly compared with the auroral and ground magnetic observations, and so the pseudobreakups can be classified as causing a small reconfiguration of the near-Earth plasma sheet, a Pi2 pulsation, a short-lived, localised auroral intensification and a very localised, ground X-component, magnetic bay.

Through the use of two case studies the plasma sheet boundary layer has been studied in great detail during all phases of substorm activity. In the first case study Polar enters the PSBL during the late expansion/recovery phase, and then observes the effects of expansion phase onset whilst just inside the CPS. In the second case study Polar enters the PSBL due to pseudobreakup during the growth phase and also observes the effects of expansion phase onset, but this time whilst just outside the PSBL. Therefore all aspects of substorm phase have been addressed by these two case studies, each having very different results.

7.3. Further Work

What is perhaps the most difficult aspect of any magnetospheric study is the lack of spacecraft sampling the same region or field line. With future multi-spacecraft missions such as Cluster II it is hoped that this may become less of a problem. This lack of spacecraft causes ambiguity in any results due to the temporal/spatial problem. This study uses background data sets to remove much of the ambiguity, but this can only be solved by using multiple spacecraft. Therefore one suggestion for further work is to repeat this work with multiple spacecraft to determine the exact cause of the features noted, either by sampling the same magnetospheric region, or by having several spacecraft located on similar field lines, thereby allowing the plasma to be traced downtail and/or traced into the ionosphere more accurately.

The statistical study presented in Chapter 4 provides worthwhile results, but unfortunately there are areas that should be improved. Firstly, the size of the statistical database needs to be increased by including future years. Ideally this study would use data from all periods in the year, and so the full seasonal variation could be determined. Unfortunately, Polar is only able to perform such a study for a limited period each year due to orbital constraints. Therefore, should the spacecraft become available, this should be performed to fully determine the characteristics of the near-Earth plasma sheet. Secondly, although some attempt has been made to characterise the effect of magnetic activity on the near-Earth plasma sheet, the most useful of the magnetic indices, AE, was unavailable. Therefore the study should be repeated when this becomes available.

Another possible area of this work to expand is to fully investigate the method by which the auroral double-oval forms in the recovery phase of the substorm. Two possible mechanisms have been suggested in Chapter 5, but further work needs to be performed to confirm or deny such a mechanism.

Another aspect of this work that should be investigated further is the relationship between the field-parallel ion beams and the magnetospheric magnetic field variations. Although sources have been suggested for these ion beams (such as ionospheric outflow) more definitive work should be performed to provide more evidence to support or deny these sources. Multiple spacecraft studies such as those described above would be an ideal starting point.

Finally, continued analysis is required to attempt to solve the problem of the cause of the expansion phase onset. Although attempts have been made to create a combined model there are still two main factions: the NENL and the CD camps. Continued work on multipoint studies, combining both spacecraft data and ground-based data, can only improve our understanding of this complicated phenomenon.

Appendix 1

Polar U Co-ordinate Systems *ril 1996*

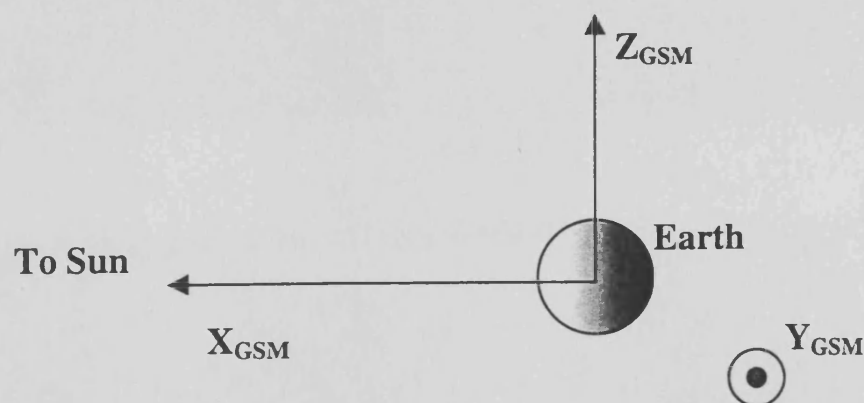
There are several different co-ordinate systems used in magnetospheric physics. These are described in detail in *Russell* [1971]. However, this section will briefly describe the co-ordinate systems used in this study – the co-ordinate systems used by the ground magnetometer networks and the Geocentric Solar Magnetospheric (GSM) co-ordinate system.

HDZ : H Horizontal Magnetic Northwards
D Horizontal Magnetic Eastwards
Z Positive vertically down (N. Hemisphere)

XYZ : X Positive geographic north
Y Positive geographic east
Z Positive vertically down (N. Hemisphere)

GSM Co-ordinates:

In GSM co-ordinates the Sun-Earth line is the X-axis and the Z-axis is chosen such that the X-Z plane contains the Earth's dipole axis. The Y-axis makes the orthogonal set.

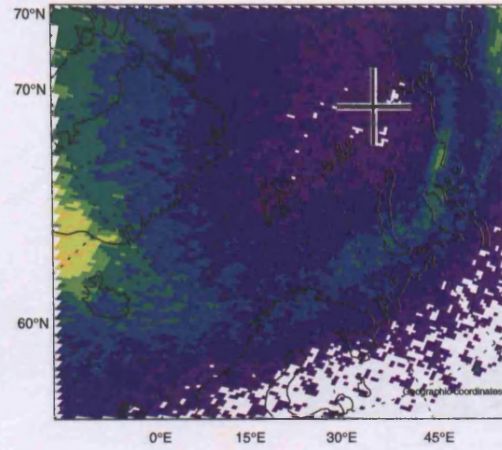


Appendix 2

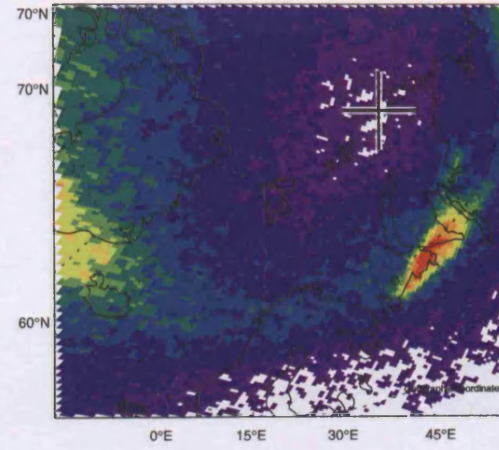
Polar UVI images from 9th April 1996.

The following pages contain images from the Ultra-Violet Imager on Polar taken on 9th April 1996 over the time interval 18:05 – 20:36 UT.

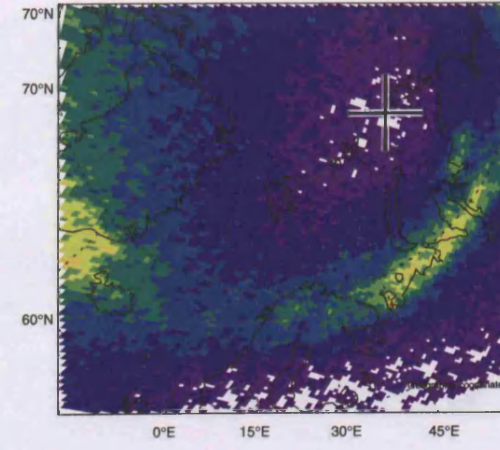
09-04-96 18:14:51



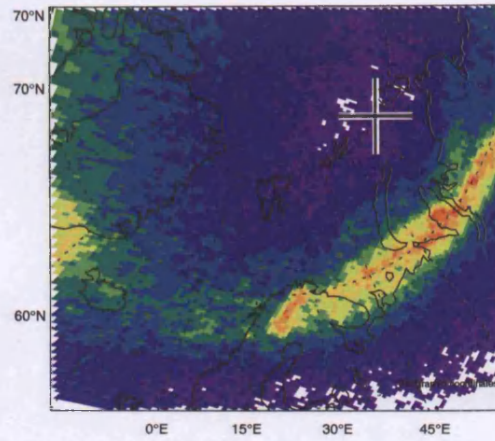
09-04-96 18:22:12



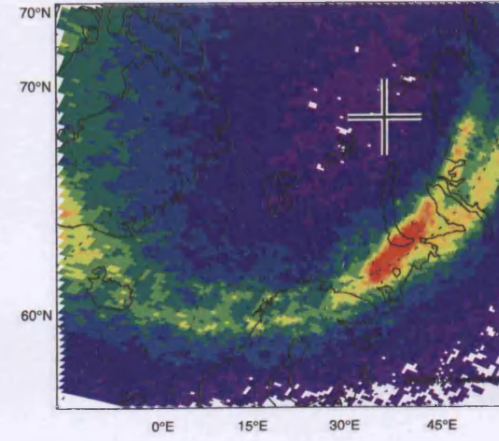
09-04-96 18:25:53



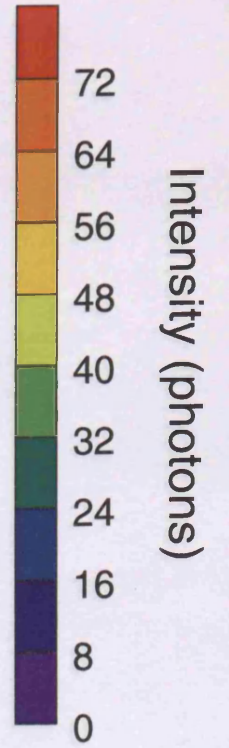
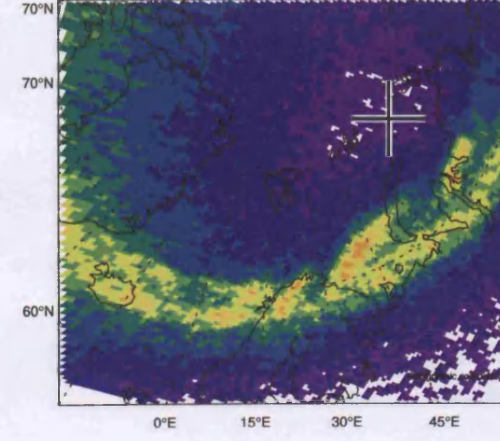
09-04-96 18:30:47



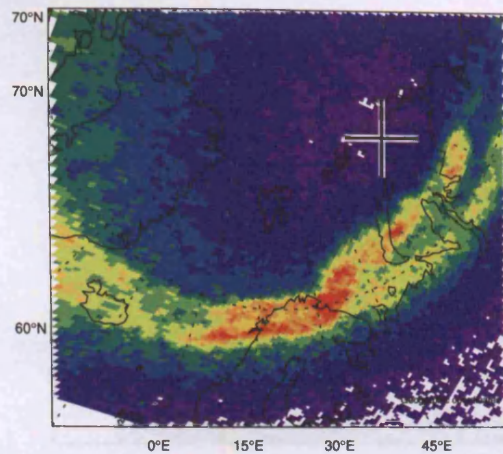
09-04-96 18:35:42



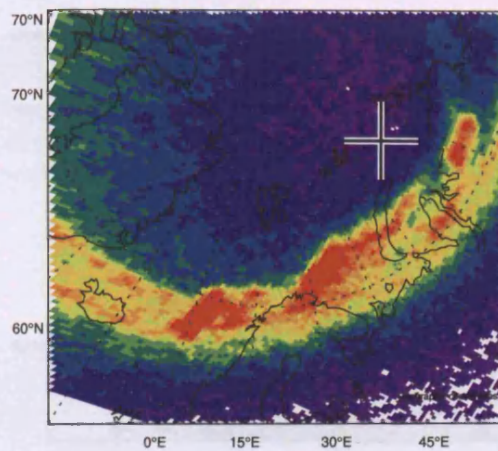
09-04-96 18:41:50



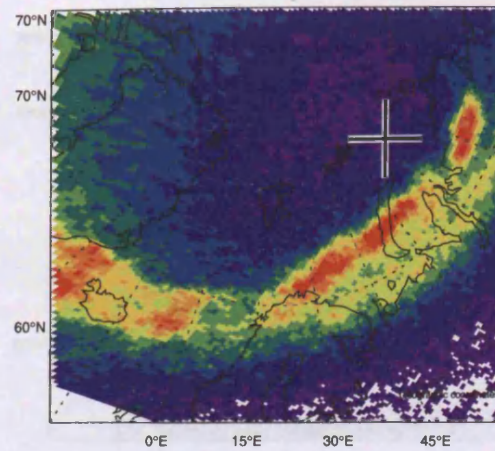
09-04-96 18:45:31



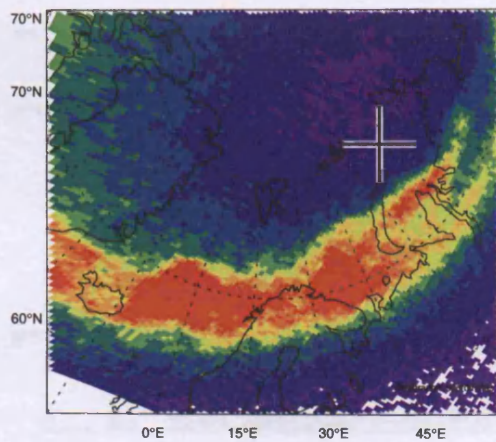
09-04-96 18:50:25



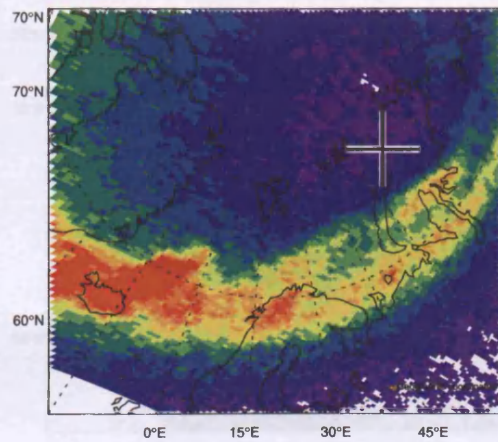
09-04-96 18:55:19



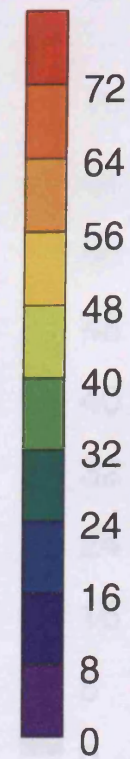
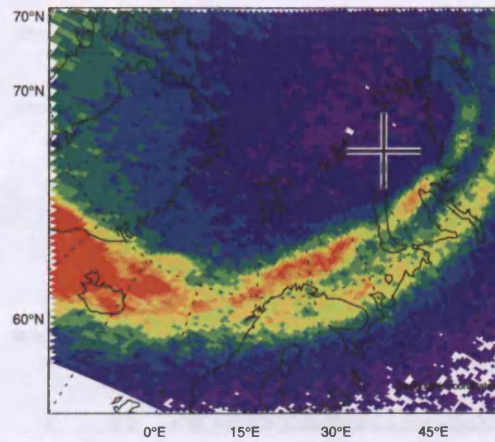
09-04-96 19:01:27



09-04-96 19:05:08

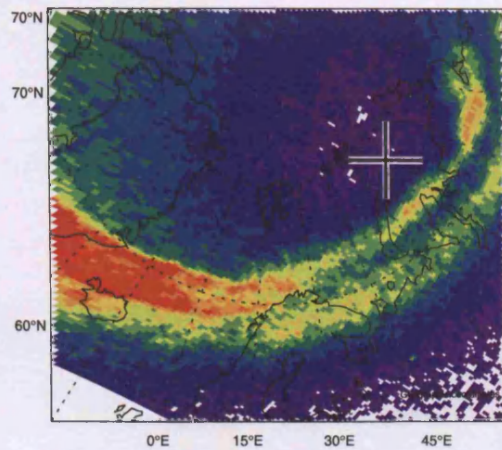


09-04-96 19:10:03

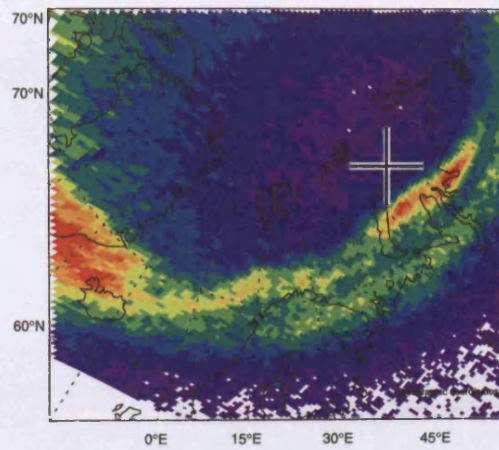


Intensity (photons)

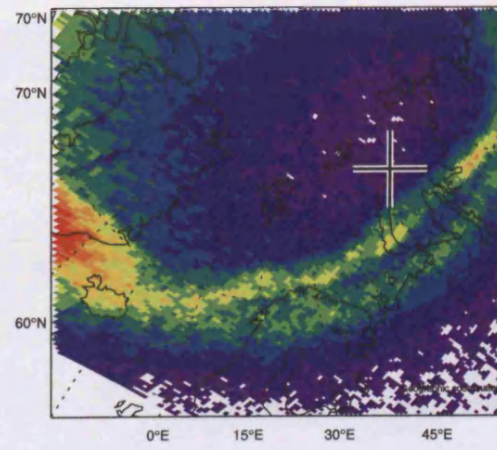
09-04-96 19:14:57



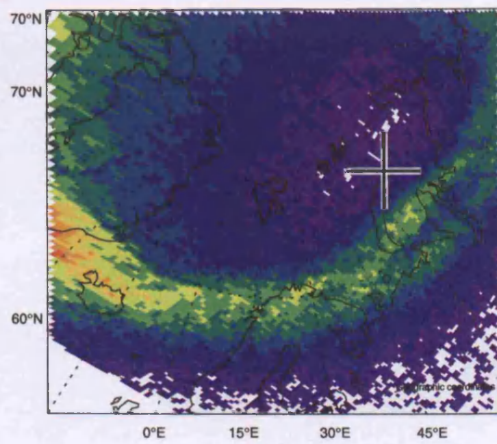
09-04-96 19:22:19



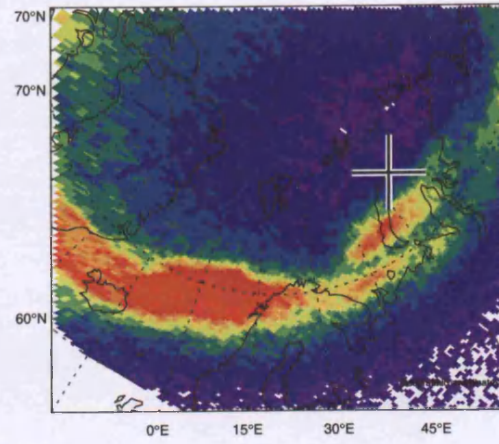
09-04-96 19:25:59



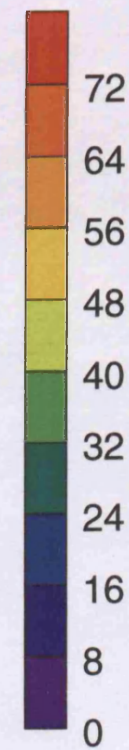
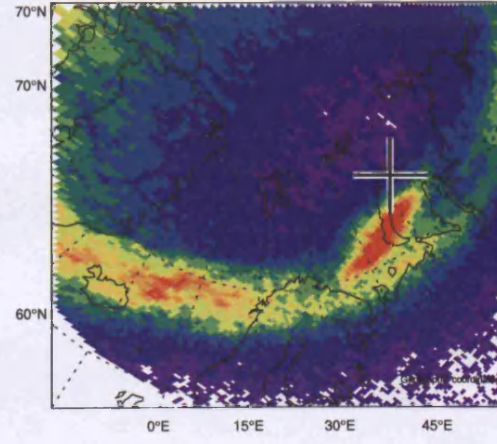
09-04-96 19:30:54



09-04-96 19:35:48

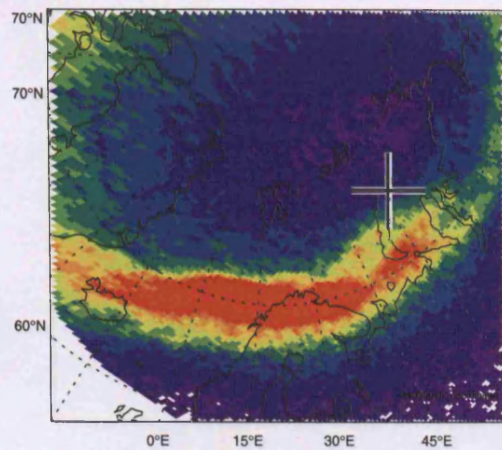


09-04-96 19:41:56

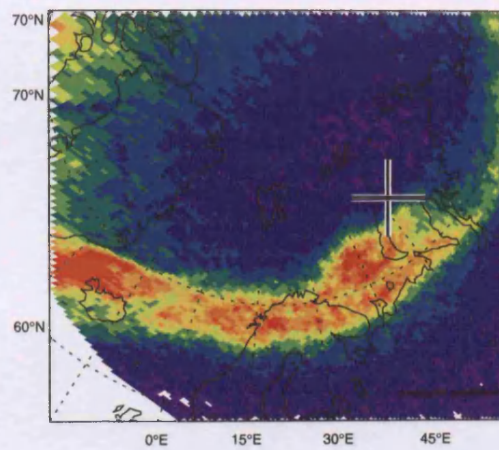


Intensity (photons)

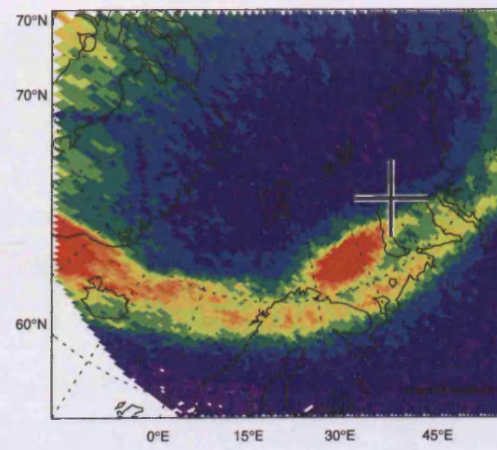
09-04-96 19:45:37



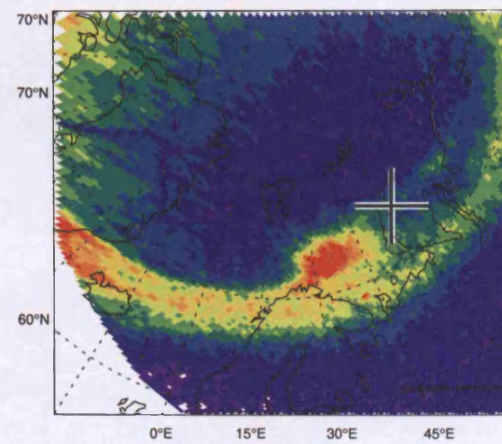
09-04-96 19:50:31



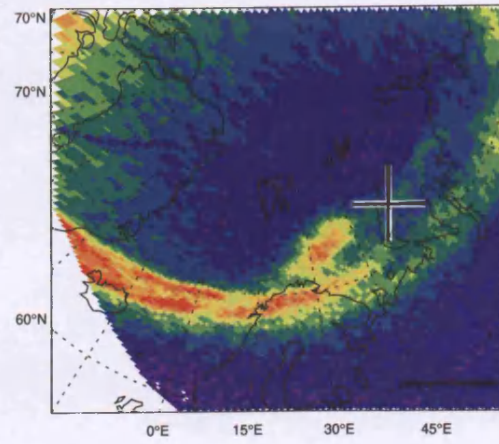
09-04-96 19:55:26



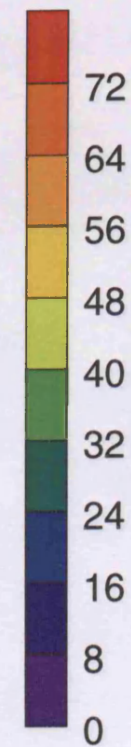
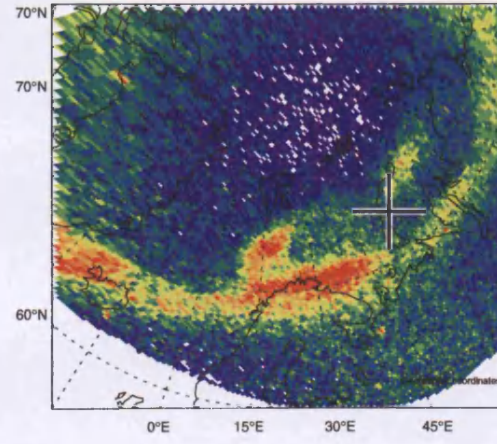
09-04-96 20:01:34



09-04-96 20:06:28

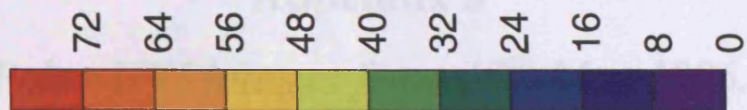


09-04-96 20:16:17

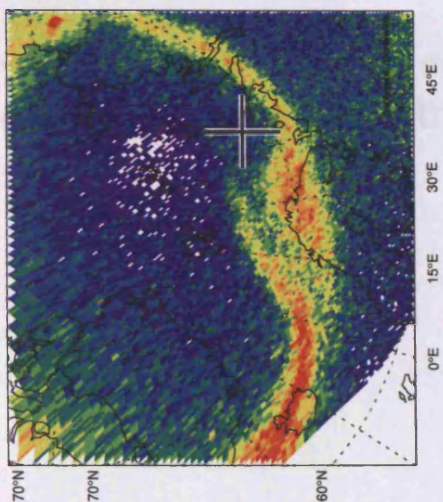


Intensity (photons)

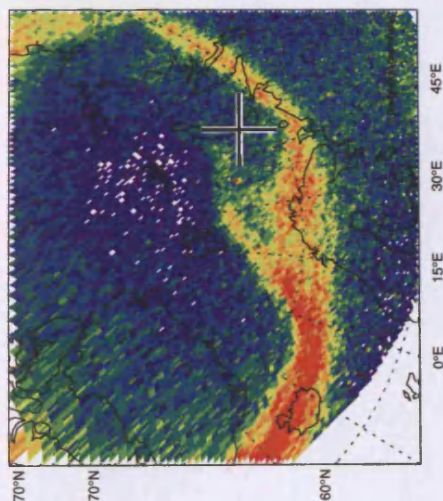
Intensity (photons)



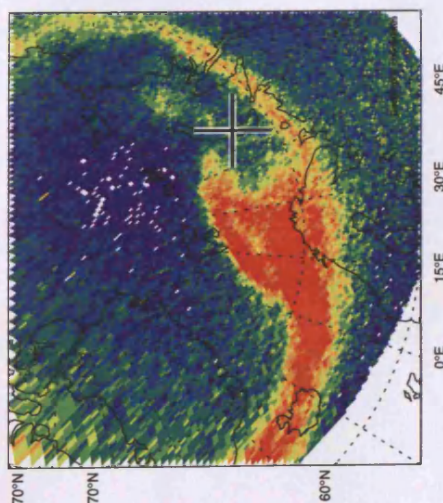
09-04-96 20:36:31



09-04-96 20:29:47



09-04-96 20:23:02

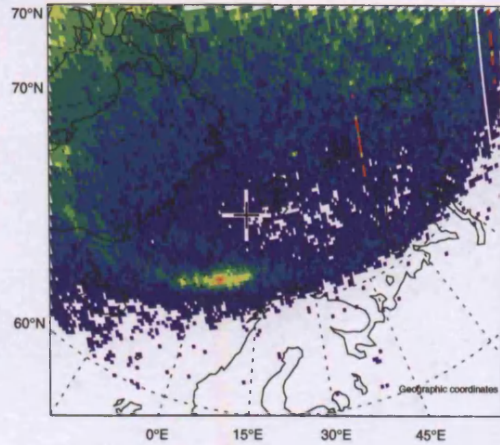


Appendix 3

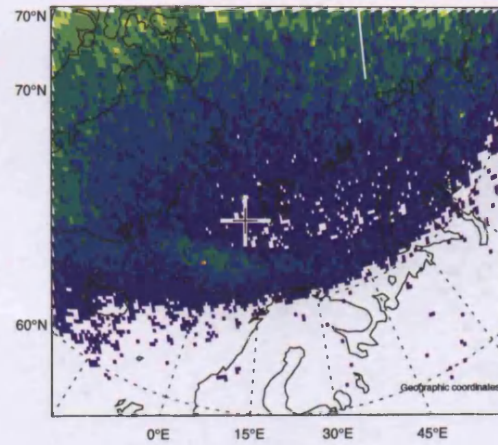
Polar UVI images from 17th May 1996.

The following pages contain images from the Ultra-Violet Imager on Polar taken on 17th May 1996 over the time interval 20:01 – 22:11 UT.

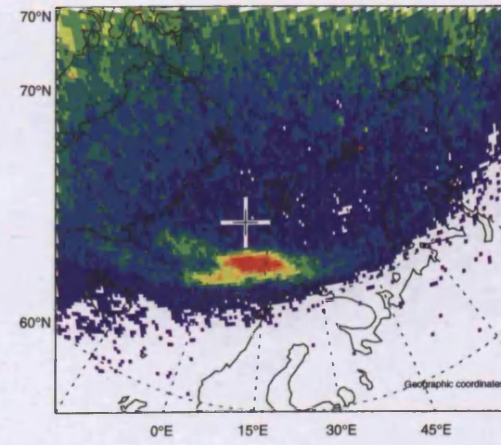
17-05-96 20:01:19



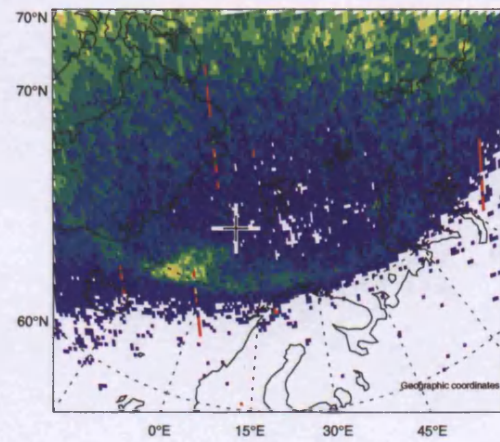
17-05-96 20:07:27



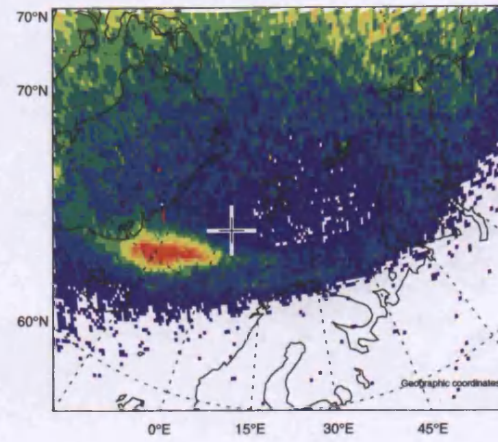
17-05-96 20:13:35



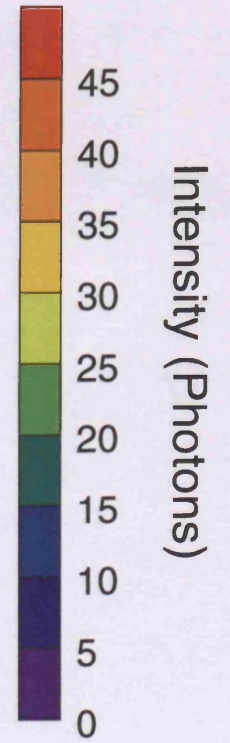
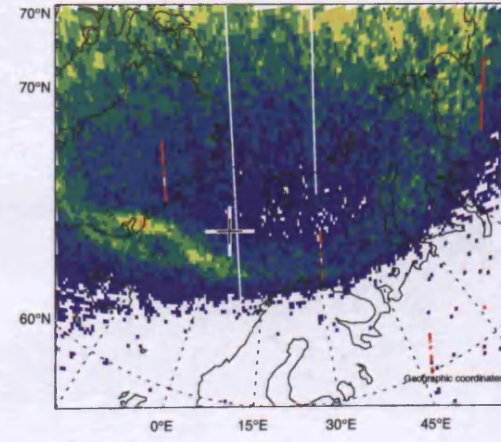
17-05-96 20:19:43



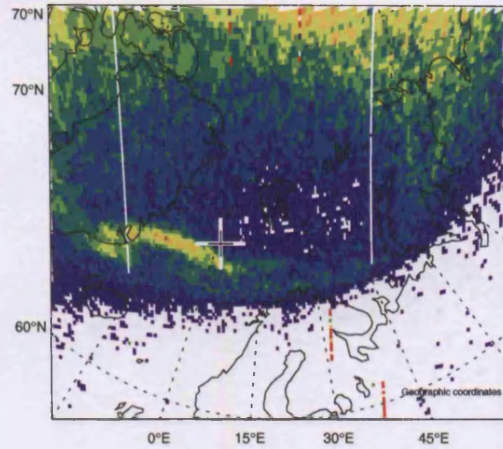
17-05-96 20:25:51



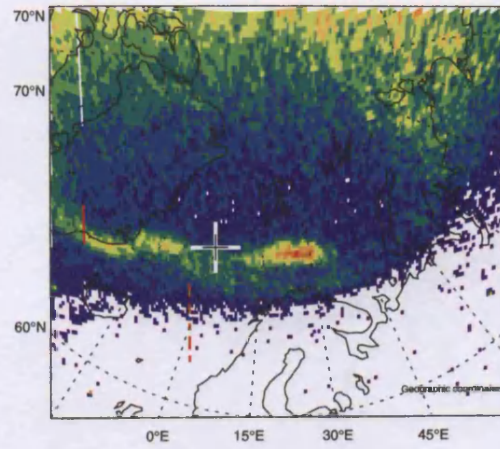
17-05-96 20:31:59



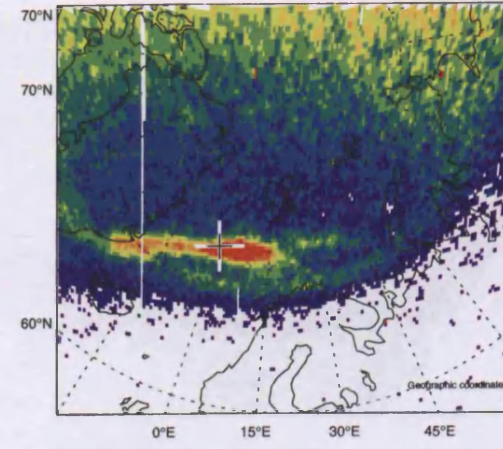
17-05-96 20:38:07



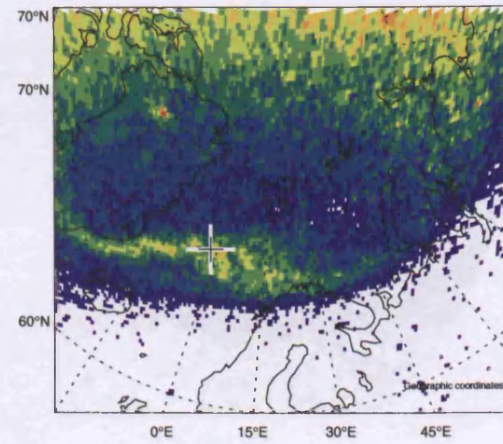
17-05-96 20:44:15



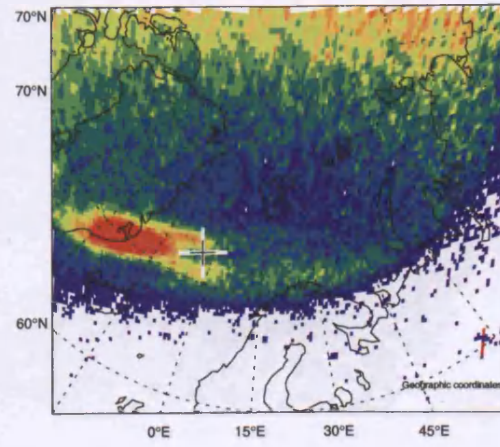
17-05-96 20:49:10



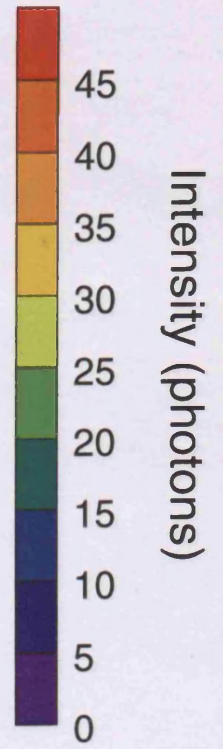
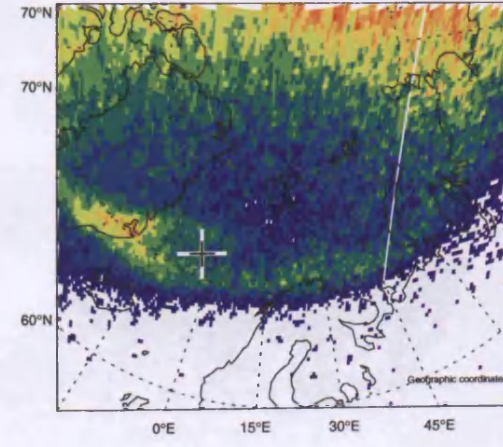
17-05-96 20:55:18



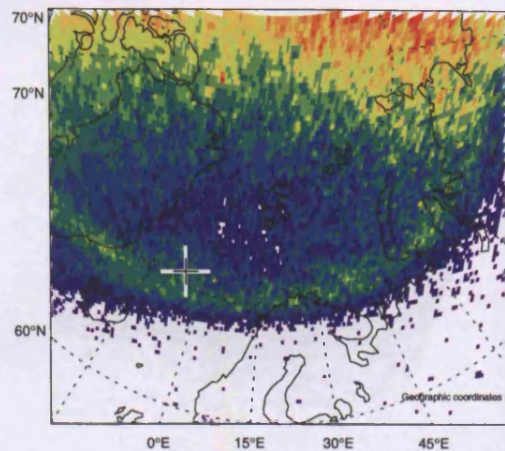
17-05-96 21:01:26



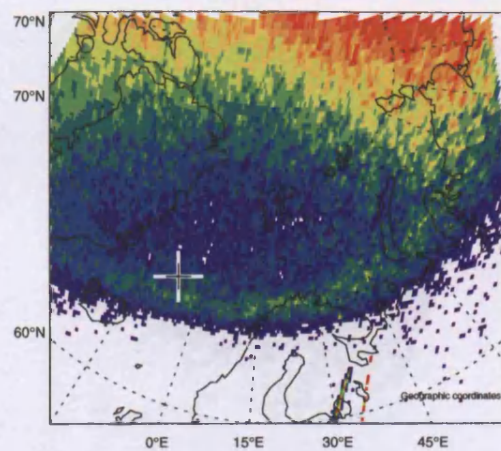
17-05-96 21:07:34



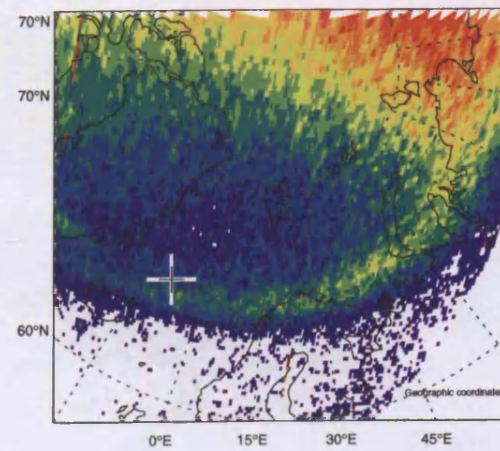
17-05-96 21:13:42



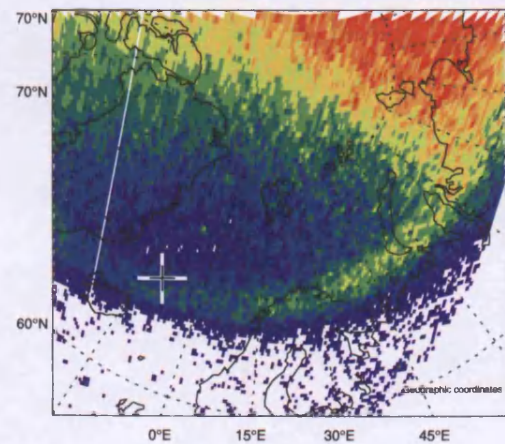
17-05-96 21:19:50



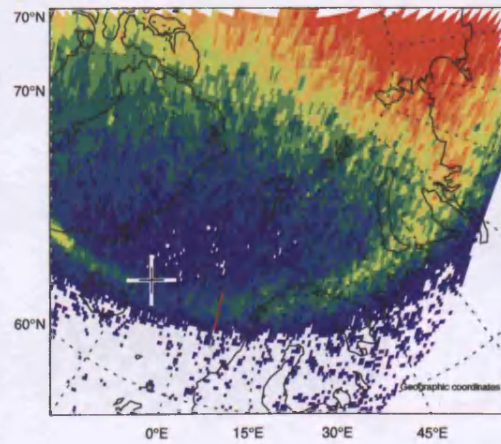
17-05-96 21:29:02



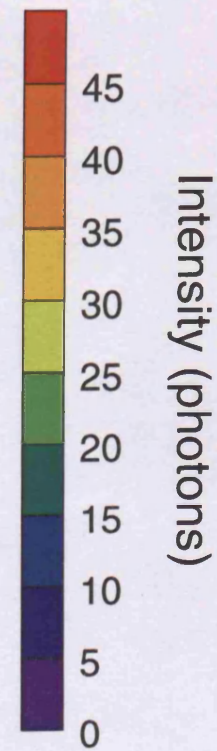
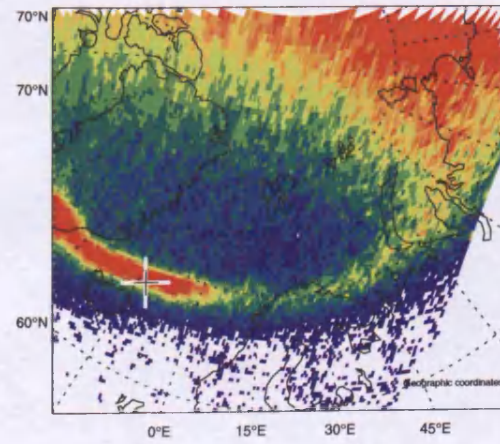
17-05-96 21:35:10



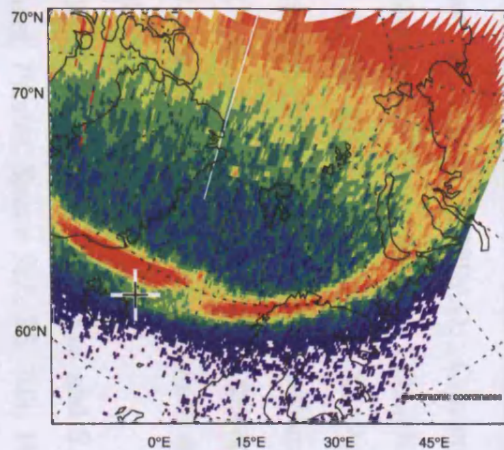
17-05-96 21:41:18



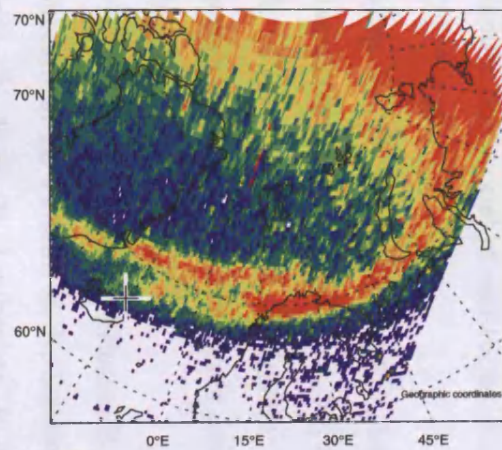
17-05-96 21:47:26



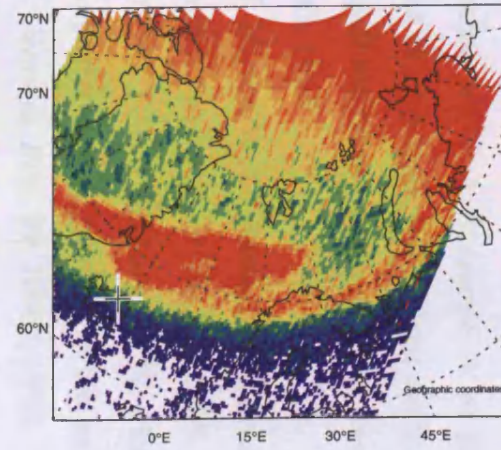
17-05-96 21:53:34



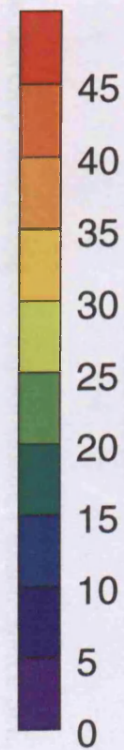
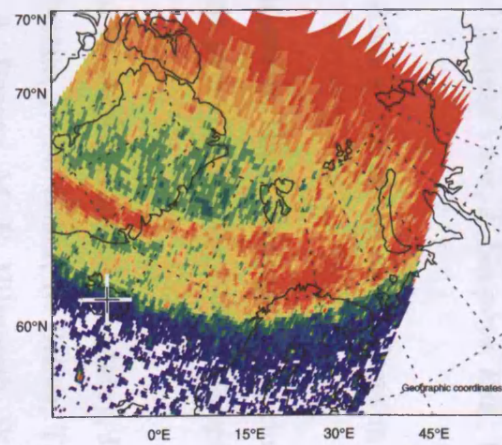
17-05-96 21:59:23



17-05-96 22:05:50



17-05-96 22:11:58



Intensity (photons)

References

- Akasofu, S. I., The development of the auroral substorm, *Planet. Space Sci.*, **12**, 273, 1964.
- Akasofu, S. I., *Polar and Magnetospheric Substorms*, D. Reidel Publ., 1968.
- Angelopoulos, V., V. A. Sergeev, D. N. Baker, D. G. Mitchell, G. D. Reeves, C. T. Russell and H. J. Singer, Multi-point study of bursty bulk flow events during a sequence of small substorms, *Proc. of the Second International Conference on Substorms (ICS-2)*, 643, 1994.
- Bahcall J. N. and W. C. Haxton, Matter-enhanced neutrino oscillations in the standard solar model, *Phys. Rev. D*, **40**, 931, 1989.
- Baker, D. N., T. I. Pulkkinen, E. W. Hones Jr., R. D. Belian, R. L. McPherron and V. Angelopoulos, Signatures of the substorm recovery phase at high-altitude spacecraft, *J. Geophys. Res.*, **99**, 10967, 1994.
- Baker, D. N., T. I. Pulkkinen, V. Angelopoulos, W. Baumjohann and R. L. McPherron, Neutral line model of substorms: Past results and present view, *J. Geophys. Res.*, **101**, 12975, 1996.
- Baumjohann, W., G. Paschmann and H. Lühr, Characteristics of high-speed ion flows in the plasma sheet, *J. Geophys. Res.*, **95**, 3801, 1990.
- Belian, R. D., G. R. Gisler, T. E. Cayton, and R. Christensen, High Z energetic particles at geosynchronous orbit during the great solar proton event of October 1989, *J. Geophys. Res.*, **97**, 16897, 1992.
- Blake, J. B., J. F. Fennell, L. M. Friesen, B. M. Johnson, W. A. Kolasinski, D. J. Mabry, J. V. Osborn, S. H. Penzin, E. R. Schnauss, H. E. Spence, D. N. Baker, R. Belian, T. A. Fritz, W. Ford, B. Laubscher, R. Stiglich, R. A. Baraze, M. F. Hilsenrath, W. L. Imhof, J. R. Kilner, J. Mobilia, D. H. Voss, A. Korth, M. Güll, K. Fisher, M. Grande and D. Hall, CEPPAD: Comprehensive Energetic Particle and Pitch Angle Distribution Experiment on POLAR, *Space Sci. Rev.*, **71**, 531, 1995.
- Büchner, J., M. Kuznetsova and L. M. Zelenyi, Sheared field tearing mode instability and creation of flux ropes in the Earth magnetotail, *Geophys. Res. Lett.*, **18**, 385, 1991.
- Cattell, C. A. and F. S. Mozer, Substorm electric fields in the Earth's magnetotail, in *Magnetic Reconnection in Space and Laboratory Plasmas*, *Geophys. Monogr. Ser.*, **30**, 208, 1984.
- Chao, J. K., J. R. Kan, A. T. Y. Lui and S. -I. Akasofu, A model for thinning of the plasma sheet, *Planet. Space Sci.*, **25**, 703, 1977.
- Chapman, S. and V. C. A. Ferraro, A new theory for magnetic storms, *Nature*, 126, 1930.

- Clauer, C. R. and R. L. McPherron, Mapping the local time-universal time development of magnetospheric substorms using mid-latitude magnetic observatories, *J. Geophys. Res.*, **79**, 2811, 1974.
- Cogger, L. L. and R. D. Elphinstone, The Viking Auroral Substorm, *Proc. of the International Conference on Substorms (ICS-1)*, 77, 1992.
- Cowley, S. W. H., Magnetic reconnection, in *Solar System Magnetic Fields*, edited by E. R. Priest, 1985.
- Cowley, S. W. H., The magnetosphere and its interaction with the solar wind and with the ionosphere, in *The behaviour of Systems in the Space Environment*, edited by R. N. DeWitt, 147, 1993.
- Daglis, I. A., N. P. Paschalidis, E. T. Sarris, W. I. Axford, G. Kremser, B. Wilken, and G. Gloeckler, Statistical features of the substorm expansion phase as observed by the AMPTEE/CCE spacecraft, in *Magnetospheric Substorms, Geophys. Monogr. Ser.*, **64**, 323, 1991.
- Dandouras, J., H. Rème, A. Saint-Marc and J. A. Sauvaud, A statistical study of plasma sheet dynamics using ISEE1 and 2 energetic particle flux data, *J. Geophys. Res.*, **91**, 6861, 1986a.
- Dandouras, J., A. Saint-Marc, H. Rème, J. A. Sauvaud and G. K. Parks, Particle dynamics of the plasma sheet boundary layer, *Adv. Space Res.*, **6**, 159, 1986b.
- Davis, T. N. and M. Sugiura, Auroral electrojet activity index AE and its universal time variations, *J. Geophys. Res.*, **71**, 785, 1966.
- DeCoster, R. J. and L. A. Frank, Observations pertaining to the dynamics of the plasma sheet, *J. Geophys. Res.*, **84**, 5099, 1979.
- Deforest, S. E. and C. E. McIlwain, Plasma clouds in the magnetosphere, *J. Geophys. Res.*, **76**, 3587, 1971.
- Dessler, A. J. and E. J. Parker, Hydromagnetic theory of magnetic storms, *J. Geophys. Res.*, **64**, 2239, 1959.
- Dungey, J. W., Interplanetary magnetic field and the auroral zones, *Phys. Rev. Lett.*, **6**, 47, 1961.
- Eastman, T. E., L. A. Frank, W. K. Peterson and W. Lennartsson, The Plasma Sheet Boundary Layer, *J. Geophys. Res.*, **89**, 1553, 1984.
- Elphinstone, R. D. and D. J. Hearn, Mapping of the auroral distribution during quiet times and substorm recovery, *Proc. of the International Conference on Substorms (ICS-1)*, 13, 1992.

- Elphinstone, R. D., J. S. Murphree and L. L. Cogger, What is a global auroral substorm, *Rev. Geophys.*, **34**, 169, 1996.
- Fairfield, D. H., Magnetotail energy storage and the variability of the magnetotail current sheet, in *Magnetic Reconnection in Space and Laboratory*, *Geophys. Monogr. Ser.*, **30**, 168, 1984.
- Feldstein, Y. I., Geographical distribution of aurorae and auroral arcs azimuths, in *Investigations of Aurorae*, 1960.
- Feldstein, Y. I., Some problems concerning the morphology of auroras and magnetic disturbances at high latitudes, *Geomagn. Aeron.*, **3**, 183, 1963.
- Forbes, T. G., E. W. Hones Jr., S. J. Bame, J. R. Asbridge, G. Paschmann, N. Sckopke and C. T. Russell, Evidence for the tailward retreat of a magnetic neutral line in the magnetotail during substorm recovery, *Geophys. Res. Lett.*, **8**, 261, 1981.
- Friis-Christensen, E., M. A. McHenry, C. R. Clauer, and S. Vennerstrøm, Ionospheric travelling convection vortices observed near the polar cleft: a triggered response to sudden changes in the solar wind, *Geophys. Res. Lett.*, **15**, 253, 1988.
- Grande, M., C. H. Perry, J. B. Blake, M. W. Chen, J. W. Fennell and B. Wilken, Observations of iron, silicon and other heavy-ions in the geostationary altitude region during late March 1991, *J. Geophys. Res.*, **101**, 24707, 1996.
- Haerendel, G., Disruption, ballooning or auroral avalanche – on the cause of substorms, *Proc. of the International Conference on Substorms (ICS-1)*, 417, 1992.
- Hall, A. M., Composition and morphology of substorm-associated ion injections, *Postgraduate Thesis*, 13, 1997.
- Hasegawa, A., Generation of field-aligned current during substorm, in *Dynamics of the Magnetosphere*, edited by S. I- Akasofu, 529, 1979.
- Hesse, M., and J. Birn, On dipolarization and its relation to the substorm current wedge, *J. Geophys. Res.*, **96**, 19417, 1991.
- Hones, E. W., J. R. Asbridge, S. J. Bame, M. D. Montgomery, S. Singer, and S. –I. Akasofu, Measurements of magnetotail plasma flow made with VELA 4B, *J. Geophys. Res.*, **77**, 5503, 1972.
- Hones, E. W., Transient phenomena in the magnetotail and their relation to substorms, *Space Sci. Rev.*, **23**, 393, 1979.
- Hones, E. W., T. Pytte and H. I. West, Associations of geomagnetic activity with plasma sheet thinning and expansion: A statistical study, *J. Geophys. Res.*, **89**, 5471, 1984.

- Hones, E. W., Poleward leaping auroras, the substorm expansive and recovery phases and the recovery of the plasma sheet, *Proc. of the International Conference on Substorms (ICS-1)*, 477, 1992.
- Kan, J. R., On the structure of the magnetotail current sheet, *J. Geophys. Res.*, **78**, 3773, 1973.
- Kan, J. R. and W. Sun, Simulation of the westward travelling surge and Pi2 pulsations during substorms, *J. Geophys. Res.*, **90**, 10911, 1985.
- Kan, J. R., A globally integrated substorm model: Tail reconnection and magnetosphere-ionosphere coupling, *J. Geophys. Res.*, **103**, 11787, 1998.
- Kennel, C. F., The Kiruna conjecture: The strong version, *Proc. of the International Conference On Substorms (ICS-1)*, 599, 1992.
- Kivelson, M. G. and C. T. Russell, *Introduction to Space Physics*, Cambridge University Press, 1995.
- Kokubun, S. and R. L. McPherron, Substorm signatures at synchronous altitude, *J. Geophys. Res.*, **86**, 1265, 1981.
- Koskinen, H. E. J., R. E. Lopez, R. J. Pellinen, T. I. Pulkkinen, D. N. Baker and T. Bösinger, Pseudobreakup and substorm growth phase in the ionosphere and magnetosphere, *J. Geophys. Res.*, **98**, 5801, 1993.
- Krimigis, S. M., G. Gloeckler, R. W. McEntire, T. A. Potemra, F. L. Scarf and E. G. Shelley, Magnetic storm of 4 September 1985: A synthesis of ring current spectra and energy densities measured with AMPTE/CCE, *Geophys. Res. Lett.*, **12**, 329, 1985.
- Lepping, R. P., M. H. Acuna, L. F. Burlaga, W. M. Farrell, J. A. Slavin, K. H. Schatten, F. Mariani, N. F. Ness, F. M. Neubauer, Y. C. Whang, J. Byrnes, R. S. Kennon, P. V. Panetta, J. Scheifele and E. M. Worley, The Wind magnetic field investigation, *Space Sci. Rev.*, **71**, 207, 1995.
- Lester, M., W. J. Hughes and H. J. Singer, Polarisation Patterns of Pi2 Magnetic Pulsations and the Substorm Current Wedge, *J. Geophys. Res.*, **88**, 7958, 1983.
- Lester, M., O. de la Beaujardiere, J. C. Foster, M. P. Freeman, H. Lühr, J. M. Ruohoniemi and W. Swider, The response of the large scale ionospheric convection pattern to changes in the IMF and substorms: Results from the SUNDIAL 1987 campaign. *Ann. Geophys.*, **11**, 556, 1993.
- Lui, A. T. Y., E. W. Hones Jr., F. Yasuhura, S.-I. Akasofu and S. J. Bame, Magnetotail plasma flow during plasma sheet expansions: VELA 5 and 6 and IMP 6 observations, *J. Geophys. Res.*, **82**, 1235, 1977.
- Lui, A. T. Y., T. E. Eastman, D. J. Williams and L. A. Frank, Observations of ion streaming during substorms, *J. Geophys. Res.*, **88**, 7753, 1983.

- Lui, A. T. Y., A. Mankofsky, C. -L. Chang, K. Papadopolous and C. S. Wu, A current disruption mechanism in the neutral sheet: a possible trigger for substorm expansions, *Geophys. Res. Lett.*, **17**, 745, 1990.
- Lui, A. T. Y., C. -L. Chang, A. Mankofsky, H. -K. Wong and D. Winske, A cross-field current instability for substorm expansions, *J. Geophys. Res.*, **96**, 11389, 1991.
- McPherron, R. L, Growth phase of magnetospheric substorms, *J. Geophys. Res.*, **75**, 5592, 1970.
- McPherron, R. L, C. T. Russell and M. P. Aubry, Satellite studies of magnetospheric substorms on August 15, 1968, 9, phenomenological model for substorms, *J. Geophys. Res.*, **78**, 3131, 1973.
- McPherron, R. L, Physical processes producing magnetospheric substorms and magnetic storms, *Geomagnetism*, **4**, 593, 1991.
- McPherron, R. L., V. Angelopoulos, D. N. Baker, and E. W. Hones Jr., Is there a Near-Earth Neutral Line? *Adv. Space Res.*, **13**, 173, 1993.
- Milan, S. E., Observations of HF radiowaves propagated over high latitude paths, *Postgraduate Thesis*, 1994.
- Moldwin, M. B., M. F. Thomsen, S. J. Bame, D. J. McComas, L. A. Weiss, G. D. Reeves and R. D. Belian, The appearance of plasmaspheric plasma in the outer magnetosphere in association with the substorm growth phase, *Geophys. Res. Lett.*, **23**, 801, 1996.
- Nagai, T., Observed magnetic substorm signatures at synchronous altitude, *J. Geophys. Res.*, **87**, 4405, 1982.
- Nagai, T., An empirical model of substorm-related magnetic field variations at synchronous orbit, in *Magnetospheric Substorms, Geophys. Monogr. Ser.*, **64**, 91, 1991.
- Nagai, T., R. Nakamura, T. Mukai, T. Yamamoto, A. Nishida and S. Kokubun, Substorms, tail flows, and plasmoids, *Adv. In Space Res.*, **20**, 961, 1997.
- Nakamura, M., G. Paschmann, W. Baumjohann, and N. Sckopke, Ion distributions and flows in and near the plasma sheet boundary layer, *J. Geophys. Res.*, **97**, 1449, 1992.
- Ogilvie, K. W., D. J. Chornay, R. J. Fritzenreiter, F. Hunsaker, J. Keller, J. Lobell, G. Miller, J. D. Scudder, E. C. Sittler, R. B. Torbert, D. Bodet, G. Needell, A. J. Lazarus, J. T. Steinberg, J. H. Tappan, A. Mavretic and E. Gergin, SWE, a comprehensive plasma instrument for the Wind spacecraft, *Space Sci. Rev.*, **71**, 55, 1995.
- Parker, E. N., *Interplanetary Dynamical Processes*, Wiley-Interscience, 1963.
- Pulkkinen, T. I., H. E. Koskinen and R. J. Pellinen, Mapping of auroral arcs during substorm growth phase, *J. Geophys. Res.*, **96**, 21087, 1991.

- Reeves, G. D., R. D. Belian and T. A. Fritz, Numerical tracing of energetic particle drifts in a model magnetosphere, *J. Geophys. Res.*, **96**, 13997, 1991.
- Roederer, J. G., *Dynamics of Geomagnetically Trapped Radiation*, Springer-Verlag, 1970.
- Rostoker, G. and T. E. Eastman, A boundary layer model for magnetospheric substorms, *J. Geophys. Res.*, **92**, 12187, 1987.
- Roux, A., Generation of field-aligned current structures at substorm onsets, *Proc. ESA Workshop on Future Missions in Solar, Heliospheric and Space Plasma Physics*, ESA Spec. Publ., 151, 1985.
- Roux, A., S. Perraut, P. Robert, A. Morane, A. Pedersen, A. Korth, G. Kremser, B. Aparicio, D. Rodgers and R. Pellinen, Plasma sheet instability related to the westward travelling surge, *J. Geophys. Res.*, **96**, 17697, 1991.
- Russell, C. T., R. C. Snare, J. D. Means, D. Pierce, D. Dearborn, M. Larson, G. Barr, and G. Le, The GGS/Polar magnetic fields investigation, *Space Sci. Rev.*, **71**, 563, 1995.
- Sauvaud, J. A., A. Saint-Marc, J. Dandouras, H. Reme, A. Korth, G. Kremser and G. K. Parks, A multi-satellite study of the plasma sheet dynamics at substorm onset, *Geophys. Res. Lett.*, **11**, 500, 1984.
- Sauvaud, J. A. Characteristics of the cross-tail current disruption at substorm onset and associated particle acceleration, *Proc. of the International Conference On Substorms (ICS-1)*, 243, 1992.
- Scudder, J., F. Hunsacker, G. Miller, J. Lobell, T. Zawistowski, K. Ogilvie, J. Keller, D. Chornay, F. Herrero, R. Fitzenreiter, D. Fairfield, J. Needell, D. Bodet, J. Googins, C. Kletzing, R. Torbert, J. Vandiver, R. Bentley, W. Fillius, C. McIlwain, E. Whipple and A. Korth, Hydra – a 3-dimensional electron and ion hot plasma instrument for the Polar spacecraft of the GGS mission, *Space Sci. Rev.*, **71**, 459, 1995.
- Schindler, K., A theory of the substorm mechanism, *J. Geophys. Res.*, **79**, 2803, 1974.
- Sergeev, V. A., V. Angelopoulos, D. G. Mitchell and C. T. Russell, In situ observations of magnetotail reconnection prior to the onset of a small substorm, *J. Geophys. Res.*, **100**, 19121, 1995.
- Shiokawa, K., W. Baumjohann and G. Haerendel, Braking of high-speed flows in the near-Earth tail, *Geophys. Res. Lett.*, **24**, 1179, 1997.
- Shiokawa, K., W. Baumjohann, G. Haerendel, G. Paschmann, J. F. Fennell, E. Friis-Christensen, H. Lühr, G. D. Reeves, C. T. Russell, P. R. Sutcliffe and K. Takahashi, High-speed ion flow, substorm current wedge, and multiple Pi2 pulsations, *J. Geophys. Res.*, **103**, 4491, 1998.
- Smith, R. A., C. K. Goertz and W. Grossman, Thermal catastrophe in the plasma sheet boundary layer, *Geophys. Res. Lett.*, **13**, 1380, 1986.

- Torr, M., D. G. Torr, M. Zukic, R. B. Johnson, J. Ajello, P. Banks, K. Clark, K. Cole, C. Keffer, G. Parks, B. Tsurutani, J. Spann, A far ultraviolet imager for the International Solar-Terrestrial Physics Mission, *Sp. Sc. Rev.*, **71**, 329, 1995.
- Viljanen, A. and L. Häkkinen, IMAGE magnetometer network. In: Satellite-Ground Based Coordination Sourcebook, ESA publications SP-1198, 111, 1997.
- Wilken, B., W. Weib, D. Hall, M. Grande, F. Søråas and J. F. Fennell, Magnetospheric ion composition spectrometer onboard the CRRES spacecraft, *J. Spacecraft and Rockets*, **29**, 585, 1992.
- Williams, D. J., Energetic ion beams at the edge of the plasma sheet: ISEE 1 observations plus a simple explanatory model, *J. Geophys. Res.*, **86**, 5507, 1981.
- Yeoman, T.K., D.K. Milling, and D. Orr, Pi2 pulsation polarisation patterns on the U.K. sub-auroral magnetometer network (SAMNET), *Planet. Space Sci.*, **38**, 589, 1990.